Jordan Journal of
PHYSICS
An International Peer-Reviewed Research Journal

Volume 18, No. 5, Dec. 2025, Rajab 1447 H

Jordan Journal of Physics (*JJP*): An International Peer-Reviewed Research Journal funded by the Scientific Research and Innovation Support Fund, Jordan, and published quarterly by the Deanship of Research and Graduate Studies, Yarmouk University, Irbid, Jordan.

Manuscripts should be submitted to:

Prof. Muhammad S. Bawa'aneh
Editor-in-Chief, Jordan Journal of Physics
Deanship of Research and Graduate Studies
Yarmouk University-Irbid-Jordan
Tel. 00 962 2 7211111 Ext. 2075
E-mail: *jjp@yu.edu.jo*
Website: *https://jjp.yu.edu.jo*

Jordan Journal of
PHYSICS
An International Peer-Reviewed Research Journal

Volume 18, No. 5, Dec. 2025, Rajab 1447 H

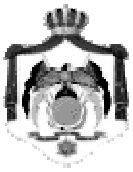

The Hashemite Kingdom of Jordan

Yarmouk University

Jordan Journal of PHYSICS

An International Peer-Reviewed Research Journal

Funded by the Scientific Research and Innovation Support Fund

Volume 18, No. 5, Dec. 2025, Rajab 1447 H

Instructions to Authors

Instructions to authors concerning manuscript organization and format apply to hardcopy submission by mail, and also to electronic online submission via the Journal homepage website (http://jjp.yu.edu.jo).

Manuscript Submission

Manuscripts are submitted electronically through the journal's website:

https://jjp.yu.edu.jo/

Original *Research Articles*, *Communications* and *Technical Notes* are subject to critical review by minimum of two competent referees. Authors are encouraged to suggest names of competent reviewers. *Feature Articles* in active Physics research fields, in which the author's own contribution and its relationship to other work in the field constitute the main body of the article, appear as a result of an invitation from the Editorial Board, and will be so designated. The author of a *Feature Article* will be asked to provide a clear, concise and critical status report of the field as an introduction to the article. *Review Articles* on active and rapidly changing Physics research fields will also be published. Authors of *Review Articles* are encouraged to submit two-page proposals to the Editor-in-Chief for approval. Manuscripts submitted in *Arabic* should be accompanied by an Abstract and Keywords in English.

Organization of the Manuscript

Manuscripts should be typed double spaced on one side of A4 sheets (21.6 x 27.9 cm) with 3.71 cm margins, using Microsoft Word 2000 or a later version thereof. The author should adhere to the following order of presentation: Article Title, Author(s), Full Address and E-mail, Abstract, PACS and Keywords, Main Text, Acknowledgment. Only the first letters of words in the Title, Headings and Subheadings are capitalized. Headings should be in **bold** while subheadings in *italic* fonts.

Title Page: Includes the title of the article, authors' first names, middle initials and surnames and affiliations. The affiliation should comprise the department, institution (university or company), city, zip code and state and should be typed as a footnote to the author's name. The name and complete mailing address, telephone and fax numbers, and e-mail address of the author responsible for correspondence (designated with an asterisk) should also be included for official use. The title should be carefully, concisely and clearly constructed to highlight the emphasis and content of the manuscript, which is very important for information retrieval.

Abstract: A one paragraph abstract not exceeding 200 words is required, which should be arranged to highlight the purpose, methods used, results and major findings**.**

Keywords: A list of 4-6 keywords, which expresses the precise content of the manuscript for indexing purposes, should follow the abstract.

PACS: Authors should supply one or more relevant PACS-2006 classification codes, (available at http://www.aip.org/pacs/pacs06/pacs06-toc.html)

Introduction: Should present the purpose of the submitted work and its relationship to earlier work in the field, but it should not be an extensive review of the literature (e.g., should not exceed 1 ½ typed pages).

Experimental Methods: Should be sufficiently informative to allow competent reproduction of the experimental procedures presented; yet concise enough not to be repetitive of earlier published procedures.

Results: should present the results clearly and concisely.

Discussion: Should be concise and focus on the interpretation of the results.

Conclusion: Should be a brief account of the major findings of the study not exceeding one typed page.

Acknowledgments: Including those for grant and financial support if any, should be typed in one paragraph directly preceding the References.

References: References should be typed double spaced and numbered sequentially in the order in which they are cited in the text. References should be cited in the text by the appropriate Arabic numerals, enclosed in square brackets. Titles of journals are abbreviated according to list of scientific periodicals. The style and punctuation should conform to the following examples:

1. Journal Article:

a) Heisenberg, W., Z. Phys. 49 (1928) 619.
b) Bednorz, J. G. and Müller, K. A., Z. Phys. B64 (1986) 189
c) Bardeen, J., Cooper, L.N. and Schrieffer, J. R., Phys. Rev. 106 (1957) 162.
d) Asad, J. H., Hijjawi, R. S., Sakaji, A. and Khalifeh, J. M., Int. J. Theor. Phys. 44(4) (2005), 3977.

2. Books with Authors, but no Editors:

a) Kittel, C., "Introduction to Solid State Physics", 8th Ed. (John Wiley and Sons, New York, 2005), chapter 16.
b) Chikazumi, S., C. D. Graham, JR, "Physics of Ferromagnetism", 2nd Ed. (Oxford University Press, Oxford, 1997).

3. Books with Authors and Editors:

a) Allen, P. B. "Dynamical Properties of Solids", Ed. (1), G. K. Horton and A. A. Maradudin (North-Holland, Amsterdam, 1980), p137.
b) Chantrell, R. W. and O'Grady, K., "Magnetic Properities of Fine Particles" Eds. J. L. Dormann and D. Fiorani (North-Holland, Amsterdam, 1992), p103.

4. Technical Report:

Purcell, J. "The Superconducting Magnet System for the 12-Foot Bubble Chamber", report ANL/HEP6813, Argonne Natt. Lab., Argonne, III, (1968).

5. Patent:

Bigham, C. B., Schneider, H. R., US patent 3 925 676 (1975).

6. Thesis:

Mahmood, S. H., Ph.D. Thesis, Michigan State University, (1986), USA (Unpublished).

7. Conference or Symposium Proceedings:

Blandin, A. and Lederer, P. Proc. Intern. Conf. on Magnetism, Nottingham (1964), P.71.

8. Internet Source:

Should include authors' names (if any), title, internet website, URL, and date of access.

9. Prepublication online articles (already accepted for publication):

Should include authors' names (if any), title of digital database, database website, URL, and date of access.

For other types of referenced works, provide sufficient information to enable readers to access them.

Tables: Tables should be numbered with Arabic numerals and referred to by number in the Text (e.g., Table 1). Each table should be typed on a separate page with the legend above the table, while explanatory footnotes, which are indicated by superscript lowercase letters, should be typed below the table.

Illustrations: Figures, drawings, diagrams, charts and photographs are to be numbered in a consecutive series of Arabic numerals in the order in which they are cited in the text. Computer-generated illustrations and good-quality digital photographic prints are accepted. They should be black and white originals (not photocopies) provided on separate pages and identified with their corresponding numbers. Actual size graphics should be provided, which need no further manipulation, with lettering (Arial or Helvetica) not smaller than 8 points, lines no thinner than 0.5 point, and each of uniform density. All colors should be removed from graphics except for those graphics to be considered for publication in color. If graphics are to be submitted digitally, they should conform to the following minimum resolution requirements: 1200 dpi for black and white line art, 600 dpi for grayscale art, and 300 dpi for color art. All graphic files must be saved as TIFF images, and all illustrations must be submitted in the actual size at which they should appear in the journal. Note that good quality hardcopy original illustrations are required for both online and mail submissions of manuscripts.

Text Footnotes: The use of text footnotes is to be avoided. When their use is absolutely necessary, they should be typed at the bottom of the page to which they refer, and should be cited in the text by a superscript asterisk or multiples thereof. Place a line above the footnote, so that it is set off from the text.

Supplementary Material: Authors are encouraged to provide all supplementary materials that may facilitate the review process, including any detailed mathematical derivations that may not appear in whole in the manuscript.

Revised Manuscript and Computer Disks

Following the acceptance of a manuscript for publication and the incorporation of all required revisions, authors should submit an original and one more copy of the final disk containing the complete manuscript typed double spaced in Microsoft Word for Windows 2000 or a later version thereof. All graphic files must be saved as PDF, JPG, or TIFF images.

Allen, P.B., "…….", in: Horton, G.K., and Muradudin, A. A., (eds.), "Dynamical…….", (North……..), pp….

Reprints

Twenty (20) reprints free of charge are provided to the corresponding author. For orders of more reprints, a reprint order form and prices will be sent with the article proofs, which should be returned directly to the Editor for processing.

Copyright

Disclaimer

Indexing

JJP is currently indexing in:

<table>
<tr><td> 
</td><td>Emerging Sources Citation Index (ESCI)

Journal Impact Factor 2022

0.7</td></tr>
<tr><td colspan="2"> 
</td></tr>
</table>

Jordan Journal of
PHYSICS
An International Peer-Reviewed Research Journal

Volume 18, No. 5, Dec. 2025, Rajab 1447 H

Table of Contents:

Volume 18, Number 5, 2025. pp. 561-571

Jordan Journal of Physics

ARTICLE

Exploring Strongly Correlated Rare-Earth Intermetallics: Theoretical Insights into RIn_3 and RSn_3 (R = Sm, Eu, Gd)

Aman Kumar[a] and **Anuj Kumar**[b]

[a] *Department of Physics, Faculty of Science, Swami Vivekanand Subharti University, Meerut, Uttar Pradesh, India.*

[b] *Department of Physics, Mahamaya Government Degree College, Sherkot, Bijnore, India.*

Doi: **https://doi.org/10.47011/18.5.1**

Received on: 23/11/2023; *Accepted on: 13/03/2025*

Abstract: The structural, electronic, magnetic, and elastic properties of Rin_3 and RSn_3 (R = Sm, Eu, Gd) were thoroughly investigated using the full potential linearized augmented plane wave plus local orbital (FP-LAPW+lo) method within the framework of density functional theory (DFT). Structural properties were evaluated using the local density approximation (LDA), generalized gradient approximation (GGA), and their band-correlated extensions, LDA+U and GGA+U. The computed lattice parameters exhibited excellent agreement with experimental results, and the divalent state of Eu was confirmed. To accurately predict the electronic properties, spin-orbit coupling (SOC) was incorporated, along with the splitting of the 4f states in rare-earth elements. Elastic properties, including bulk modulus, shear modulus, Young's modulus, anisotropic ratio, Kleinman parameters, Poisson's ratio, Lamé coefficients, sound velocities for shear and longitudinal waves, and Debye temperature, were calculated. Additionally, the Cauchy pressure and the B/G ratio were analyzed to determine the ductile or brittle nature of these compounds.

Keywords: Electronic properties, LDA+U, GGA+U, Elastic properties.

Introduction

Rare-earth elements, particularly those of the lanthanide series, are distinguished by their incomplete 4f electron shell, with unpaired electrons in the 4f subshell playing a pivotal role in determining their physical properties and those of their compounds [1-2]. Rare-earth intermetallic compounds have drawn substantial attention due to their unique properties, such as high melting points, excellent high-temperature ductility, superior mechanical strength, and advantageous electrical and magnetic characteristics. These attributes render them highly suitable for applications in the automotive, aviation, and aerospace industries. Additionally, rare-earth intermetallics outperform other metals by offering enhanced strength and stiffness, low specific weight, and excellent corrosion resistance, making them ideal for the development of commercial aviation turbines [3]. Approximately 90% of intermetallic compounds exhibit ductility due to the lack of d electrons near the Fermi level [4]. The intermetallic complexes RIn_3 and RSn_3 (R = rare-earth element) demonstrate intriguing properties arising from their incomplete 4f shell. These properties include diverse magnetic topologies, transitions between magnetic and non-magnetic states, valence fluctuations, and the formation of magnetic moments [5, 6]. Furthermore, RSn_3 intermetallic compounds have been identified as effective substitutes for lead, enhancing the efficiency of lead-free solder materials [7]. Rare-earth intermetallic compounds Rin_3 and RSn_3 (R = Sm, Eu, Gd) exhibit several remarkable properties [8, 9]. They adopt a cubic $AuCu_3$-type crystal structure within the space group *Pm-3m* (No. 221). In this structure, rare-earth atoms (R) occupy the 1a (0,

Corresponding Author: Aman Kumar **Email**: amankumar@gmail.com

0, 0) position, while non-magnetic elements like In and Sn are situated in the 3c position at (0, 1/2, 1/2). Most RIn_3 and RSn_3 compounds exhibit antiferromagnetic (AFM) ordering below 45 K [10-12]. Among the light rare-earth elements, the stability of Rin_3 and RSn_3 phases decreases from La to Gd [13]. Magnetic studies and lattice constant measurements confirm the characteristic lanthanide contraction of rare-earth elements, with exceptions observed in Eu and Yb compounds, where the rare-earth ions are divalent [14]. Antiferromagnetic transitions in the RIn_3 series occur at Néel temperatures (T_n) of 16, 10, and 42 K for $SmIn_3$, $EuIn_3$, and $GdIn_3$, respectively [15-17]. Similarly, in the RSn_3 series, $SmSn_3$, $EuSn_3$, and $GdSn_3$ exhibit antiferromagnetic transitions at T_n values of 12, 36.5, and 16.5 K, respectively [18]. Buschow *et al.* [12] investigated the magnetic properties and lattice parameters of the RIn_3 lanthanide family. Magnetic susceptibility measurements confirm that most compounds in the RIn_3 series exhibit antiferromagnetic ordering at low temperatures. Sanchez *et al*. [18] evaluated the electrical and magnetic properties of RSn_3 compounds (R = La, Ce, Pr, Nd, Sm, Eu, Gd, Yb) using Mössbauer spectroscopy, revealing complex magnetic structures in europium and gadolinium compounds. The Fermi surface properties of RIn_3 and RSn_3 were explored by Onuki and Settai [19], while Asadabadi *et al*. computed structural properties, such as lattice parameters and bulk modulus for RSn_3 (R = Sm, Eu, Gd), using local density approximation (LDA), generalized gradient approximation (GGA), and GGA+spin-polarized methods within the WIEN2K framework. Endoh *et al*. [20-21] conducted ultrasonic experiments to determine the elastic constants and investigated the influence of crystalline electric fields on the elastic constants of SmX compounds (X = Pd, In, Sn, Tl, Pb). Additionally, the role of rare-earth elements in RIn_3 and RSn_3 and their effects on electric field gradients (EFG) were analyzed by Asadabadi *et al*. [8] using density functional theory (DFT). Elastic constants play a crucial role in determining a material's response to external forces. They define the strength, brittleness, or ductility, and hardness of materials, while also providing valuable insights into bonding characteristics, anisotropy, and structural stability [22]. This study investigates the structural, electronic, elastic, and mechanical properties of rare-earth compounds RIn_3 and RSn_3 (R = Sm, Eu, Gd) using the full-potential linearized augmented plane wave plus local orbitals (FP-LAPW+lo) method within the framework of density functional theory (DFT).

Notably, this research is groundbreaking as it presents, for the first time, a detailed analysis of the elastic, mechanical, and thermal properties of these compounds through ab initio calculations.

Theoretical Method

This study utilized density functional theory (DFT) calculations implemented in the WIEN2K code [23] and employed the full-potential linearized augmented plane wave plus local orbitals (FP-LAPW+LO) method [24]. Exchange-correlation effects were computed using the local density approximation (LDA) [25] and generalized gradient approximation (GGA) [26], incorporating spin polarization. Recognizing Sn, Eu, and Gd as strongly correlated systems with localized 4f electrons, we applied the LDA+U and GGA+U methodologies to accurately determine their electronic structures. The GGA+U approach, based on the Hubbard model, effectively addresses strongly correlated systems by incorporating an orbital-dependent potential for Coulomb and exchange interactions [27]. Additionally, spin-orbit coupling (SOC) was included as a relativistic correction.

The muffin-tin sphere radii were set to 2.50 atomic units for rare-earth elements, tin, and indium. The basis set expansion was performed using plane waves with a product RMT × Kmax = 7, where RMT represents the smallest atomic radius in the unit cell, and Kmax is the largest k-vector value in the plane wave expansion. The angular momentum for the valence wave functions within the muffin-tin spheres was expanded up to lMAX = 10, and the charge density in the interstitial region was extended using Fourier analysis with a maximum reciprocal lattice vector of Gmax = 12. A dense k-point mesh of 165 k-points in the irreducible wedge of the Brillouin zone was generated using a Monkhorst-Pack grid of 18 × 18 × 18 [28], ensuring high accuracy in elastic property calculations.

The elastic constants (C_{11}, C_{12}, and C_{44}) were computed using the IR-elastic program implemented within the WIEN2K framework [29]. These calculations employed the GGA [26]

with spin polarization for the precise determination of elastic properties. Results were obtained for both spin-polarized and non-spin-polarized cases, and comparisons were made. Details regarding the IR-elastic methodology can be found in Ref. [30].

The energy-based methodology [31], as implemented in the WIEN2K code [23], was used to calculate the elastic constants. By employing Voigt notation and leveraging the symmetry of the cubic crystal lattice, the number of independent elastic constants was reduced to three: C_{11}, C_{12}, and C_{44}. This approach ensures computational efficiency while maintaining accuracy.

Result and Discussion

Structural and Electronic Properties

The structural properties of RIn_3 and RSn_3 (R = Sm, Eu, and Gd) were determined by calculating the total energy of the unit cell as a function of volume. Bulk moduli were derived using LDA, GGA, LDA+U, and GGA+U potentials. Table 1 compares the theoretically computed results with available experimental data. The GGA-derived lattice constants for $SmSn_3$ and $GdSn_3$ exhibit closer agreement with experimental values than those obtained using GGA+U. Conversely, the GGA+U lattice constant for $EuSn_3$ aligns better with experimental data compared to GGA. This suggests that $SmSn_3$ and $GdSn_3$ exhibit itinerant behavior, while $EuSn_3$ functions as a localized compound. These results confirm that $EuSn_3$ is a divalent system, whereas $SmSn_3$ and $GdSn_3$ are trivalent. A similar trend is observed in the RIn_3 compounds. As shown in Table 1, lattice constants contract progressively from Sm to Gd, a phenomenon attributable to the lanthanide contraction. This contraction arises from the reduction in atomic radius across the lanthanide series, caused by the insufficient shielding effect of the 4f electrons. Exceptions include Eu and Yb, which exhibit divalent behavior in their 4f series (e.g., $EuIn_3$ and $EuSn_3$). Our findings corroborate these trends for both the RIn_3 and RSn_3 series. The results also reveal that LDA and LDA+U tend to underestimate lattice parameters, consistent with the general behavior of these approximations. Bulk moduli for the compounds, computed using the Birch-Murnaghan equation of state [32], are presented in Table 1. Currently, no experimental data are available for the bulk moduli or their pressure derivatives; hence, our results serve as predictions for these properties in RIn_3 and RSn_3 (R = Sm, Eu, and Gd).

TABLE 1. The calculated value of lattice parameters (a_0 in A) and bulk modulus (B_0 in GPa) of RIn_3 and RSn_3 compounds.

Compound	E_{xc}	a_0	B_0
$SmIn_3$ This work	LSDA	4.5645	60.4711
	GGA	4.6246	53.6537
	LDA +U	4.5595	56.2006
	GGA+U	4.7198	52.0019
	Exp [36]	4.626	
$EuIn_3$ This work	LSDA	4.5707	63.7229
	GGA	4.6269	53.2488
	LDA +U	4.5639	63.2119
	GGA+U	4.7592	54.2521
$GdIn_3$ This work	LSDA	4.5167	62.3367
	GGA	4.5743	66.5797
	LDA +U	4.5075	66.2844
	GGA+U	4.6557	68.5292
	Exp [36]	4.607	
$SmSn_3$ This work	LSDA	4.6052	68.8160
	GGA	4.6545	54.4352
	LDA +U	4.6135	65.4388
	GGA+U	4.7523	54.2082
	Exp [18]	4.687	

Compound	E_{xc}	a_0	B_0
$EuSn_3$ This work	LSDA	4.6313	73.2400
	GGA	4.6727	52.9966
	LDA +U	4.6316	58.2304
	GGA+U	4.7742	44.4547
	Exp [18]	4.774	
$GdSn_3$ This work	LSDA	4.6412	61.0454
	GGA	4.6412	61.0453
	LDA +U	4.5947	72.2621
	GGA+U	4.7227	67.5417
	Exp [18]	4.678	

To investigate the electronic properties of the studied compounds, we combined the total density of states (DOS) and the 4f density of states using the local density approximation (LDA) and the generalized gradient approximation (GGA). Electronic correlations are significantly pronounced in systems with 4f orbital electrons, such as lanthanides. To better understand the effects of the 4f states, we employed LDA+U, GGA+U, and incorporated spin-orbit coupling (SOC). Figs. 1–3 display the total and 4f density of states calculated using various exchange-correlation potentials for RIn_3 and RSn_3 (R = Sm, Eu, and Gd), with the Fermi level set at 0 eV.

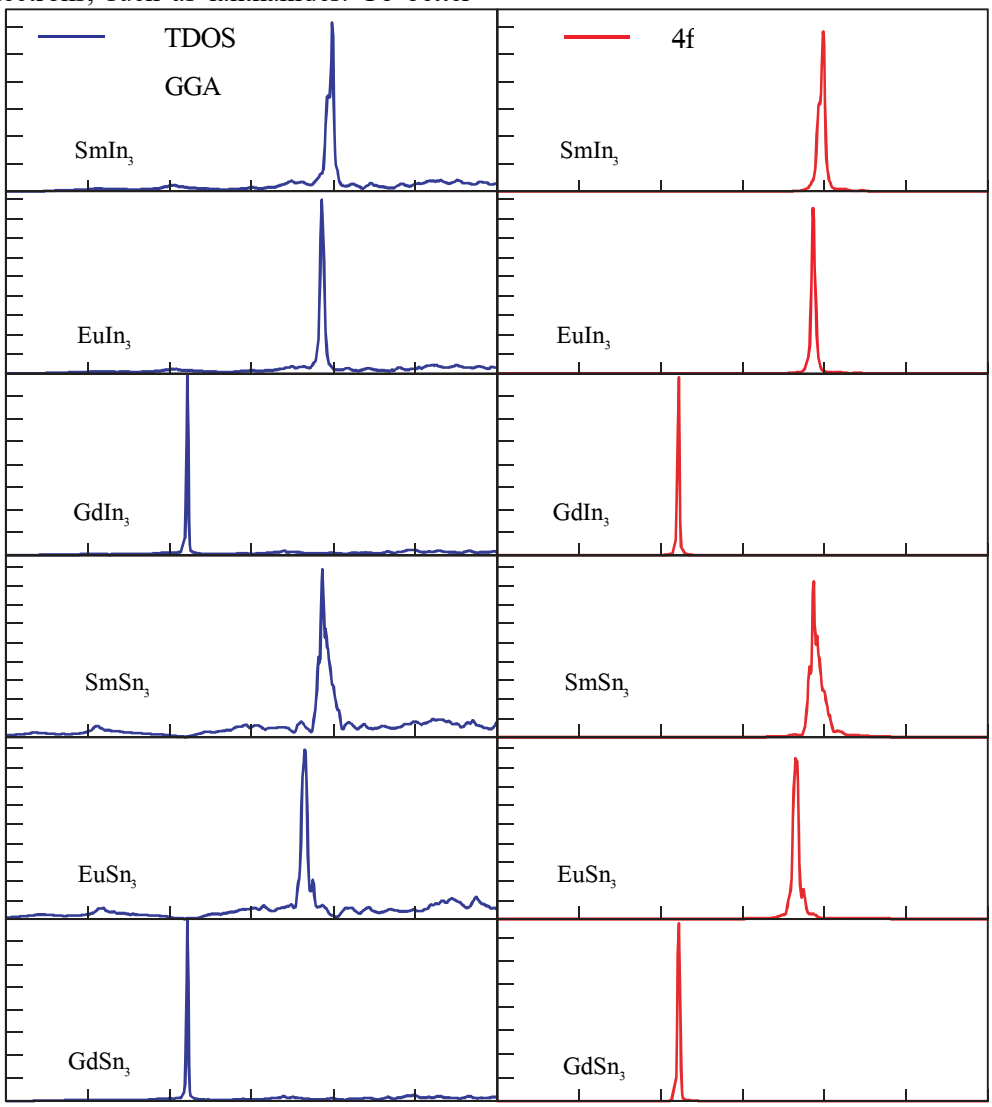

FIG. 1. Total density of states (TDOS, blue lines) and partial 4f DOS (red lines) for RIn_3 and RSn_3 (R = Sm, Eu, and Gd) calculated with GGA.

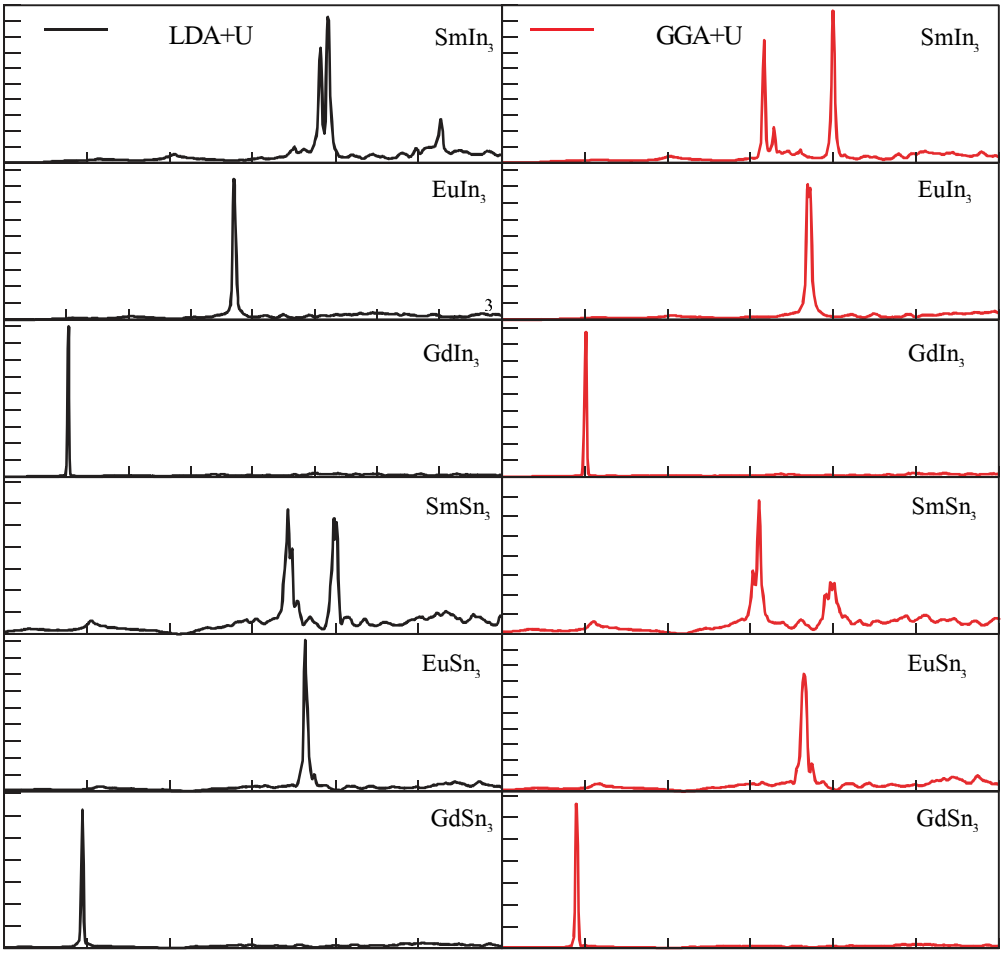

FIG. 2. Total density of states (TDOS) with LDA+U (black lines) and GGA+U (red lines) of RIn_3 and RSn_3 for R = Sm, Eu, and Gd.

Figures 1–3 reveal that no band gaps exist at the Fermi level for these intermetallic compounds, confirming their metallic nature. Figure 1 shows the total DOS (blue lines) and 4f DOS (red lines) calculated using the GGA. The dominant contribution at the Fermi level originates from the rare-earth elements. The tails of the 4f states intersect the Fermi level, except in $GdIn_3$ and $GdSn_3$, where the 4f states are positioned below the Fermi level. Peaks corresponding to 4f states are observed at specific energy levels: -0.1, -0.38, -4.5 eV ($SmIn_3$), -0.45, -0.90 eV ($EuIn_3$), and -4.5 eV ($GdIn_3$). Figure 2 presents the total and 4f DOS using the LDA+U (black lines) and GGA+U (red lines) methodologies.

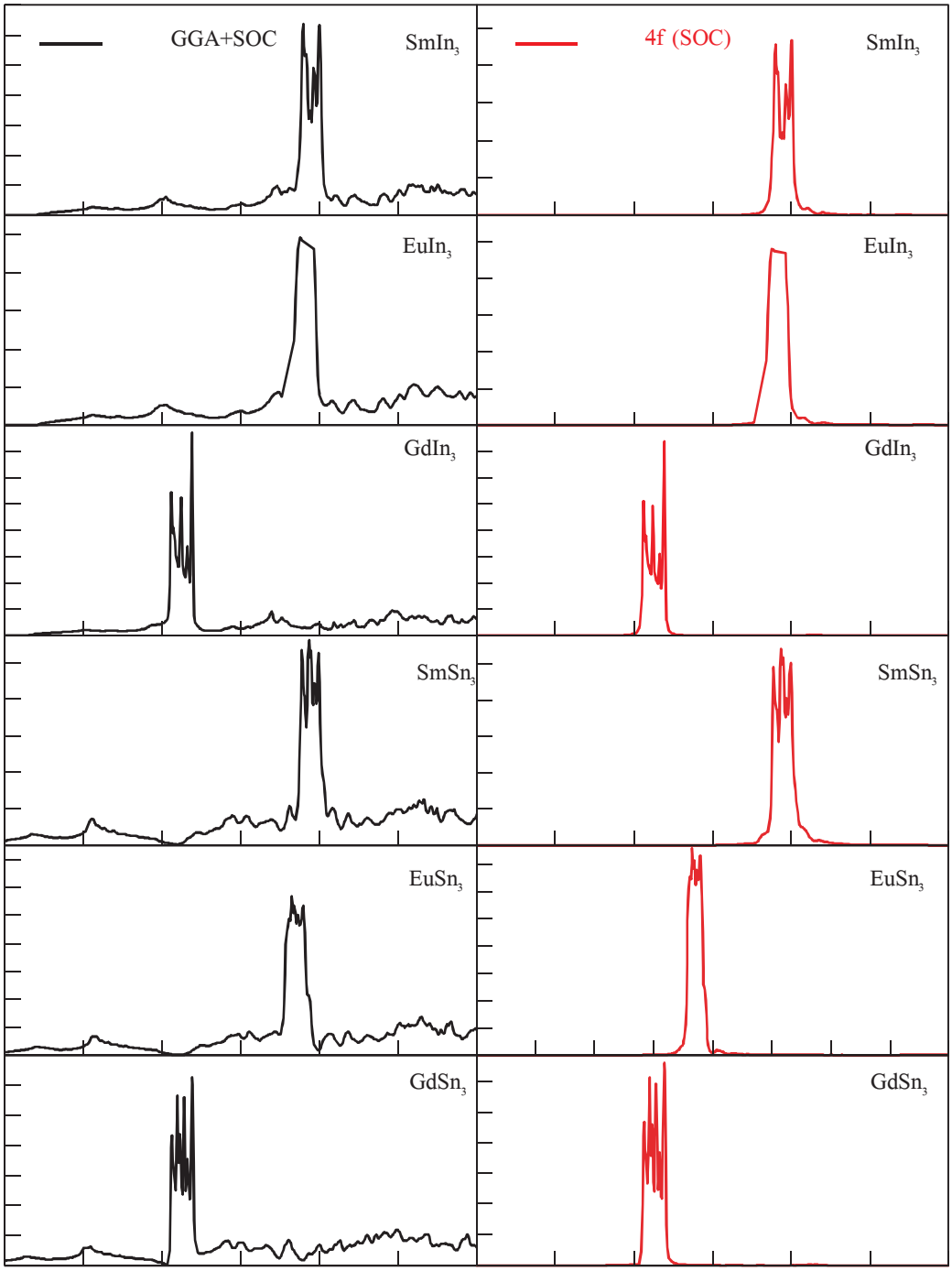

FIG. 3. Total density of states (TDOS, black lines) of RIn_3 and RSn_3 and partial 4f DOS (red lines) for R = Sm, Eu, and Gd calculated with GGA+SOC.

These results show that the inclusion of the Hubbard U parameter pushes the peaks associated with the 4f states to lower energies compared to the GGA results. This behavior is consistent with previous DFT studies, which show that the Hubbard U increases the separation between occupied and unoccupied states [33]. Figure 3 illustrates the total and 4f DOS obtained using GGA+SO. The SOC does not alter the energy positions of the 4f states but eliminates spin degeneracy, splitting the 4f DOS (determined by GGA, LDA+U, and GGA+U) into two distinct peaks. These peaks correspond to the j = 5/2 and j = 7/2 states. The j = 5/2 peaks are fully occupied in all compounds, whereas the j = 7/2 peaks are fully occupied in $GdIn_3$ and $GdSn_3$ but only partially occupied in other compounds.

Magnetic Properties

The magnetic properties of the RIn_3 and RSn_3 (R = Sm, Eu, and Gd) compounds were

investigated in terms of their magnetic moments. The RIn_3 and RSn_3 (R = Sm, Eu, and Gd) consist of the rare earth elements Sm, Eu, and Gd. Rare earth elements are renowned for their robust magnetic characteristics, rendering them a subject of interest for diverse applications such as implementation in magnetic materials and utilization as contrast agents in the field of medical imaging. The magnetic moments of these compounds would be contingent upon the computational methodology and parameters employed in the calculations. In general, magnetic moments are computed for the complete unit cell and can be further analyzed to determine the contributions from individual atoms. The magnetic moment of an atom, as used in these computations, pertains to the comprehensive magnetic moment linked to the atom within the crystal lattice. The interstitial region corresponds to the voids or gaps in the crystal structure where no atoms are present. All computed values are summarized in Table 2. The total magnetic moments of $SmIn_3$, $EuIn_3$, $GdIn_3$, $SmSn_3$, $EuSn_3$, and $GdSn_3$ compounds are dominated by the contribution of individual moments of Sm^{3+}, Eu^{3+}, and Gd^{3+}. R-4f (R=Sm, Eu, and Gd) electronic shell is responsible for the magnetic moment.

TABLE 2. Calculated spin magnetic moments (μB) of RIn_3 and RSn_3 (R = Sm, Eu, and Gd) using PBE-GGA.

	$SmIn_3$	$EuIn_3$	$GdIn_3$	$SmSn_3$	$EuSn_3$	$GdSn_3$
Interstitial region	0.02020	0.05023	0.03023	0.04129	0.01359	0.02439
R [Sm, Eu, and Gd]	6.53513	6.93514	6.63515	6.73710	6.23500	6.83974
In or Sn	-0.0370	-0.0313	-0.0119	-0.0896	-0.0245	-0.0268
Total	6.49123	6.89129	6.50127	6.67800	6.10890	6.78347

Elastic Properties

The elastic constants of a solid are crucial, as they characterize the material's response to applied stress. They are particularly relevant to various fundamental solid-state phenomena, including intraatomic bonding, equations of state, phonon spectra, and structural stability. The elastic properties are thermodynamically associated with specific heat, thermal expansion, Debye temperature, and the Gruneisen parameter. The elastic properties of solids also serve as indicators of mechanical strength, which is of considerable practical importance. Table 3 presents the calculated elastic constants C11, C12, and C44 for RIn3 and RSn3 (where R = Sm, Eu, Gd), both with and without spin polarisation, using the GGA approximation. We have compared the available experimental values of C11 and C44 for SmIn3 and SmSn3 [21]. We obtained the experimental values of C11 and C44 at 100 K and calculated the elastic constants at 0 K. Consequently, the varying temperatures result in a minor discrepancy between our calculated and experimental values. The stability of a specific crystal structure adheres to established criteria. Additionally, the computed elastic constants met the necessary stability criteria for cubic structures, specifically: C11–C12 > 0; C44 > 0; C11 + 2C12 > 0 [34, 35]. The fulfilment of the aforementioned requirements justifies the fact that these intermetallic compounds are elastically stable. Table 3 indicates that the nonmagnetic phase significantly affects the elastic characteristics of RIn_3 and RSn_3 compounds. Nonmagnetic ordering diminishes the value of the elastic constants. We derive the mechanical parameters, including bulk modulus B0, shear modulus G, Young's modulus Y, Poisson's ratio, and anisotropic ratio A, which are critical elastic parameters for industrial applications, from the elastic constants C11, C12, and C44 of the examined compounds and present them in Table 4. These are critical parameters for characterizing the mechanical properties of materials. We elucidate the mechanical properties based on the results. We define the Hill37 average shear modulus, G, as the arithmetic mean of the Voigt shear modulus, GV, and the Reuss shear modulus, GR, in terms of elastic constants.

$$G = \frac{1}{2}(G_V - G_R) \quad (1)$$

$$B = \frac{1}{2}(B_V - B_R) \quad (2)$$

where,

$$G_R = 15[4(S_{11} + S_{22} + S_{33} - S_{12} + S_{13} + S_{23}) + 3(S_{44} + S_{55} + S_{66})]^{-1} \quad (3)$$

$$G_V = \frac{1}{2}[C_{11} + C_{22} + C_{33} - (C_{12} + C_{13} + C_{23}) + 3(C_{44} + C_{55} + C_{66})] \quad (4)$$

$$B_V = \frac{1}{2}[C_{11} + C_{22} + C_{33} + 2(C_{12} + C_{13} + C_{23})] \quad (5)$$

$$B_R = [S_{11} + S_{22} + S_{33} + 2(S_{12} + S_{13} + S_{23})]^{-1} \quad (6)$$

Table 4 presents the computed values of GH, revealing that $GdSn_3$ possesses the highest GH value (44.082 GPa), while $GdIn_3$ has the lowest shear modulus value of 27.962 GPa. These two values define an interval that encompasses the remaining compounds.

TABLE 3. Calculated values of elastic constants C_{11}, C_{12}, and C_{44} (GPa) with spin polarization (GGA+SP) and without spin polarization (GGA).

Compound	E_{xc}	$SmIn_3$	$EuIn_3$	$GdIn_3$	$SmSn_3$	$EuSn_3$	$GdSn_3$
C11	GGA +SP	139.068	113.716	119.369	93.191	118.316	128.143
	GGA	100.476	100.413	118.385	99.429	94.142	114.310
	Exp. [21]	125.3			95.4		
C12	GGA +SP	60.276	56.308	63.034	42.836	61.175	59.806
	GGA	59.290	67.402	75.417	39.203	65.844	63.171
	Exp. [21]						
C44	GGA +SP	28.171	28.450	27.862	43.003	51.377	52.275
	GGA	30.426	22.588	31.348	32.211	28.788	44.195
	Exp. [21]	32.9			34.3		

Young's modulus Y, which quantifies a solid material's resistance to linear strain along its edges, is defined as the ratio of stress to strain. The compound exhibits increased stiffness with a higher value of Y. We can determine the computed values of the Voigt shear modulus G_V and the bulk modulus B_0 using the following equation:

$$Y = \frac{9BG}{3B+G} \quad (7)$$

Table 4 shows that the GdSn compound has a higher Young's modulus value compared to the other compounds. The elevated values of Young's modulus, in comparison to the bulk modulus, indicate the stiffness of these compounds.

TABLE 4. Calculated values of Voigt's shear modulus G_V, Reuss's shear modulus G_R, Hill's shear modulus G_H, B/G ratio, Cauchy pressure (C''), Poisson's ratio (v), Kleinman parameter (ξ), Anisotropy constant (A), Lames coefficient (λ and μ), and shear constant (C').

	$SmIn_3$	$EuIn_3$	$GdIn_3$	$SmSn_3$	$EuSn_3$	$GdSn_3$
G_v	32.661	28.552	27.963	35.873	42.254	45.032
G_R	31.795	28.551	27.962	33.512	38.943	43.132
G_H	32.228	28.551	27.962	34.693	40.598	44.082
Y	87.034	76.060	75.308	89.640	107.831	114.318
B/G	2.685	2.642	2.926	1.719	1.976	1.873
C''	32.105	27.858	35.208	-0.167	9.798	7.531
υ	0.332	0.332	0.347	0.249	0.276	0.269
ξ	0.728	0.826	0.879	0.769	0.861	0.780
A	0.715	0.991	0.988	1.708	1.798	1.530
λ	64.766	56.410	63.171	35.706	52.052	52.563
μ	32.661	28.552	27.963	35.873	42.254	45.032
C'	39.396	28.704	28.168	25.178	28.571	34.169

According to Pugh [34], the ratio of bulk modulus to shear modulus (B/G) can determine whether a material is ductile or brittle. We determined 1.75 as the key value that distinguishes ductile from brittle behavior. A high B/G ratio indicates ductility, while a low value signifies brittleness in materials. Table 4 clearly indicates that all compounds exhibit ductile behavior, but $SmSn_3$ is brittle. Cauchy's pressure is the disparity between two specific elastic constants (C" = C12—C44). Pittifor [35-59] suggests using Cauchy's pressure to characterize the bonding nature of the compounds under examination. The positive value of Cauchy's pressure indicates metallic bonding, whereas materials exhibiting negative Cauchy's pressure are associated with angular or directional bonding, such as covalent bonding.

An increase in the negative value of Cauchy pressure results in enhanced directional bonding and reduced mobility of the material. The calculated Cauchy's pressure for RIn_0 and RSn_0 (R = Sm, Eu, Gd) is shown in the table. All of these compounds have a positive Cauchy's pressure, which means that their bonds are metallic, except for SmSn3, which has a negative Cauchy's pressure value. The fact that $SmSn_3$ has a negative Cauchy pressure value means that it has directed or covalent bonding, which makes it brittle. Moreover, the positive and negative values of Cauchy's pressure indicate ductility and brittleness, confirming that $SmSn_3$, $EuIn_3$, $GdIn_3$, $EuSn_3$, and $GdSn_3$ are ductile, whereas $SmSn_3$ is brittle. The following formula determines the Poisson's ratio:

$$\upsilon = \frac{3B-2G}{2(3B+G)} \quad (8)$$

Poisson's ratio quantifies compressibility. As Poisson's ratio approaches 0.5, the material exhibits a tendency toward incompressibility; at v = 0.5, it is nearly incompressible. The computed values for v fall within the range of 0.25–0.5, characteristic of solids dominated by central forces. The computed values of v for the examined compounds indicate that the interatomic forces are predominantly central, with the exception of $SmSn_3$, where the central interatomic force is not prominent. Kleinman introduced a parameter known as the internal strain parameter. It delineates the comparative propensity of bond bending in relation to bond stretching. The lower limit (ξ = 0) corresponds to the minimisation of the bond bending term, while the upper limit (ξ = 1) relates to the minimisation of the bond stretching term. Subsequently, Harrison approximated the Kleinman parameter [ξ] in relation to the elastic constants using the following equation:

$$\xi = \frac{C_{11}+8C_{12}}{7C_{11}-2C_{12}} \quad (9)$$

Our computed results of ξ, which range from 0.879 to 0.728, show that bond bending predominates in our materials. However, the larger value of n suggests that bond stretching also contributes to these molecules. The elastic anisotropic ratio (A) is a crucial parameter that determines whether the elastic properties stay invariant in different directions. The following equation [33] computes the anisotropic ratio A, which directly correlates with the potential for micro-crack formation in materials:

$$A = \frac{5G_v}{G_R} + \frac{B_v}{B_R} - 6 \quad (10)$$

A equals 1 for entirely isotropic materials, and the divergence from one quantifies the degree of elastic anisotropy. The calculated values listed in Table 4 clearly suggest that these compounds are anisotropic. We can derive Lame's constants (λ, μ) from Young's modulus and Poisson's ratio using the following equation:

$$\lambda = \frac{Y\nu}{(1+\nu)(1-2\nu)}, \text{ and } \mu = \frac{Y}{2(1+\nu)} \quad (11)$$

The higher the value of Young's modulus, the greater the values of Lame's coefficients will be. The two parameters collectively form a parameterization of the elastic moduli for homogeneous isotropic media. We designate λ as Lame's first constant and μ as Lame's second constant. Values for RIn3 and RSn3 (R = Sm, Eu, Gd) are presented in Table 4. Our findings indicate that Lame's second modulus is equivalent to Voigt's shear modulus (λ = GV). For isotropic materials, λ equals C12 and μ equals C0. Our compounds exhibit high anisotropy and do not meet the criteria for isotropy, specifically $\lambda = C_{12}$ and μ = C'. We have computed the shear constant, another significant parameter, using the relation.

$$C' = \frac{1}{2}(C_{11} - C_{12}) \quad (12)$$

Table 4 presents the values for the compounds under examination. People often refer to it as the tetragonal shear modulus. Dynamical stability necessitates that $C_0 > 0$. The positive results of our computed materials show their mechanical stability. A larger shear modulus indicates more stiffness in the material against tetragonal deformation. No experimental data are available in the literature for the comparison. Subsequent experimental investigations will validate these findings. We see the current findings as a predictive analysis for these chemicals, anticipating that further experimental investigations would validate our computed results.

Conclusions

First-principles calculations were performed to theoretically investigate the structural, elastic, mechanical, and electronic properties of RIn_3 and RSn_3 (R = Sm, Eu, Gd) compounds using density functional theory (DFT). The calculated ground-state lattice parameters show excellent agreement with experimental data. The electronic density of states confirms the intermetallic nature of these compounds. Spin-orbit coupling (SOC) further splits the 4f states into two distinct peaks, modifying their energy positions.

The results demonstrate that these compounds exhibit elastic stability and anisotropy. The high values of Young's modulus indicate that certain compounds possess significant stiffness. Analysis of the B/G ratio reveals that all compounds, except $SmSn_3$, are ductile. The deviation observed in $SmSn_3$, characterized by its brittleness, suggests unique bonding characteristics that differ from those of the other compounds. Further exploration of the microstructural properties of $SmSn_3$ could provide deeper insights into the underlying mechanisms responsible for this anomaly.

Reference

[1] Tsuchida, T. and Wallace, W.E., J. Chem. Phys., 43 (1965) 3811.

[2] Buschow, K.H.J., Ferromagnetic Mater., 1 (1980) 297.

[3] Jr. Gschneidner, K.A., Russell, A., Pecharsky, A., Morris, J., Zhang, Z., Lograsso, T., Hsu, D., Lo, C.H.C., Ye, Y., Slager, A., and Kesse, D., Nature Mater., 2 (2003) 587.

[4] Jr. Gschneidner, K.A., Ji, M., Wang, C. Z., Ho, K.M., Russell, A.M., Mudryk, Y., Becker, A.T., and Larson, J.L., Acta Mater., 57 (2009) 5876.

[5] Iizuka, T., Mizuno, T., Min, B.H., Kwon, Y.S., and Kimura, S., J. Phys. Soc. Jpn., 81 (2012) 043703.

[6] Lin, C.L., Yuen, T., and Mihalisin, T., Phys. Rev. B, 54 (1996) 9254.

[7] Li, C.F., Liu, Z.Q., Shang, P.J., and Shang, J.K., Scr. Mater., 65 (2011) 1049.

[8] Asadabadi, S.J., Cottenier, S., Akbarzadeh, H., Saki, R., and Rots, M., Phys. Rev. B, 66 (2002) 195103.

[9] Bajorek, A., Chelkowska, G., Chrobak, A., and Grudziecka, M.K., Intermetallics, 26 (2012) 142.

[10] Nagai, N., Umehara, I., Ebihara, T., Albessard, A.K., Sugawara, H., Yamazaki, T., Satoh, K., and Onuki, Y., Physica B, 186 (1993) 139.

[11] Kletowski, Z., Solid State Commun., 72 (1989) 901.

[12] Buschow, K.H.J., de Wijn, H.W., and van Diephen, A.M., J. Chem. Phys., 50 (1969) 137.

[13] Percheron, A., Crorochov, O., and Achard, J.C., C. R. Acad. Sci. Paris C, 277 (1973) 81.

[14] Harris, R. and Raynor, G.V., J. Less-Common Met., 9 (1965) 7.

[15] Buschow, K.H.J., Phys. Lett. A, 29 (1969) 12.

[16] Gorlich, E., Hrynkiewicz, H., Kmied, R., Catka, K., Tomala, K., Czopnik, A., and Iliew, N., Phys. Status Solidi A, 30 (1975) K17.

[17] Buschow, K.H.J., Rep. Prog. Phys., 42 (1979) 1373.

[18] Sanchez, J.P., Friedt, J.M., Shenoy, G.K., Percheron, A., and Achard, J.C., J. Phys. C: Solid State Phys., 9 (1976) 2207.

[19] Onuki, Y. and Settai, R., Low Temp. Phys., 38 (2012) 89.

[20] Asadabadi, S.J. and Akbarzadeh, H., Physica B, 349 (2004) 76.

[21] Endoh, D., Goto, T., Tamaki, A., Liu, B., Kasaya, M., Fujimura, T., and Kasuya, T., J. Phys. Soc. Jpn., 58 (1989) 940.

[22] Suna, Z., Lib, S., Ahuja, R., and Schneidera, J.M., Solid State Commun., 129 (2004) 589.

[23] Blaha, P., Schwarz, K., Madsen, G.K.H., Kuasnicka, D., and Luitz, J., "WIEN2K, An Augmented Plane WaveþLocal Orbitals Program for Calculating Crystal Properties", edited by K. Schwarz, (Technical Universitat, Wien, Austria, 2001).

[24] Andersen, O.K., Phys. Rev. B, 12 (1975) 3060.

[25] Perdew, J.P. and Zuanger, A., Phys. Rev. B, 23 (1981) 5048.

[26] Perdew, J.P., Burke, K., and Ernzerhop, M., Phys. Rev. Lett., 77 (1996) 3865.

[27] Anisimov, V.I., Solovyev, I.V., Korotin, M.A., Czyzyk, M.T., and Sawatzky, G.A., Phys. Rev. B, 48 (1993) 16929.

[28] Monkhorst, H.J. and Pack, J.D., Phys. Rev. B, 13 (1976) 5188.

[29] Jamal, M., Cubic-elastic, http://www.wien2k.at/ reg_user/unsupported/ (2012).

[30] Jamal, M. and Jalali, S., Asadabadi, e-print arXiv:submit/0630082 [cond-mat.mtrl-sci] (2013).

[31] Stadler, R., Wolf, W., Podloucky, R., Kresse, G., Furthmuller, J., and Hafner, J., Phys. Rev. B, 54 (1996) 1729.

[32] Birch, F., Phys. Rev., 71 (1947) 809.

[33] Hill, R., Proc. Phys. Soc. London, 65 (1952) 349.

[34] Pugh, S. F., Philos. Mag., 45 (1954) 823.

[35] Pettifor, D.G., Mater. Sci. Technol., 8 (1992) 345.

[36] Schwartz, G.P. and Shirley, D.A., Hyperfine Interact., 3 (1977) 67.

[37] Gautam, R., Kumar, A., and Singh, R., Acta Phys. Pol. A, 132 (4) (2017) 1371.

[38] Kumar, A., Gautam, R., Chand, S., Kumar, A., and Singh, R.P., Mater. Phys. Mech., 42 (1) (2019) 112.

[39] Kumar, A., Gautam, R., Singh, R.P., and Kumar, A., Int. J. Adv. Sci. Technol., 29 (08) (2020) 1150.

[40] Annveer, Gautam, R., Kumar, A., Kumar, A., Singh, P.K., and Singh, R.P., Optik, 223 (2020) 165317.

[41] Annveer, Gautam, R., Kumar, A., Kumar, A., Gautam, Y.K., Saroj, A.L., and Singh, R.P., J. Mater. Sci.: Mater Electron, 32 (2021) 727.

[42] Kumar, A., Kumar, A., Kumar, K., Singh, R.P., Singh, R., and Kumar, R., East Eur. J. Phys., 1 (2023) 109.

[43] Kumar, A., Singh, N.K., Israil, M., Gupta, E., Singh, N., and Sharma, A.K., Subharti J. Interdiscip. Res., 6 (1) (2023) 1.

[44] Narayan, Y., Kumar, A., Singh, A.P., Ahsan, M., Upadhayay, R.K., and Rao, L.M., Eur. Chem. Bull., 12 (2023) 494.

[45] Veerta, Kumar, A., and Kumar, A., Int. Res. J. Manag. Sci. Technol., 14 (2023) 176.

[46] Lal, B., Kumar, A., and Kumar, A., Int. J. Res. Anal. Rev., 10 (2) (2023) 952.

[47] Kumar, A., Kumari, K., and Sharma, S.K., Twist, 19 (2024) 275.

[48] Singh, N.K., Kumar, A., and Kiran, A., Twist, 19 (2024) 338.

[49] Kumar, A., Gupta, H., Kumar, D., Sharma, R., Kumar, A., Sharma, S.K., and Singh, A.P., East Eur. J. Phys., 1 (2024) 355.

[50] Kumar, A., Kumar, A., Pundir, S.K., and Singh, N., Twist, 19 (2024) 377.

[51] Kumar, A., Singh, M., and Kumar, R., Twist, 19 (2024) 439.

[52] Kumar, A., Kumar, A., Kumar, A., and Iram, N., Hybrid Adv., 6 (2024) 100197.

[53] Kumar, A., Kumar, A., and Iram, N., Hybrid Adv., 6 (2024) 100211.

[54] Kumar, A., Gupta, H., Kumar, A., Kumar, A., Sharma, S.K., Lal, B., and Iram, N., Indian J. Phys., (2024), https://doi.org/ 10.1007/s12648-024-03273-6.

[55] Kumar, A., Kumar, A., Jain, P., Pundir, S.K., and Singh, N., Optik, 315 (2024) 172039.

[56] Kumar, A., Kumar, S., Pundir, S.K., Nautiyal, V.K., Kumar, A., and Iram, N., Opt. Quantum Electron., 56 (2024) 1742.

[57] Kumar, A., Kumar, R., Kumar, R., and Kumar, A., Mater. Phys. Mech., 52 (4) (2024) 23.

[58] Peng, Q., Iram, N., Sharma, R., Kumar, A., Alsubaie, A.S., and Rehman, J., Inorg. Chem. Commun., 170 (1) (2024) 113240.

[59] Iram, N., Sharma, R., Ahmad, J., Kumar, A., Kumar, A., Almutairi, F.N., and Alturaifi, H.A., Inorg. Chem. Commun., 172 (2024) 113573.

Volume 18, Number 5, 2025. pp. 573-581

Jordan Journal of Physics

ARTICLE

Spectroscopic Diagnostic and Preparation of CuSi Plasma Produced Via Plasma Jet

Wadaa S. Hussein[a], **Riyam N. Muhsen**[a], **Kadhim A. Aadim**[a] and **Abdulrhman H. Shaker**[b]

[a] *Department of Physics, College of Science, University of Baghdad, Baghdad, Iraq.*
[b] *Al Hikma university college, Baghdad, Iraq.*

Doi: **https://doi.org/10.47011/18.5.2**
Received on: 21/02/2024; *Accepted on: 28/01/2025*

Abstract: Copper silica (CuSi) plasma was generated under atmospheric pressure using argon gas by immersing a piece of (Si) metal in the prepared nano-Cu liquid for periods of 6 and 8 min. Then, a spectroscopic diagnosis of the generated plasma was performed at a constant applied voltage of 11 kV and a frequency of 50 kHz under direct-current conditions, with the argon flow rate varied between 0.5 and 2 L/min. Changing the duration of immersion within the nano-Cu liquid and the flow rate of argon affected the intensity of the resulting spectral peaks. The generated plasma had the following parameters: T_e values of 3.732 – 4.981 eV and 1.220 – 1.396 eV, and n_e values of $2.700 \times 10^{18} - 3.588 \times 10^{18}$ cm^3 and $1.290 \times 10^{18} - 2.074 \times 10^{18}$ cm^3 for the two times used. When CuSi nanoparticles (NPs) were synthesized under the same laboratory conditions, with the argon flow rate fixed at 2 L/min, the energy gap was 3.74 eV, prepared by Si for 6 min in Cu-liquid for 6 min, and 3.62 eV, prepared of Si for 6 min in Cu-liquid for 8 min. The results showed that the Cu-liquid increased the electrical conductivity in the CuSi cold jet plasma system, which affected the values of the plasma parameters and the synthesis of CuSi NPs as a result of increased energy gain, which accelerated and increased the electron process and ultimately increased the ionisation process.

Keywords: CuSi cold plasma jet, CuSi nanoparticle, Optical emission spectroscopy (OES), Spectral diagnostics, Silicon-copper plasma.

1. Introduction

Plasma science is one of the most extensively studied and developed fields in the modern era. The atmospheric pressure plasma jet remains an advanced method for generating cold plasma, and it is widely used in scientific applications [1, 2]. This is also called a cold plasma jet [3]. Cold jet plasma is formed by the ionisation of molecules or atoms of the substance at a certain temperature, which then becomes a highly reactive gas containing radicals, electrons, extremely active free ions, and electric fields [4]. Both noble gases, such as helium and argon, and chemically active gases, such as nitrogen and oxygen, can be used in this production process [5]. Non-thermal plasma jets are effective tools for industrial, medical, and biological uses due to their ability to interact with cells, tissues, and various industrial applications easily and without significant effects [6, 7]. Each type of plasma possesses distinct characteristics that determine its suitability for specific applications [8]. Temperature and density are the most important dynamics in plasma, and they enable us to predict the particle velocity distributions and relative energy levels [9].

To measure the plasma parameters such as electron temperature (T_e) and electron density (n_e), optical emission spectroscopy (OES) is adopted [10]. This technique allows for plasma diagnostics without disturbing its structure, condition, or shape [11]. The method's principal

Corresponding Author: Abdulrhman H. Shaker **Email**: Abd.Hamed2204m@sc.uobaghdad. edu.iq

work is calculating the radiated optical emission from the produced plasma, which represents its characteristics in an environment of chemical, ionic, and molecular radiation [12, 13]. As ionised plasma particles interact with each other and emit radiation, three high-speed electronic transitions that control collision excitation and ionisation can occur: boundary transitions, important transitions, and free transitions [14]. A band or spectral line is formed from the emitted light as electrons pass through different levels in it, thereby resulting in the energetic gas molecules, ions, and atoms emitting radiation [15].

To determine the properties of a plasma, its parameters must be calculated. As noted above, the temperature and density of the electrons are considered among the most important properties, from which the remainder of the parameters can be derived. The temperature of the plasma in local thermal equilibrium can be calculated using the following equation [16]:

$$T_e = \frac{(E_2 - E_1)}{k \ln\frac{(I_1\lambda_1 A_2 g_2)}{(I_2\lambda_2 A_1 g_1)}} \quad (1)$$

where A_1g_1 is the transition strength of the first wavelength, A_2g_2 is the transition strength of the second wavelengths, k is Boltzmann's constant, I_1 and I_2 are the peak intensity of the first and second wavelength of the plasma spectrum, E_1 is the peak energy of the first wavelength, and E_2 is the peak energy of the second wavelength in the resulting plasma spectrum. Moreover, A is the transition probability for spontaneous emission from an upper energy level to a lower level, and g is the statistical weight of the upper level [17]. Here, the unit of measurement is eV.

From the Saha-Boltzmann equation, which depends on spectral lines, the plasma electron density can be calculated as follows [16]:

$$n_e = \frac{I_1}{I_2^*} 6.04 \times 10^{21} (T_e)^{3/2} e^{\frac{(E_1 - E_2 - X_z)}{kT_e}} \quad (2)$$

where I_1 and I_2 are the peak intensity of the first and second wavelength of the plasma spectrum, E_1 and E_2 are the peak energy of the wavelengths, as defined above, and X_z represents the amount of ionisation energy. Here, the unit of measurement is cm^{-3}.

$$I_2^* = \frac{I_2\lambda_2}{g_2 A_2} \quad (3)$$

The synthesis of nanoparticles (NPs) has been widely investigated because their extremely small atomic and molecular dimensions impart properties that differ significantly from those of bulk materials [18]. The potential of the NP technology lies in the fact that increasing the ratio of particle area to volume gives different and variable properties [19].

This work aims to determine copper-silica (CuSi) plasma parameters when using a variable argon gas flow rate of 0.52 L/min, and a high voltage of 11 kV as a direct current power supply, and to measure the energy gap of the CuSi compound. To this end, a spectroscopic diagnostic method is adopted.

2. Experimental Setup

Figure 1 shows a non-thermal plasma jet system based on argon gas using DC and an applied voltage of 11 kV. A slice of Cu measuring 6 cm in length and 1 cm in width was immersed in a non-ionic liquid inside a 10 ml beaker connected to the positive pole. The electrically conductive plasma jet needle was connected at one end to a gas flow meter and an argon gas bottle and connected by a metal wire to the negative pole. When the system was turned on, and the jetting process began, plasma was produced, as shown in Fig. 2. The nano-Cu liquid was prepared for durations of 6 and 8 min at an argon gas flow rate of 2 L/min, during which the gas interacted with the non-ionic liquid and the immersed metal. The gas molecules interacted with the liquid in the beaker and produced a series of reactions on the metal surface. As a result of the production of NPs, the liquid changed to a brown color, and it became darker as the preparation time increased. The plasma needle was almost perpendicular to the beaker in which the water was placed, and a metal holder was placed on the beaker to control the distance of the flowing plasma column, which was measured during the experimental conditions at 2.35 cm (Fig. 2).

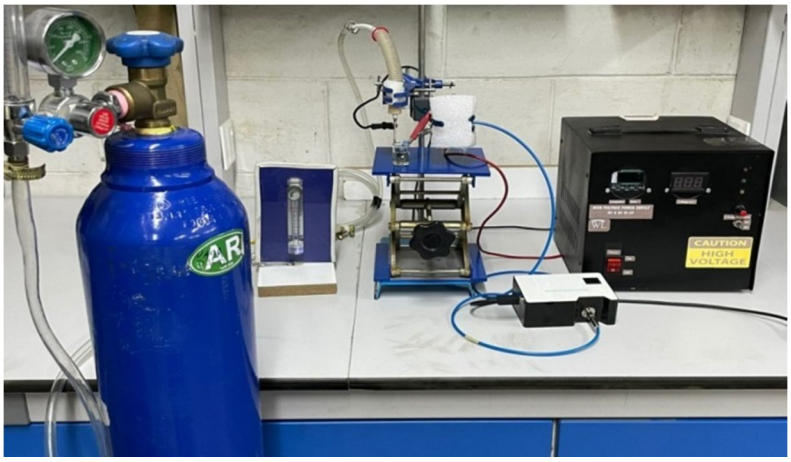

FIG. 1. Configuration of the non-thermal plasma jets system, spectrometer, and electronic controller.

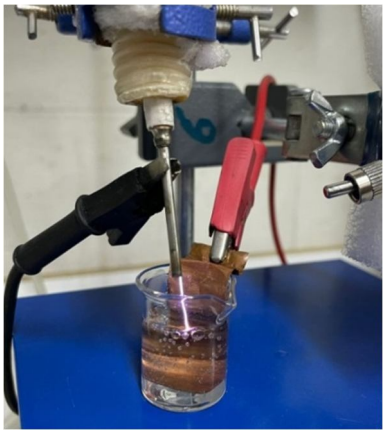

FIG. 2. Cold plasma jet, its interaction with the liquid and the metal surface, and electrode connection.

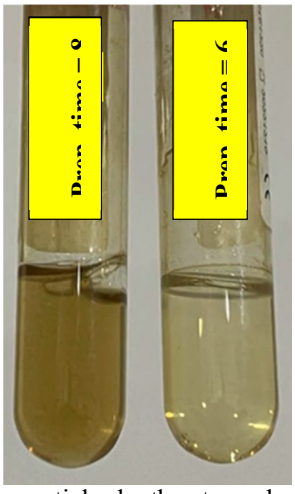

FIG. 3. Image of the synthesized Cu nanoparticles by the atmospheric plasma jet prepared for specific time periods (6 and 8 min).

In the next step, a slide of silicon metal with a length of 4 cm and a width of 1 cm (connected to the anode electrode) was immersed in the previously prepared nano-Cu liquid, using DC and an applied voltage of 11 kV at an argon gas flow of 0.52 L/min from the tip of the plasma jet (connected to the cathode). Plasma was produced, and its parameters were measured using a spectrophotometer. Using the same plasma production mechanism with an argon gas flow rate of 2 L/min for 6 min, CuSi NPs were produced. The color of the liquid changed to light brown when NPs of Si were produced in the nano-Cu liquid prepared with a time of 6 min for both Cu and Si. The color of the liquid changed to light green when NPs were produced in the liquid prepared for 8 min for Cu and 6 min for Si, as shown in Fig. 4.

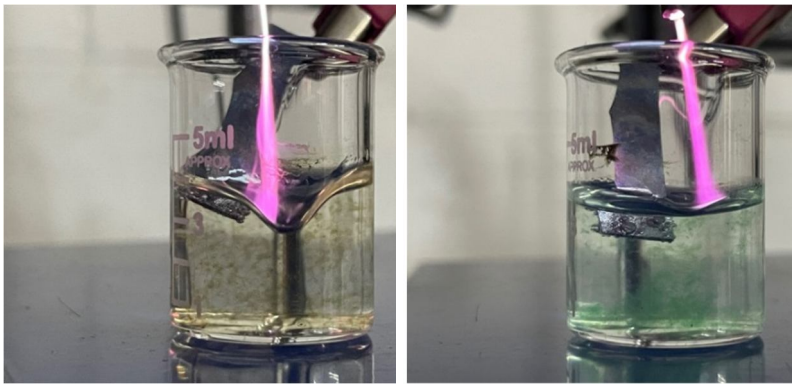

(a) (b)

FIG. 4. Images of nanoparticle liquid samples manufactured for CuSi by atmospheric plasma jet: (a) 6 min for Cu and 6 min for Si; (b) 8 min for Cu and 6 min for Si.

The optical properties (absorption and energy gap) of the NPs produced by the plasma jet were measured using a UV-visible spectroscopy device (UV-Vis 1800, Shimadzu), which is considered the practical method for determining pure substances [20]. Optical characterization provides important physical information about the material, such as its absorption behavior and band-gap energy. These parameters were determined using Planck's relation and the Tauc relation for direct electronic transitions [21]:

$$E_g^{opt.} = \frac{hc}{\lambda_{cut}} = \frac{1240}{\lambda_{cut}} \quad (4)$$

and

$$(\alpha h)^r = A\left(h - E_g\right) \quad (5)$$

In Eq. (4), E_g represents the optical energy gap, h = m (6.626l × 10^{34} J.s) is Planck's constant, c = (3×10^8 m/s) is the light velocity in a vacuum, and λ_{cut} represents the cut-off wavelength corresponding to the optical band gap. In Eq. (5), α is the absorption coefficient, h is Planck's constant, υ is the incident photon frequency, A is a constant equal to 0.9, and r is a value depending on the nature of the transition type (r = 2) for an allowed direct transition.

3. Results and Discussion

Optical Emission Spectrum (OES)

The optical emission spectrum used in the plasma jet system produced by Cu and Si under atmospheric pressure conditions, and the effect of the applied voltage of 11 kV and the variable argon gas flow rate (0.52 L/min) on the properties and parameters of the plasma were studied. Information was collected, and Si plasma emissions were examined using a fibre-optic beam connected to a spectrometer. This provided information on the decay of the excited emissions in the plasma. The physical properties of the metals employed and the laboratory operating conditions significantly affected the observed spectral emission lines and, consequently, the accuracy of the plasma-parameter calculations. As shown in Fig. 5, the spectroscopic diagnosis of the argon plasma jet operating under DC conditions with a silicon metal immersed in nano-Cu liquid prepared for 6 min revealed several emission peaks. Ar +2 peaks were observed at wavelengths of 223.54, 244.04, 253.57, 335.56, 396.98, 706.61, 810.54, and 839.85 nm. It was found that five Cu +2 peaks appeared at 226.35, 294.77, 419.27, 696.73, and 809.62 nm, while three CuSi +2 peaks were detected at 308.6, 379.42, and 671.99 nm. Under identical operating conditions, but using nano-Cu liquid prepared for 8 min, the spectroscopic analysis showed Ar +2 emission peaks at 223.54, 244.05, 253.57, 335.56, 396.98, 706.61, 810.54, and 839.85 nm. The Cu +2 emission peaks were observed at 280.90, 308.05, 355.79, 380.24, and 749.91 nm, while CuSi +2 peaks appeared at 211.41, 234.23, 378.61, and 671.74 nm. In addition, Si emission lines were detected at 613.22 and 762.83 nm.

It was observed that the intensities of the emission peaks increased when Si plasma was generated using nano-Cu liquid prepared for 8 min. This enhancement can be attributed to the increased electrical conductivity of the nanoliquid, which promotes more effective interactions between argon gas molecules and the silicon metal surface. As a result, the ionization levels of electrons, ions, and free radicals increased. These findings are consistent with previous studies [22], which reported that the use of Cu nanoparticles in liquid media enhances electrical conductivity and accelerates

plasma formation. Accordingly, the plasma behavior and parameter trends observed in the present study are in good agreement with those reported in Ref. [22].

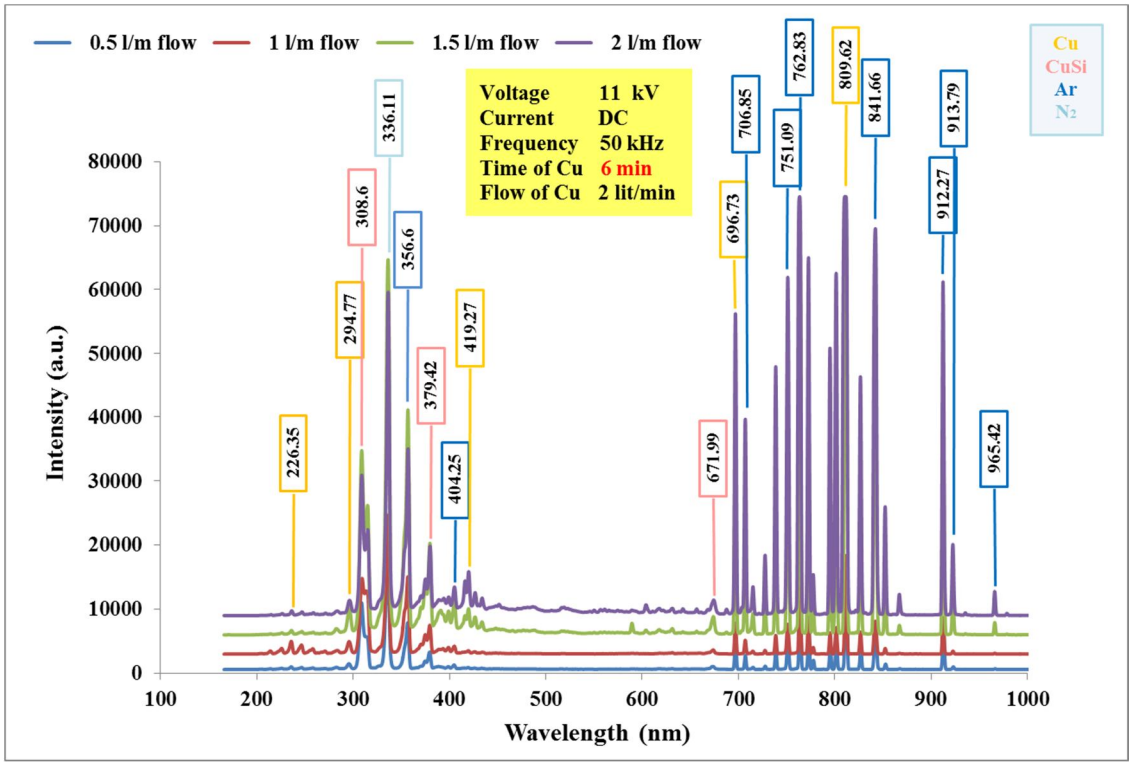

FIG. 5. Plasma emission spectra of Si in nano-Cu liquid prepared for 6 min in a non-ionic liquid at various argon gas flow rates.

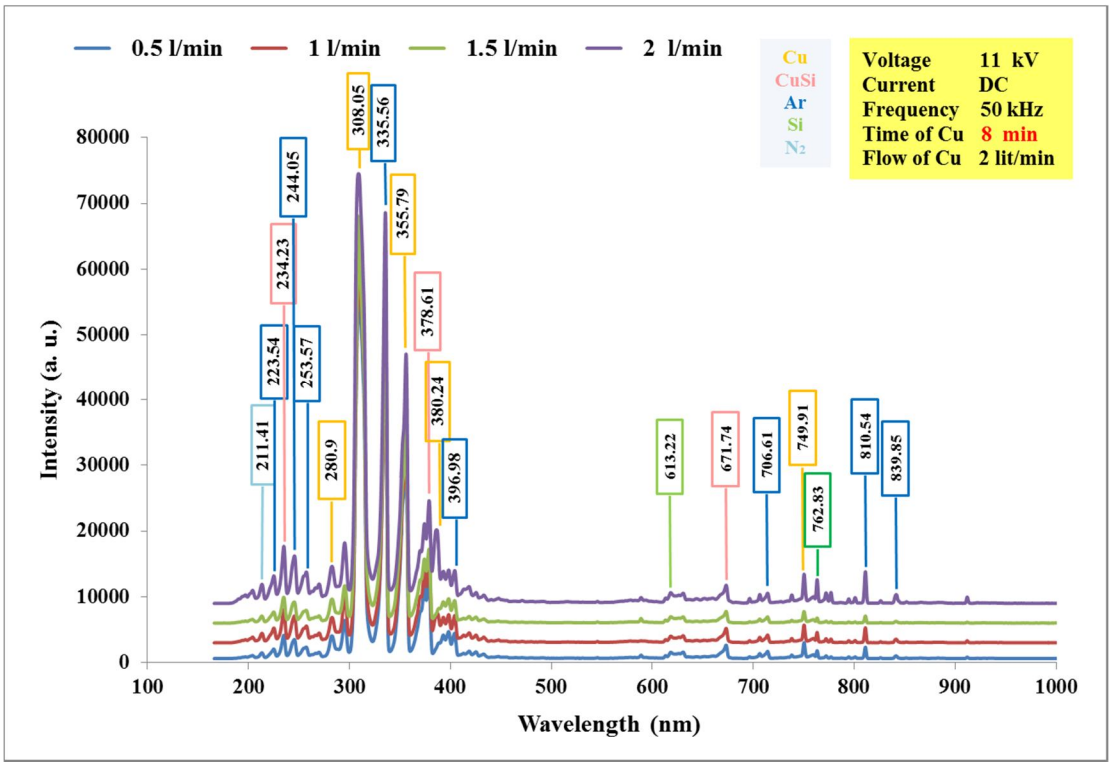

FIG. 6. Plasma emission spectra of Si in nano-Cu liquid prepared for 8 min in a non-ionic liquid at various argon gas flow rates.

Using Eq. (3), the parameters of CuSi plasma produced under two different Cu nanoliquid preparation times (6 and 8 min) were calculated. As Fig. 7 shows, T_e and n_e increased to 3.732 4.981 eV and 2.700 × 10^{18} - 3.588 × 10^{18} cm^3 with the increase in the flow rate of argon gas

(0.5–2 L/min) for Si-anode plasma in the nano-Cu liquid (6 min). This increase is attributed to enhanced collisions between the argon gas molecules and the surface of the nano-Cu liquid containing the immersed Si plate. This led to an increase in the ionization process, providing electrons with more energy to move from a lower level to a higher level. As the temperature increased, the electron density increased accordingly. As Fig. 8 shows, T_e and n_e increased (1.220 – 1.396 eV; 1.290 × 10^{18} 2.074 × 10^{18} cm^{3}) with the increase in the flow rate of argon gas for the Si-anode plasma in the nano-Cu liquid (8 min), which was a result of the increase in collision between the gas column and the surface of the liquid in which the metal was immersed. Finally, there was an increase in plasma ionization processes, with the observed behavior similar to that observed in previous research [16]. It is the increase in the value of plasma parameters with different metals.

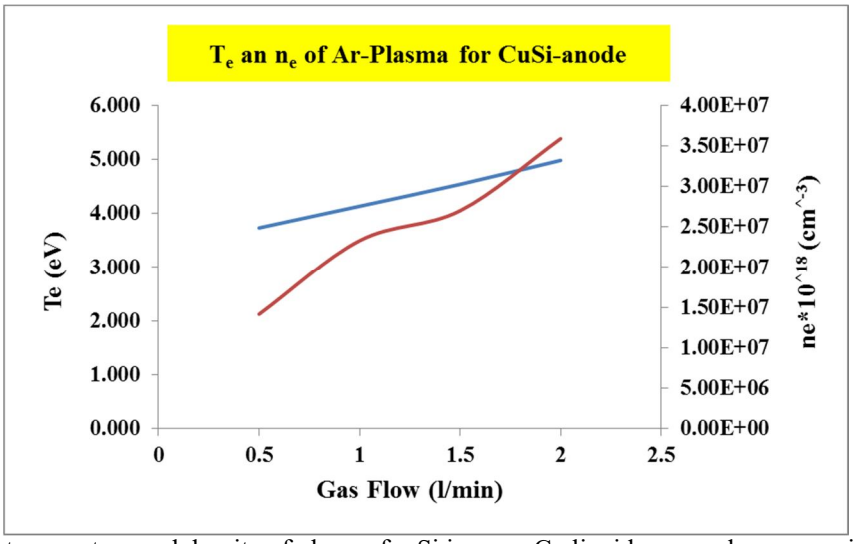

FIG. 7. Electron temperature and density of plasma for Si in nano-Cu liquid prepared over a period of 6 min as a function of argon gas flow rate.

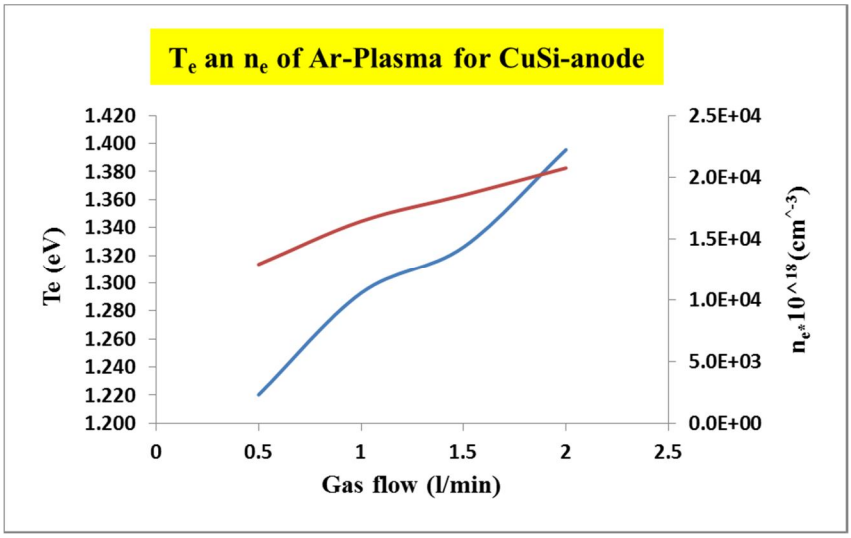

FIG. 8. Electron temperature and density of plasma for Si in nano-Cu liquid prepared over a period of 8 min as a function of argon gas flow rate.

Immersion of the silicon metal sheet in the nano-Cu liquid increased the collision process of argon gas atoms with the liquid surface, which led to an increase in the excitation of electrons and the speed of their transition to a higher level, thus increasing their value. This led to an increase in the ionization process during the generation of the plasma column, which again was in line with previous research results, which led to an increase in the temperature and electron density of the produced plasma, and this behavior is consistent with the results of the aforementioned study [23].

Optical Properties

Figures 9 and 10 show the optical absorption spectrum of the CuSi NPs produced via the plasma jet with an applied voltage of 11 kV and a constant Ar flow rate of 2 L/min over two time periods: 6 min for both Cu and Si. Using Eqs. (4) and (5), the energy gap was calculated. From the absorption spectra, the energy gap was determined by projecting the intersection of the extrapolated linear portion of the absorption curve onto the photon energy axis. The energy gap value was estimated using the standard energy gap band estimation method, in which a straight line is drawn that settles at the horizontal axis diagonally, and were found to be 3.74, 3.62 eV. From a physical perspective, an electron requires an energy of 3.74, 3.62 eV to release a photon from the valence band to the conduction band, as the same conduction and valence bands exist in the direct band gap of the hole momentum and the electron. This result was close to that obtained in terms of value in previous research [24].

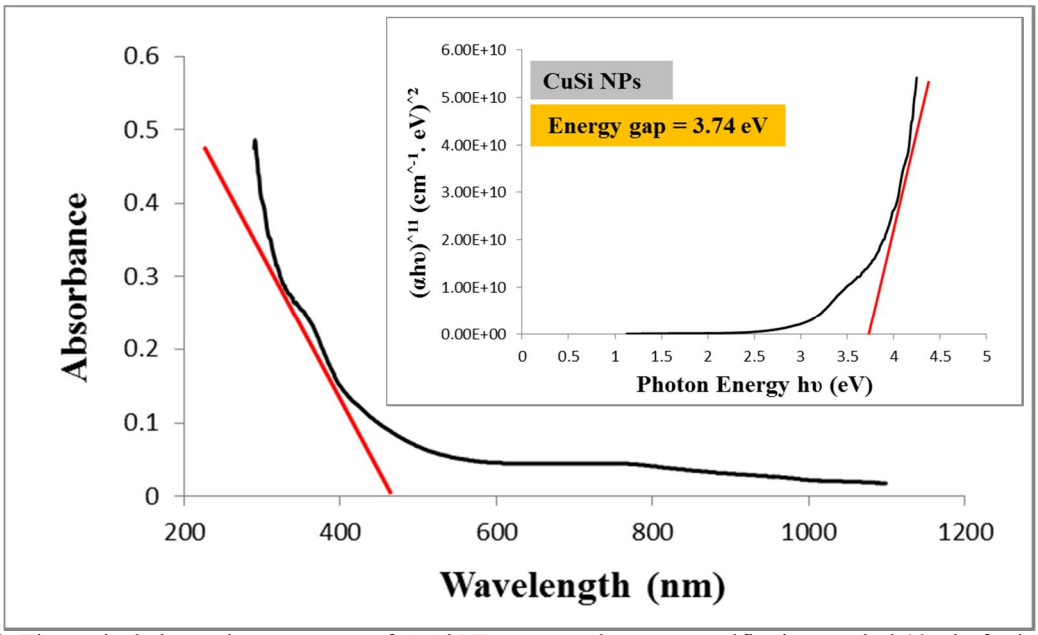

FIG. 9. The optical absorption spectrum of CuSi NPs prepared over a specific time period (6 min for both Cu and Si) along with the energy gap.

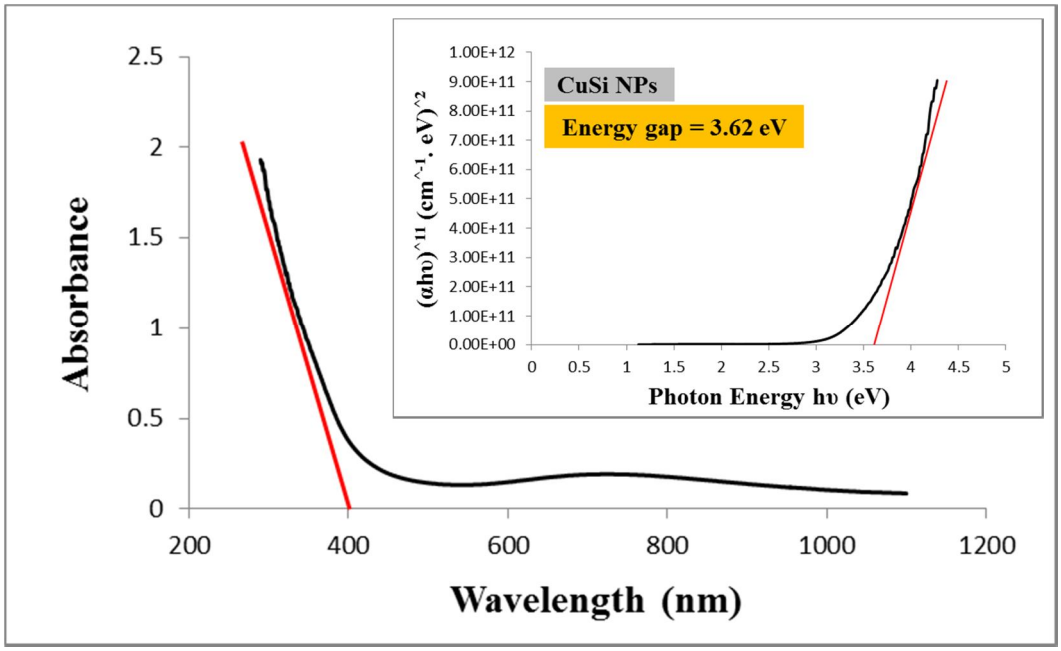

FIG. 10. The optical absorption spectrum of CuSi NPs prepared over a specific time period (8 min for Cu and 6 min for Si) along with the energy gap.

4. Conclusion

The nano-Cu liquid affected the gas ionization processes in the Ar plasma jet system, increasing the intensity of the spectral lines of Cu and Si metals. The external factors, such as the applied voltage (11 kV) and the variable gas flow rate (0.2–5 L/min), had a further effect on increasing the number of colliding gas molecules. As such, the energy supplied as a result of the high excitation process was sufficient to cause ionization, meaning that the intensity of the spectral lines increased. The spectral peaks were lower at the gas flow rate of 0.5 L/min and higher at the rate of 2 L/min, which was reflected in the plasma parameters: T_e of 3.732 – 4.981 eV and 1.220 – 1.396 eV, and n_e values of $2.700 \times 10^{18} - 3.588 \times 10^{18}$ cm^3 and $1.290 \times 10^{18} - 2.074 \times 10^{18}$ cm^3 for the two different times. The changes obtained in the plasma parameters give the generated plasma the ability to be used in different applications.

The optical properties of the Cu and Si NPs produced via Ar plasma jetting exhibited a change in optical absorption rate and energy gap value. The optical band-gap values were measured as 3.74 and 3.62 eV for the time applied in the experiment, as a result of changing the preparation time of the Cu liquid from 6 to 8 min and using it to immerse the Si metal and synthesize the Cu and Si NPs at a constant applied voltage of 11 kV and a gas flow rate of 2 L/min. This result indicates the increase in the electrical conductivity of the Cu particles and the collision process of the gas molecules with the metal surface from the moment the gas came into contact with the liquid surface to the moment its molecules collided with the Si metal surface. This was due to an increase in the uprooting of the Si particles to form the Cu and Si NPs.

5. Acknowledgment

We would like to express our gratitude and thanks to the plasma laboratory in the Physics Department, College of Science, University of Baghdad.

Statements & Declarations

The authors confirm that all information and data have been presented in this manuscript

Funding Declaration in the Manuscript

The authors did not receive support or assistance from any organization for the submitted work.

Conflicts of Interest/ Competing Interests

All authors certify that they have no affiliations with or involvement in any organization or entity with any financial interest or non-financial interest in the subject matter or materials discussed in this manuscript.

Contributions

All authors contributed to this work. Riyam N. Muhsen, Wadaa S. Hussein, Abdulrhman H. Shaker, and Kadhim A. Aadim produced the idea and method of work, and Abdulrhman, Riyam, and Wadaa conducted the practical application, calculations, and data analysis. Riyam N. Muhsen and Abdulrhman worked on writing the theoretical part. All authors contributed to writing the summary and conclusion.

References

[1] Tabares, F.L. and Junkar, I., Molecules, *26* (7) (2021) 1903.

[2] Winter, J., Brandenburg, R., and Weltmann, K.-D., Plasma Sources Sci. Technol., 24 (2015) 064001.

[3] Stryczewska, H.D. and Boiko, O., Appl. Sci., 12 (9) (2022) 4405.

[4] Moravský, L., Klas, M., and Matejčík, Š., WDS'13 Proc. Contrib. Pap., Part II, (2013), 149–153.

[5] Shaker, A.H., Aadim, K.A., and Nida, M.H., J. Opt., 53 (2024) 1273.

[6] Hameed, M.M., Al-Samarai, A.-M.E., and Aadim, K.A., Iraqi J. Sci., 61 (10) (2020) 2582.

[7] Hashim, H. et al., Mater. Lett., 373 (2024) 137077.

[8] Wang, D. and Namihira, T., Plasma Sources Sci. Technol., 29 (2020) 023001.

[9] Mohammed, R.S., Aadim, K.A., and Ahmed, K.A., Appl. Nanosci., 12 (12) (2022) 3783.

[10] Akatsuka, H., Adv. Phys.: X, 4 (1) (2019) 1592707.

[11] Zaplotnik, R., Primc, G., and Vesel, A., Appl. Sci., 11 (5) (2021) 2275.

[12] Pauna, H., Aula, M., Seehausen, J., Klung, J.-S., uttula, M., and Fabritius, T., Steel Res. Int., 91 (2020) 20000.

[13] Qusnudin, A., Kusumandari, K., and Saraswati, T.E., J. Phys.: Conf. Ser., 1825 (2021) 012072.

[14] Aadim, K.A. and Yousef, A.A., Iraqi J. Sci., 95 (1C) (2018) 494.

[15] Samarkhanov, K., Khasenov, M., Batyrbekov, E., Kenzhina, I., Sapatayevn, Y., and Bochkov, V., Sci. Technol. Nucl. Install., 2020 (2020) 8891891.

[16] Tabares, F.L. and Junkar, I., Molecules, 26, 1903, (2021).

[17] Shaker, A.H., Aadim, K.A., Iraqi J. Appl. Phys., 20 (3B) (2024) 675.

[18] Afkhami, A. and Norooz-Asl, R., Colloids Surf. A Physicochem. Eng. Asp., 346 (1–3) (2009) 52.

[19] Imran, H.J., Hubeatir, K.A., and Aadim, K.A., Sci. Rep., 13 (1) (2023) 5441.

[20] Akash, M.S.H. and Rehman, K., "Ultraviolet-Visible (UV-VIS) Spectroscopy", In: "Essentials of Pharmaceutical Analysis", (Springer, Singapore, 2020), pp 29–56.

[21] Baniya, H.B., Shrestha, R., Guragain, R.P., Kshetri, M.B., Pandey, B.P., and Subedi, D.P., Int. J. Polym. Sci., 2020 (2020) 9247642.

[22] Hussein, T.S., Ahmed, A.F., and Aadim, K.A., Iraqi J. Sci., 63 (2) (2022) 548.

[23] Shehab, M.M. and Aadim, K.A., Iraqi J. Sci., 62 (9) (2021) 2948.

[24] Pligovka, A., Hoha, A., Turavets, U., Poznyak, A., Zakharau, Y., Mater. Today: Proc., 37 (4) (2021) A8.

Volume 18, Number 5, 2025. pp. 583-595

Jordan Journal of Physics

ARTICLE

Resonance Frequency Correlation with Negative Refractive Index and Impedance in SRR Structures

Lamyaa A. Jasim[a] and **Hassan A. Yasser**[b]

[a] *Physics Department, Education College, Thi-Qar University, Thi-Qar, Iraq.*
[b] *Physics Department, Science College, Thi-Qar University, Thi-Qar, Iraq.*

Doi: **https://doi.org/10.47011/18.5.3**
Received on: 01/04/2024; *Accepted on: 28/01/2025*

Abstract: This paper underlines the need to improve SRR cell design parameters to achieve both a negative refractive index and optimal impedance matching for advanced metamaterial applications. Metamaterials have unique light manipulation characteristics because of their negative refractive index and excellent impedance matching. This paper looks at numerous split-ring resonator (SRR) cell designs to find the best combinations. Square SRR cells consistently achieved a negative refractive index and excellent impedance matching throughout simulations, outperforming alternative forms such as circular SRRs. Increasing strip width often improves the negative refractive index, although it may create dispersion. Optimal separation distance resulted in a negative refractive index and perfect impedance for particular SRR forms (SSRR, HSRR, and OSRR); however, CSRR designs degraded with greater separations. All SRR forms produced satisfactory results, however CSRR designs had a somewhat poorer performance. Notably, a greater outer side ($a = 22mm$) SSSR cells resulted in a much higher negative refractive index throughout varying strip widths and separation distances.

Keywords: SRR structures, Resonance frequency correlation, Negative refractive index.

1. Introduction

In the world of electromagnetic engineering, split voltage engineering, known as split ring resonator (SRR), has been truly revolutionary, achieving an unprecedented transformation in our understanding of electromagnetic materials, opening up amazing new opportunities for designing cutting-edge technical systems and devices [1, 2]. Major contributions to metamaterials research were made by R. Shelby *et al*., who empirically established the existence of a negative refractive index [3]. This pioneering accomplishment set the path for future research into the fundamental principles driving metamaterial behavior, notably SRR structures. Concurrently, theoretical investigations to explicate the function of bianisotropy in producing negative permeability, creating the theoretical framework for comprehending the complexities of SRR-based metamaterials, were conducted by R. Marqués *et al*. [4]. The search to understand the resonance frequency association with negative refractive index in SRR structures has resulted in novel metamaterial characterization techniques [5]. J. Pendry *et al.* introduced a method for determining the effective permittivity and permeability of metamaterials using reflection and transmission coefficients, offering valuable insights into the design and optimization of SRR topologies [6]. Theoretical frameworks that permitted the research of typical electromagnetic phenomena, resulting in the realization of negative refractive index metamaterials, are presented in J. Pendry *et al*. [6]. Furthermore, comprehensive works have served as invaluable resources, providing in-depth analyses of metamaterial physics and engineering explorations that cover the fundamental principles and practical applications of SRR structures [7, 8].

Corresponding Author: Lamyaa A. Jasim **Email**: lamyaa.jasim@utq.edu.iq

Achieving a negative refractive index is the major objective of SRR development. This unusual trait occurs when both the effective permittivity and permeability of the SRR structure become negative at the same time [9, 10]. However, a hidden player, effective impedance, has a substantial impact on performance. Perfect power transmission requires a real part of effective impedance equal to z_0 (the characteristic impedance of open space), which is seldom achieved. In SRRs with a negative refractive index, the imaginary part of the effective impedance frequently differs from zero [11, 12]. This non-zero impedance imaginary part, together with the corresponding real part, adds to energy losses within the SRR, reducing its efficacy. Careful optimization of SRR shape and materials is required to achieve a compromise between obtaining a negative refractive index and reducing energy losses [13]. Researchers can tune the structure's electromagnetic response by precisely altering the size, shape, and composition of the SRR unit cells [14]. This enables them to attain the necessary negative refractive index while reducing the energy losses indicated by the non-zero imaginary element of impedance [15, 16]. The tricky balancing act of getting a negative n while avoiding energy losses is an ongoing focus of research in SRR development. Advances in material science and nanofabrication techniques are paving the way for the development of SRRs with higher performance and lower energy losses [17]. This offers great potential for the creation of new gadgets and applications that take advantage of the unique qualities of negative refraction [18]. Impedance matching is vital in electromagnetic systems to minimize wave reflection and maximize transmission. In metamaterials, particularly those using split-ring resonators (SRRs), it ensures efficient energy transfer and optimal functionality, such as negative refractive indices and enhanced resonance [19]. Proper SRR design aligns impedance with the surrounding medium, reducing energy loss and improving performance in applications like medical imaging, communication systems, and advanced optical devices [20]. This makes impedance matching a cornerstone in SRR-based metamaterial design, enabling broader and more efficient applications [21].

This paper presents a finite element method (FEM)–based simulation study of several SRR unit cell configurations within the COMSOL environment. Also, it focuses on the impedance imaginary part that accompanies this phenomenon and the possibility of achieving an ideal impedance matching, which is a necessary condition in electromagnetic systems.

2. Design of Split Ring Resonators

After conducting simulations in the COMSOL environment, the study aimed to investigate the influence of geometric dimensions and dielectric constants on the bandwidth and resonant frequency of SRRs within the frequency range of 2-6 GHz, essential for modern communication systems. To achieve this, appropriate designs for SRRs were implemented, and a mesh that provided an appropriate balance between result quality and implementation speed was chosen. By altering the shape, number, and dimensions of the rings, specific resonant frequencies with desired bandwidths could be achieved, potentially leading to multiple resonant frequencies within the same frequency range. Four main types of SRR cells were analyzed: square (SSRR), hexagonal (HSRR), octagonal (OSRR), and circular (CSRR). Each SRR cell consists of two metal strips on an insulating surface with a dielectric constant ε_r and thickness h, in the form of two concentric rings, each ring with a width C and separated by a distance D; each ring has a gap of width g, with the gaps oriented in opposite directions. In our work, these rings were in the form of a square, hexagon, octagon, or circle. The length of the dielectric side is L, the distance from the center to the outer edge of the shape is r_{ext} (which is the outer radius of the large ring in the case of CSRR). The background of all the rings is the same: five rectangular strips with width w, length ℓ, and the distance between the strips s. Figure 1 illustrates the model structure in the COMSOL environment.

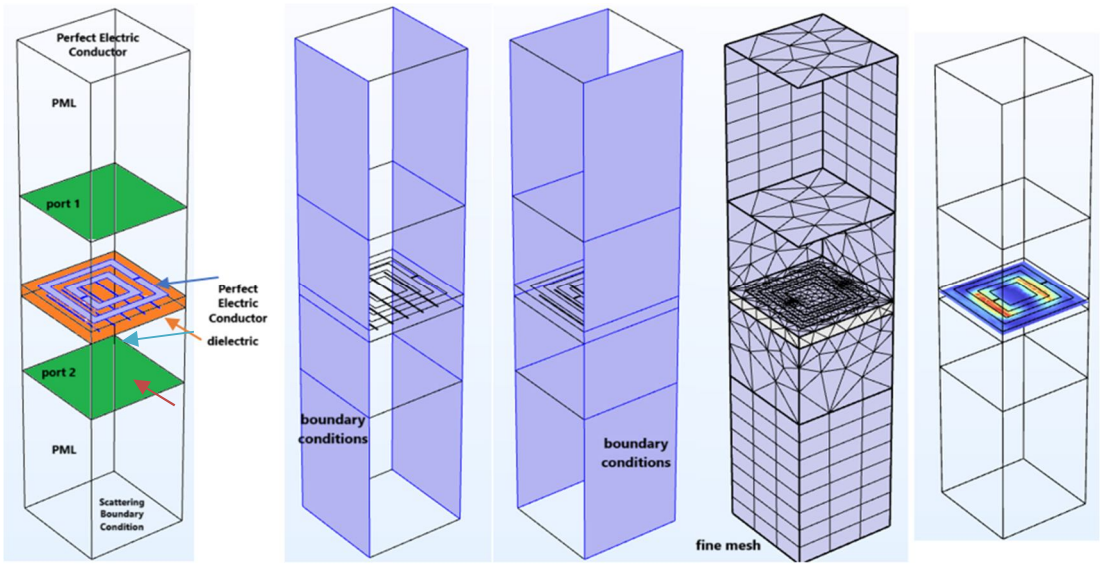

FIG. 1. Structure, ports, PML, periodic conditions, and mesh in COMSOL.

Figure 2 shows the structure of the SSRR unit cell. The rest of the cells differ only in geometric shape and employ the same notation for the engineering parameters. The figure also presents the background structure. The dimensions of the metallic strips, gap width, the distance between strips, dielectric thickness, dielectric constant, the distance between strips in the background, strip width in the background, strip length in the background, cell width, the outer side length, and the outer ring radius are listed in Table 1 for all SRRs, with any changes noted accordingly during the study. Figure 3 shows the convergence test.

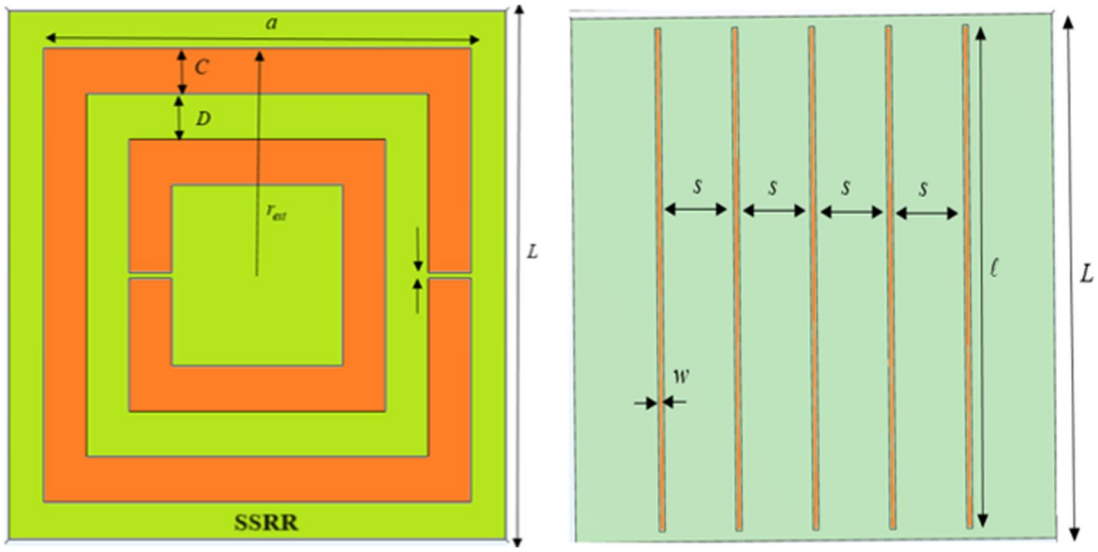

FIG. 2. SSRR structure and background.

TABLE 1. Simulation parameters.

Parameter	SSRR	HSRR	OSRR	CSRR
L	24mm	24mm	24mm	24mm
a	22mm	13.856mm	9.941mm	-
C	2mm	2mm	2mm	2mm
D	2mm	2mm	2mm	2mm
g	0.3mm	0.3mm	0.3mm	0.3mm
r_{ext}	11mm	12mm	11mm	11mm
h	2mm	2mm	2mm	2mm
s	4mm	4mm	4mm	4mm
w	0.3mm	0.3mm	0.3mm	0.3mm

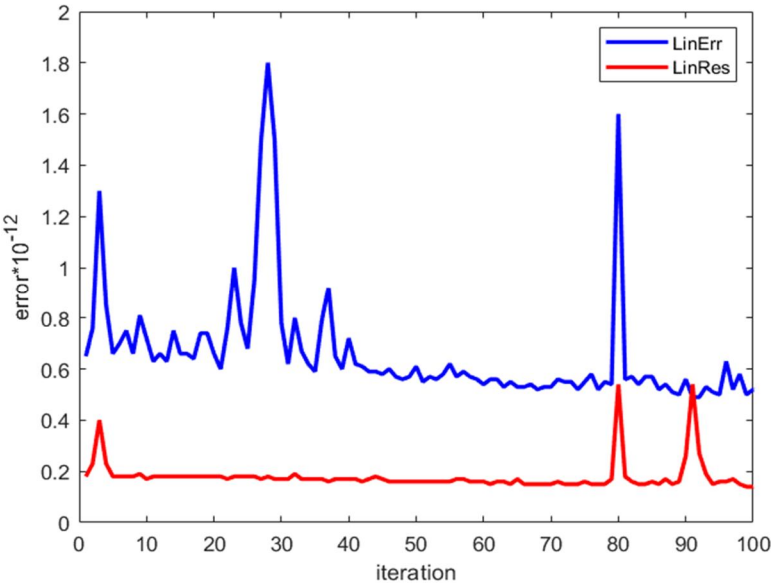

FIG. 3. Convergence test.

3. Retrieval Method Formation

Excitation of SRR with an external magnetic field causes the current to flow from one ring structure to another through the slot between them. As a result, this structure has a very strong displacement current flow. The slots in SRR behave like distributed capacitance, and it behaves like an LC circuit. In technical terms, metallic ring structures are modelled by inductance L and capacitance C. The structure behaves like an LC circuit having a resonant frequency given below as [22]:

$$w_R = \frac{1}{\sqrt{L_T C_T}} \tag{1}$$

where L_T is the total inductance and C_T is the total capacitance of the LC circuit. The effective parameters of a metamaterial slab are determined by the free-space reflection and transmission coefficients. To determine the parameters at N different frequency points, one can either measure the complicated S-parameters or employ full-wave electromagnetic simulators. For normal incident plane waves on a homogeneous metamaterial slab, the relation between the S-parameters, the complex impedance, and the complex refractive index is provided by [23]:

$$S_{11} = \frac{\Gamma(1-e^{-2in_{eff}kt})}{1-\Gamma^2 e^{-2in_{eff}kt}} \tag{2}$$

$$S_{21} = \frac{(1-\Gamma^2)e^{-in_{eff}kt}}{1-\Gamma^2 e^{-2in_{eff}kt}} \tag{3}$$

where $\Gamma = (z_{eff}-1)/(z_{eff}+1)$, t is the metamaterial slab thickness, and n_{eff} is the complex effective refractive index ($n_{eff} = n' + in''$), with n' and n'' being the real and imaginary parts of n_{eff}, respectively. The parameters S_{11} and S_{21} are complex and related to reflectance and the transmittance, respectively, as: $r = |S_{11}|^2$ and $t = |S_{21}|^2$.

The complex effective wave impedance z_{eff} is defined as [24]:

$$z_{eff} = R + iX = R + i\left(wL_T - \frac{1}{wC_T}\right) \tag{4}$$

The parameters z_{eff}, n_{eff} are related to S-parameters as [22]:

$$z_{eff} = \pm\sqrt{\frac{(1+S_{11})^2 - S_{21}^2}{(1-S_{11})^2 - S_{21}^2}} \tag{5}$$

$$n_{eff} = \pm\frac{1}{k_o a}cos^{-1}\left(\frac{1-S_{11}^2+S_{21}^2}{2S_{21}}\right) + \frac{2\pi m}{k_o a}, m = 0,1,2\ldots \tag{6}$$

where k_o is the free-space wavenumber, m is the multivalued logarithmic function's branch index, and a is the metamaterial slab thickness. As seen in [25], when the metamaterial thickness is modest, m is set to zero. When a is large, these branches can lie arbitrarily close to one another, making the selection of the correct branch difficult in the case of dispersive materials. For this reason, the best results are obtained for the smallest possible thickness of the sample, as is commonly known in the analysis of continuous materials. Even with a small sample, more than one thickness must be measured to identify the correct branches of the solution that yield consistently the same values for n.

The real value of the complex wave impedance and the imaginary value of the complex refractive index must both be greater than or equal to zero for a passive metamaterial, i.e., $R \geq 0, n'' \geq 0$. Therefore, the sign of z_{eff} must be decided in light of those circumstances. Specifically, the real and imaginary components of the complex refractive index are $n' = Re\{n_{eff}\}$, $n'' = Im\{n_{eff}\}$, respectively [26]. There are ambiguities in the formulations of the metamaterial's effective permittivity and permeability due to the resultant branch uncertainty in the real part of the complex refractive index. The following formulas connect the complex permittivity and complex permeability to the complex refractive index and the wave impedance [27]:

$$\varepsilon_{eff} = n_{eff}/z_{eff} \quad (7)$$

$$\mu_{eff} = n_{eff} z_{eff} \quad (8)$$

4. Results and Discussion

Figure 4 depicts the relationship of S_{11} with frequency in the 2-6 GHz band using various values of *D*, which denote the distance between two strips. It is worth noting that each *D* value results in various behaviors in terms of resonance frequency, bandwidth, and minimum attainable value. While it is possible to achieve another resonant frequency within the same range, our attention is on the case with a greater bandwidth, also known as the fundamental resonant frequency. Furthermore, when *D* grows, the fundamental resonant frequency shifts to the right. However, it is critical to understand that *D* cannot expand indefinitely since it is inextricably tied to cell size.

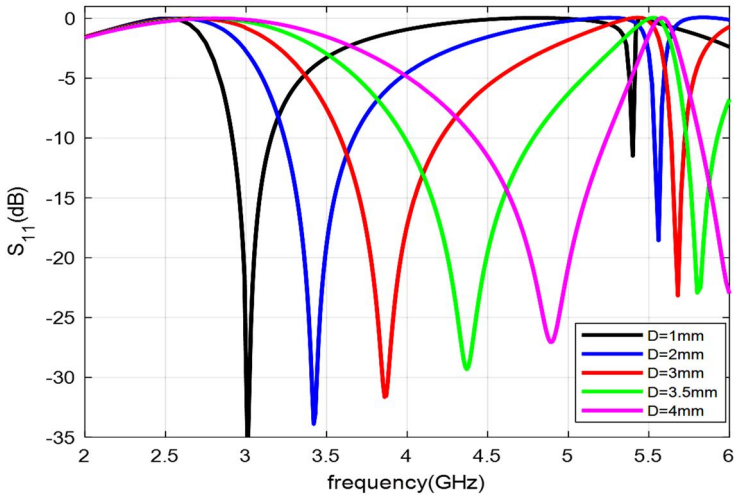

FIG. 4. S_{11} as functions of frequency using many values of *D* for SSRR.

In Fig. 5, we show the connection between the normalized real refractive index and the normalized frequency for various *C* values inside the SSRR cell. Our primary focus is on the fundamental resonance frequency, which demonstrates a clear relationship between the refractive index and resonance frequency regions. Although comparable patterns appear when additional parameters such as *C*, *s*, *h*, *a*, and dielectric constant are changed, it is worth noting that the resonant frequency and bandwidth vary with time. As a result, we avoid demonstrating these recurrent actions. Instead, we stress the resonance frequency's relationship with the negative refractive index, as well as the real and imaginary parts of impedance.

Figure 6 presents the real part of the refractive index, the imaginary part of the impedance, and the real part of impedance at resonance as functions of strip width for many SRRs at $h = 3\ mm$, $D = 2\ mm$, $\varepsilon_r = 4.3$, $s = 4\ mm$. Figure 6(a) shows that the resonance frequency occurs when the refractive index is negative. In general, raising *C* leads to an increase in the real refractive index. The CSRR cell exhibits the highest real refractive index, while the SSRR shows the lowest. The figure shows that the real refractive index is negative until it approaches $C > 3$, after which it is positive in the case of cell CSRR. However, it always remains negative in SSRR and OSRR cells. When *C* is less than 3.5, the HSRR cell produces a negative refractive index. The metamaterial property is attained for all cells by creating $C < 3$. It is clearly evident from Fig. 6(b) that the imaginary part of the impedance is close to zero at first and then increases slowly as

the strip width increases for square, hexagonal, and octagonal cells, but it increases strongly in the case of the circular cell and then decreases to negative values. Losses and imperfect coupling between the cell and wire may increase the imaginary value of impedance. Additionally, nonlinear effects can introduce extra frequency components into the cell response, further causing deviations of the impedance imaginary part from zero. In general, increasing the strip width makes the impedance imaginary part non-zero.

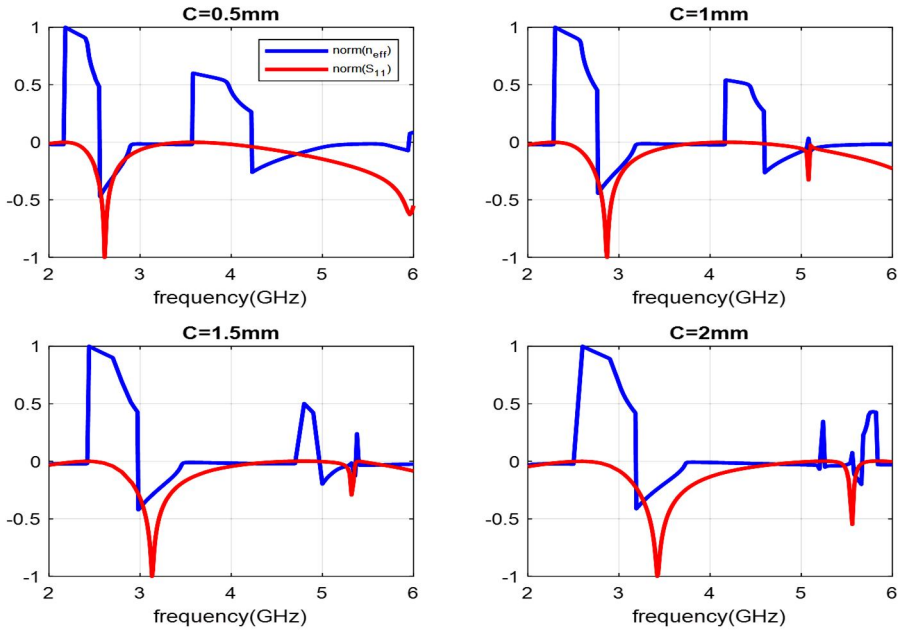

FIG. 5. Normalized S_{11} and effective refractive index as functions of frequency using many values of strip width for SSRR.

In Fig. 6(c), the matching between the system impedance and the characteristic impedance happens at $z_{eff}/z_0 = 1$. When condition $z_{eff}/z_0 = 1$ is met, the ideal case for electromagnetic systems occurs. Note that condition $z_{eff}/z_0 = 1$ is achieved almost at the beginning for all cells, but it is not achieved as C continues to increase, and the cell furthest from condition $z_{eff}/z_0 = 1$ is the CSRR cell. The cases $z_{eff}/z_0 > 1$ indicate that the SRR cell's effective impedance exceeds the line's characteristic impedance. The entering electromagnetic wave may be reflected at the SRR cell interface due to an impedance mismatch. The greater the ratio z_{eff}/z_0, the stronger the reflection may be. When $z_{eff}/z_0 < 1$, the SRR cell's effective impedance is lower than the line's characteristic impedance. In this situation, the SRR cell may cause dispersion, which means that the propagation speed of different frequencies within the electromagnetic wave will vary. The smaller the ratio z_{eff}/z_0, the greater the dispersion impact may be.

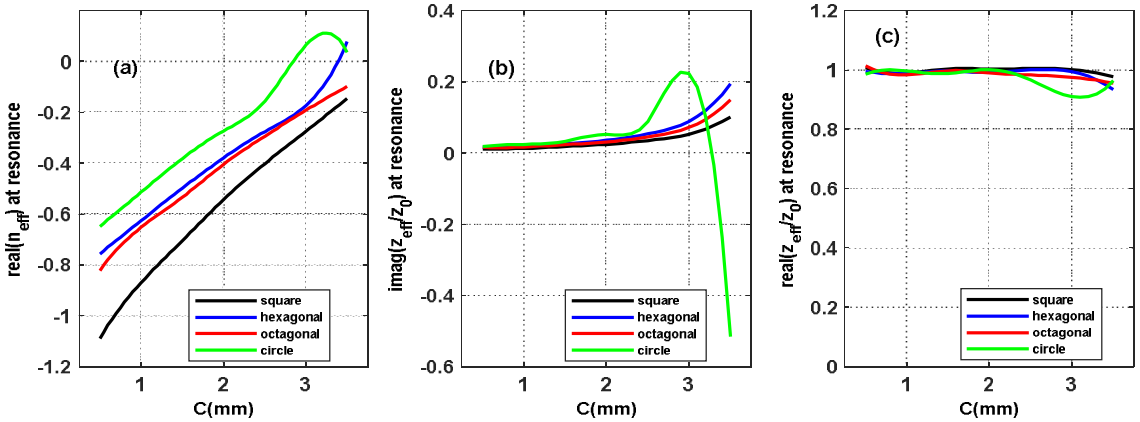

FIG. 6. Real part of the refractive index, imaginary part of the impedance, and real part of the impedance at the resonance frequency as functions of strip width for many SRRs.

Figure 7 shows the dependence of the real part of the refractive index, the imaginary part of the impedance, and the real part of impedance at resonance on the distance between the strips for many SRRs at h = 3 *mm*, C = 2 *mm*, $\varepsilon_r = 4.3$, and s = 4 *mm*. Figure 7(a) shows that the real part of the refractive index is negative at the resonance frequency when $D < 4.7$ *mm* for square, HSRR, and OSRR cells, and it is negative in the case of the CSRR cell when $D <$ 3.8 *mm*. Note that the SSRR/CSRR cells always represent the lowest/highest real refractive index. Figure 7(b) shows that the imaginary part of the impedance starts close to zero for all cells except the CSRR case, and after $D > 3.5$ *mm,* the values begin to increase or decrease depending on the cell type, with HSRR and OSRR cells maintaining some degree of stability until D = 3.5 *mm*. In the case of the CSRR cell, the impedance imaginary part is not the same as its predecessors but rather alternates between positive and negative. Also, the SSRR cell will have values far from zero when D = 3 *mm*. In general, the negative imaginary part of the impedance moves away from zero in response to the corresponding negative refractive index. Positive values mean that the characteristic of inductance is dominant, and negative values mean that the characteristic of capacitance is dominant, while a zero value means that the impedance is composed of resistance only. Figure 7(c) shows that the condition $z_{eff}/z_0 = 1$ is met for HSRR and OSRR cells at $D < 3.8$ *mm*, while it is met at $D < 3$ *mm* for SSRR cells. In the case of the CSRR cell, the impedance varies greatly, and condition $z_{eff}/z_0 = 1$ is not met except at a few points. In general, for all cells except the CSRR cell, a wide range of D values can be obtained that achieve a negative refractive index, zero impedance imaginary part, and meet the necessary condition $z_{eff}/z_0 = 1$ for the ideal case in electromagnetic systems.

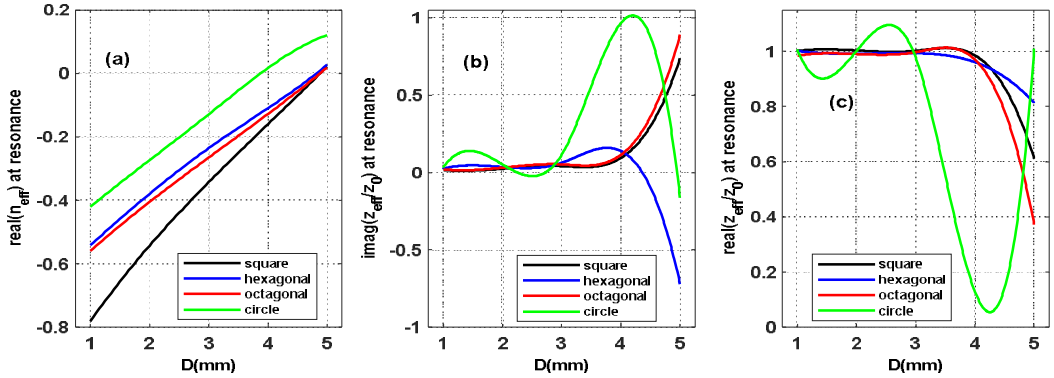

FIG. 7. Real part of the refractive index, imaginary part of the impedance, and real part of the impedance at the resonance frequency as a function of distance between the strips for many SRRs.

Figure 8 shows the dependence of the real part of the refractive index, the imaginary part of the impedance, and the real part of impedance at resonance on the dielectric thickness for many SRRs at D = 2 *mm*, C = 2 *mm*, $\varepsilon_r = 4.3$, s = 4 *mm*. Figure 8(a) shows that a negative refractive index is achieved in HSRR and CSRR cells as long as $h < 2.3$ *mm*. It is achieved for SSRR and OSRR cells as long as $h < 2.8$ *mm*. The SSRR/CSRR cells achieve the lowest/highest negative refractive index. Figure 8(b) shows a slight increase in the impedance imaginary part values for all cells, with the impedance imaginary part of the CSRR/SSRR cells being the highest/lowest. We can confirm here that the impedance imaginary part is small under the simulated conditions. Also, we note that the impedance imaginary part corresponding to negative refractive indices is the lowest. Note that the imaginary part of impedance should be zero at the resonant frequency, but this was not achieved due to neglecting the phenomena of loss, coupling, and nonlinearity. This is due to the following: at the resonance frequency $z_{eff} = z_0$, the effective impedance will be real, and the imaginary impedance will be zero; and due to absorption effects, coupling within the cell parts, and perhaps also nonlinear effects that can occur in the insulator, the imaginary part of the impedance will not be zero at the resonance frequency.

Figure 8(c) shows the fulfillment of the condition $z_{eff}/z_0 \approx 1$, which is necessary for electromagnetic systems for all values of h using every SRR cell. The sign of approximation, not equality, is used due to the presence of a small amount of impedance imaginary part, depending on the cell type.

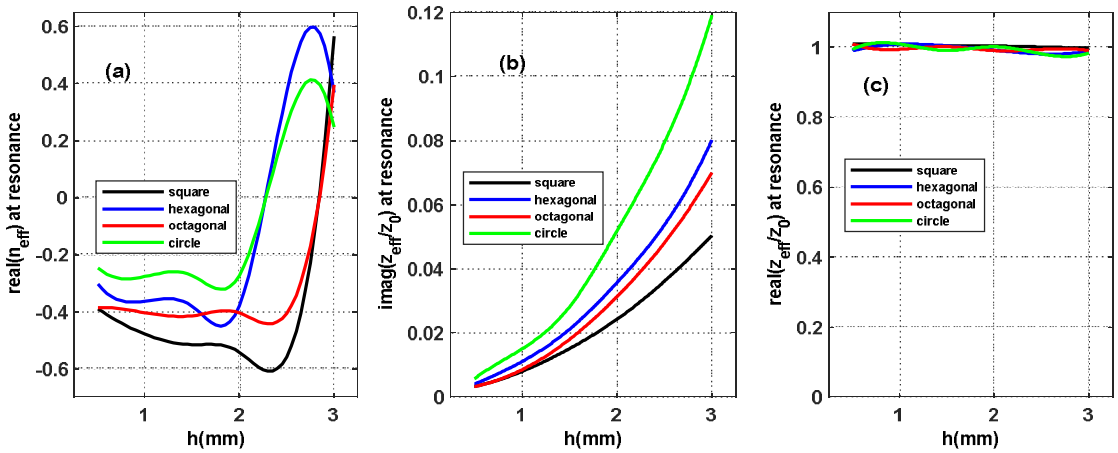

FIG. 8. Real part of the refractive index, imaginary part of the impedance, and real part of the impedance at resonance frequency as a function of dielectric thickness for many SRRs.

Figure 9 shows the dependence of the real part of the refractive index, the imaginary part of the impedance, and the real part of the impedance at resonance on the dielectric thickness for many SRRs at $D = 2\ mm$, $C = 2\ mm$, $\varepsilon_r = 4.3$, $h = 3\ mm$. Figure 9(a) shows that a negative refractive index is achieved at all values of s and for all cells, with SSRR/CSRR cells achieving the lowest/highest negative refractive indices. It can also be noted that the variation of the refractive index in all cases is small. The figure shows that the impedance imaginary part in all cells has small values and that SSRR/CSRR achieves the lowest/highest values, and the impedance imaginary part in the case of the CSRR cell is three or four times greater than that of the SSRR cell. In general, it can be understood from this that the conditions causing negative impedance (losses, coupling, and nonlinearity) are minimal under the simulated conditions. Figure 9(c) shows that condition $z_{eff}/z_0 \approx 1$ is met at the resonance frequency for all values of s and for all cells used. Accordingly, under the present simulation conditions, a metamaterial with a near-zero impedance imaginary part can be obtained, and the ideal impedance condition can be achieved.

Figure 10 shows the dependence of the real part of the refractive index, the imaginary part of the impedance, and the real part of the impedance at resonance on the dielectric constant value for SSRR and CSRR cells at $D = 2\ mm$, $C = 2\ mm$, $s = 4\ mm$, $h = 3\ mm$. Figure 10(a) shows that SSRR/CSRR achieve the lowest/highest negative refractive indices over every dielectric constant range. In Fig. 10(b), the impedance imaginary part achieved in the case of CSRR is much larger than in SSRR, but in general, it is very small. Figure 10(c) demonstrates that near-ideal impedance matching is maintained across all dielectric constant values for the two cells used. The current simulation conditions achieved the metamaterial property, reduced the impedance imaginary part to the lowest possible level, and achieved the ideal impedance condition.

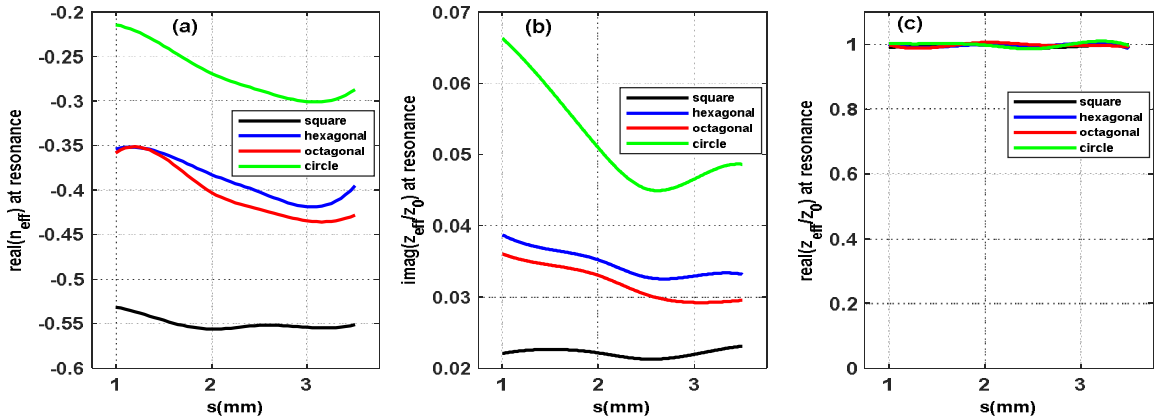

FIG. 9. Real part of the refractive index, imaginary part of the impedance, and real part of the impedance at resonance frequency as a function of distance between strips in the background for many SRRs.

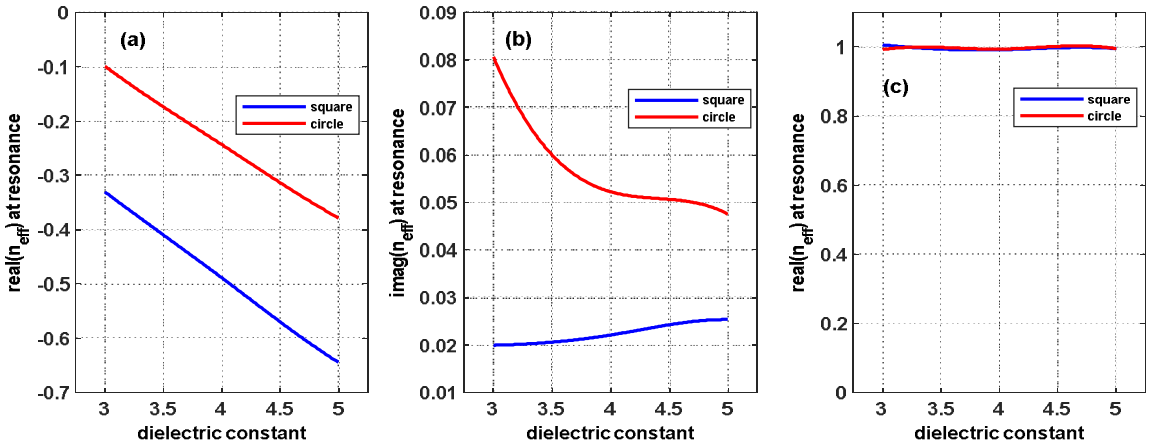

FIG. 10. Real part of the refractive index, imaginary part of the impedance, and real part of the impedance at the resonance frequency as a function of dielectric constant for SSRR and CSRR cells.

Figure 11 shows the dependence of the real part of the refractive index, the imaginary part of the impedance, and the real part of impedance at resonance on strip width for SSRR (a = 22 mm, a = 20 mm) and CSRR ($r_{ext} = 11\ mm, r_{ext} = 10\ mm$) cells at D = 2 mm, s = 4 mm, h = 2 mm, $\varepsilon_r = 4.3$. Figure 11(a) shows that the SSRR cell (a = 22 mm) exhibits the lowest negative refractive index for all strip widths. The SSRR (a = 20 mm) and CSRR ($r_{ext} = 11\ mm$) cells have a negative refractive index up to a strip width C < 2.9 mm. The CSRR ($r_{ext} = 10\ mm$) cell has the largest negative refractive index up to strip width C < 2.3 mm. Figure 11(b) shows an impedance imaginary part that increases slightly with the increase in the strip width of the SSRR cell (a = 22 mm). For the SSRR (a = 22 mm) and CSRR($r_{ext} = 11\ mm$) cells, the impedance imaginary part starts small, then increases slightly, and then increases strongly and decreases to negative values. For the CSRR cell ($r_{ext} = 10\ mm$), we see that the impedance imaginary part changes severely, which is the worst case. This means that the nature of the impedance imaginary part depends on the achievement of the negative refractive index. In general, a near-zero imaginary impedance is observed only within a limited range of strip widths.

Figure 11(c) confirms this trend for impedance matching. Ideal impedance condition $z_{eff}/z_0 \approx 1$ is achieved only over a small strip width range for most cells.

For C > 1.5 mm, all cells except the SSRR (a = 22 mm) deviate from the ideal condition. The SSRR cell (a = 22 mm) maintains near-ideal impedance $z_{eff}/z_0 \approx 1$ across the full range of strip widths. Overall, for all cells, near-ideal impedance consistently coincides with a negative refractive index at the resonance frequency.

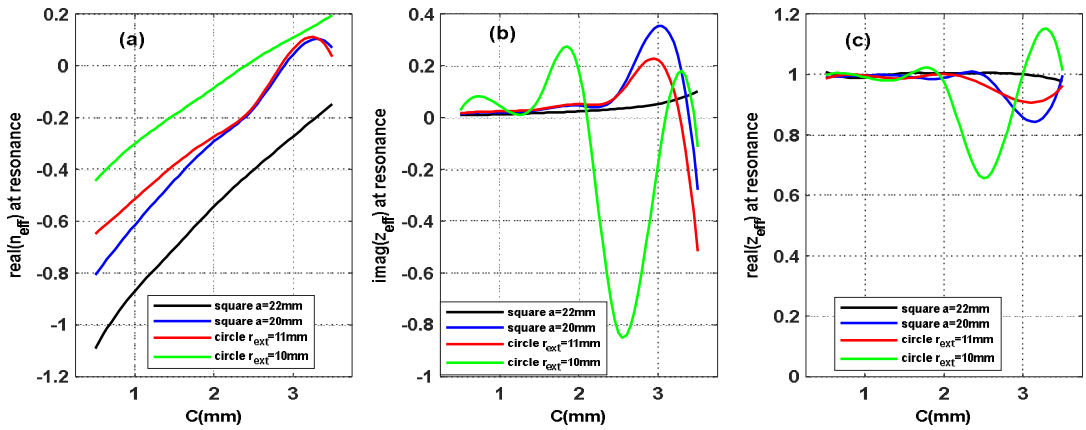

FIG. 11. Real part of the refractive index, imaginary part of the impedance, and real part of the impedance at resonance frequency as a function of strip width for many SRR cells.

Figure 12 shows the dependence of the real part of the refractive index, the imaginary part of the impedance, and the real part of the impedance at resonance on the distance between strips for SSRR (a = 22 mm, a = 20 mm) and CSRR ($r_{ext} = 11\ mm, r_{ext} = 10\ mm$) cells at C

= 2 *mm*, s = 4 *mm*, h = 2 *mm,* and $\varepsilon_r = 4.3$. Figure 12(c) shows that the SSRR cell (a = 22 *mm*) achieves a negative refractive index at $D <$ 4.8 *mm*, and that the two cells, SSRR (a = 20 mm) and CSRR ($r_{ext} = 11\,mm$), achieve a negative refractive index at $D <$ 3.7 *mm*. The CSRR ($r_{ext} = 10\,mm$) cell shows the most irregular behavior, with the refractive index initially negative, then becoming positive, and returning to negative values. Figure 12(b) shows that the SSRR cell (a = 22 *mm*) initially achieves near zero impedance imaginary part and then increases, while the other cells exhibit significant variations in the imaginary impedance across the range.

Figure 12(c) shows the impedance matching condition. Near-ideal impedance is achieved only at the beginning for the SSRR cell (a = 22 *mm*). All other cells remain far from the ideal impedance condition throughout the examined range.

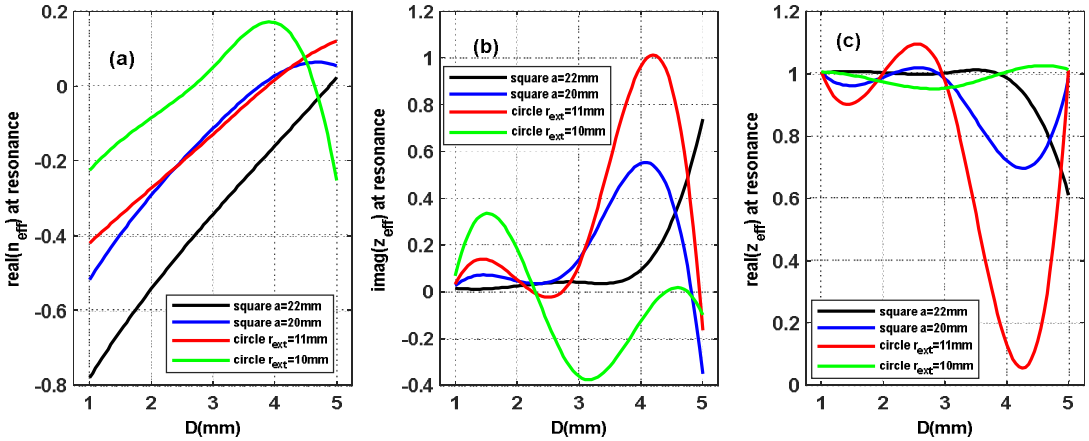

FIG. 12. Real part of the refractive index, imaginary part of the impedance, and real part of the impedance at the resonance frequency as a function of distance between strips for many SRR cells.

Figure 13 shows the bandwidth, resonance frequency, and minimum S_{11} as functions of the dielectric thickness h for the four types of SRR.

The bandwidth decreases as h increases. The octagonal cell exhibits the smallest bandwidth, while the circular and square cells show similar bandwidth values at h = 0.7, 2 mm. The figure representing the resonance frequency as a function of h shows that the resonance frequency is inversely proportional to the dielectric thickness. Among the geometries, the circular cell achieves the highest resonance frequency, whereas the square cell exhibits the lowest. The figure that represents the minimum value of S_{11} as a function of h shows a direct proportion between the minimum value of S_{11} and the dielectric thickness. We notice that the minimum value of S_{11} is the highest possible in the case of circuit, but when it is less than h = 1 mm, it begins to decline and achieves the lowest value for the minimum value of S_{11} and also in the octagonal state, at less than h = 1.5 mm, it begins to decline and is less than the square case.

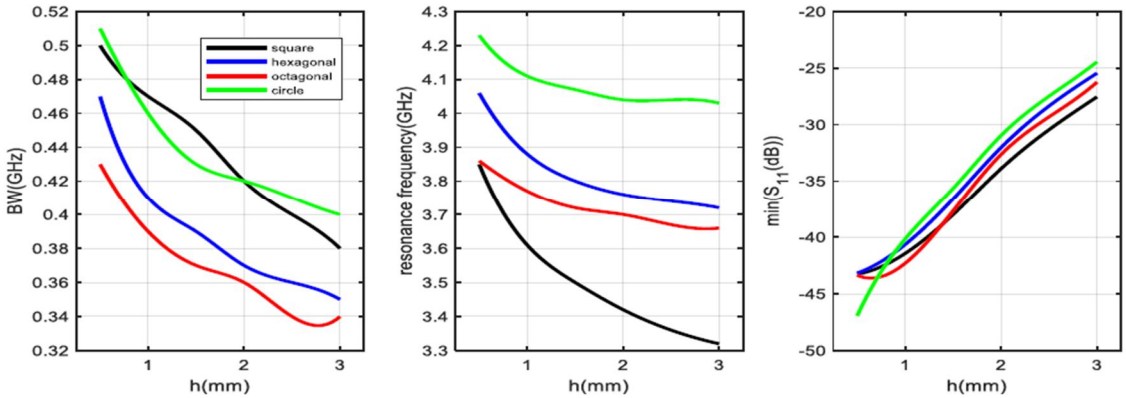

FIG. 13. Bandwidth, resonance frequency, and minimum value of S_{11} as functions of h for different SRRs.

Figure 14 shows the bandwidth, resonance frequency, and minimum value of S_{11} as functions of D using four types of SRR. It appears from the figure representing the bandwidth as a function of D that the bandwidth increases with increasing D for all four types of SRR, but for the case of the circuit, we notice that it tends to stabilize from D = 4.5 mm and above. The largest bandwidth is obtained for the square, while the octagonal exhibits the smallest. The resonance frequency appears to increase with increasing D in the case of a circle and decrease correspondingly in the case of a square. The minimal value of S_{11} appears to increase as D increases; however, in the case of an octagonal, the minimum value of S_{11} tends to stabilize between D = 1 mm and D = 1.5 mm. The peak is the largest in the case of a circle and the least in the case of a square. Figure 15 shows the bandwidth, resonance frequency, and minimum value of S_{11} as functions of C for the four types of SRR. The bandwidth increases with increasing C for all cases; however, for the circuit, it tends to stabilize for C = 2.5 mm and above. The bandwidth is the largest possible in the case of a square and the smallest possible in the case of an octagonal. The resonance frequency increases with increasing C in the case of a circle and decreases as much in the case of a square. The minimal value of S_{11} appears to increase as C increases; however, in the case of an octagonal, the minimum value of S_{11} tends to stabilize between C = 0.5mm and C = 1.5mm. The peak is the largest possible in the case of a circle and the least possible in the case of a square. When the strip width in the SRR is increased, reflections and deviations in the signal transmission are reduced, and this is reflected by increasing the minimum value of S_{11}.

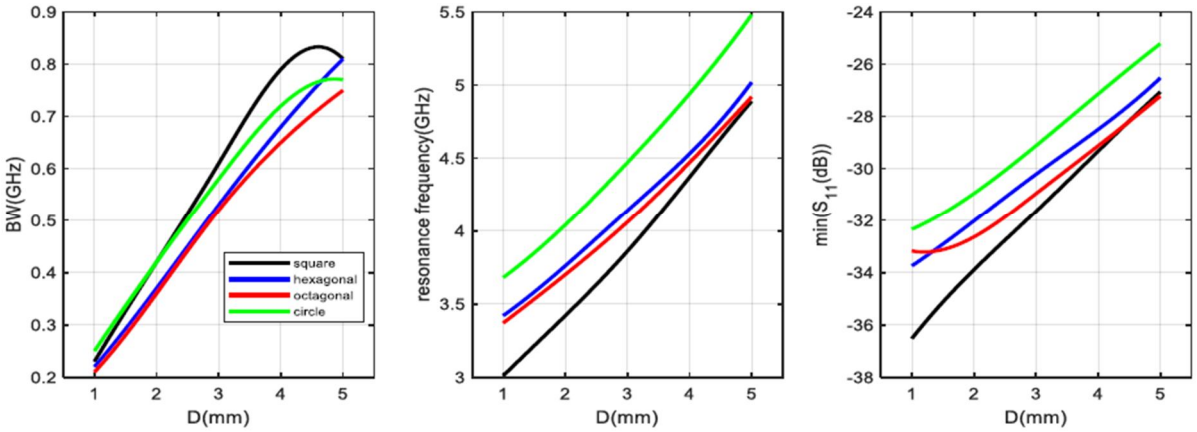

FIG. 14. Bandwidth, resonance frequency, and minimum of S_{11} as functions of D for different SRRs.

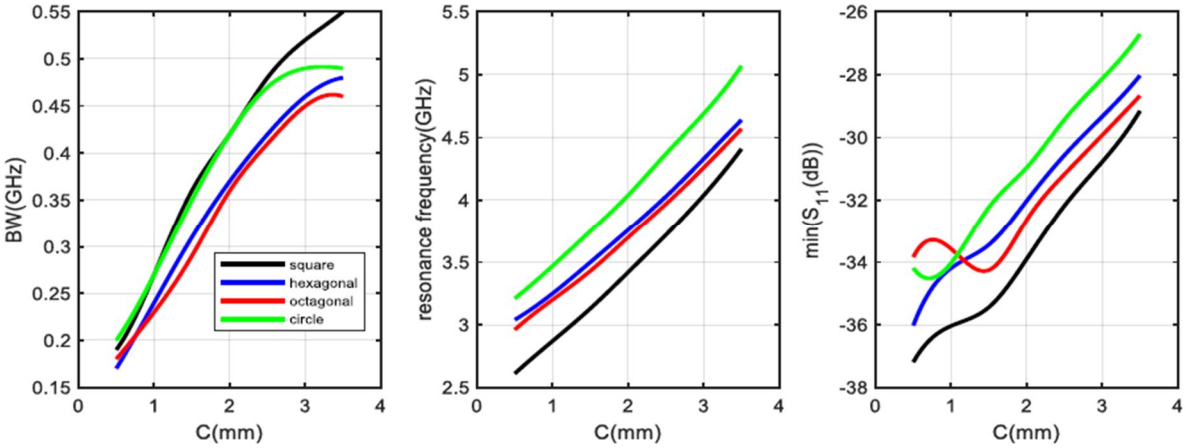

FIG. 15. Bandwidth, resonance frequency, and minimum of S_{11} as functions of C for different SRRs.

5. Conclusions

In conclusion, increasing *C*, *D*, and h leads to an increase in the resonant frequency and bandwidth, and, in some cases, to the appearance of additional resonant modes for the four types of SRR. The resonant frequency, the bandwidth, and the minimum value of S_{11} increase with increasing *C* and *D* for all types of SRR, and there may be some cases of stability in some types of SRR. The SSRR cell consistently achieved a negative refractive index and excellent impedance matching throughout several simulations. This shows that the metamaterials have strong characteristics, making them suitable designs. Other cell forms, such as CSRR, often fared poorly. Wider strips enhance the negative refractive index but may add undesirable features, such as dispersion. The optimal spacing between strips resulted in a negative refractive index and perfect impedance $z_{eff} \approx z_0$ for SSRR, HSRR, and OSRR cells, whereas CSRR designs suffered at wider separations. For varying strip widths and dielectric constants, all SRR forms obtained a negative refractive index and excellent impedance matching. However, the performance of the CSRR design was marginally lower. Larger side lengths (a = 22mm) resulted in improved negative refractive index values for both strip width and strip separation changes. The work emphasizes the need to improve SRR cell design characteristics, particularly the outer radius, to achieve both a negative refractive index and optimal impedance matching for metamaterial applications.

References

[1] Tian, S., Zhang, X., Wang, X., Han, J., and Li, L., Nanophotonics, 11 (9) (2022) 1697.

[2] Rhee, J., Kim, Y., Yi, C., Hwang, J., and Lee, Y., J. Electromagn. Waves Appl., 34 (2020) 1338.

[3] Shelby, R., Smith, D., Nemat-Nasser, S., and Schultz, S., Appl. Phys. Lett., 78 (2001) 489.

[4] Marqués, R., Medina, F., and El-Idrissi, R., Phys. Rev. B, 65 (2002) 144440-1.

[5] Smith, D., Schultz, S., Markoš, P., and Soukoulis, C., Phys. Rev. B, 65 (2002) 195104.

[6] Pendry, J., Holden, A., Robbins, D., and Stewart, W., IEEE Trans. Microw. Theory Tech., 47 (1999) 2075.

[7] Eleftheriades, G. and Balmain, K., "Negative Refraction Metamaterials: Fundamental Principles and Applications", 1st Edition, (John Wiley and Sons, Hoboken, 2005).

[8] Engheta, N. and Ziolkowski, R., "Metamaterials: Physics and Engineering Explorations", (IEEE Press, The Institute of Electrical and Electronics Engineers, Inc., 2006).

[9] Esmail, B., Majid, H., Saparudin, F., Jusoh, M., Ashyap, A., Al-Fadhali, N., and Rahim, M., Bull. Electr. Eng. Inform., 9 (3) (2020) 1038.

[10] Kalel, S. and Wang, W., Prog. Electromagn. Res. C, 132 (2023) 159.

[11] Sifat, R., Faruque, M., Ramachandran, T., Abdullah, M. and Al-Mugren, K., Heliyon, 10 (1) (2024).

[12] Qiong Zhang, Z., Cao, W., Gao, M., Liu, Y., and Chu, W., Heliyon, 9 (11) (2023).

[13] Ramachandran, T., Mri, F., Ahamed, E., and Abdullah, S., Results Phys., 15 (2019) 1.

[14] Singh, H., Mittal, N., and Arora, O., Mater. Today, Proc., 33 (3) (2020) 1552.

[15] Singh, H., Sohi, B.S., and Gupta, A., Bull. Mater. Sci., 42 (2019) 1.

[16] Islam, S.S., Rahman, M.A., Faruque, M.R.I., and Islam, M.T., Sci. Eng. Compos. Mater., 25 (1) (2018) 59.

[17] Islam, S.S., Khan, M.S., and Faruque, M.R.I., Mater. Res. Express, 6 (12) (2020).

[18] Shah, A. and Ghalsasi, P., Navrachana Univ. Interdiscip. J., 5 (2) (2022).

[19] Madhavamoorthi, S., Marishwari, M., Kashif, H., Shen, S., Chen, B., Xie, H., Ouyang, Z., and Liu, Q., Opt. Express, 32 (22) (2024) 38422.

[20] Nguyen, Q. and Zaghloul, A., IEEE Int. Symp. Antennas Propag. USNC/URSI Natl. Radio Sci. Meet., Boston, MA, USA, (2018) 439.

[21] Portosi, V., Loconsole, A., and Prudenzano, F., Appl. Sci., 10 (2020) 6740.

[22] Khalili, F. , Honarvar, M. , Moghadasi, M., and Dolatshahi, M., Int. J. RF Microw. Comput.-Aided Eng., 30 (1) (2020) e22006.

[23] Islam, M., Islam, M.T., Moniruzzaman, M., and Muhammad, G., Results Phys., 19 (2020) 103556.

[24] Hossain, Md., Faruque, M., Islam, S., and Islam, M., Sci. Rep., 11 (1) (2021) 19331.

[25] Moniruzzaman, Md., Islam, M., Samsuzzaman, Md., Salaheldeen, M., Sahar, N., Bawri, S., Almalki, S., Alsaif, H., and Islam, Md., Sci. Rep., 12 (1) (2022) 1.

[26] Islam, Md., Islam, M., Soliman, M., Baharuddin, M., Mat, K., Moubark, A., and Almalki, S., Sci. Rep., 11 (2021) 21782.

[27] Aladadi, Y. and Alkanhal, M., Opt. Mater. Express, 9 (9) (2019) 3765.

Volume 18, Number 5, 2025. pp. 597-611

Jordan Journal of Physics

ARTICLE

Magnetothermal Properties of Exciton In TMD_ WS_2 Monolayer

Reham Reda Kmail[a], **Muayyad Abu Saa**[a] and **Mohammad K. ElSaid**[b]

[a] *Physics Department, Arab American University of Jenin (AAUJ), Jenin, West Bank, Palestine.*

[b] *Physics Department, An-Najah National University (ANNU), Nablus, West Bank, Palestine.*

Doi: **https://doi.org/10.47011/18.5.4**

Received on: 16/08/2024; *Accepted on: 16/02/2025*

Abstract: The Hamiltonian of an exciton in a thin layer of WS_2-transition metal dichalcogenide (TMD) was solved by the 1/N expansion method, and the corresponding exciton bound-state energies were obtained. The Hamiltonian describes an electron-hole particle system interacting through an attractive Rytova-Keldysh potential (V_{RK}) in a sheet of WS_2, which is presented in an external uniform magnetic field applied perpendicular to the material sheet plane. We used the computed eigenenergies to calculate the partition function, which depends on the temperature and magnetic field. We calculated the magnetic and thermal quantities of WS_2 TMD material sheet for various values of magnetic field strength and temperature range. The comparisons show that the calculated exciton energy spectra against experimental and theoretical corresponding results are in very good agreement. We have displayed the dependence of magnetization, susceptibility, entropy, and heat capacity as a function of magnetic field and temperature. The paramagnetic behavior of materials over a wide range of magnetic fields was considered. In addition, the density of states (DOS) of TMD-WS_2 material was calculated, and the resulting DOS plot shows an oscillator peak behavior for various ranges of the magnetic field strengths.

Keywords: TMD material, Exciton, 1/N expansion, Magnetic susceptibility, Heat capacity, Entropy, Density of states.

1. Introduction

Transition metal chalcogenide dimers (TMDC or TMD) monolayers are atomically thin MX_2-type semiconductors, where M denotes a transition metal atom (such as Mo or W), and X represents a chalcogen atom (S, Se, or Te). One layer of M atoms is sandwiched between two layers of X atoms. They are part of a large family of so-called two-dimensional materials [1]. Monolayers of MoS_2, WS_2, $MoSe_2$, WSe_2, and $MoTe_2$ exhibit direct bandgaps, and can be used in electronics as transistors and in optics as emitters and detectors. [2-5]. Their two-dimensional nature, combined with strong spin–orbit coupling, makes TMD layers particularly attractive for advanced electronic and spintronic applications [6]. Basically, when a positive hole (an empty electron particle in the valence band) and an electron combine and can move freely through a non-metallic crystal as a unit, the mixing of these two particles is called an exciton. Excitons play an important role in transition metal chalcogenide (TMD) monolayers.

The two-dimensional nature and high spin-orbit coupling of TMD layers render them useful for electronic applications [7]. Work on and use of TMD monolayers is an important research and development area for potential applications in electronics. TMDs are combined with 2D materials such as graphene and hexagonal boron nitride to make van der Waals heterostructures. This is to work on optimizing these heterogeneous structures for use as building blocks for many different devices, such as transistors, solar cells, LEDs, photodetectors, fuel cells, photocatalysts, and sensors. We need to use these devices in our daily lives so that

Corresponding Author: Reham Reda Kmail **Email**: reham.kmail@aaup.edu

they become smaller, cheaper, and more efficient by using single layers [8, 9].

In recent years, the study of excitons in (TMD) monolayers has attracted much attention because their presence has a significant positive impact on the performance of semiconductor devices and their electrical, optical, and transport properties. TMD have emerged as an ideal material platform for exploring the phenomenon of exciton transfer in the works of Malic, Perea-Causin, Rosati, Erkensten**,** and Samuel Brem [10-12]. In many scientific researches, many authors have solved the Schrödinger equation for a quantum dot (QD) in the presence of a constant magnetic field. Elsaid used the 1/N expansion method to calculate the energy states of an electron bound to the donor impurity in the presence of a magnetic field of arbitrary strength. [13-15]. The 1/N expansion method is an effective technique used by many authors, including Shiau, Frenkel, and others, to solve many Hamiltonian bound state systems in reduced dimensions [16-19]. For example, Wannier, Gregory *et al*. [20-22] studied the Hamiltonian quantum dot using this method. Also, Al-Hayek used the 1/N shifted expansion method to calculate the binding energy and energy of the donor impurities with Gaussian confinement in the quantum dot. The 1/N method is considered one of the most powerful and successful methods for solving the Schrödinger equation for the spherical analog potential, and it is used in various branches of theoretical physics. Using this method, we obtain accurate results for calculations of the eigenenergy values of the system, without dealing with path wave functions. Motivated by these studies, the present work applies the shifted 1/N expansion method to solve the exciton Hamiltonian for a thin WS_2 TMD material.

In this work, we investigate the electronic energy spectra, magnetic and thermal properties, the density of states (DOS), and the magnetocaloric effect (MCE) of the exciton system made from an atomic sheet of TMD (WS_2), presented in a magnetic field. All these thermal and magnetic quantities are calculated from the statistical partition function and the well-known statistical relations.

The rest of this work is organized as follows. The Hamiltonian and Schrödinger equation for 2D electron-hole particles in a single-layer interacting TMD, which interact through an attractive Rytova-Keldysh potential, solved by the 1/N- expansion method, is presented in II, the Theory and calculation method Section. In Section III, Results and Discussion, the energy spectra values obtained by 1/N are presented against the magnetic field, discussed, and compared with other studies. This section also examines thermomagnetic quantities, including heat capacity Cv, entropy (S), magnetization (M), susceptibility(X), and magneto-caloric effect (MCE), as well as the density of energy of states (DOS) of the nanosheet TMD -WS_2 material. The conclusion is presented in the final Section.

2. Theory and Method of Calculation

The Hamiltonian for electron and hole particles interacting through an attractive 2D non-Coulombic potential type is used. The model of a system has an exciton with effective mass m* and charge e, moving in a two-dimensional (2D) plane under the influence of a uniform magnetic field applied perpendicular to the monolayer. The corresponding Schrodinger equation is given as [23]:

$$\hat{\mathrm{H}}\psi(x,y) = E\psi(x,y) \tag{1}$$

$$\hat{\mathrm{H}} = -\frac{1}{2}\left(\frac{d^2}{dx^2}+\frac{d^2}{dy^2}\right) - \frac{i}{2}\gamma\left(x\frac{d}{dy} - y\frac{d}{dx}\right) + \frac{1}{8}\gamma^2(x^2+y^2) + V_K(r,\alpha) \tag{2}$$

where: $r = \sqrt{x^2+y^2}$.

Where γ, a dimensionless magnetic parameter, is related to the magnetic field.

$V_K(r,\alpha)$ is the Rytova-Keldysh type potential.

The nonlocally screened electron–hole interaction in two-dimensional systems, such as monolayer transition metal dichalcogenides (TMDs), is described by the Rytova–Keldysh potential [23]:

$$V_{RK}(r) = -\frac{e^2}{8\varepsilon_0 r_0}\left[H_0\left(\frac{kr}{r_0}\right) - Y_0\left(\frac{kr}{r_0}\right)\right] \tag{3}$$

where:

H_0 and Y_0 are zero-order Struve and Bessel functions, respectively;

r_0 is related to the screening length related to the 2D polarizability of the monolayer material;

ε_0 is the vacuum permittivity;

k is the average dielectric constant for the surrounding material;

α is the parameter for characterizing potential and is defined as $\alpha = r_0/ka_0^*$, where a_0^* is the effective Bohr radius.

This potential describes two charges in the electrostatic interaction for thin semiconductor and semi-metal films, predicted by Rytova-Keldysh and then discussed in many research works [24, 25].

The Hamiltonian, Eq. (2), of the system after adding Rytova-Keldysh potential, Eq. (3), is given as:

$$\hat{\mathrm{H}} = -\frac{1}{2}\left(\frac{d^2}{dx^2}+\frac{d^2}{dy^2}\right) - \frac{i}{2}\gamma\left(x\frac{d}{dy} - y\frac{d}{dx}\right) + \frac{1}{8}\gamma^2 r^2 - \frac{e^2}{8\varepsilon_0 r_0}\left[H_0\left(\frac{kr}{r_0}\right) - Y_0\left(\frac{kr}{r_0}\right)\right] \quad (4)$$

The analytic solution of the Hamiltonian in Eq. (4) is not attainable. We found that 1/N-expansion is an effective and accurate technique in solving the Hamiltonian given by Eq. (4).

We can write the radial part of the Schrödinger equation in N-dimensional space as follows:

$$\left(-\frac{\hbar^2}{2m^*}\left(\frac{d^2}{dr^2}+\frac{N-1}{r}\frac{d}{dr}\right) + \frac{l(l+N-2)\hbar^2}{2m^* r^2} + V(r)\right)\emptyset(r) = E\emptyset(r) \quad (5)$$

where m^* is the electron effective mass, e is the charge of the electron, ħ is related to the Planck constant, and N is the number of dimensions. $l = |m_l|$, where $|m_l|$ is the magnetic quantum number $(m_l = 0, \pm1, \pm2, \pm3, \ldots)$ that labels the quantum dot (QD) energy states and appears in the term $l(l+N-2)$.

By using the parameter $k, \bar{k} = k - a = N + 2l - a$, we can rewrite Eq. (5) to become:

$$\left(-\frac{\hbar^2}{2m^*}\frac{d^2}{dr^2} + \bar{k}^2\left((\hbar^2\left(1-\frac{1-a}{\bar{k}}\right)(1-3-a)/\bar{k})\right)/8m^* r^2 + V(r)/Q\right)\emptyset(r) = E\emptyset(r) \quad (6)$$

where $Q = \bar{k}^2$ is a scaling constant used to make Eq. (5) and Eq. (6) equivalent.

We can use the parameter $\bar{k}$ and the shift parameter a to expand the Schrodinger equation to calculate the energy eigenvalues $E(n_r, m_l)$. The complete mathematical steps that lead us to the eigenvalues of QD energy expressions in terms of powers of 1/k̄ are given explicitly in the Appendix. The intrinsic energy values $E(n_r, m_l)$ are in powers of $1/\bar{k}$ and are given as follows: $E(n_r, m_l) = E_0 + E_1 + E_2 + E_2{+}$..... These energy terms are defined in terms of quantum numbers, potential roots (r_0), and derivatives ($V^n(r_0)$) [26, 27].

The shift parameter a is chosen to make a second-order contribution E_1 vanish. In general, the presence of this condition ensures exact analytical energy results with the 1/N method for both the harmonic oscillator and hydrogen Hamiltonian [28, 29].

The Thermodynamic Properties: Heat Capacity (Cv) and Entropy (S)

We evaluate the mean energy, $< E((n_r, m_l, B, T) >$ expression from the partition function Z.

The complete thermodynamic quantities, including heat capacity and entropy, start by evaluating the partition function at any temperature and magnetic field strength [30]:

$$< Z >= \sum_{j=1}^{i} e^{-E_j/K_B T} \quad (7)$$

where K_B is the Boltzmann constant, T is the temperature, j is the index for the microstates of the system, and E_j is the total energy of the system in the respective microstate.

$$< E >= \frac{\sum_{j=1}^{i} E_j e^{-\frac{E_j}{K_B T}}}{\sum_{j=1}^{i} e^{-\frac{E_j}{K_B T}}} \quad (8)$$

The heat capacity C_v is the temperature derivative of the mean energy given as [30]:

$$C_v = \frac{\partial <E>}{\partial T} \quad (9)$$

Similarly, the entropy S of the exciton system can also be computed using the expression

$$S = \frac{\partial(K_B \mathrm{T} \ln <\mathrm{Z}>)}{\partial \mathrm{T}} \quad (10)$$

The Magnetic Properties: Magnetization (M) and Susceptibility (χ)

The magnetization (M) is defined as the negative derivative of the average energy of the two-dimensional exciton system with respect to the magnetic field strength BBB [30]:

$$M = -\frac{\partial <E>}{\partial B} \quad (11)$$

where $< E >$ is the average energy of the exciton system in the magnetic field (B).

The magnetic susceptibility χ is obtained by differentiating the magnetization with respect to the magnetic field strength [30]:

$$\chi = \frac{\partial M}{\partial B} \quad (12)$$

The Density of States (DOS):

The DOS of the exciton system of TMD-WS_2 material is another property that can reveal important information about the electronic structure of nanomaterials. It is expressed as the sum of a series of delta functions, given by [31, 32]:

$$DOS(E) = \frac{1}{A}\sum_{n=1}^{N} \delta(E - E_n) \quad (13)$$

The delta function can be replaced by a more practical computation Gaussian distribution as:

$$DOS(E) = \frac{1}{\sqrt{2\pi\Gamma^2}}\sum_n \exp\left[\frac{-(E-E_n)^2}{2\Gamma^2}\right] \quad (14)$$

where Γ is the broadening factor, E_n is the eigenenergy of the exciton system, which was calculated by the 1/N expansion method, and A is the area of the material sample [32].

The Magneto-Caloric Effect (MCE)

The magnetocaloric effect (MCE) is defined as the change in the entropy of the system, $\triangle S_m$, as a response to the change in the magnetic energy of the exciton system presented in an applied magnetic field, given as [33, 34]:

$$\Delta S_m = S(T_0, B_{=0}) - S(T_0, B_{\neq 0}) \quad (15)$$

where:

ΔS_m is magnetic entropy change (eV/K);

S_m is magnetic entropy;

T_0 is temperature;

$B_{=0}$ is the magnetic field equal to zero;

$B_{\neq 0}$ is the magnetic field not equal to zero.

3. Results and Discussion

In this part, the computed physical quantities will be listed in tables and displayed in figures. The discussion of the results consists of two main steps. In the first step, the accuracy of the energy spectra obtained using the 1/N expansion method is evaluated by comparison with previously reported experimental and theoretical results. In the second step, these excitonic results are used to explain the dependence of the magnetothermal properties, DOS and MCE of the WS_2 material as the magnetic field strength changes to include a strong range, B=60 T.

The physical parameters used for WS_2, in numerical computations are: the effective mass of an electron $m^* = 0.16m_e$, the average dielectric constant of the material $k = 1$, the effective screening length of the monolayer $r_0 = 75A^{\circ}$, and the effective Bohr radius $a = 3.779$. [23]

Tables 1.a-1.c list the results computed using the 1/N expansion method and compare them with the reported results in Ref. [23]. The quantitative comparison demonstrates the accuracy of the 1/N expansion method over the entire range of magnetic field strengths.

TABLE 1.a. Ground-state energies (1s, 2s) (in eV) at different magnetic field strengths (in T in the present work and in units of γ in Ref [23], where γ = 0.01 corresponds to a magnetic field B = 60.16T) for WS_2, calculated using the 1/N-shift expansions method and compared with the reported results in Ref. [23].

WS_2		1s $\|1,0>$		2s $\|2,0>$	
B(T)	Γ	E (present work) (eV)	E(Ref [23]) (eV)	E (present work) (eV)	E (Ref[23]) (eV)
0.00	0.00000	-0.3179	-0.3187	-0.1523	-0.1516
7.52	0.00125	-0.3179	-0.3184	-0.1520	-0.1513
15.0	0.00250	-0.3178	-0.3186	-0.1514	-0.1507
30.0	0.00500	-0.3175	-0.3179	-0.1488	-0.1478
45.1	0.00750	-0.3170	-0.3178	-0.1446	-0.1436
60.1	0.01000	-0.3163	-0.3128	-0.1392	-0.1378
150	0.02500	-0.3086	-0.3094	-0.0888	-0.0853
300	0.05000	-0.2854	-0.2862	0.0303	0.0339
601	0.10000	-0.2188	-0.2188	0.3092	0.3106
3008	0.50000	0.5246	0.5259	2.7905	2.9713
4512	0.75000	1.0328	1.0344	4.3861	4.3874
6016	1.00000	1.5568	1.5525	5.9913	5.9938

TABLE 1.b. Ground-state energies (3s, 4s) (in eV) at different values of magnetic field strength (in a unit of T in present work and a unit of γ in Ref [23], where γ = 0.01 corresponds to a magnetic field of B = 60.16T) for WS_2, calculated using the 1/N-shift expansions method, compared with the reported results in Ref. [23].

WS_2		3s $\|3,0>$		4s $\|4,0>$	
B (T)	Γ	E (present work) (eV)	E (Ref [23]) (eV)	E (present work) (eV)	E (Ref[23]) (eV)
0.00	0.00000	-0.0952	-0.0944	-0.0657	-0.0648
7.52	0.00125	-0.0944	-0.0936	-0.0639	-0.0631
15.0	0.00250	-0.0922	-0.0909	-0.0591	-0.0579
30.0	0.00500	-0.0843	-0.0827	-0.0439	-0.0404
45.1	0.00750	-0.0730	-0.0700	-0.0227	-0.0178
60.1	0.01000	-0.0591	-0.0552	0.0027	0.0074
150	0.02500	0.0562	0.0596	0.1868	0.1872
300	0.05000	0.2868	0.2886	0.5277	0.5285
601	0.10000	0.7839	0.7845	1.2436	1.2408
3008	0.50000	5.0074	5.0114	7.2089	7.2151
4512	0.75000	7.6905	7.6978	10.979	10.993
6016	1.00000	10.383	10.392	14.759	14.777

TABLE 1.c. Ground-state energies (5s, 6s) (in a unit of eV) at different values of magnetic field strength (in a unit of T in present work and a unit of γ in Ref [23], where γ = 0.01 corresponds to a magnetic field B = 60.16T) for WS_2, calculated using the 1/N-shift expansions method, compared with the reported results in Ref. [23].

WS_2		5s $\|5,0>$		6s $\|6,0>$	
B (T)	γ	E (present work) (eV)	E (Ref [23]) (eV)	E (present work) (eV)	E (Ref[23]) (eV)
0.00	0.00000	-0.0481	-0.0474	-0.0367	-0.0361
7.52	0.00125	-0.0448	-0.0439	-0.0312	-0.0300
15.0	0.00250	-0.0366	-0.0304	-0.0196	-0.0156
30.0	0.00500	-0.0119	-0.0069	0.0180	0.0226
45.1	0.00750	0.0220	0.0261	0.0642	0.0674
60.1	0.01000	0.0595	0.0631	0.1132	0.1158
150	0.02500	0.3109	0.3121	0.4312	0.4310
300	0.05000	0.7616	0.7619	0.9917	0.9883
601	0.10000	1.6961	1.6937	2.1446	2.1421
3008	0.50000	9.4029	9.4133	11.592	11.581
4512	0.75000	14.260	14.276	17.537	17.559
6016	1.00000	19.127	19.153	23.491	23.524

In addition, energy values at different quantum levels (| n,m>) were calculated for the same field values that were defined in the previous tables in order to make the work more comprehensive. We changed the quantum state from $< s >$ to $< p >$ to see how energy essentially depends on these values and to see the changes that occur in energy at these quantum numbers, as shown in Table 2.

TABLE 2. Ground-state energies (in a unit of eV) at different values of magnetic field strength (in a unit of T in the present work and unit of γ in Ref [23], where γ = 0.01 corresponds to the magnetic field B = 60.16T) for WS_2, calculated using the 1/N-shift expansions method.

WS_2		1p	2p	3p	4p	5p	6p
		|1,1 >	|2,1 >	|3,1 >	|4,1 >	|5,1 >	|6,1 >
B(T)	γ	E(eV)	E(eV)	E(eV)	E(eV)	E(eV)	E(eV)
0.00	0.00000	-0.1843	-0.1098	-0.0739	-0.0532	-0.0401	-0.0313
7.52	0.00125	-0.1815	-0.1065	-0.0698	-0.0477	-0.0326	-0.0213
15.0	0.00250	-0.1784	-0.1023	-0.0633	-0.0378	-0.0188	-0.0027
30.0	0.00500	-0.1717	-0.0912	-0.0451	-0.0106	0.0195	0.0481
45.1	0.00750	-0.1640	-0.0773	-0.0220	0.0236	0.0657	0.1058
60.1	0.01000	-0.1557	-0.0614	0.0040	0.0611	0.1146	0.1660
150	0.02500	-0.0944	0.0517	0.1883	0.3123	0.4324	0.5502
300	0.05000	0.0299	0.2879	0.5289	0.7627	0.9927	1.2201
601	0.10000	0.3095	0.7848	1.2444	1.6969	2.1453	2.5911
3008	0.50000	2.7907	5.0073	7.2089	9.4030	11.592	13.779
4512	0.75000	4.3861	7.6903	10.979	14.260	17.537	20.811
6016	1.00000	5.9912	10.382	14.759	19.127	23.491	27.852

In Figs. 1(a) and 1(b), for the sake of more qualitative comparisons, the tabulated energy values are also displayed against the magnetic field for different s-states. The effect of magnetic field confinement on the ground-state energies is illustrated. The figures show that the first level is not affected by an increase in the magnetic field, as it maintains an almost constant value. However, for higher energy levels, a noticeable dependence on the magnetic field is observed, with the energy values increasing as the magnetic field strength increases. This is completely consistent with the results of Ref. [23]. Comparing the two figures, we can see a good match between the two works.

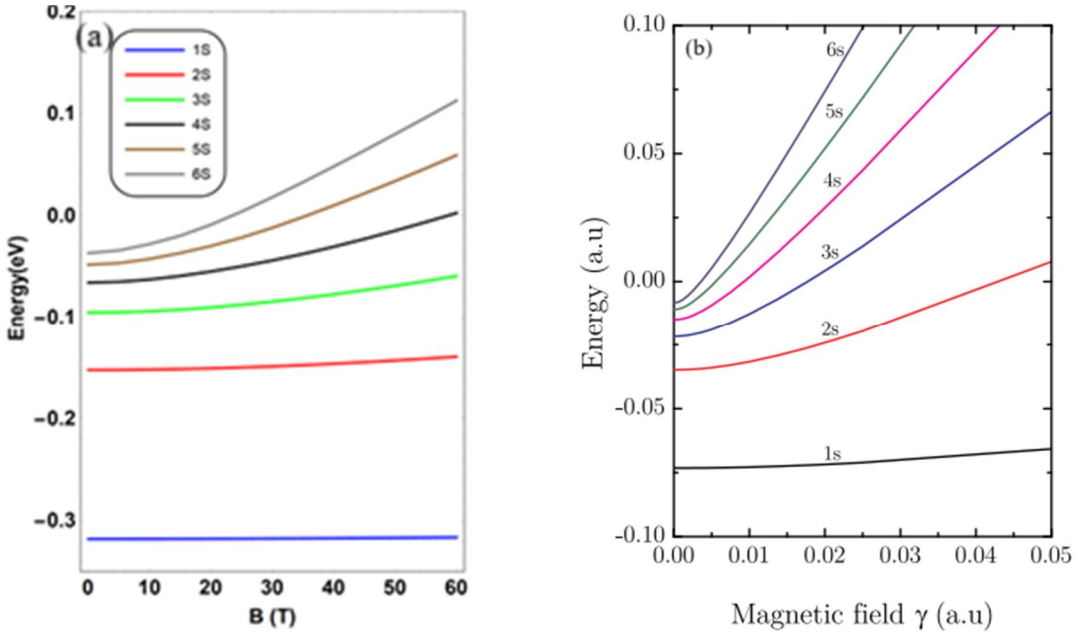

FIG. 1. Ground-state energy as a function of magnetic field for WS_2. Figures are taken from Ref. [23]. Different systems of energy and magnetic field units are used in both plots. (a) present work, (b) Ref. [23]. The two figures have different scales, where γ = 0.01 corresponds to the magnetic field of B = 60.16T.

Figure 2 shows the influence of the magnetic field effect on the ground-state energies for higher quantum p-states labelled by magnetic quantum number m. As the magnetic field increases, the energy values also increase.

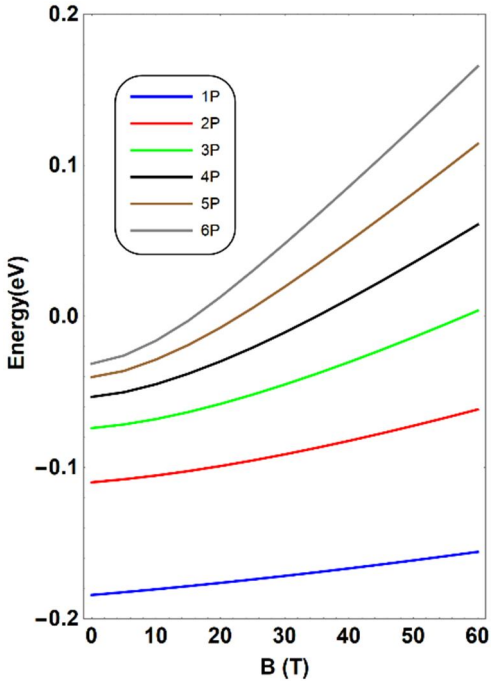

FIG. 2. Ground-state energy <E> as a function of magnetic field (B) on the ground-state energies for quantum number (p) of WS_2.

Next, we studied the ground state energy as a function of temperature at different values of the magnetic field. As shown in Fig. 3, when we turn off the magnetic field (B = 0T), we find that the average energies increase with increasing temperature. In addition, the average energy convergence is achieved as we increase the number of exciton states from 15 to 20.

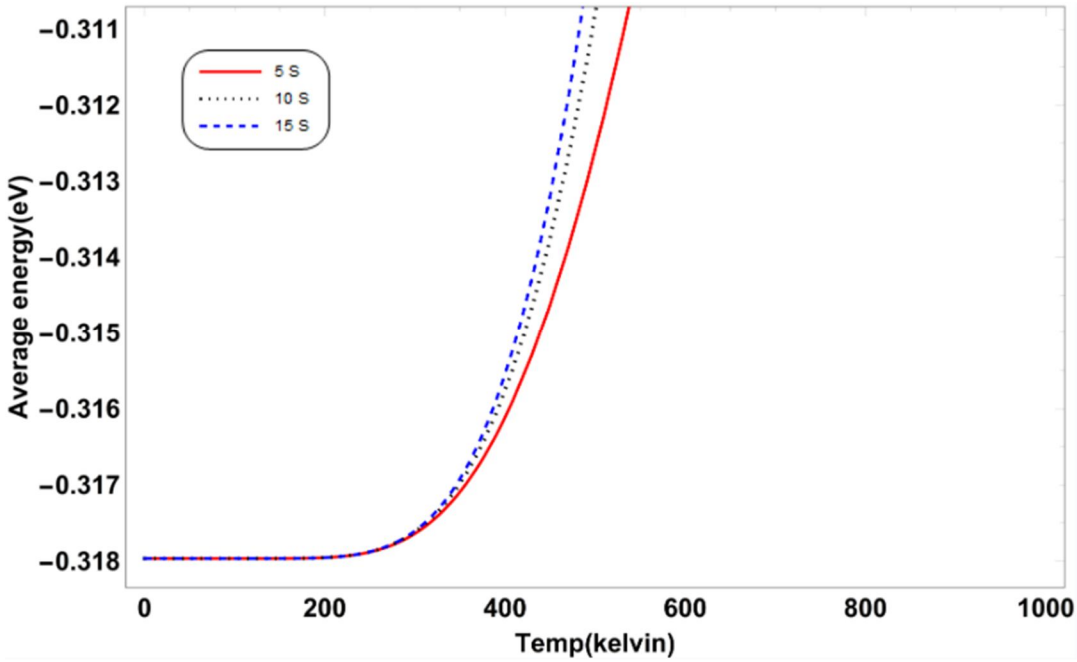

FIG. 3. Average energy as a function of temperature when we turn off the magnetic field (B=0T) for WS_2, computed for different numbers of S-states.

In Fig. 4, we now switched on the magnetic field and tested again the convergence of the average energy of the exciton system against the temperature, calculated at fixed magnetic field strength, $B \approx 60\,T$, and various numbers of bases. The figure clearly shows a very good convergence behavior of the average energy for taking only 15 bases of exciton S-states.

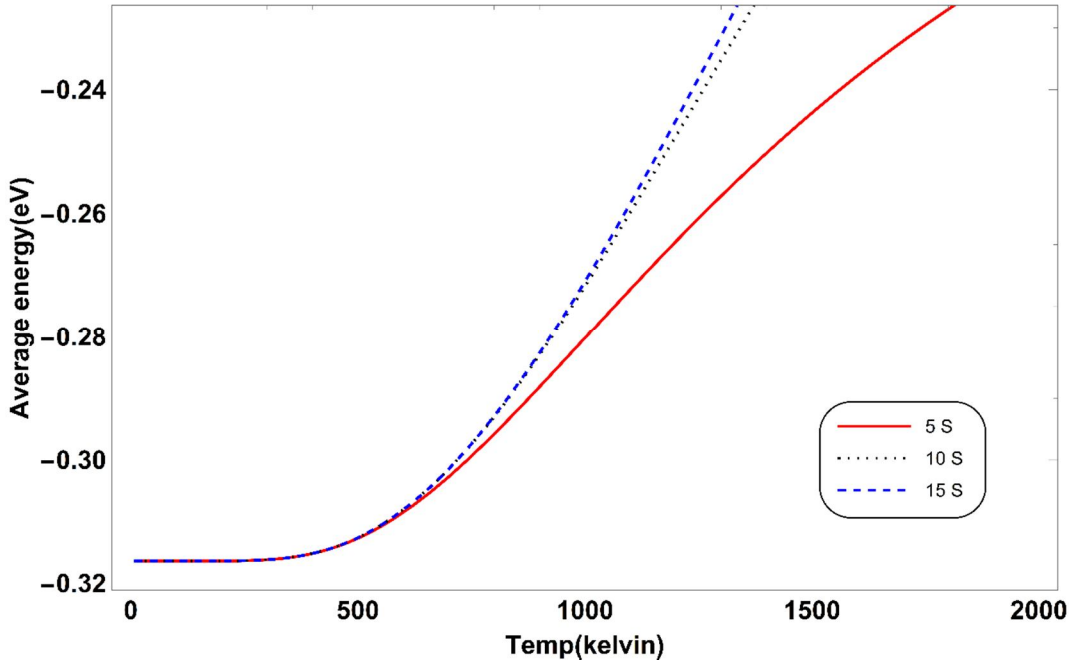

FIG. 4. Average energy ∈ as a function of temperature (T) when we switched the magnetic field (B = 60.16T) for different numbers of S-states for WS_2.

The dependence of the heat capacity on temperature and magnetic field for the WS_2 sheet is shown in Fig. 5. For the zero magnetic field case (B = 0), the heat capacity increases with temperature, reaching a peak value, known as the Schottky anomaly, at $C_v/k_B \approx 2.4$ at 1000^0 K. The heat capacity starts decreasing until it reaches almost asymptotic zero value at T≈3000K for WS_2. In the presence of a strong magnetic field B $\approx 60\,T$, the exciton becomes more confined, and the exciton heat capacity reaches a peak value of approximately 1.8 at 1200K.

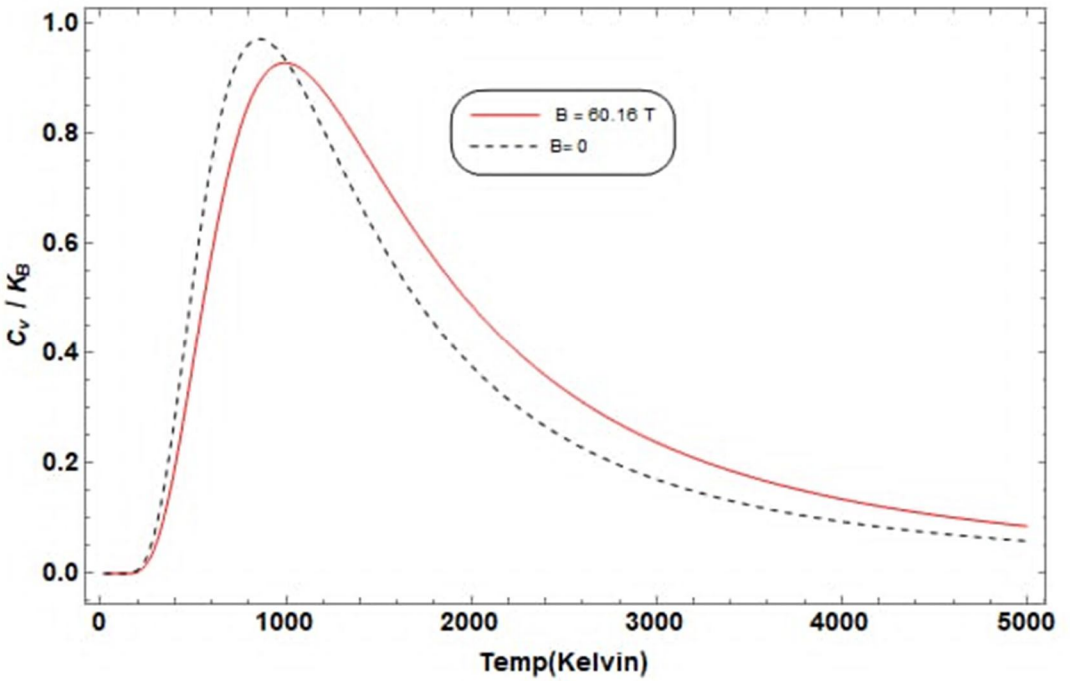

FIG. 5. Heat capacity as a function of temperature and magnetic field for WS_2.

Figure 6 shows the entropy as a function of temperature and magnetic field. The plot shows that the entropy increases with increasing temperature until it reaches a saturation entropy limit of $S/k_B \approx 1.7$ for zero magnetic field at

3000 K, and 1.6 at 60.16 T at the same temperature. We reduced the temperature to 2000^0 K to see the stability of entropy in the sub-figure for both cases, with and without a magnetic field.

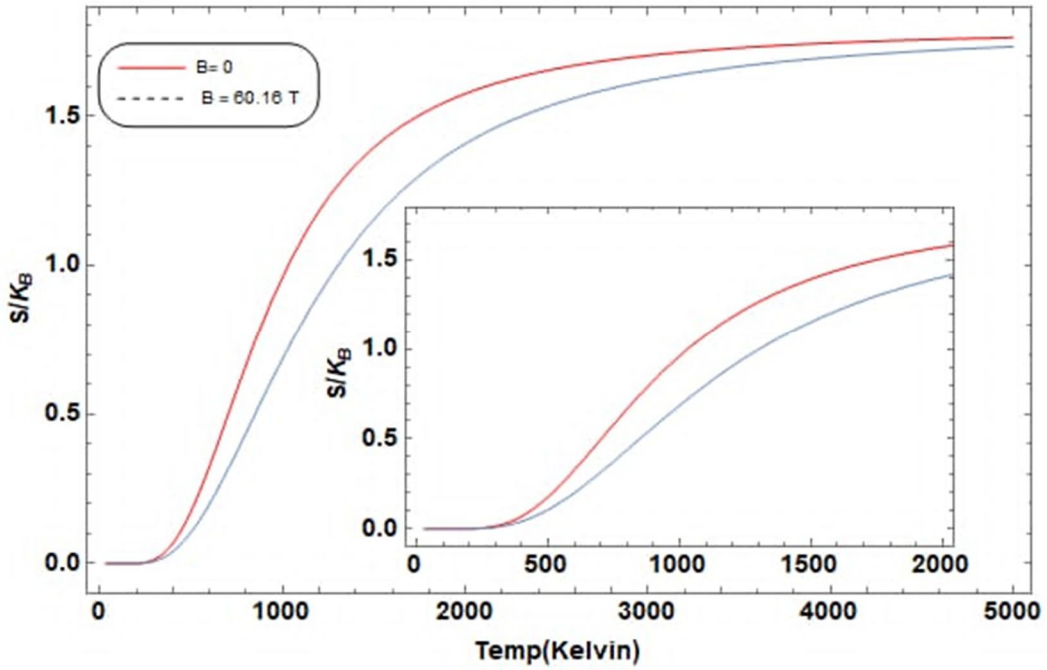

FIG. 6. Entropy as a function of temperature for different magnetic field strengths for WS (the inset figure is plotted for the low temperature range).

Magnetic properties were also studied, starting with the computation of statistical energy for WS_2 under the effect of temperature and magnetic field. The statistical energy, shown in the present work for WS_2 in Fig. 7, is calculated at 100 K and 300 K for a magnetic field range from 0 to 60 T. The statistical energy is found to reach -0.318 eV at 100 K and -0.317 eV at 300 K.

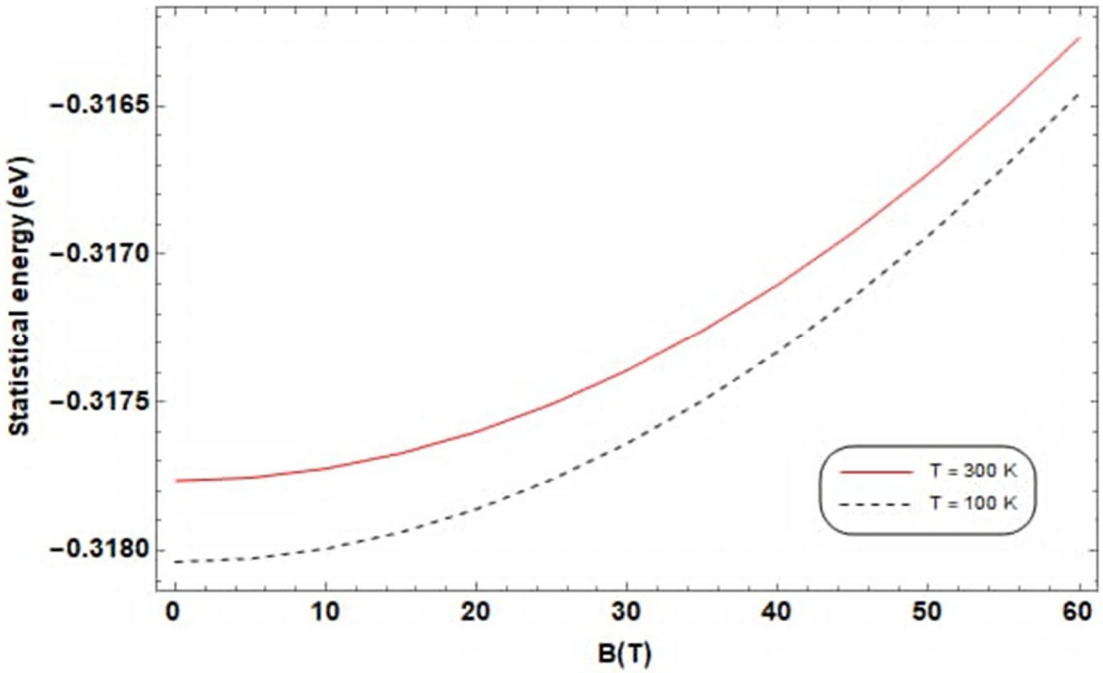

FIG. 7. Statistical energy as a function of magnetic field for WS_2.

We have calculated the magnetization in units of effective Bohr magneton [35], $\mu_B = e\hbar/2m^* = 0.3622*10^{-3}$ eV/T, for WS_2. Also, we studied the magnetization as a function of magnetic field at different values of temperature. Figure 8 shows that the magnetization curve

decreases with increasing magnetic field, starting from zero at 0 T to reach -0.05 at 60 T at 900 K.

When we decreased the temperature to 10 K, the magnetization reached -0.14 at 60 T, see Fig. 8. This means that, when we decrease the temperature, the magnetization increases at high magnetic fields (60 T), but at low magnetic fields (0 T) the magnetization takes the same value and starts from zero.

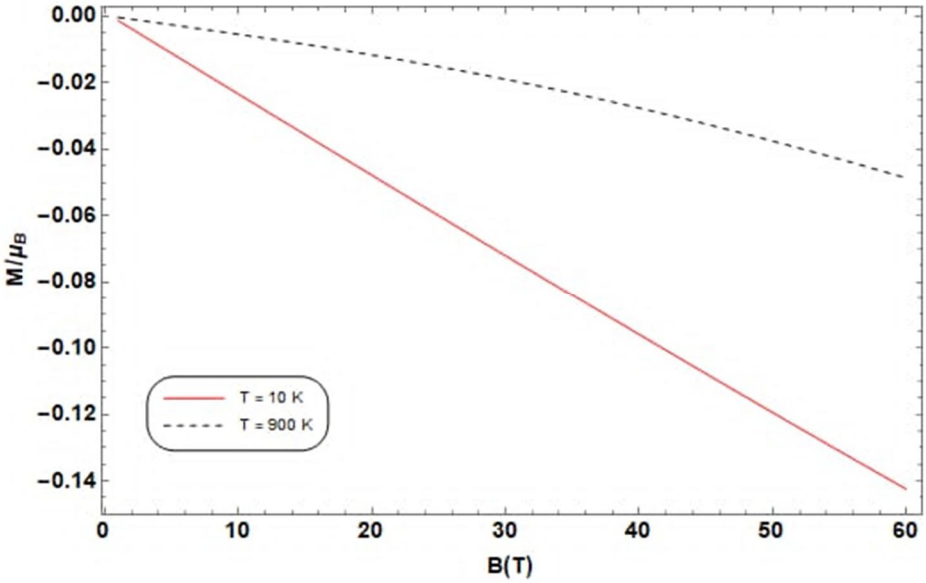

FIG. 8. Magnetization as a function of magnetic field at 900 K and 10 K for WS_2.

In Fig. 9, we studied the behavior of computed magnetic susceptibility for both low and high temperature ranges in the presence of a magnetic field for WS_2. The results are displayed for temperatures of 10 K and 150 K.

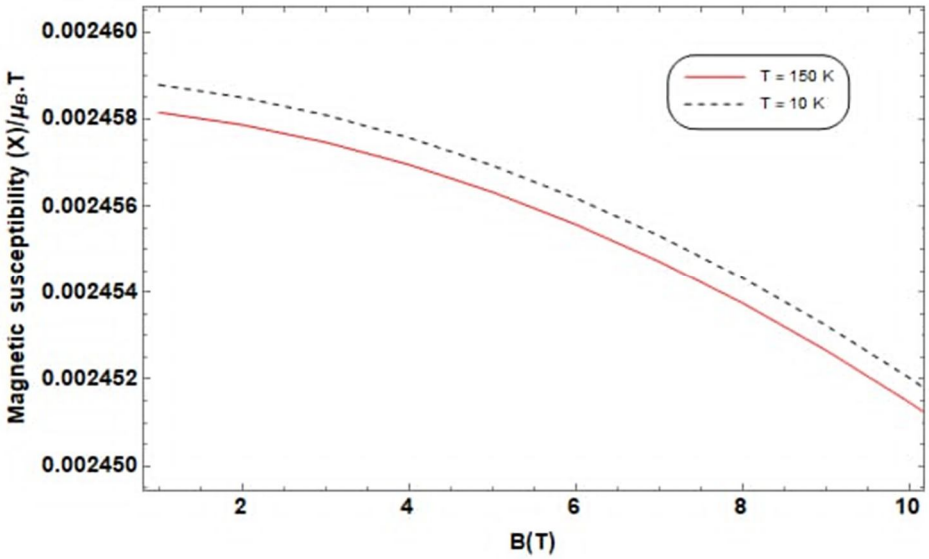

FIG. 9. Magnetic susceptibility as a function of a magnetic field at 10 K and 150 K for WS_2.

The density of states (DOS) is a significant physical quantity to reveal information about the electronic properties of materials, by describing the system's responses to Hamiltonian parameters, such as the magnetic field and confinement potential.

In Fig. 10, the DOS is plotted as a function of energy at different values of the magnetic field (50 T, 60.16 T). The plot for WS_2 below shows that the presence of the external magnetic field removes the degeneracy of the states, so the DOS gives one at each value of the energy spectrum. We observe that as the magnetic field strength increases, the Landau level energy separation $\hbar\omega_c$ also increases, leading to a reduction in the number of LL-states in the DOS

of WS_2 material. For example, the number of states (3 states) at B = 60 T (black color, dashed plot) is smaller than the number of states (4 states) for a lower magnetic field strength (red color, solid line plot) and for a fixed energy range (E).

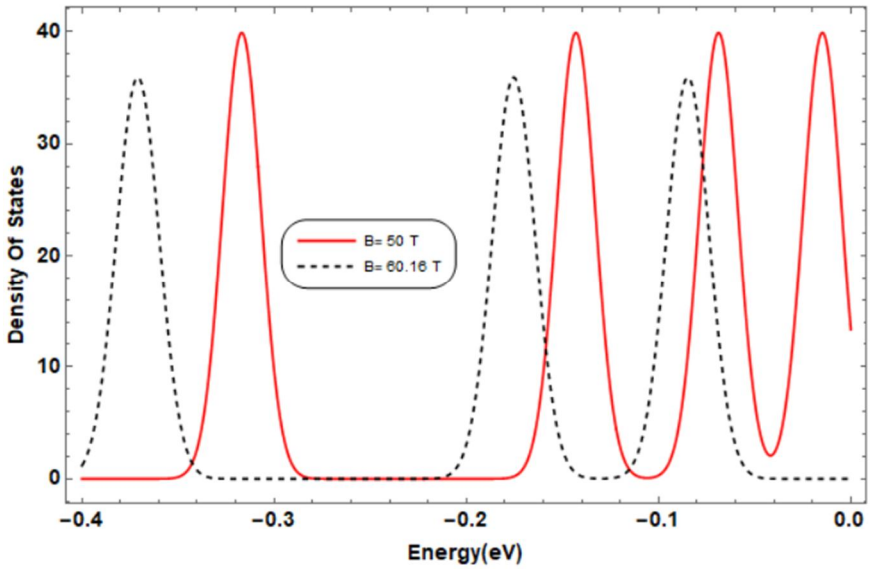

FIG. 10. DOS vs. energy for WS_2 at different magnetic field values.

The magnetocaloric effect (MCE) was studied in order to identify the thermomagnetic properties by investigating the behavior of the material with the temperature changes when the material is exposed to a changing magnetic field. Our study is devoted to a sheet made from TMD materials (WS_2). The MCE, represented by ΔS against the temperature T, shows a Gaussian distribution. A high temperature is required to see the MCE in TMD since the binding energy for an exciton in a strong magnetic field is very large, and thus more thermal energy is needed to be absorbed by the exciton. We observe that this temperature is far from the room temperature range, as TMD materials require very high thermal energy (E_{th}) in order to increase the kinetic energy (K) of the electron. Under these conditions, the exciton system transitions randomly between states, producing the observed entropy variation, as shown in Fig. 11 [36, 37].

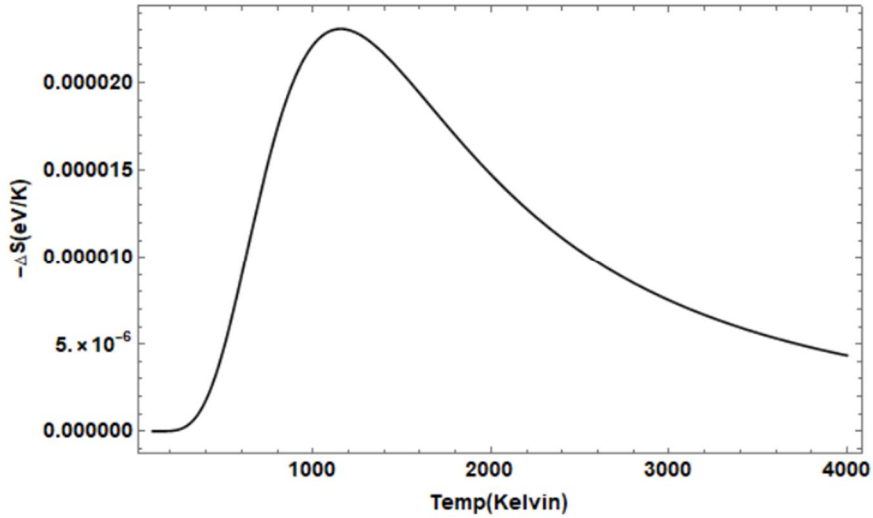

FIG. 11. MCE vs temperature for WS_2 at different magnetic field values, $\Delta S_m = S(B_{=60.16}) - S(B_{=0})$.

4. Conclusions

In conclusion, we have investigated the magnetothermal properties of WS_2 TMD material. Additionally, we have studied the DOS and MCE of the same material as functions of the magnetic field. The Schrödinger equation for the exciton system in a magnetic field was solved by using the shifted 1/N expansion method to find the eigenenergy states. We have

tested the computed results by the 1/N method against different computation results calculated by various numerical methods. The results show that the 1/N method is both accurate and effective for solving the exciton Hamiltonian system with a spherically symmetric potential such as V_{RK}. We have ensured the convergence issue of the statistical energy by varying the number of states in each computation step. The behavior of the magnetothermal properties of the exciton system for WS_2 nanosheet had been studied as a function of magnetic field and temperature. The results show that the heat capacity curve exhibits a Schottky anomaly. Furthermore, the magnetic susceptibility curve for WS_2 was calculated and displayed. We have calculated the density of the state function, DOS, of the exciton system. The DOS plots show an oscillatory-type behavior for different values of the magnetic field, reflecting the Landau-level (LL) states of the exciton system presented in a magnetic field.

The present study also investigates the MCE of an exciton in TMD material, which is defined as the magnetothermodynamic phenomena that has an application in magnetic refrigeration. We have found that the calculated $\Delta S - T$ plot for the exciton system of the WS_2 monolayer has a Gaussian distribution shape.

This study reveals that the WS_2-TMD material has attractive magnetic and thermal properties, which make WS_2 a very promising material in the next generation of nanoelectronics.

Appendix

Shifted 1/N Expansion Method

The 1/N expansion method is used to solve Eq. (5) systematically in terms of the expansion parameter 1/k̄. At large k̄, the contribution of energy comes from the effective potential:

$$V_{eff} = \frac{\hbar^2}{8m^* r^2} + \frac{V(r)}{Q} \tag{A1}$$

where $Q = k^2$ is a scaling constant. V_{eff} has a minimum value at r_0, so that we have:

$$4m^* r_0^3 V'(r_0) = \hbar^2 Q \tag{A2}$$

To shift the origin of the coordinate system to the position of the minimum of the effective potential, a new variable x is defined:

$$x = \frac{k^{\frac{1}{2}}}{r_0}(r - r_0) \tag{A3}$$

Using a Taylor expansion around the effective minimum r0 (corresponding to x = 0), an analytical equation similar to the Schrödinger equation for a one-dimensional solvable nonharmonic oscillator is obtained. The coefficients of both equations are compared to determine all parameters of the anharmonic oscillator in terms of k̄, Q, r0, and the potential derivatives, allowing the determination of the energy spectrum. The oscillator frequency is then given by:

$$\omega = \frac{\hbar}{2m^*}\left(3 + \frac{r_0 V''(r_0)}{V'(r_0)}\right)^{1/2} \tag{A4}$$

To calculate the energy eigenvalues, the Schrödinger equation is expanded in powers of $1/\bar{k}$, where $\bar{k} = N + 2l - a$, N is the number of spatial dimensions and (a) is the so-called shifted parameter. The shifted parameter a is defined as:

$$a = 2 - \frac{2(2n_r - 1)m^*\omega}{\hbar} \tag{A5}$$

For any values of radial quantum numbers n_r and m_l, the energy eigenvalues $E(n_r, m_l)$ are given by:

$$E(n_r, m_l) = E_0 + E_1 + E_2 + E_3 \tag{A6}$$

where:

$$E_0 = V(r) + \left(\frac{Q}{8 * m^* * r^2}\right)$$

$$E_1 = \frac{(c_1 * c_3)}{(8 * m^*)}$$

$$E_2 = (E_1 + \alpha_1)/r^2$$

$$E_3 = \frac{\alpha_2}{k * r^2}$$

where:

$$Q = (N + 2 * l - a)^2$$

$$c_1 = (1 - a)$$

$$c_2 = (2 - a)$$

$$c_2 = (2 - a)$$

$$c_3 = (3 - a)$$

$$\alpha_1 = n_1 * e_2 + 3 * n_2 * e_4 - c_5 * \left(e_1{}^2 + 6 * n_1 * e_1 * e_3 + n_4 * e_3^2\right)$$

$$\alpha_2 = t_7 + t_{12} + t_{16}$$

$$c_5 = \omega^{-1}$$

The forms of previous parameters are given in the following:

$$t_7 = t_1 - c_5 * (t_2 + t_3 + t_4 + t_5 + t_6)$$

$$t_{12} = c_5^2 * (t_8 + t_9 + t_{10} + t_{11})$$

$$t_{16} = -\, c_5^3 * (t_{13} + t_{14} + t_{15})$$

with:

$$t_1 = n_1 * d_2 + 3 * n_2 * d_4 + 5 * n_3 * d_6$$

$$t_2 = n_1 * e_2{}^2 + 12 * n_2 * e_2 * e_4$$

$$t_3 = 2 * e_1 * d_1 + 2 * n_5 * e_4{}^2$$

$$t_4 = 6 * n_1 * e_1 * d_3 + 30 * n_2 * e_1 * d_5$$

$$t_5 = 6 * n_1 * e_3 * d_1 + 2 * n_4 * e_3 * d_3$$

$$t_6 = 10 * n_6 * e_3 * d_5$$

$$t_8 = 4 * e_1{}^2 * e_2 + 36 * n_1 * e_1 * e_2 * e_3$$

$$t_9 = 8 * n_4 * e_2 * e_3^2$$

$$t_{10} = 24 * n_1 * e_1^2 * e_4 + 8 * n_7 * e_1 * e_3 * e_4$$

$$t_{11} = 12 * n_8 * e_3^2 * e_4$$

$$t_{13} = 8 * e_1^3 * e_3 + 108 * n_1 * e_1^2 * e_3^2$$

$$t_{14} = 48 * n_4 * e_1 * e_3^3$$

$$t_{15} = 30 * n_9 * e_3^4$$

where (n's), (d's), and (e's) are parameters given as:

$$n_1 = 1 + 2 * n_r$$

$$n_2 = 1 + 2 * n_r + 2 * n_r{}^2$$

$$n_3 = 3 + 8 * n_r + 6 * n_r{}^2 + 4 * n_r{}^3$$

$$n_4 = 11 + 30 * n_r + 30 * n_r{}^2$$

$$n_5 = 21 + 59 * n_r + 51 * n_r{}^2 + 34 * n_r{}^3$$

$$n_6 = 13 + 40 * n_r + 42 * n_r{}^2 + 28 * n_r{}^3$$

$$n_7 = 31 + 78 * n_r + 78 * n_r{}^2$$

$$n_8 = 57 + 189 * n_r + 225 * n_r{}^2 + 150 * n_r{}^3$$

$$n_9 = 31 + 109 * n_r + 141 * n_r{}^2 + 94 * n_r{}^3$$

$$c_4 = 2 * m^* * \omega$$

$$e_1 = \epsilon_1/\sqrt{c_4}$$

$$e_2 = \epsilon_2/c_4$$

$$e_3 = \epsilon_3/c_4{}^{3/2}$$

$$e_4 = \epsilon_4/c_4{}^2$$

$$d_1 = \delta_1/\sqrt{c_4}$$

$$d_2 = \delta_2/c_4$$

$$d_3 = \delta_3/c_4{}^{3/2}$$

$$d_4 = \delta_4/c_4{}^2$$

$$d_5 = \delta_5/c_4{}^{5/2}$$

$$d_6 = \delta_6/c_4{}^3$$

also:

$$\epsilon_1 = c_2/(2 * m^*)$$

$$\epsilon_2 = -\, 3 * c_2/(4 * m^*)$$

$$\epsilon_3 = -\, 1/(2 * m^*) + \left(r_5 * \mathrm{der}_3\,(r)\right)/(6 * Q)$$

$$\epsilon_4 = 5/(8 * m^*) + \left(r_6 * \mathrm{der}_4\,(r)\right)/(24 * Q)$$

$$\delta_1 = -\, c_1 * c_3/(4 * m^*)$$

$$\delta_2 = 3 * c_1 * c_3/(8 * m^*)$$

$$\delta_3 = c_2/m^*$$

$$\delta_4 = -\, 5 * c_2/(4 * m^*)$$

$$\delta_5 = -\, 3/(4 * m^*) + \left(r_7 * \mathrm{der}_5\,(r)\right)/(120 * Q)$$

$$\delta_6 = 7/(8 * m^*) + \left(r_8 * \mathrm{der}_6\,(r)\right)/(720 * Q)$$

where:

$$\mathrm{der}_1\,(r) = \frac{\mathrm{dV}}{\mathrm{dr}}$$

$$\mathrm{der}_2\,(r) = \frac{d^2\mathrm{V}}{\mathrm{dr}}$$

$$\mathrm{der}_3\,(r) = \frac{d^3\mathrm{V}}{\mathrm{dr}}$$

$$\mathrm{der}_4\,(r) = \frac{d^4\mathrm{V}}{\mathrm{dr}}$$

$$\mathrm{der}_5\,(r) = \frac{d^5\mathrm{V}}{\mathrm{dr}}$$

$$\mathrm{der}_6\,(r) = \frac{d^6\mathrm{V}}{\mathrm{dr}}$$

References

[1] Eftekhari, A., J. Mater. Chem. A, 5 (35) (2017) 18299.

[2] Splendiani, A., Sun, L., Zhang, Y., Li, T., Kim, J., Chim, C.Y., Galli, G., and Wang, F., Nano Lett., 10 (4) (2010) 1271.

[3] Radisavljevic, B., Radenovic, A., Brivio, J., Giacometti, V., and Kis, A., Nat. Nanotechnol., 6 (3) (2011) 147.

[4] Shinn, E., Complexity, 18 (3) (2012) 24.

[5] Elishakoff, I., Pentaras, D., Dujat, K., Versaci, C., Muscolino, G., Storch, J., Bucas, S., Challamel, N., Natsuki, T., Zhang, Y.Y., Wang, C.M., and Ghyselinck, G., "Carbon Nanotubes and Nano Sensors: Vibrations, Buckling, and Ballistic Impact", (ISTE-Wiley, London, 2012), XIII+421 pp.

[6] Husain, S., Kumar, A., Kumar, P., Kumar, A., Barwal, V., Behera, N., Choudhary, S., Svedlindh, P., and Chaudhary, S., Phys. Rev. B, 98 (18) (2018) 180404.

[7] Husain, S., Kumar, A., Kumar, P., Kumar, A., Barwal, V., Behera, N., Choudhary, S., Svedlindh, P., and Chaudhary, S., Phys. Rev. B, 98 (18) (2018) 180404.

[8] Mak, K.F., He, K., Shan, J., and Heinz, T.F., Nat. Nanotechnol., 7 (8) (2012) 494.

[9] Zeng, H., Dai, J., Yao, W., Xiao, D., and Cui, X., Nat. Nanotechnol., 7 (8) (2012) 490.

[10] Malic, E. et al., Nat. Commun., 14 (1) (2023) 3430.

[11] Combescot, M. and Shiau, S.-Y., "Excitons and Cooper Pairs: Two Composite Bosons in Many-Body Physics", (Oxford University Press, 2015).

[12] Eftekhari, A., J. Mater. Chem. A, 5 (35) (2017) 18299.

[13] Elsaid, M., Physica B, 202 (1994) 202.

[14] Nie, Z. et al., Commun. Phys., 2 (1) (2019) 103.

[15] Malic, E. et al., Nat. Commun., 14 (1) (2023) 3430.

[16] Combescot, M. and Shiau, S.-Y., "Excitons and Cooper Pairs: Two Composite Bosons in Many-Body Physics", (Oxford University Press, 2015).

[17] Frenkel, J., Phys. Rev., 37 (1) (1931) 17.

[18] Jiles, D., "Introduction to Magnetism and Magnetic Materials", 3rd ed., (Boca Raton, 2015).

[19] Gonano, C.A., Zich, R.E., and Mussetta, M., Prog. Electromagn. Res. B, 64 (2015) 83.

[20] Wannier, G., Phys. Rev., 52 (3) (1937) 191.

[21] Nawaz, S. and Tahir, M., Physica E, 76 (2016) 169.

[22] Han, S.A., Bhatia, R., and Kim, S.-W., Nano Converg., 2 (1) (2015) 17.

[23] Nguyen, D.-A.P. et al., Physica E, 113 (2019) 152.

[24] Keldysh, L.V., Sov. J. Exp. Theor. Phys. Lett., 29 (1979) 658.

[25] Cudazzo, P., Tokatly, I.V., and Rubio, A., Phys. Rev. B, 84 (8) (2011) 085406.

[26] Sarkar, S., Sarkar, S., and Bose, C., Physica B, 541 (2018) 75.

[27] Liang, S.J. and Xie, W.F., Eur. Phys. J. B, 81 (1) (2011) 79.

[28] Sukhatme, U. and Imbo, T., Phys. Rev. D, 28 (2) (1983) 418.

[29] Imbo, T., Pagnamenta, A., and Sukhatme, U., Phys. Rev. D, 29 (8) (1984) 1669.

[30] Baghdasaryan, D.A. et al., Physica E, 101 (2018) 1.

[31] Nawaz, S. and Tahir, M., Physica E, 76 (2016) 169.

[32] Shaer, A.A.A., "The Gaussian Impurity Effect on the Electronic and Magnetic Properties of an Electron Confined in a Lateral Quantum Dot", (2023).

[33] Gschneidner, K.A. Jr. and Pecharsky, V.K., Annu. Rev. Mater. Sci., 30 (2000) 387.

[34] Pecharsky, V.K. and Jr. Gschneidner, K.A., J. Magn. Magn. Mater., 200 (1999) 44.

[35] Svensson, J., "A Study of the Magnetic Properties of Yb_4LiGe_4: Unusual Magnetism", (Diss., Boston College, 2010).

[36] Ma, N. and Reis, M.S., Sci. Rep., 7 (1) (2017) 13257.

[37] Cortés, N. et al., Phys. Rev. B, 105 (1) (2022) 014443.

Volume 18, Number 5, 2025. pp. 613-628

Jordan Journal of Physics

ARTICLE

Semi-Empirical D-L Correlation for Profiling and Parameterizing Alpha Particle Tracks in Nuclear Detector CR-39 at Various Etching Temperatures

Saeed Hassan Saeed[a] and **Abrar Qasim Al-Ramadhani**[b]

[a] *Department of Cosmetic Techniques and Laser, Al-Hadba University-College of Health and Medical Techniques, Mosul, Iraq.*

[b] *Education Directorate of Kirkuk, Iraq.*

Doi: **https://doi.org/10.47011/18.5.5**

Received on: 10/08/2024; *Accepted on: 27/02/2025*

Abstract: Imaging track profiles and directly measuring their lengths is more challenging than imaging and measuring their diameters. This paper focuses on determining alpha-particle track profiles and lengths in the CR39 nuclear detector by utilizing the track's diameter-length (D-L) correlation to obtain actual track lengths from direct measurements of track diameters. Alpha particles with energies ranging from 3.5 to 5.3 MeV were used to irradiate the detector, which was then etched with a 6.25N NaOH solution at varying temperatures. The track parameters, such as the experimental bulk etch rate (VB), alpha energies, etching temperatures, and etching times, were input into the Track-Test program to calculate theoretical track lengths and create D-L calibration curves based on the Green *et al.* equation. The measured track diameters were projected onto curves to extract semi-empirical track lengths (L), track depth (x), etch rate (VT), etch rate ratio (V), and residual range (R'). MATLAB was used to plot the relationship between V and R', enabling the determination of optimal V(R') curves and new coefficients for the Green *et al*. equation. Using these newly derived coefficients, the Track-Test program applied the Green et al. equation to determine the profiles and evolution stages of the tracks. The D–L correlation method yielded track lengths and associated parameters that were consistent with direct microscopic measurements. This approach offers a viable, efficient, and straightforward alternative to direct imaging of longitudinal track profiles, which often demands considerable time, effort, and specialized techniques. Overall, the D–L correlation method provides reliable results comparable to those obtained from direct track-length measurements and thus represents a valuable tool for determining actual track lengths in nuclear detector applications.

Keywords: Track profiles, CR-39 detector, Etching temperature, Etching rates, Track depth, Track-Test.

1. Introduction

Solid-state nuclear track detectors (SSNTDs) are recognized as reliable tools for identifying the tracks of charged particles and ions. Polyallyl diglycol carbonate (PADC) detectors, specifically the CR-39, are among the most widely used types in many scientific fields [1-4]. Measurements of track length (depth), rather than the width, have received increasing attention in recent studies on the track geometry of charged particles in SSNTDs. The use of microscopic images of etched track profiles facilitates the direct measurement of track lengths, the monitoring of the evolution of track shapes, and the subsequent determination of their parameters. Calculating the track parameters directly from microscopic images of the track lengths results in exact estimates that closely reflect how the track evolves as the etching process progresses [5-7].

Corresponding Author: Saeed Hassan Saeed **Email**: profdrsaeed@gmail.com

The lengths and depths of etched tracks in the CR-39 detector are measured and recorded using a variety of imaging techniques. One of these methods is the resin-replica technique, which employs a certain epoxy to create exact copies of the etched tracks whose heights are determined using contact stylus profilometry [8-10]. Track depths can also be obtained, along with three-dimensional imagery, using a confocal microscope [11-13]. Another approach involves selectively fracturing the etched detector along a plane perpendicular to its surface to expose lateral profiles and estimate track depths [14, 15].

In the majority of our articles [7, 16-18], the "lateral irradiation" technique of the detector is proposed, which involves irradiating the detector's sharp side rather than its surface. The longitudinal sections of the etched tracks are photographed from the detector surface with a digital camera mounted on a conventional optical microscope. The collected track photos are then analyzed, and the necessary measurements are made using a PC connected to the camera. This method is straightforward and produces good results compared to other ways, as it does not require sophisticated techniques. In addition, we have suggested a semi-empirical method (under specific initial assumptions) for determining track lengths based on direct experimental measurements of track diameters rather than profile photographs [18]. This indirect method accurately predicts track lengths and depths, residual range, track etching rates, and the profiles of etched tracks.

Several computer programs, such as TRAK-TEST, TRACK-VISION, CR39, and the TRACK-P programs, have been developed to simulate and plot the etched track profiles in the CR-39 detector in two and three dimensions, as well as to determine a number of parameters. These parameters include the major and minor diameter, length, depth, residual range, and track etching rates [16, 19-21].

The main objective of this work is to present a different semi-experimental method for determining precise lengths and plotting the profiles of etched tracks in the CR-39 detector. This method, referred to as the track's diameter-length (D-L) correlation method [22], is based on calculating the track lengths by measuring their diameters instead of measuring them directly from the experimental track photos. So, by obtaining D-L calibration curves for the alpha particle energies and etching temperatures used, we can determine the rates at which the track lengths L'(t) and other parameters change. These parameters are the track length (L), residual range (R'), and etching rates (V_T & V). Using the Track-Test program and the obtained data, we can also plot the etched-track profiles and trace their development stages.

2. Experiment

2.1. Track Diameter Measurement

A CR-39 detector slice was cut into 1 x 1cm^2 pieces and irradiated under vertical incidence with alpha particles from a radioactive ^{241}Am source (0.5 μCi) at energies of 5.3, 4.7, 4.1, and 3.5 MeV. SRIM software was used to obtain energies less than the source's primary energy of 5.485 MeV by adjusting the distance between the detector and the radioactive source [23]. An aqueous NaOH solution of molarity 6 N was used to etch the irradiated detectors at 60, 70, and 80$\pm$1 ^{o}C for successive etching intervals ranging from 0.5 to 20 h. Following etching, the detectors were thoroughly cleaned with distilled water, dried, and then examined to measure the diameters of the tracks utilizing a digital camera (MDC E-5C) mounted on an optical microscope (Noval) and linked to a PC, as shown in Fig.1. This procedure was repeated for studied alpha energies and etching temperatures for the required etching times in each case.

The thickness difference approach was used to compute the bulk etching rate (V_B). Unirradiated detector pieces were etched in a 6 N NaOH for 1-10 h at temperatures of 60, 70, and 80 ^{o}C. The layer thickness peeled from the detector surface was obtained by subtracting the detector thicknesses prior to and following etching. From the plot of etching time versus removed thickness, V_B was computed as $V_B = \Delta h/\Delta t$ (μm/h) [1]. In this work, V_B was found to be 1.421 μm/h.

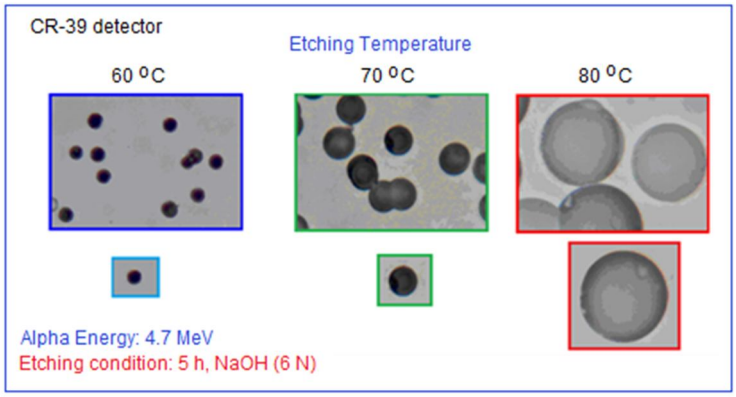

FIG. 1. Images of alpha particle track diameters at 4.7 MeV in the CR-39 detector, etched in NaOH(6N) solution for 5 hours at various temperatures.

2.2. Extracting Track Length, Profile, and Other Parameters

Instead of directly measuring the track lengths, we suggested the D-L correlation approach to infer the track lengths indirectly from experimental observations of the track diameters. By entering our experimental data into the TRACK-TEST (T-T) software [20] and using the Green *et al* (1982) formula of the etch rate ratio (V), provided in the T-T software with its default coefficients for CR-39, we can theoretically determine the profiles and lengths of the etched tracks. The entered data include alpha particle energy (E), bulk etching rate (V_B) at a given temperature (T), iterative etching times (t), and normality (N) of the chemical solution. From the generated track profiles, the track lengths and diameters are identified for each alpha energy and etching temperature over a set of selected etching periods, including the times of the experimentally measured diameters under given conditions.

The obtained D-L data set was plotted to extract the track D-L calibration curves, which were subsequently used to estimate the semi-empirical track lengths corresponding to the experimentally recorded diameters at the specified periods. By projecting the experimentally measured track diameters onto the appropriate calibration curve for each energy and etching temperature, we determine the semi-empirical lengths associated with the measured diameters for the relevant etching times, as well as for additional selected times in each case. Using these semi-empirical lengths together with the measured V_B, a number of track parameters are calculated, including the track length growth rate (dL/dt), track depth (x), residual range (R'), track etching rate (V_T), and etch rate ratio (V).

The resulting V values are plotted versus corresponding R' values for selected etching intervals and for alpha-particle energies of 5.3, 4.7, 4.1, and 3.5 MeV at etching temperatures of 60, 70, and 80 °C. To obtain optimal curve fits and updated coefficients for the V equation, the $V(R')$ data for all conditions are fitted using MATLAB in accordance with the Green et al. relation [24]. These optimized coefficients, along with the experimental inputs, are then supplied to the Track-Test program, where the Green *et al*. formula is applied again to determine the actual track profiles (longitudinal sections) in CR-39 corresponding to the experimentally measured diameters. As the etching process proceeds, the evolution of track growth and the successive development stages are also determined according to the specified alpha-particle energy, etching temperature, and etching interval.

3. Results and Discussion

3.1. Track Diameter and Its Growth Rate

The sizes of the tracks vary with the energy of the alpha particles used to irradiate the detector; higher alpha energies produce smaller track diameters. Figure 2 illustrates the change in track diameter (D) with etching period (t) for alpha particles with energies ranging from 5.3 to 3.5 MeV. The figure also shows that, for the same etching period, track diameters increase with increasing temperature of the chemical solution. Thus, the track size grows as the etching temperature rises from 60 to 80 °C.

The track diameter growth rate (V_D) is defined as the rate at which the track diameter

increases due to chemical etching of the detector exposed to charged particles. Since the track diameter varies linearly with etching time, V_D has a single value for particles incident perpendicularly on the detector surface. As a result, the created track exhibits a circular opening in the homogeneous and isotropic detector, as in the case of CR-39. The slope ($\Delta D/\Delta t$) of the lines in Fig. 2 represents the V_D values for alpha particle energies and etching temperatures used, as shown in Table 1. It is clear that V_D has a single value in each case, and this value varies depending on the alpha particle energy and etching temperature. Figure 3 shows that V_D decreases linearly with increasing alpha energy for the three chemical solution temperatures of 60, 70, and 80 °C. On the other hand, Fig. 4 shows that V_D follows a similar pattern for all alpha energies, as it increases exponentially with the temperature of the etchant under given etching circumstances.

It is well-known that raising the chemical etchant temperature enhances the energy (velocity) of the interaction of the chemical etchant molecules with the detector material. This causes more molecules to degrade in the areas that are affected by the incident particles, accelerating the growth of the track diameter. Accordingly, within the energy range and etching conditions used here, the value of V_D is larger at high etching temperatures and low alpha energies, and vice versa. This is evident from the values of V_D listed in Table 1 and in their dependence on energy and temperature as shown in Figs. 3 and 4.

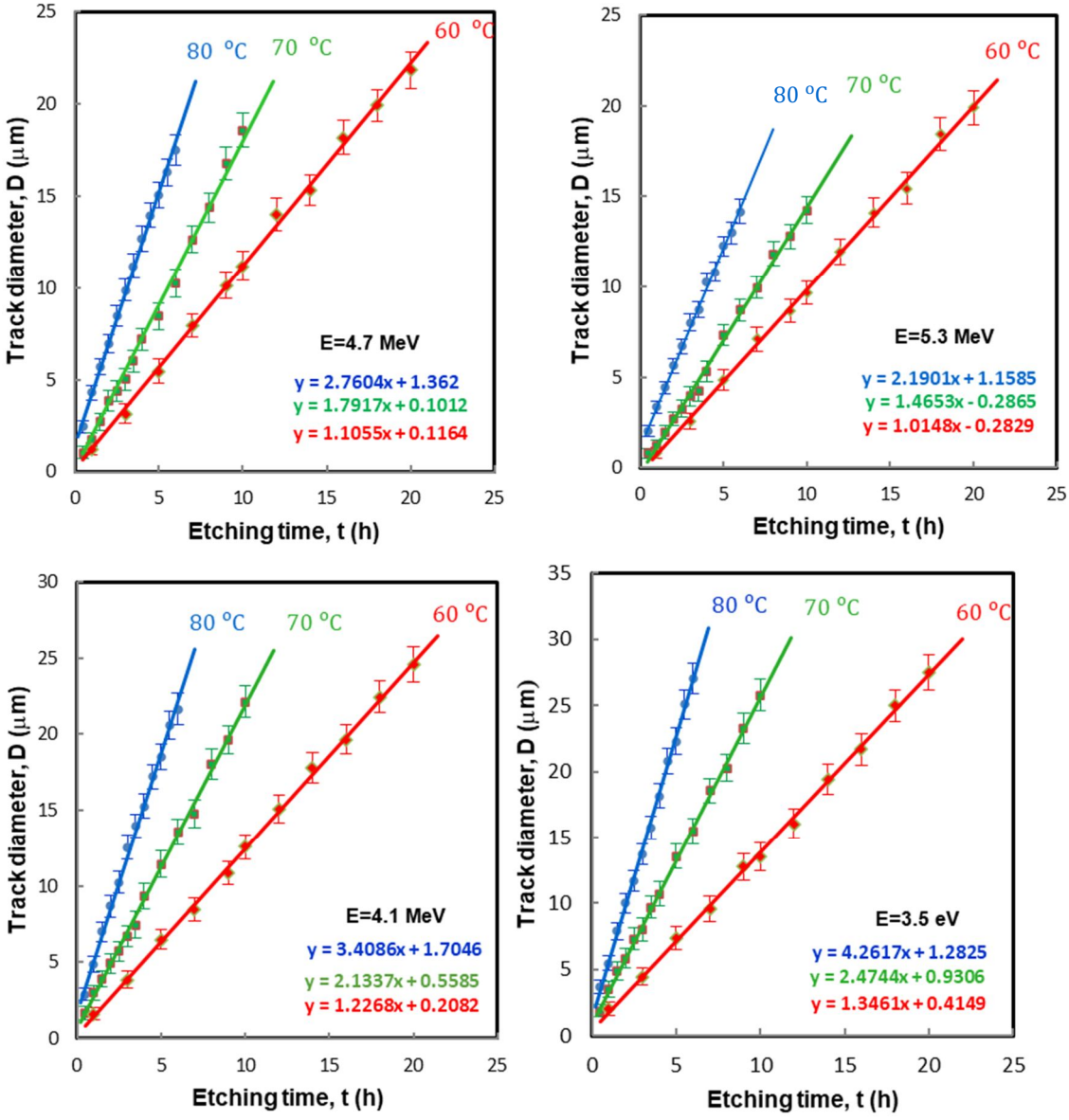

FIG. 2. Track diameter versus etching time for alpha energies of 5.3-3.5 MeV at different etching temperatures.

TABLE 1. Track diameter growth rate in CR-39 for various alpha energies and etching temperatures.

Etching Temp. (°C)	60	70	80
E (MeV)	Track diameter grow rate, V_D (µm/h)		
5.3	1.0148	1.4653	2.1901
4.7	1.1103	1.7917	2.7604
4.1	1.2268	2.1337	3.4994
3.5	1.3461	2.4744	4.2617

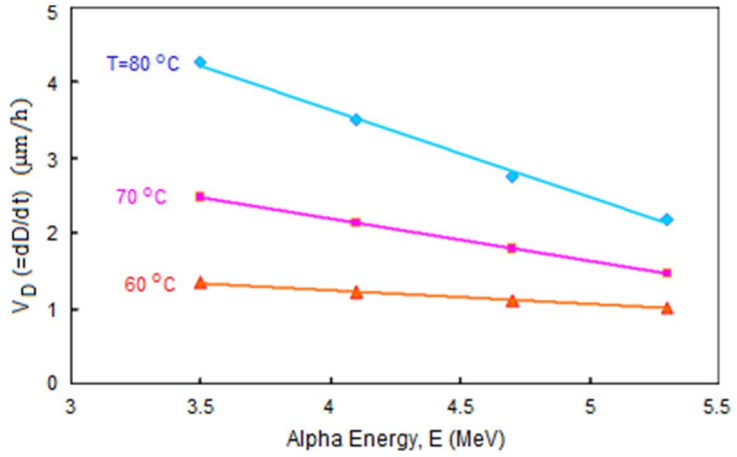

FIG. 3. Track diameter growth rate in relation to alpha energy at various etching solution temperatures.

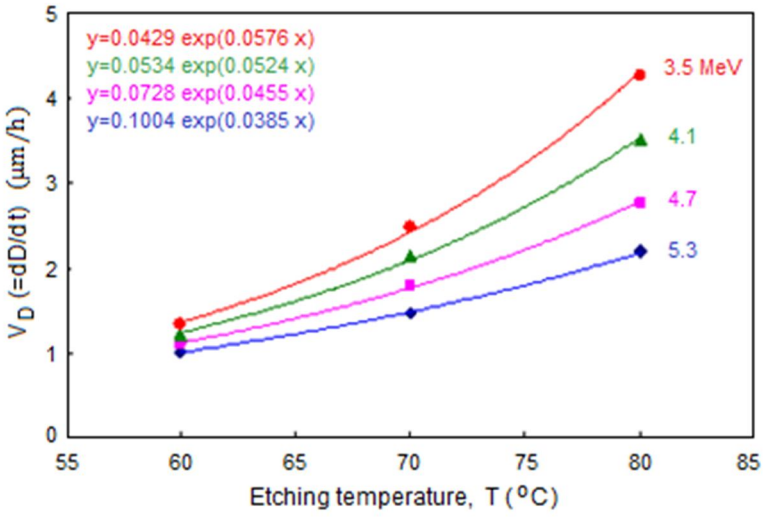

FIG. 4. Track diameter growth rate in relation to etching solution temperature for various energies of alpha particles.

3.2. Track Length

Figure 5 illustrates the change of semi-empirical track lengths with the time of etching in CR-39 for various energies and etching temperatures. The track length exhibits two distinct growth phases. In the first phase, where $V_T/V_B > 1$, the track length increases nonlinearly until it reaches a constant maximum value L_{max} at the saturation point (i.e., the start of track length saturation) [18, 25]. The track length achieves its maximum at this point when the etching extends to the end of the alpha range in the detector (the tail of the damaged path). Following this, the track length remains at its maximum saturation value (L_{max}), and the growth rate of the track length is kept at zero ($dL/dt = 0$) as the etching continues. It is also evident that the track length increases with decreasing alpha energy, corresponding to an increase in the particle's energy loss rate per unit distance in the detector. This indicates that more energy is being deposited, resulting in the rise of the energy of the damaged areas. Consequently, the etching process proceeds more quickly, enabling the removal of more damaged molecules from these regions.

The stage from the beginning of the track's appearance until the point of saturation is called the acute-cone phase. During this phase, the etched track is conical, terminating in a pointed tip located at the end of the damaged path; this structure is commonly referred to as an "etched-out" track. After saturation, the track enters the over-etching phase, during which the etchant progresses beyond the end of the damaged trajectory (i.e., beyond the alpha-particle range) into the undamaged region [12, 18]. At the beginning of this phase, the value of V_T approaches V_B, causing the pointed tip of the conical track to round off and gradually evolve into a more spherical shape as $V_T \approx V_B$.

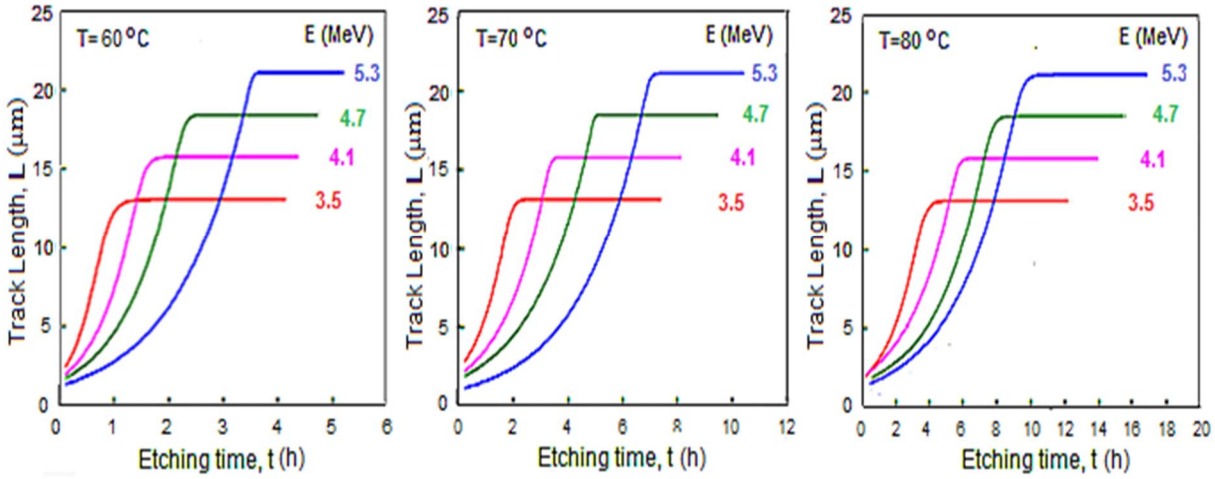

FIG. 5. Semi-empirical track lengths obtained from the D-L calibration curves versus etching time for different energies of alpha particles at etching temperatures of 60, 70, and 80 °C.

Regarding the effect of temperature on the track lengths, the graphs in Fig. 6 show that increasing the etchant temperature speeds up the degradation of the detector molecules and reduces the time required to get the same length at the same moment for the specified alpha energy. The figure also shows that, for each alpha energy, the change in track length with etching time appears as bundles corresponding to the etching temperatures 60, 70, and 80 °C at a constant concentration of etching solution. The length bundles show that the value of the maximum length (L_{max}) does not depend on the etching temperature, as it is constant in each bundle, but differs with alpha particle energy. This is evident from the leftward and downward shift of the bundles as the particle energy decreases.

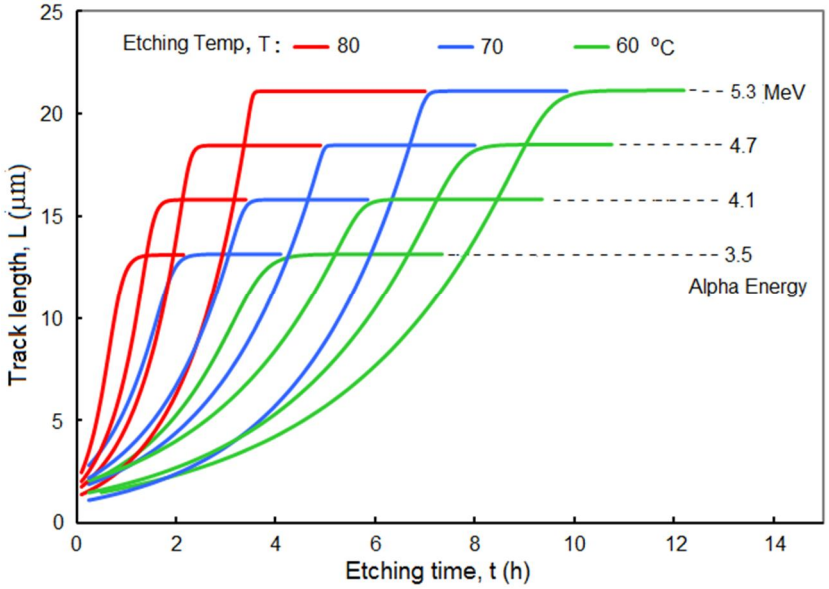

FIG. 6. Bundles of lengths against etching time for a range of alpha energies (5.3-3.5 MeV) at various etching temperatures (60, 70, and 80 °C).

3.3. Track Length Growth Rate

The track-length growth rate, denoted as $L'(t) = dL/dt$, is defined as the rate at which the track length changes over time as a result of the etching process. It is a measurement of how much material is removed from the damaged area as the etching deepens. The calculation of $L'(t)$ is important because it is related to the etching rate toward the depth of the track, V_T, which is regarded as one of the fundamental and crucial parameters in describing the track shape. Figures 7 and 8 show the change in track length growth rate with etching time and alpha particle energy, respectively.

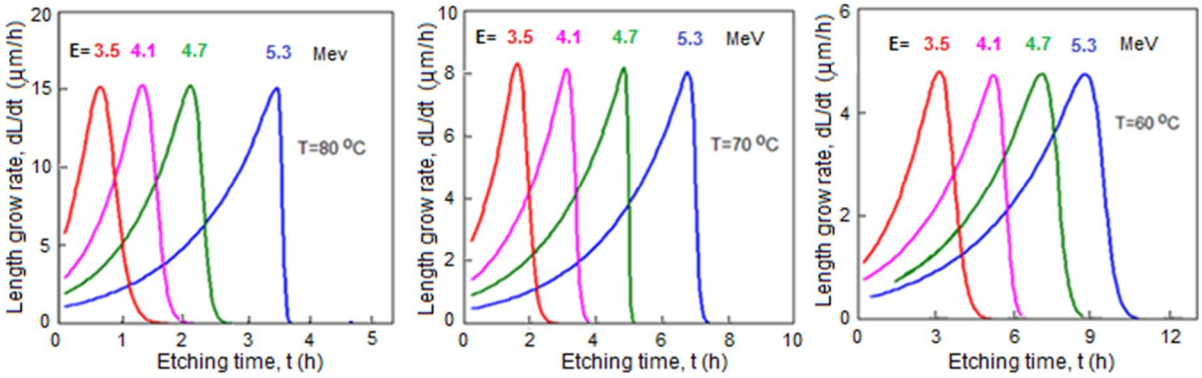

FIG. 7. Track's length growth rate versus etching time for various alpha energies at etching temperatures of 60, 70, and 80 °C.

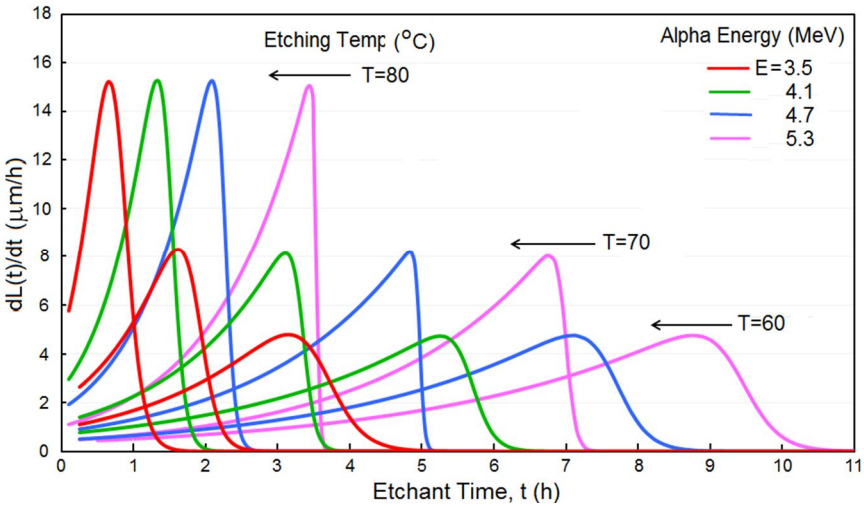

FIG. 8. Track's length growth rate versus etching time at various etching temperatures for alpha energies of 5.3-3.5 MeV.

3.4. Track Etch Rate

The track etch rate (V_T) plays an essential role in profiling the etched track. The stages of track growth, as well as the development of its length and profile, are closely connected to V_T and its variation against the etching period (t) and depth of track (x). It quantifies the velocity at which the material is eliminated from the detector along the damaged depth, which is influenced by the etching circumstances and the energy loss rate per unit distance in the detector. The V_T is calculated using the following equation [5, 26, 27]:

$$V_T = dL/dt - V_B t \quad (1)$$

Figures 9 and 10 illustrate the variation of V_T with etching time for various etching temperatures and alpha particle energies, respectively. The shape of curves is in good agreement with those recorded under different conditions [5, 7, 18].

The track depth $x(t)$ is the separation between the initial surface of the detector and the pointed head of the etched track. It is strongly correlated to V_T and can be calculated using Eq. (2) [27]:

$$x(t) = V_T(t).t\ (\mu m) \quad (2)$$

On the other hand, Eq. (3) can be used to compute the residual range $R'(t)$ [13, 20]:

$$R'(t) = R - x(t)\ (\mu m) \quad (3)$$

It is worth mentioning that there is a strong and dialectical relation between the etching rate (V_T) and the energy loss rate ($-dE/dx$), and then with the amount of damage caused in the detector by the incident particles.

The chemical etching solution attacks the damaged portions more aggressively, raising the potential energy of these areas and thereby increasing the V_T even more. As the etching process advances, V_T reaches its maximum value of V_{Tmax} just before the tip of the conical track reaches the tail of the damaged path, i.e., the alpha range in CR-39. This maximum point corresponds to the position of the Bragg peak on the stopping power curve of alpha particles in air, as illustrated in Fig. 11, where the etching rate and the number of degraded molecules are at their highest. Following that, V_T drops and begins to approach the V_B value at the damaged end as it quickly reaches equality $V_T = V_B$ (1.421 µm/h in this study) once the etchant enters the undamaged area beneath the damaged region. This is consistent with the results obtained by others using different methods [6, 7, 18].

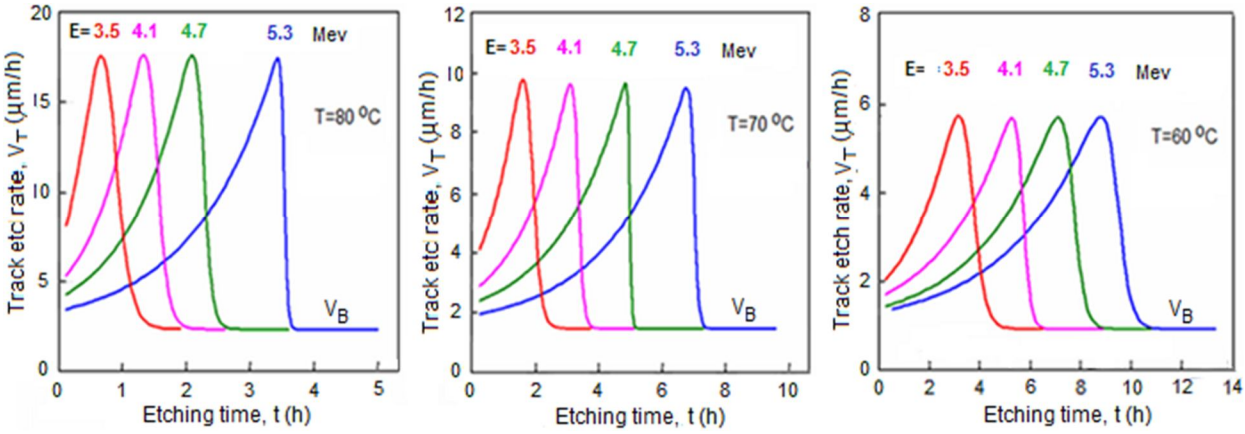

FIG. 9. Track etch rate versus etching time for various alpha energies at etching temperatures of 80, 70, and 60 °C.

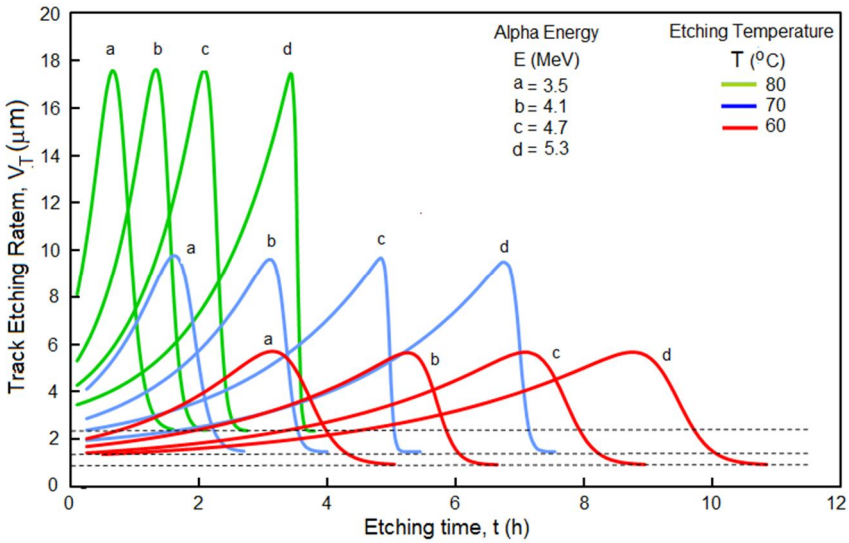

FIG. 10. Track etch rate versus etching time for alpha energies of 5.3-3.5 MeV at various etching temperatures.

3.5. Etch Rate Ratio

The etch rate ratio (V), known as the response, is another fundamental parameter describing the track, since it is related to V_T, which is an essential factor in determining the track shape evolution. For normally incident particles on the detector, V is given as [1]:

$$V = V_T / V_B \quad (4)$$

V_B is usually constant, depending on the etching conditions. Thus, the temporal pattern of V follows the same trend as V_T, differing only by a constant factor of V_B^{-1}.

Figure 11 illustrates the one-to-one correspondence among three curves: the stopping power (S) of alpha particles in air versus path length, the etch rate ratio versus track depth V(x), and the track length versus etching interval L(t). The figure highlights several key features: the residual range R', the maximum etch rate V_m, the maximum track-length growth rate $(dL/dt)_{max}$ corresponding to the Bragg peak, the saturation time t_{sat}, the maximum track length L_{max} at the end of the alpha range or damaged trajectory, and the behavior of other parameters related to track-profile development throughout both stages of track growth.

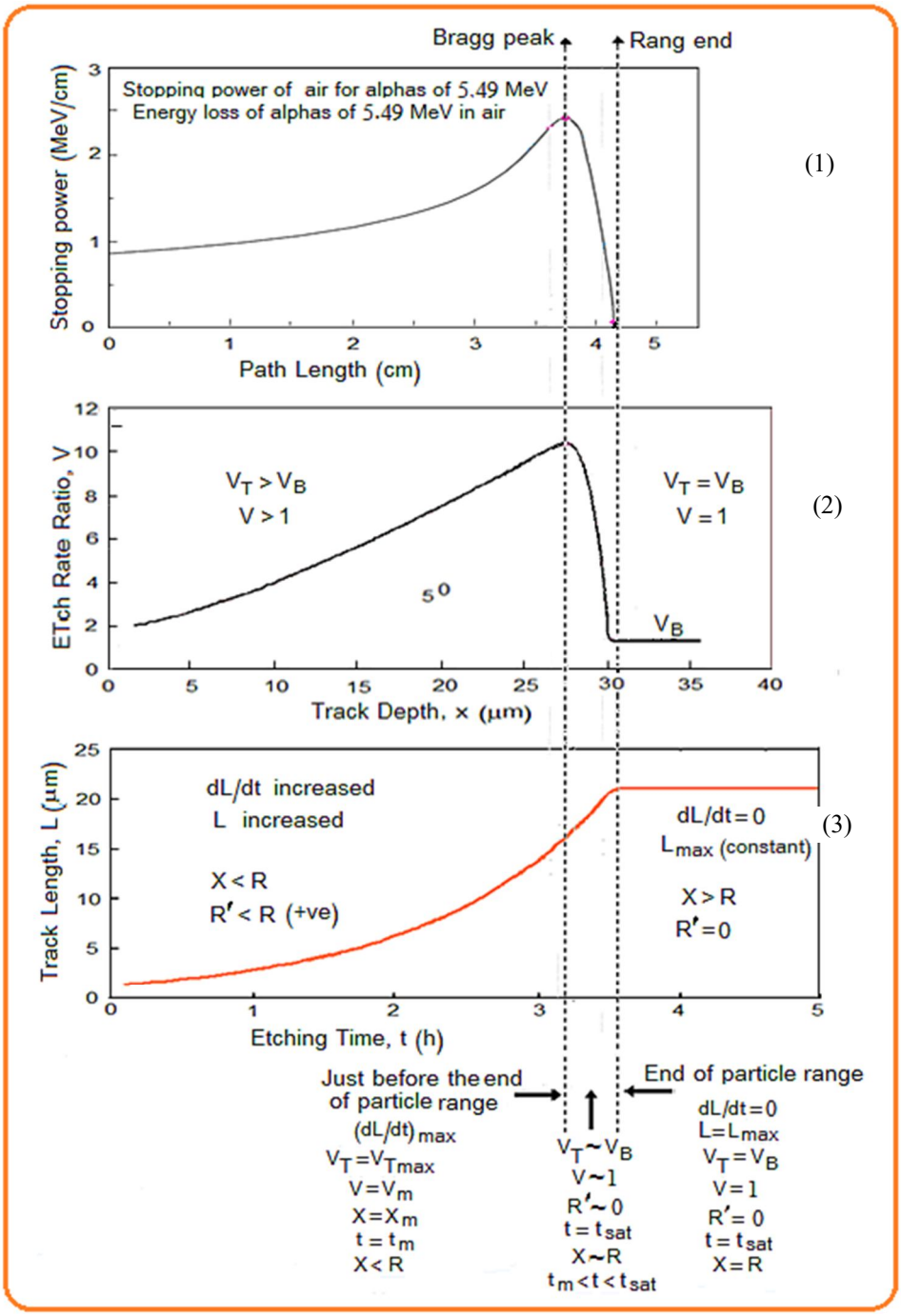

(1) https://en.wikipedia.org/wiki/Bragg_peak Wagenaar, Douglas (1995). "7.1.3 The Bragg Curve". *Radiation Physics Principles.* (2) & (3) The present work.

FIG. 11. Coincidence among three curves: the stopping power of alpha particles in air, the etch rate ratio versus track depth, and the track length versus etching interval.

3.6. Etch Rate Ratio and Residual Range

One of the crucial steps in analyzing the track profiles and drawing them in accordance with the measured experimental data is the determination of etching rates, particularly the V_T and V, and plotting them with respect to R′. Several researchers presented and used a number of computer programs to theoretically sketch the profile of the track and compute its parameters for protons and alpha particles in CR-39 and LR115 detectors [16, 19-21]. These programs are based on specific mathematical formulae for V(R′), as proposed by various researchers [7, 8, 24, 28, 29].

Figure 12 shows that the V function initially increases as the residual range (R′) increases, reaching its maximum value, $V_m(R')$, where R′ becomes very small at the point corresponding to the Bragg peak. This happens shortly before the etching reaches the limit of particle range. Once the chemical etchant reaches the damaged tail, V rapidly decreases after a short etching interval. At the same time, the track length reaches the beginning of saturation and attains a constant maximum value (L_{max}). At this point, the residual range becomes zero ($R' = 0$), the track depth equals the particle's range ($x = R$), the value of V is getting close to one ($V \approx 1$), and $V_T \approx V_B$. This shows that the conical etched track tip has arrived at the damaged tail at the alpha range end, where the track is completely etched and is referred to as the "out-etched" track. More prolonged etching times result in non-directional (scalar) etching that moves at the same rate of $V_T = V_B$ $(i.e., V = 1)$ in all directions within the undamaged area beneath the damaged path. In this case, the track is known as an "etching pit" [18, 20].

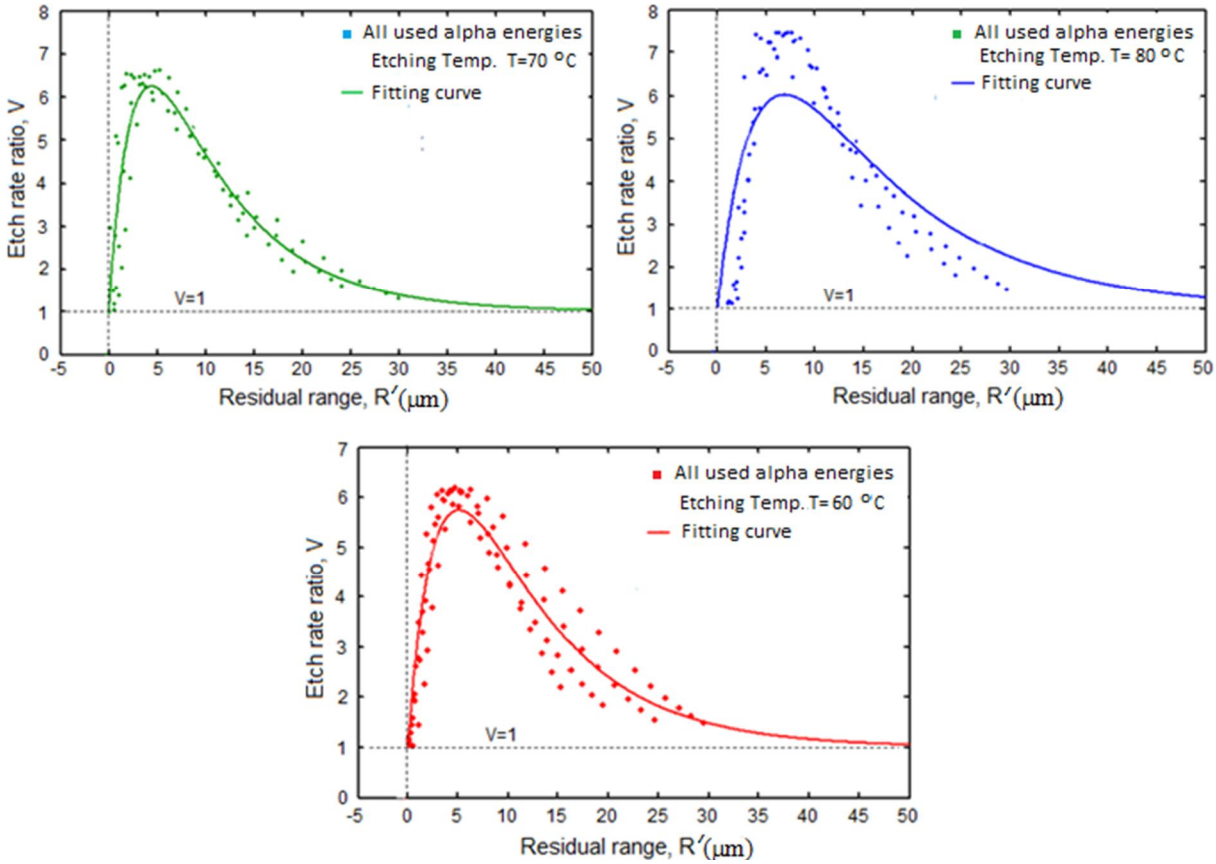

Fig. 12. The fit curves of V(R′) obtained using combined data from all alpha-particle energies for each etching temperature separately, according to the Green *et al.* (1982) formula.

3.7. Fit Curve of Etch Rate Ratio and the Coefficients

Since the etch rate ratio (V) does not vary significantly with alpha-particle energy, as shown in Fig. 12, and because it is directly related to the track depth (x) in the detector, it can be fitted as a function of the residual range. The resulting fitted curves are represented by the solid lines in the figure. By incorporating the newly obtained fitting coefficients into the Track-Test program [20], the theoretical profiles of etched tracks can be determined, and their

evolution can be traced for the investigated alpha-particle energies at the examined etching temperatures. The curve fitting between V and R' was performed using MATLAB software, based on the Green *et al.* equation [24], given by

$$V = 1 + [A_1 \exp(-B_1 R') + A_2 \exp(-B_2 R')][1 - \exp(-B_3 R')] \quad (5)$$

where $A_1, A_2, B_1, B_2,$ and B_3 are the formula's coefficients, and R' is the residual range.

The solid curves in Fig. 12 represent the optimal fits of $V(R')$ for various alpha-particle energies at each etching temperature considered individually. In contrast, Fig. 13 presents the optimal fit of the $V(R')$ function obtained by combining all alpha-particle energies and all etching temperatures simultaneously. The coefficients $A_1, A_2, B_1, B_2,$ and B_3, as well as $V_m(R')$ and R' corresponding to the maximum values, were identified from the fitting process based on our experimental data and the used etching conditions. It was found that the average values of the coefficients $A_1, A_2, B_1, B_2,$ and B_3, obtained by fitting the $V(R')$ values for all alpha energies (5.3, 4.7, 4.1, and 3.5 MeV) and all etching temperatures (60, 70, and 80 °C) simultaneously, are very close to those obtained by fitting the $V(R')$ data for all alpha-particle energies combined at each etching temperature separately. This agreement is evident from Figs. 12 and 13 and the values listed in Table 2.

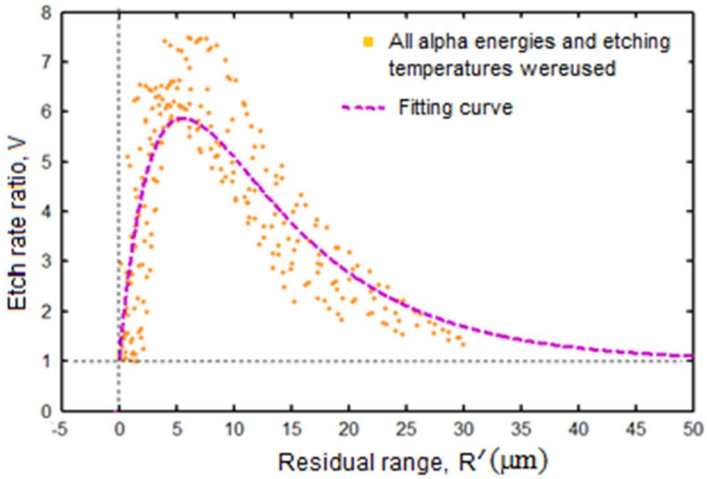

FIG. 13. Optimal fit curve of $V(R')$ obtained using combined data for all alpha-particle energies and etching temperatures, according to the Green *et al.* (1982) formula.

TABLE 2. The new coefficients of the Green *et al.* formula for V, the maximum V_m values, and the corresponding residual range (R'), for various alpha energies and etching temperatures.

Coffiecients and Parameters	Using optimal fit of V(R') values for all alpha energies together at once for each etching temperature separately				Using optimal fit of V(R') values for all alpha energies and etching temperatures together at once
	Etching Temperature °C				
	60	70	80	Average	
A_1	6.18	6.233	6.158	6.1903	6.207
A_2	6.181	5.925	5.998	6.0347	5.997
$B_1(\mu m^{-1})$	0.1079	0.1132	0.0759	0.0990	0.0948
$B_2(\mu m^{-1})$	0.1083	0.1141	0.0760	0.0995	0.0948
$B_3(\mu m^{-1})$	0.2149	0.2819	0.1731	0.2233	0.2039
V_m	5.716	6.29	6.043	6.016	5.92
R' (μm)	5.193	4.487	6.784	5.488	5.556

This indicates that the values of V are nearly independent of both the etching temperature and the alpha-particle energy to which the detector was exposed. Therefore, the $V(R')$ data for all alpha energies and etching temperatures were fitted collectively using the formula proposed in the present study. The coefficients $A_1, A_2, B_1, B_2,$ and B_3 extracted from the optimal fit were subsequently implemented in the Track-Test program,

together with other experimental parameters, to generate the alpha-particle track profiles (longitudinal sections) in CR-39. These parameters include the etching time, alpha-particle energy, and the bulk etching rate corresponding to each etching temperature. As shown in Table 2, the maximum values V_m obtained from both fitting approaches are nearly identical. This confirms the validity of performing a unified fit using the combined V data for all alpha energies and etching temperatures to determine the coefficients employed in generating track shapes and parameters that are consistent with our experimental data.

The shape and behavior of the graph representing the optimal etching rate function V(R') is consistent with the findings of Nikezic and Yu [30], who measured the track lengths directly from the track profile images for various alpha particle energies and etching conditions, as shown in Fig. 14(a). Furthermore, the behavior of the current V(R') function graph based on the D-L approach also agrees with that shown by Younis [22], who utilized the D-L approach to determine the track lengths indirectly from direct measurements of the track diameters, as shown in Fig. 14(b). He selected alpha energies of 4.4, 3.6, 2.8, and 2.0 MeV and used the etchant NaOH at 70 °C and molarities of 4, 5, 6, and 7 N, while the present study utilized alpha particles with energies of 5.3, 4.7, 4.1, and 3.5 MeV and NaOH as an etchant of molarity 6 N, where the etching was conducted at different temperatures of 80, 70, and 60 °C.

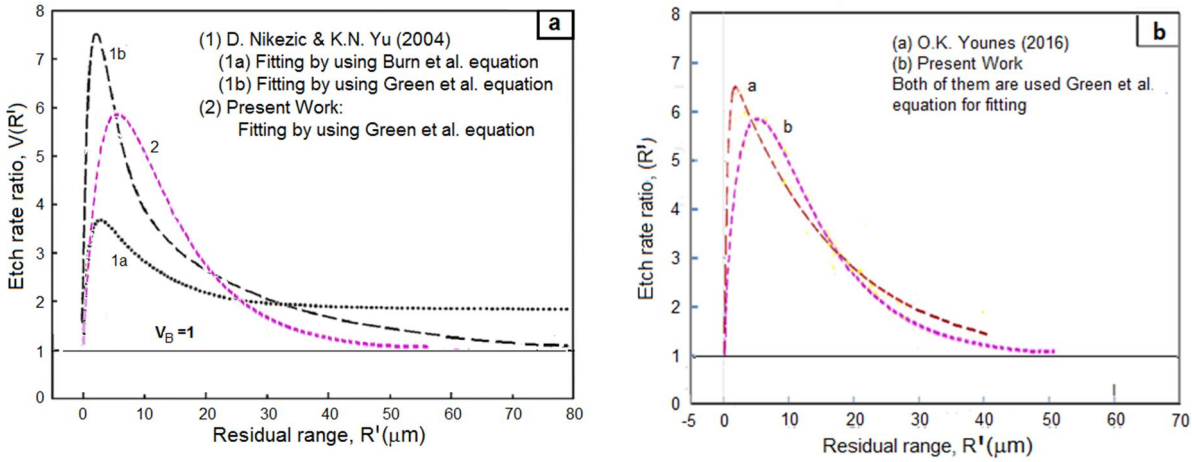

FIG. 14. Comparison of the V(R') function obtained in the present study with those reported by Nikezić and Yu [30] and Younis [22] for various alpha-particle energies and etching conditions.

3.8. Track Profiles Optimal Fit Curve of Alpha Particles Tracks in CR-39

The track profiles (longitudinal sections) and their associated parameters in the CR-39 detector were theoretically obtained by inputting the coefficients derived from the optimal fit of the V(R') curve, together with the experimental data from the present study, into the Track-Test program using the Green *et al.* equation. As inferred from the path-length behavior in Fig. 5 and illustrated in Fig. 15, the formation of track profiles during the etching process occurs in two distinct phases: the acute-cone phase within the damaged region and the over-etched phase in the intact material beneath the damaged path, beyond the alpha-particle range in the detector. As an example, Fig. 15 shows the simulated profiles of 4.7 MeV alpha-particle tracks in CR-39, together with the corresponding growth phases, track diameters, and lengths, as determined using the Track-Test software based on our experimental data. The input parameters used for this simulation are as follows: alpha-particle energy $E = 4.7$ MeV; particle incident angle $\theta = 90^{o}$; etching molarity and temperature $N = 6$, $T = 70\,^{o}C$; etching time $t = 1\text{–}10$ h; bulk etch rate $V_B = 1.421\ \mu m/h$; and the coefficients listed in Table 2, namely $A_1 = 6.207$, $A_2 = 5.997$, $B_1 = 0.09481\ \mu m^{-1}$, $B_2 = 0.09481\ \mu m^{-1}$, $B_3 = 0.2039\ \mu m^{-1}$, as applied in the Green *et al.* function given in Eq. (5)

Similar results can be obtained for the other alpha-particle energies investigated in this work (5.3, 4.1, and 3.5 MeV) and for etching temperatures of 60, 70, and 80 °C.

Acute -cone stage (sharp-track phase)						
L – changes with etching time					saturation point "*etched-out track*"	
	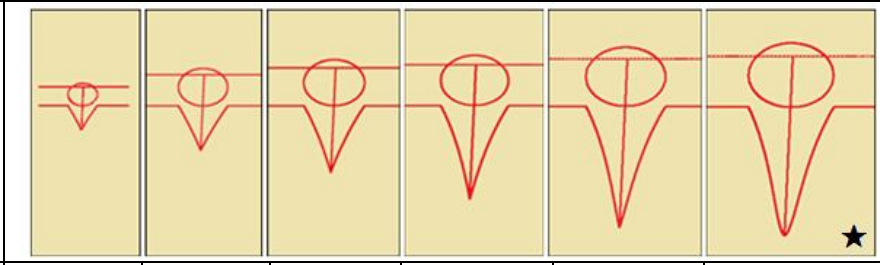					
t (h)	1.5	2	3	4	4.5	**5** = t_{sat}
L (μm)	2.852	4.175	7.806	13.644	17.043	18.544 = L_{max}
D (μm)	2.631	3.352	5.387	7.297	8.275	9.273
Over-etched Stage (spherical- track phase)						
L is approximately constant = L_{max}, & $dL/dt = 0$						
	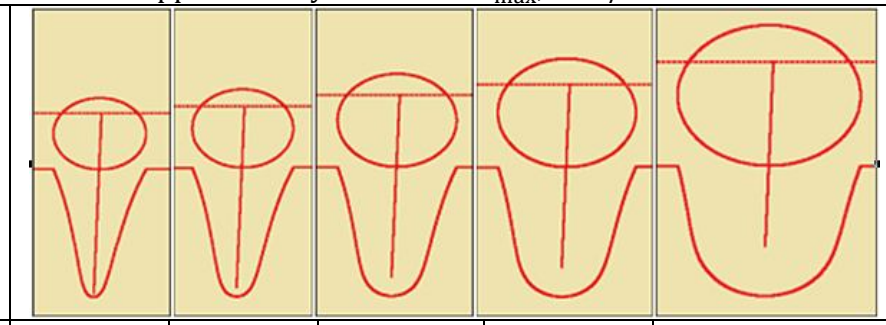					
t (h)	5.5	6	7	8	10	
L (μm)	18.544	18.571	18.571	18.571	18.571	
D (μm)	10.275	11.299	13.391	15.544	20.023	

FIG. 15. Profiles or longitudinal sections of 4.7 MeV alpha particle tracks in CR-39 under etching conditions of NaOH (6 N) at 70 °C, using the Track-Test software.

Table 3 and Fig.16 show the maximum lengths (L_{max}) of the alpha tracks in CR-39 with energies of 5.3-3.5 MeV and etching temperatures of 60, 70, and 80 °C. These values were obtained from the theoretical track profiles generated by the Track-Test software using the optimal values of A_1, A_2, B_1, B_2, and B_3 obtained from fitting the V(R') curve, given in Table 2.

TABLE 3. Comparison of maximum track lengths in CR-39 for various alpha-particle energies at all etching temperatures, obtained theoretically using the Track-Test software with the new coefficients from the optimal fit of the V(R′) curve, and experimentally using the D–L correlation method.

	L_{max} (μm)	
E (MeV)	using (T-T) Track-Test program	using D-L correlation (present method)
5.3	20.76	21.10
4.7	18.55	18.46
4.1	15.99	15.81
3.5	13.14	13.11
	For all used etching temperatures (60, 70, 80 °C)	

D-L: Track Diameter-Length calibration curve based on the track's diameter measurements.
T-T: Track-Test program based on the new estimated coefficients of the V function.

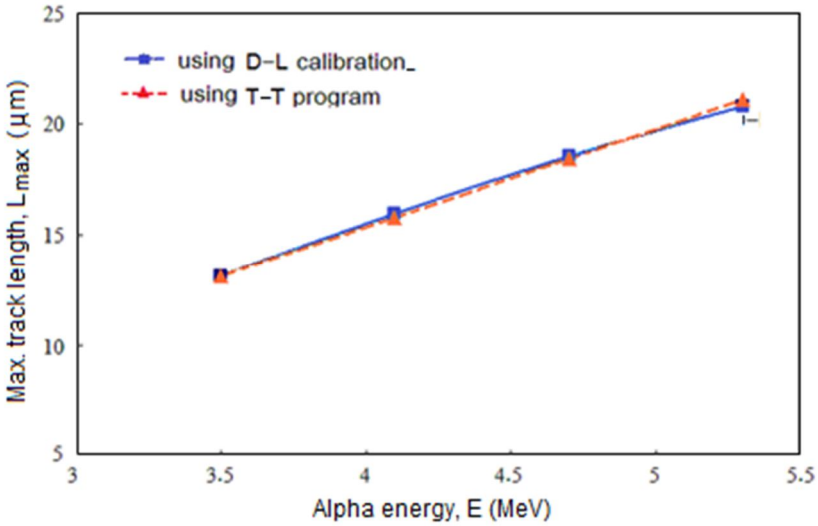

FIG. 16. Comparison of maximum track lengths in CR-39 for alpha energies at all etching temperatures, calculated theoretically using the Track-Test software using the new coefficients obtained from the optimal fit curve of V(R′), and experimentally using the D-L correlation method.

Figure 17 illustrates a comparison between the theoretical and experimental track diameters of 4.7 MeV alpha particles in CR-39 at an etching temperature of 70 °C. The theoretical diameters, calculated using the Track-Test program with the optimal fitting coefficients of the V equation derived from the D–L correlation method, show excellent agreement with the experimentally measured diameters for the same alpha-particle energy and etching conditions.

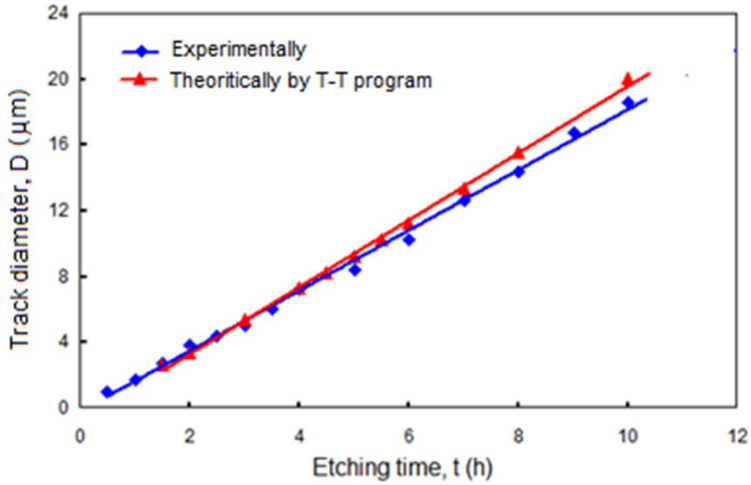

FIG. 17. Comparison of empirical diameters of 4.7 MeV alpha tracks in CR-39 at an etching temperature of 70 °C. The theoretical diameters were calculated using the Track-Test software with the new optimal fitting coefficients derived from the track D–L correlation method.

4. Conclusion

The alternative "D-L correlation" method, which relies on directly measured track diameters in CR-39, successfully determined track profiles and parameters that are in good agreement with results obtained by studies relying on direct measurements of track lengths from etched track images.

The track length curves for different alpha-particle energies display bundle-like patterns corresponding to changes in the etching temperature. While increasing the etching temperature does not affect the maximum track length (L_{max}) at saturation, it reduces the time (T_{sat}) required to reach this maximum. Conversely, for a constant etching temperature, both Lmax and tsat increase with decreasing alpha-particle energy, reflecting the higher energy deposition in the detector material.

It was proved that the evolution of the track profile is greatly influenced by the change of

the track etching rate with its depth, $V_T(x)$. Based on direct measurements of track diameters, the present method yields depth-dependent values of V_T for a given incident particle energy, which represents a key advantage of this approach. This behavior contrasts with earlier studies that relied on direct diameter measurements but assumed a single constant value of V_T with track depth for a single specified energy of the incident particles and used the elementary equations generated for this case, which were unable to accurately predict the real changes in track parameters and shapes.

Finally, the D-L correlation method is easy to use and doesn't require a lot of skill or effort. It shows realistic changes in the track profiles and parameters that are comparable to those obtained by directly measuring the lengths of the tracks from their experimental photos. As a result, this methodology is an alternative to the method of direct measurement of the track length, which requires an appropriate technique, accuracy, and experience in obtaining experimental images of track profiles in the detector.

References

[1] Durrani, S.A. and Bull, R.K., "Solid State Nuclear Track Detection", (Pergamon Press, Oxford, UK, 1987).

[2] Sinenian, N., Rosenberg, M.J., Manuel, M., McDuffee, S.C., Casey, D.T., Zylstra, A.B., Rinderknecht, H.G., Gatu Johnson, M., Seguin, F.H., Frenje, J.A., Li, C.K., and Petrasso, R.D., Rev. Sci. Instrum., 82 (2011) 1.

[3] Thomas, H.S.P., Deas, R.M., Kirkham, L.N., Dodd, P.M., Zemaityte, E., Hillier, A.D., and Neely, D., Plasma Phys. Control. Fusion, 63 (2021) 124001.

[4] Khan, A., Al Qahtani, S., Al-Maqbool, W., Al-Naggar, T.I., Alhamami, A., and Abdalla, A.M., Radiat. Phys. Chem., 213 (2023) 111237.

[5] Dörschel, B., Hermsdorf, D., Kadner, K., and Kühne, H., Radiat. Prot. Dosimetry, 78 (3) (1998) 205.

[6] Hermsdorf, D. and Hunger, M., Radiat. Meas., 44 (9-10) (2009) 766.

[7] Azooz, A.A., Al-Nia'emi, S.H., and Al-Jubbori, M.A., Radiat. Meas., 47 (2012) 67.

[8] Yu, K.N., Ng, F.M.F., and Nikezic, D., Radiat. Meas., 40 (2005) 380.

[9] Yu, K.N., Ng, F.M.F., Ho, J.P.Y., Yip, C.W.Y., and Nikezic, D., Radiat. Prot. Dosimetry, 111 (1) (2004) 93.

[10] Ng, F.M.F., Luk, K.Y., Nikezic, D., and Yu, K.N., Nucl. Instrum. Methods Phys. Res. B, 263 (2007) 266.

[11] Wertheim, D., Gillmore, G., Brown, L., and Petford, N., Nat. Hazards Earth Syst. Sci., 10 (2010) 1033.

[12] Nikezic, D., and Yu, K.N., Radiat. Meas., 37 (2003) 39.

[13] Dörschel, B., Hermsdorf, D., Reichelt, U., Starke, S., and Wang, Y., Radiat. Meas., 37 (2003) 563.

[14] Tse, K.C.C., Nikezic, D., and Yu, K.N., Radiat. Meas., 43 (2008) 98.

[15] Dörschel, B., Fülle, D., Harmann, H., Hermsdorf, D., Kadner, L., and Radlach, CH., Radiat. Prot. Dosimetry, 69 (4) (1997) 267.

[16] Azooz, A.A., Al-Nia'emi, S.H., and Al-Jubbori, M.A., Comput. Phys. Commun., 183 (2012) 2470.

[17] Al-Nia'emi, S.H.S., Iraqi J. Sci., 59 (2B) (2018) 856.

[18] Al-Nia'emi, S.H.S., J. Phys. Sci., 29 (2) (2018) 89.

[19] Nikezic, D. and Yu, K.N., Comput. Phys. Commun., 178 (2008) 591.

[20] Nikezic, D. and Yu, K.N., Comput. Phys. Commun., 174 (2006) 160.

[21] Nikezic, D., Ivanovic, M., and Yu, K.N., Softw. X, 5 (2016) 74.

[22] Younes, O.K., MSc. Thesis, Department of Physics, College of Education for Pure Scince, University of Tikrit, (2016).

[23] Ziegler, J.F., Ziegler, M.D., and Biersack, J.P., The stopping and range of ions in matter,

SRIM-2008, (2008), http://www.srim.org.

[24] Green, P.G., Ramli, A.G., Al-Najjar, S.A.R., Abu-Jarad, F., and Durrani, S.A., Nucl. Instrum. Methods, 203 (1982) 551.

[25] Saeed, S.H. and Mustafa, A.Q., Kirkuk Univ. J. Sci. Stud., 16 (3) (2021) 12.

[26] Ditlov, V.A., Awad, E.M., Fromm, M., and Hermsdorf, D., Radiat. Meas., 40 (2005) 249.

[27] Yamauchi, T., Ichijo, H., Oda, K., Dörschel, B., Hermsdorf, D., Kadner, K., Vaginay, F., and Fromm, M., Radiat. Meas., 34 (2001) 37.

[28] Brun, C., Fromm, M., Jouffroy, M., Meyer, P., Groetz, J.E., Abel, F., Chanbaudet, A., Dörschel, B., Hermsdorf, D., Bertschneider, R., Kadner, K., and Kuhne, H., Radiat. Meas., 31 (1999) 89.

[29] Fromm, M., Awad, M., and Ditlov, V., Nucl. Instrum. Methods Phys. Res. B, 226 (2004) 565.

[30] Nikezic, D. and Yu, K.N., Mater. Sci. Eng. R, 46 (2004) 51.

Volume 18, Number 5, 2025. pp. 629-642

Jordan Journal of Physics

ARTICLE

The Photothermal Conversion Characteristics of a Selective Coating Decorated with ZrO_2 and Fe Powders

Mustafa Ashoor Ryadh and **Ahmed A. Al-Tabbakh**

Department of Physics, College of Science, Al-Nahrain University, Jadiriya, Baghdad, Iraq.

Doi: **https://doi.org/10.47011/18.5.6**

Received on: 10/11/2024; *Accepted on: 23/02/2025*

Abstract: The photothermal conversion characteristics of black, composite, and selective coatings were investigated. ZrO_2 and Fe particles were incorporated into the heat-resistant black paint (HRP) to improve the conversion capability of the coating. The coatings and the particles were applied onto aluminium substrates using the direct spraying method. This resulted in layers having thicknesses of 323.5 μm and 837 μm for the ZrO_2- and Fe-containing coatings. The addition of these powders led to a decrease in the coating density from 1.67 g/cm^3 to 0.31 g/cm^3 and 0.5 g/cm^3 for the ZrO_2/HRP and Fe/HRP coatings, respectively. The addition of the particles was found to improve the solar-to-thermal conversion of the primary paint significantly. Maximum absorbance of 97.81% and a substrate temperature of 382.65 K after 40 minutes of radiation exposure were achieved using the Fe/HRP system. The photothermal conversion characteristics were analyzed based on the structural, compositional, and physical properties of the composite coatings. The absorption spectra in the UV-Vis range of the Fe/HRP coating showed higher peaks than those exhibited by the ZrO_2/HRP coating, emphasizing the higher photo-thermal conversion of the Fe/HRP coating. Owing to their ease of application and high conversion performance, the developed coatings are superior to many existing coating systems for flat-plate collectors.

Keywords: Coating, Photothermal effects, Optical absorption, Nanopowders.

PACS Nos: 42.79. Wc, 78.20. nb, 42.25. Bs, 81.07. Wx.

1. Introduction

Solar-thermal collectors are devices used to capture solar radiation and convert it to heat. They have various designs, structures, and a wide range of applications across industrial and residential sectors. These include space heating, swimming pool and domestic water heating, solar steam generation, and water desalination [1]. Other applications may extend to bacteria killing, catalysis, and sensors. The concentrated and non-concentrated solar collectors for residential and industrial applications depend, in their photothermal conversion and energy harvesting capabilities, on the selective coating on the top of their surfaces [2, 3]. These coatings are responsible for the conversion of solar radiation into thermal energy. The conversion efficiency of the selective coating depends on the coating's structural, elemental, geometrical, and physical characteristics [4-9]. New-generation selective coatings increasingly incorporate nanomaterials and nanostructures in their design to achieve higher absorption coefficients, reduced reflectivity of incident radiation, and enhanced absorption mechanisms such as radiation trapping [8]. In addition, the coatings have to maintain a minimal emittance of energy (i.e., minimal thermal emissivity) at moderate and elevated temperatures. These coatings may be comprised of single or multiple layers of thin or thick films. A large number of materials may also be incorporated for the direct solar conversion application, such as multiwall carbon

Corresponding Author: Ahmed A. Al-Tabbakh **Email**: tabbakh2013@gmail.com

nanotubes (see, for example, Ref. [2]). Atchuta *et al.* produced a thin film of nickel-doped cobaltite spinel on a stainless steel substrate as a selective coating using a wet-chemical dip-coating method [10]. They reported an absorbance of 0.92 of the as-coated substrates. They also succeeded in improving the substrate absorbance to 0.94 by adding an optical enhancement layer on top of the thin film coating. Rubin *et al*. investigated the thermal stability and optical properties of Cu spinel oxide nanoparticles for photothermal conversion [9]. They reported a maximum thermal absorption of 97.2% with high thermal stability of porous Cu-based spinel structures. They investigated the effect of the structural and compositional properties of the coatings on solar absorption. However, no experimental data on the solar-to-thermal conversion were reported in that work.

Sivakumar *et al*. reported a maximum plate-collector temperature of 370 K after coating with a nanofluid composed of black paint mixed with cupric oxide nanoparticles [11]. Mediha *et al*. investigated the effect of doping copper oxide thin films with aluminum on the films' optical and photocatalytic properties [12]. They found that Al-doping affects the crystallite size slightly and improves the electrical conductivity of the thin films. In addition, the energy band gap decreased from 2.62 to 1.8 eV due to the Al-doping. The photocatalysis efficiency of the thin films improved, as shown by the photocatalytic degradation of the orange dye. The photocatalysis mechanism was analyzed based on the generation of electron-hole pairs due to exposure to UV radiation, leading to the production of hydroxyl radicals and reduction of oxygen, which then becomes responsible for dye degradation. The dependence of the photocatalytic effect on temperature and aluminum concentration was also investigated, showing the optimal conditions of these two parameters. The surface morphology of the thin film was found to depend on the aluminum concentration, and this was found to enhance the photocatalytic property of the thin film. This work emphasizes the significant impact of doping with aluminum on the physical and functional properties of copper oxide thin films.

Dikra *et al*. synthesized Zr-doped ZnO thin films for photocatalysis application [13]. They investigated the difference in depositing these films on glass or ceramic substrates, especially on the photocatalytic properties. They found that depositing Zr-doped ZnO films on a ceramic substrate leads to a prominent enhancement of the photocatalytic functionality of the thin films compared with the glass substrate. This was attributed to the effect of the substrate on the structural and electronic properties of the thin films. The substrate seemed to affect the surface roughness of a thin film, the crystallite size, and the material's electronic properties. A notable decrease in the energy band gap was reported to affect the optical and photocatalytic properties of the deposited films. The photocatalytic mechanism was discussed and analyzed based on the electron/hole production and enhanced trapping of the resulting hydroxyl ions on the surface. This work demonstrates that a clear correlation between materials engineering and their functional properties is crucial to developing thin films for different applications. Luka and Ivan reviewed different types of mid- and high-temperature absorber coatings and their fabrication methods [2]. They investigated coatings based on their solar absorptance, thermal emittance, and thermal stability. They showed that spectral selectivity of the coatings is essential for low- and mid-temperature ranges, while highly solar absorption coatings are preferred over their selective counterparts. They also demonstrated the significance of the coating fabrication to be industrially feasible.

The present work aims to investigate the photothermal conversion of a selective coating and the effect of primarily two different particles, these are ZrO_2 and Fe particles, on the solar-thermal conversion parameters. The primary paint, the heat-resistant paint (HRP), was selected due to its pigment type (manganese ferrite), its thermal stability, adhesion characteristics, and availability. Manganese ferrite is known to exhibit excellent optical properties and high solar radiation absorption. achieving efficiencies over 92% in the UV, visible, and near-infrared ranges [14, 15]. Our previous investigation of the paint showed relatively adequate but not sufficiently high conversion characteristics [16, 17]. Thus, we aimed to improve its photothermal conversion by adding micro- and nano-particles. The sought target was to enhance the absorbance by radiation trapping and multiple reflections. The Fe and ZrO_2 particles were not used as a standalone material as they do not fulfill the required photothermal properties. The other

objective was the augmentation of thermal conductivity of the paint without affecting the conversion characteristics of the primary paint. The work is based on measuring and comparing the photothermal responses after the structural and surface modifications made due to the addition of these powders. A key advantage of the proposed approach lies in the development of composite coatings that are simple to apply while maintaining high photothermal conversion efficiency. The photothermal conversion is analyzed based on the compositional, structural, and morphological features of the coatings.

2. Materials and Methods

I. Preparation of Substrates

The substrates used in the present work were cut out from 2 mm-thick aluminum sheets of moderate purity. The 4 cm × 4 cm substrates were subjected to mechanical cleaning, brushing, and degreasing to remove unwanted contaminants from their surfaces. The substrates were washed with detergents, rinsed thoroughly with deionized water, and soaked in acetone to remove grease and other contaminants. The final step of cleaning was air drying. The cleanliness of the surface and its effect on various parameters, such as adhesion of paint and other functional characteristics, is beyond the scope of the present work [18-20]. However, the cleaning procedure adopted presently is believed to maintain the minimum requirements for the successive work and measurements. It is also practically feasible and cost-effective when applied to large surfaces.

II. Application of Primary Paint

Prior to the application of coatings, the substrates were placed in the furnace to ensure their dryness. A heat-resistant black paint from Rust-Oleum Corporation (USA) was used as a primary coating layer. This paint has been utilized in similar research and proved to be compatible with a wide range of additives, allowing for their homogeneous distribution. It is also operable in low to moderate temperatures and has anti-crack characteristics, as will be shown later in this presentation [16, 17]. Table 1 exhibits some of the paint specifications. The substrates were photographed by an ordinary camera before and after being coated, as shown in Figs. 1(a)-(d).

TABLE 1. Specifications of the heat-resistant paint from Rust-Oleum (USA).

Property	Description	
Resin type	V2176838 - Silicone modified alkyd	
Pigment type	Black manganese ferrite	
Solvent	Acetone, Xylene, Toluene, and liquid petroleum gas propellant.	
Dry time at 10-32 °C and 65% relative humidity	1-2 hours	
Relative density with respect to water	0.821	
Dry heat resistance	538 °C	
Composition (%wt.)	Toluene	21 %
	Propane	17 %
	Acetone	14 %
	Black pigment	8.4 %
	Other ingredients	39.6 %

III. The Powders

Two different powders, ZrO_2 and Fe, were added individually to the high-resistant paint. The effect of these additions on solar-to-thermal conversion is compared and discussed in this work. The addition of these powders was performed by an air-spraying process. The powders were initially loaded on the spraying device. After the HRP was applied, the powders were immediately sprayed out from a distance of 30 cm or more while the substrate was slowly rotated to avoid a unidirectional fall of the particles on the substrate surface and maintain a more homogeneous distribution of the powder particles.

IV. Characterization

All the applied coatings were initially inspected visually under an optical microscope. A portable, LED-light source illuminated digital microscope (CoolingTech, 1600× magnification) was used for primary inspection of paint homogeneity. The coating thickness was

measured by means of an LS220 coating thickness gauge (Shenzhen Linshang Technology, China). This gauge provides high-accuracy measurements of coating thickness on ferrous and non-ferrous substrates. The coating thickness was determined by performing several measurements and calculating the average for each substrate. The coatings were also investigated using a scanning electron microscope (Inspect S50 SEM, FEI, Netherlands). This enables inspecting the coating morphology at a microscale or less and investigating the nature of particle integration into the composite coatings.

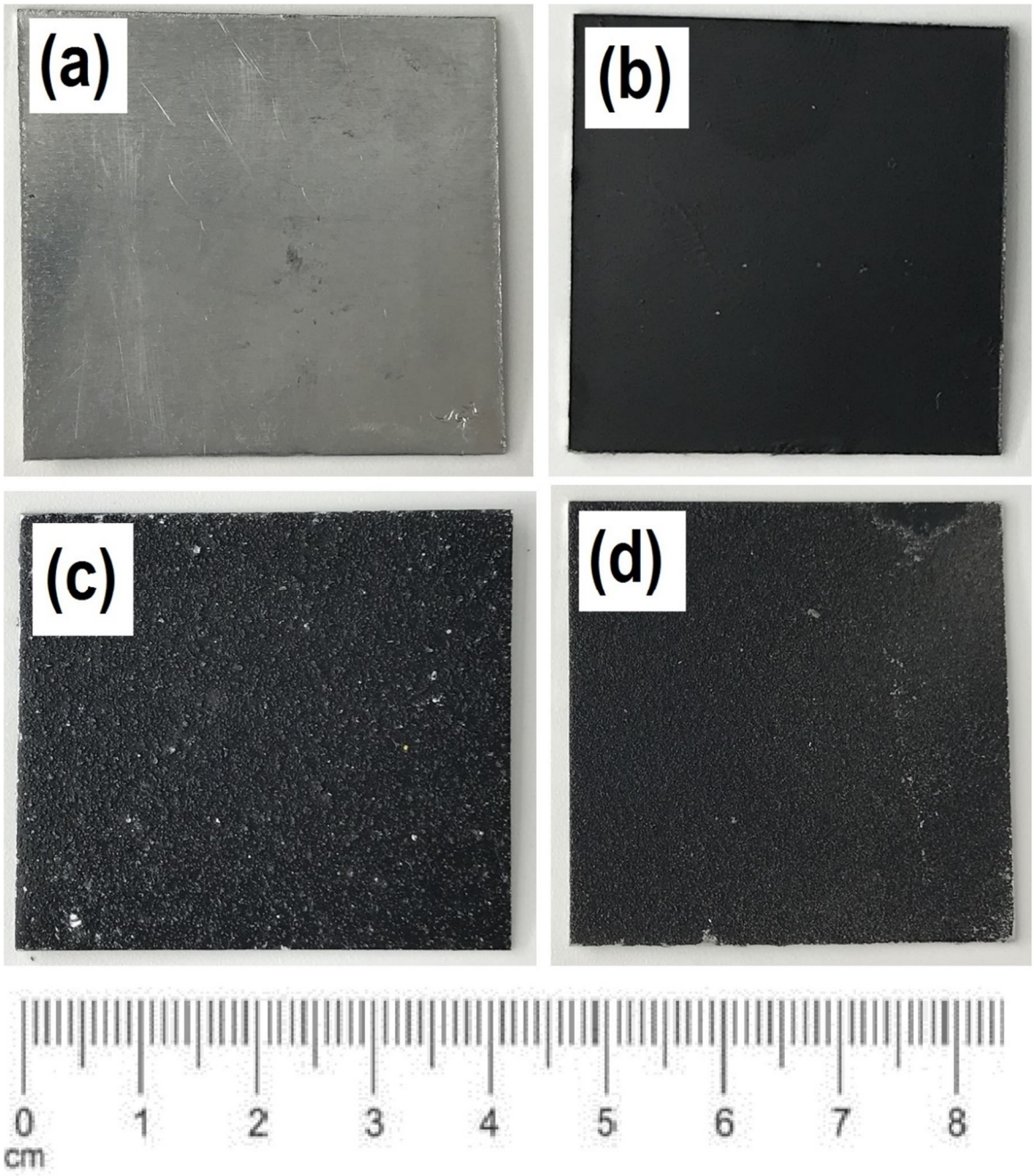

FIG. 1. The aluminum substrates as photographed by an ordinary camera: (a) uncoated substrate, (b) substrate coated with heat-resistant paint (HRP), (c) substrate coated with ZrO_2 powder sprayed over the HRP, and (d) substrate coated with Fe powder sprayed over the HRP.

The coated substrates were also subjected to elemental analysis and mapping via electron energy-dispersive spectroscopy (EDS). This was accomplished using the XFlash-6l10 detector (Bruker Company) attached to the scanning electron microscope. The detector used is advantageous in providing an outstanding resolution of 38 – 121 eV and high pulse load capability. With this detector, low concentrations can be detected with a high degree of relative

precision of 2-4% over a relatively large area (for further details, see Ref. [21]). To compare the coatings and analyze their solar-to-thermal conversion response, UV-Vis spectroscopy was utilized. Comparison of UV-Vis spectra provides valuable insight into the effect of the coating components on their functionality as selective coatings. It also shows the regions where the absorbance of the incident radiation is taking place. By comparing multiple spectra, the degree of radiation absorption at a certain wavelength may further be investigated with the variation of the coating composition (spectral absorbance).

V. Measurements and Test

The solar-to-thermal conversion of the as-prepared coatings was verified by exposing the substrates to radiation and measuring their temperature with time. Each substrate was placed inside a solar collector, as shown in Fig. 2. The solar collector was made of thermally insulating material. The incident radiation passed through the transparent glass window to the substrate. A thermocouple probe attached to a GM1312 digital thermometer (Benetech, Shenzhen Jumaoyuan Science and Technology Co., Ltd., China) was used to measure the substrate temperature. Temperature measurement was performed every 60 seconds, starting from the substrate exposure to radiation until a constant temperature was reached. Two sources of radiation were used in the present work: solar radiation and an artificial source of radiation from a tungsten hot-filament bulb. In the case of an artificial source of radiation, the source-to-collector distance was adjusted such that the total incident irradiance was comparable to that of the solar radiation.

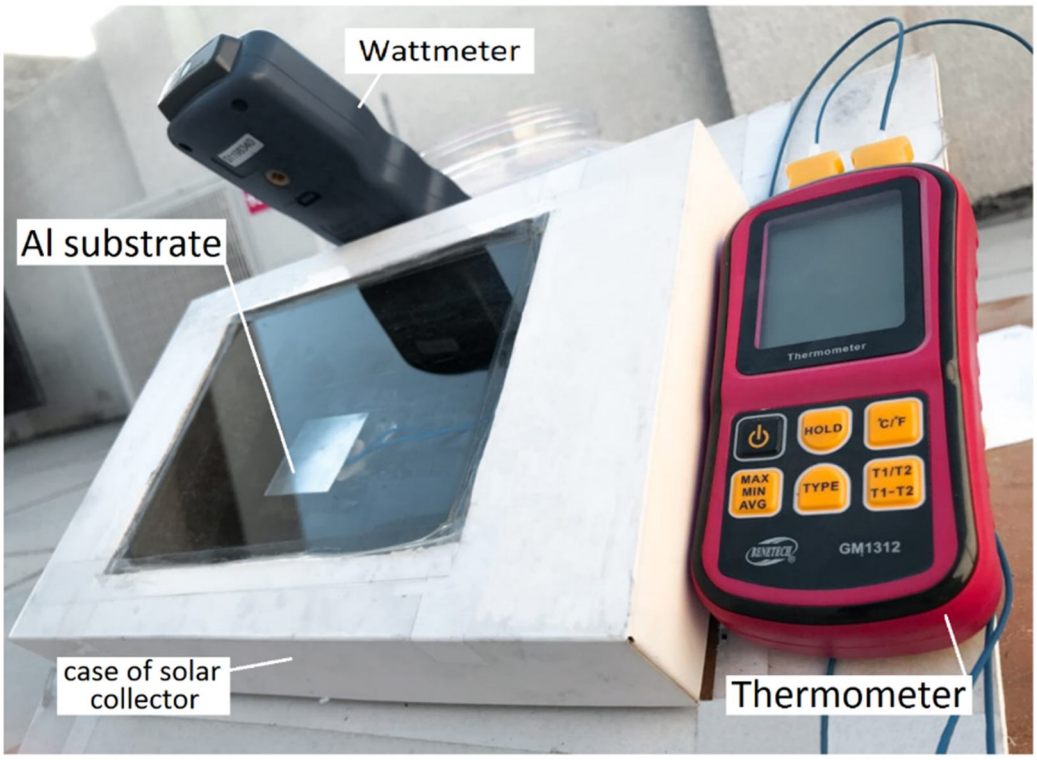

FIG. 2. The solar collector setup used to measure photothermal conversion.

The total reflection of the incident radiation was measured via a homemade pyrheliometer-like setup, as shown in Fig. 3. The device setup allowed measuring the total reflected radiation relative to the incident radiation after excluding the diffused radiation. An SM206-SOLAR digital solar-power meter (Hangzhou Yucheng Industrial Co., Ltd., China) was used to measure irradiance. During the measurement of the total reflectance, the tube was oriented such that the incident radiation formed an angle of 45° with respect to the substrate plane. This guaranteed that most of the reflected radiation was incident perpendicularly on the power meter detector. Comparison of the total reflectance from the substrates can directly be associated with the UV-Vis spectra. The total reflectance is useful in the explanation of the behavior of the solar-to-thermal conversion of the coated substrates.

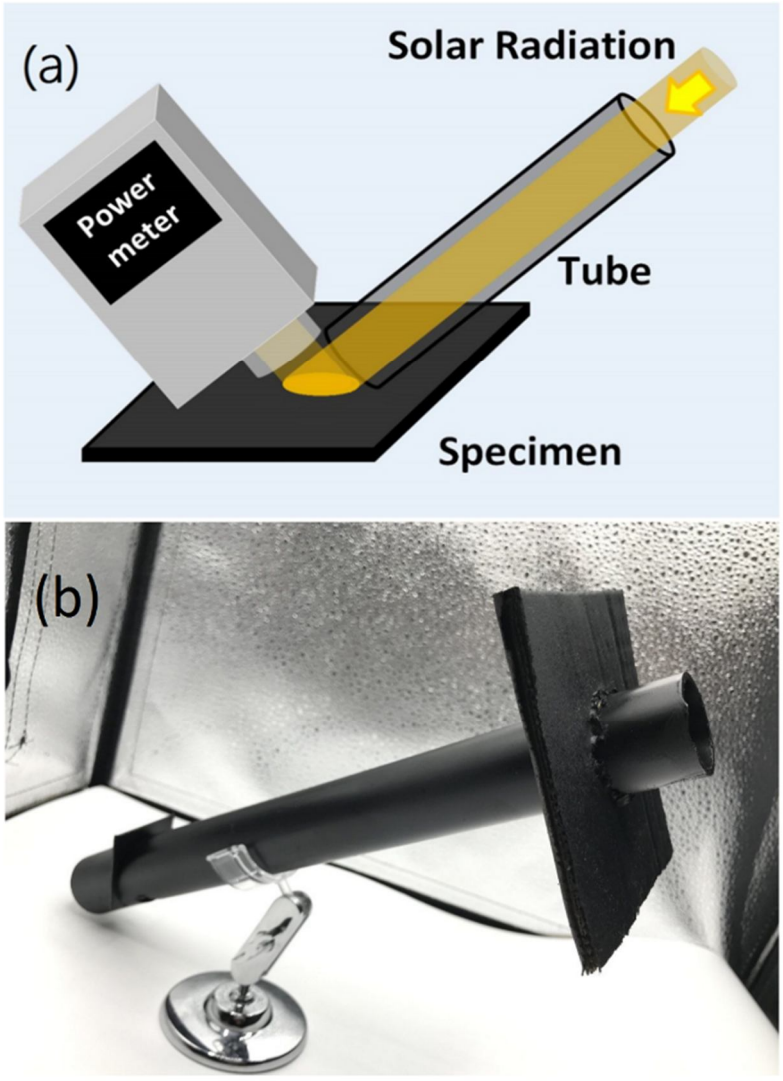

FIG. 3. Homemade pyrheliometer-like setup used to measure the total reflection of incident radiation from the substrate surface: (a) schematic diagram showing the paths of incident and reflected beams of the solar radiation; (b) the experimental setup.

3. Results and Discussion

Figure 4 shows the as-coated substrates under an optical microscope. Primary inspection of the uncoated substrate shows the presence of longitudinal and unidirectional grooves resulting from the brush cleaning performed on the substrate. These grooves became less visible as being filled with the primary coating (the HRP). This ensures the required adhesion of the primary coating on the Al substrate. The addition of the powders on the top of the primary coating is evident in Figs. 4 (c) and 4(d). Comparison of these images shows that the ZrO_2 particles are less homogeneously distributed on the surface of the substrate. The ZrO_2 particles (or their agglomerates) are larger than the Fe particles, as was primarily observed in the photographed substrates (Fig. 1). The distribution feature of the particles is believed to be a direct result of the spraying process adopted in the present work: smaller particles are more easily dispersed uniformly over the substrate surface. Consequently, the Fe particles exhibited better dispersion and more uniform coverage than the ZrO_2 particles.

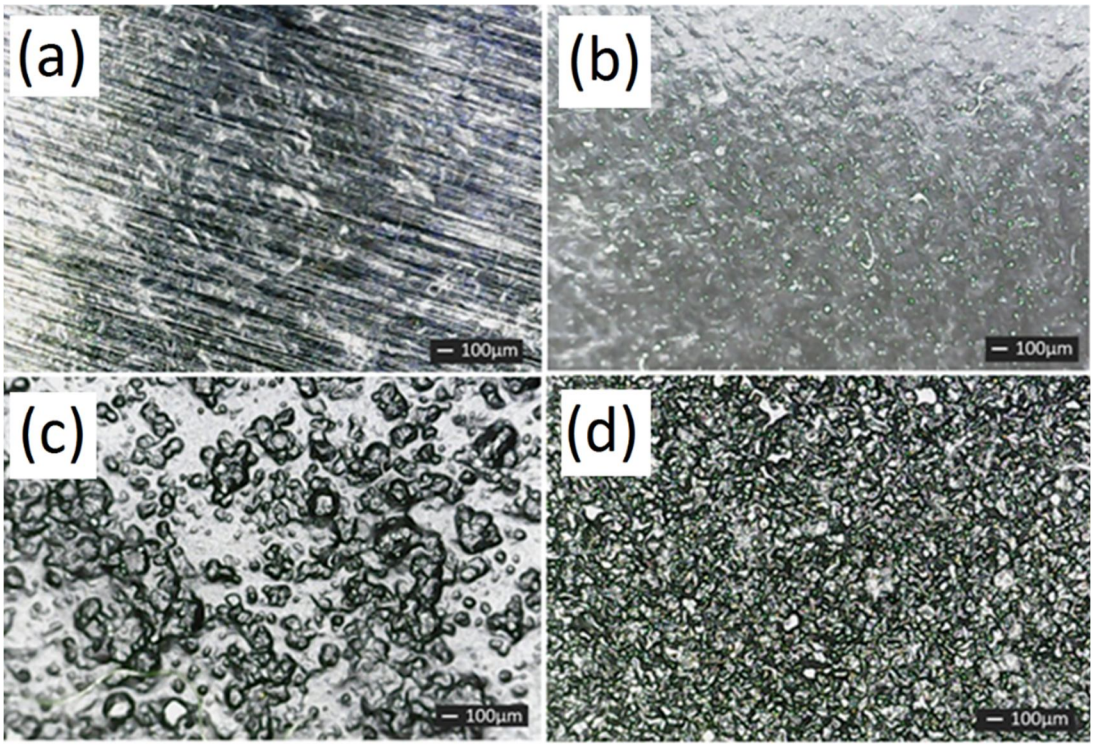

FIG. 4. The substrates under the optical microscope: (a) uncoated, (b) coated with HRP, (c) coated with ZrO_2/HRP, and (d) coated with Fe/HRP.

Table 2 summarizes the average coating thicknesses obtained from multiple measurements, along with the coating masses measured using a coating thickness gauge and a high-accuracy digital balance. The gross density of the coating layer was determined, in addition to its volume and weight. These specifications will be associated with the coatings' photothermal conversion characteristics at the end of this discussion. It is clear that adding ZrO_2 and Fe particles increased the coating thickness and mass and decreased the coating density. This is attributed to the increase in surface roughness due to the partial submerging of particles in the primary coating.

TABLE 2. Coatings thicknesses and densities.

Coating	Coating thickness (μm)	Coatings mass (g)	Coating Density (g/cm^3)
HRP	41	0.11	1.67
ZrO_2/HRP	323.5	0.16	0.31
Fe/HRP	837	0.67	0.50

A further inspection of the coating morphology and particle distribution was performed using scanning electron microscopy. The SEM images of the ZrO_2/HRP and the Fe/HRP are shown in Fig. 5. The former composite coating exhibited agglomeration of the ZrO_2 particles. The high-magnification image showed the presence of sub-micro and nanoparticles diffused in the HRP. The Fe/HRP coating exhibited a denser distribution of the Fe particles, which also showed a high degree of agglomeration. The HRP was highly occupied with the Fe agglomerates, submerged partially in the primary coating. Closer inspection of the powders revealed the presence of boundaries between agglomerated grains, indicating that the actual sizes of these grains were in the sub-micro and nanoscale. These microstructural features were expected to play a significant role in the functional performance of the coatings. The particles were anticipated to act as absorption centers for incident electromagnetic radiation, while the interparticle spaces and voids could serve as radiation-trapping sites. Such effects were expected to enhance solar absorption through scattering and multiple internal reflections [22]. The higher particle density observed in the Fe/HRP coating compared with the ZrO_2/HRP coating was a direct consequence of the coating process, as reflected in the increased thickness and mass of the Fe-containing coating layer (Table 2).

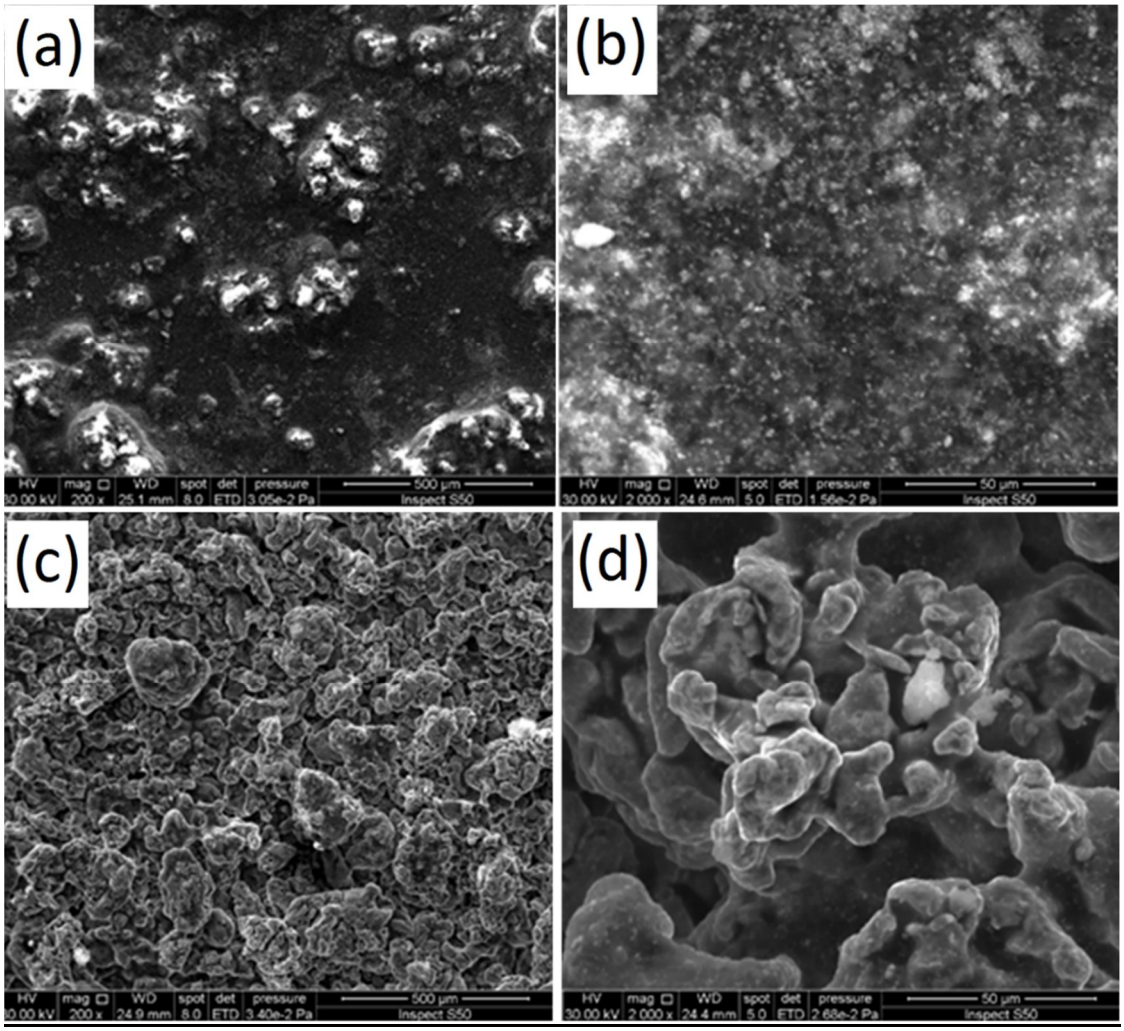

FIG. 5. Low- and high-magnification scanning electron micrographs of the substrates: (a), (b) as coated with the ZrO_2/HRP, and (c), (d) as coated with the Fe/HRP. High-magnification images show that particles are submerged in the HRP.

The elemental analysis results emphasized the distribution nature of these particles. The EDS spectra and the elemental mapping images of the ZrO_2 and Fe particles are shown in Figs. 6 and 7, respectively. The presence of Zr and Fe in their respective substrates can easily be observed. The elemental mapping emphasized that the Fe density distribution was much higher than that of Zr. These results agree with the earlier inspection made under optical and scanning electron microscopes. As for the remaining elements detected (such as carbon and chromium), these are due to the constituting materials of the heat-resistant paint used in the present work and the impurities present at the surface of the substrates.

The photothermal conversion of the as-prepared coatings was examined using the solar and artificial radiation sources. Figure 8 shows the variation of substrate temperature with the duration of exposure to the radiation. The photothermal conversion graphs show that the substrate temperature increased rapidly starting from the room-temperature value with radiation exposure. Initially, the temperature rose rapidly due to radiation conversion into thermal energy and the substrate's low rate of energy loss. After approximately 10 minutes of exposure to radiation, the rate of temperature increase of the substrate decreased, and the solar-to-thermal conversion curve gradually flattened. The substrate temperature reached a maximum and constant value after 35 minutes of radiation exposure. At this point, the rate of solar-to-thermal conversion became equal to the rate at which the substrate lost energy. The uncoated substrate exhibited the lowest temperature due to the low coefficient of absorption of the uncoated surface. The Fe/HRP-coated substrate showed the highest temperature of 382.65 K after 40 minutes of radiation exposure. This was due to

the high coefficient of absorption of the composite coating, which improved the photothermal conversion. In addition, the morphological and surface features (roughness as observed under the scanning electron microscope and reduced density as discussed earlier in this section) are believed to play a crucial role in improving the conversion efficiency via trapping of incident light and its absorption by scattering and multiple reflections (see Ref. [8]). Based on that, future work will attempt to investigate the effect of surface gap density on photothermal conversion efficiency. The quantification of such an effect is believed to provide an effective means to advance selective coatings. As mentioned earlier, the enhancement of the photothermal conversion of ZrO_2/HRP and Fe/HRP may involve different mechanisms. Presently, the results were analyzed by comparing the elemental, compositional, and structural features of the coating in addition to comparing the absorption spectra in the UV-Vis wavelengths, as shown below.

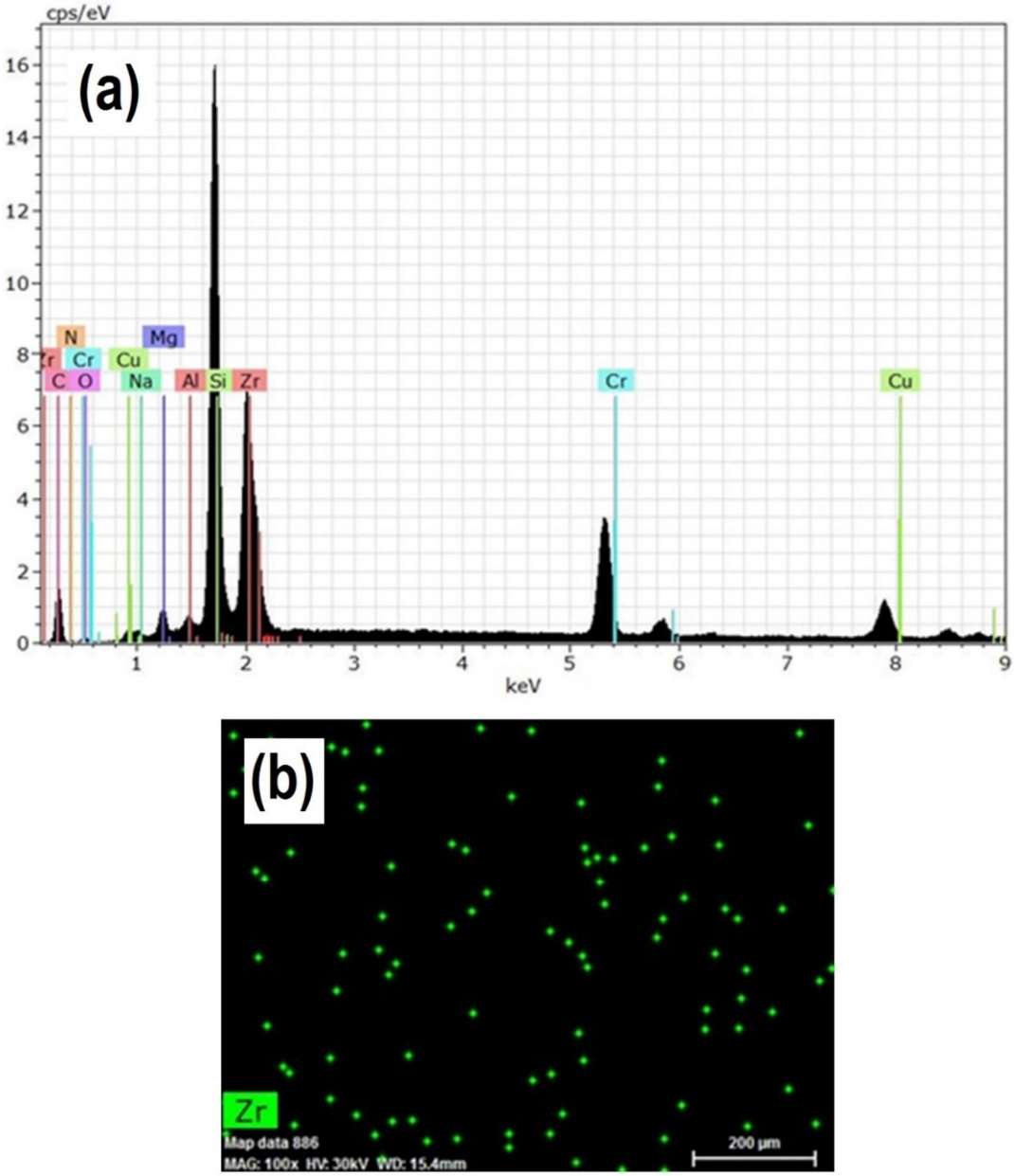

FIG. 6. (a) EDS spectrum and (b) elemental mapping image of the ZrO_2/HRP coating.

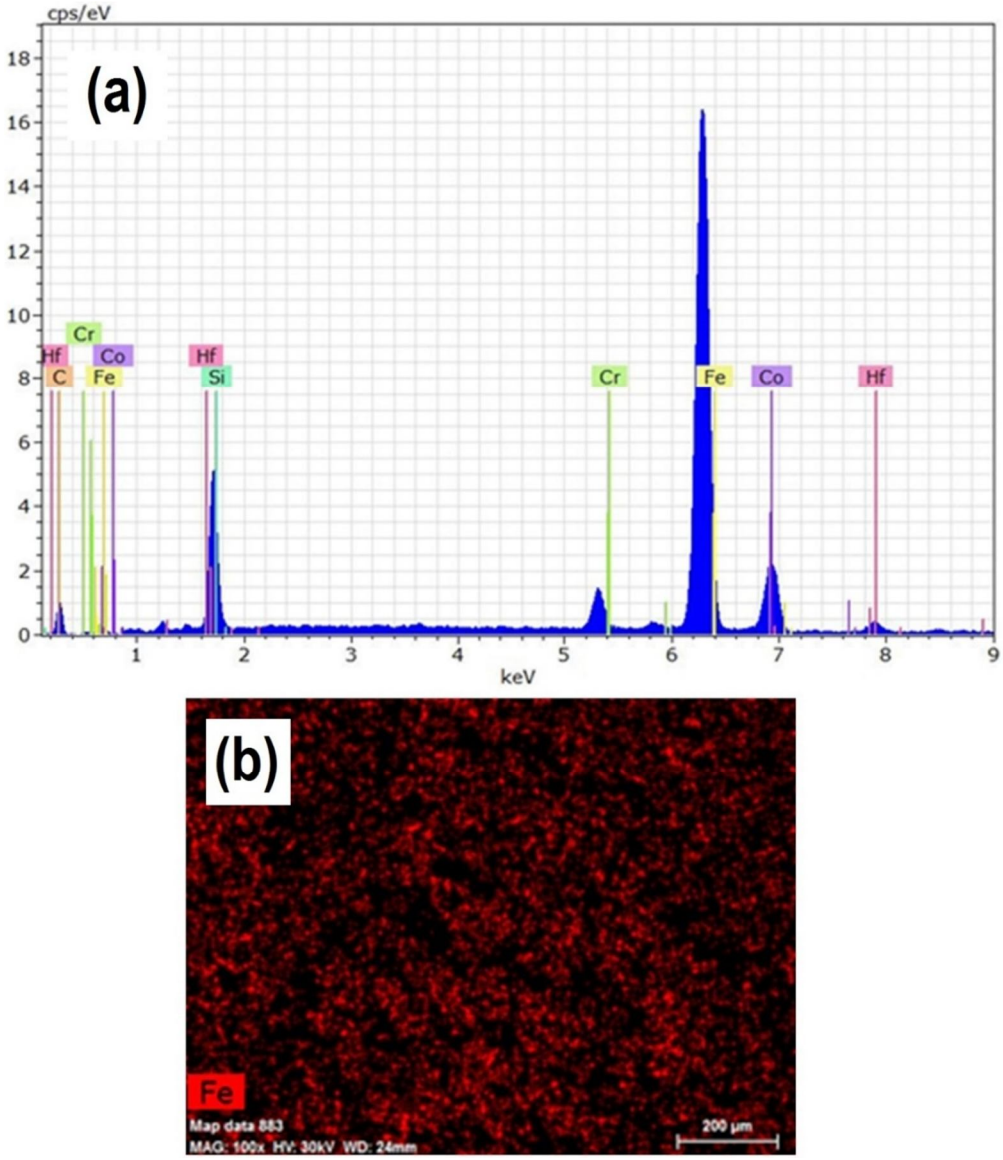

FIG. 7. (a) EDS spectrum and (b) elemental mapping image of the Fe/HRP coating.

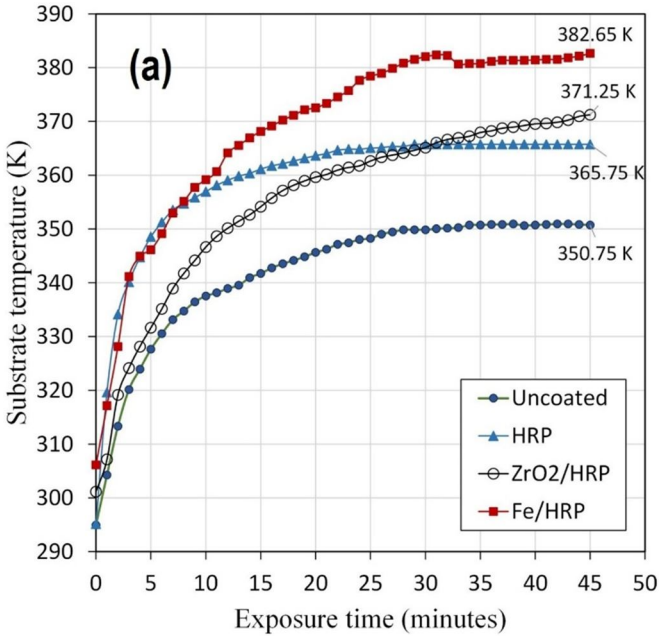

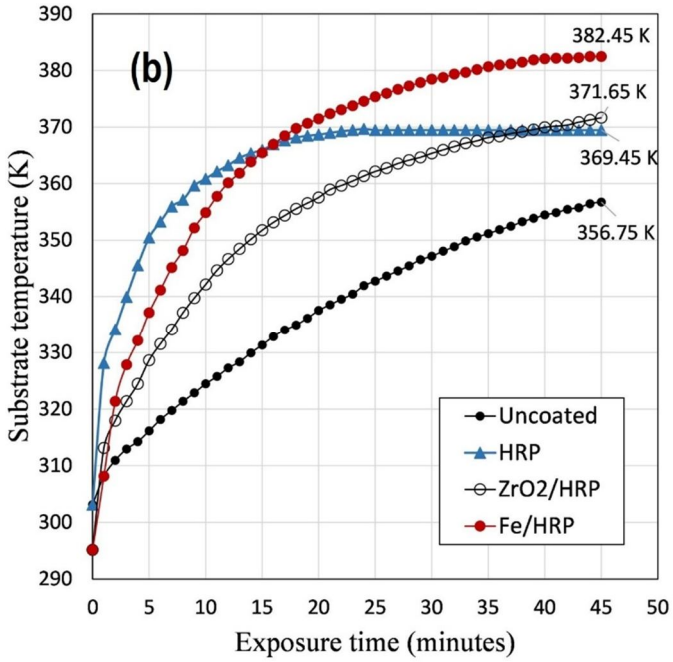

FIG. 8. Photothermal conversion curves of the substrates: (a) exposure to solar radiation and (b) exposure to an artificial source of radiation (hot filament bulb).

As far as we know, the substrate temperature reported presently is the highest for a flat-plate collector setup. Table 3 shows a comparison of the maximum temperature achieved for flat-plate collectors with different composite coatings.

TABLE 3. Comparison of the substrate maximum temperatures for different coatings.

Coating Type	Irradiance (W/m^2)	$T_{substrate}\,(K)$	Reference
Fe/HRP	1130	382.65	Present work
ZrO_2/HRP	1074	371.25	Present work
CNT-CuO NPs dispersed in black paint	964	357.45	[23]
CuO NPs mixed with black paint	1100	370.15	[11]
NiAl alloy embedded in black paint	1000	342.85	[24]

To shed more light on the thermal conversion characteristic of the coatings, UV-Vis spectra were measured for the composite coatings. The absorption spectra of the ZrO_2/HRP and Fe/HRP coatings are shown in Figs. 9(a) and 9(b), respectively. Both spectra showed absorption peaks at 314 nm, 437 nm, 471 nm, and 495 nm. The absorption bands in the wavelength 314 nm might be attributed to the $n \rightarrow \pi^*$ transition due to promoting a non-bonding electron to an anti-bonding π^* orbital [25]. This transition was attributed to the presence of C = O bonds in acetone and xylene in the heat-resistant paint (see Table 1). The absorption peak at 437 nm was attributed to conjugated planar ring structures with delocalized π-electron systems involving alternating single and double bonds, primarily associated with the toluene component of the base paint. The absorption peaks at 471 and 495 nm were attributed to pigments and dyes used in the paint formulation [26, 27]. Accordingly, the ZrO_2/HRP and Fe/HRP composite coatings exhibited identical UV-Vis spectra in the visible wavelengths and differed in the near-infrared regions, signifying the higher contribution of molecular vibrations as compared with the electronic transitions in the overall absorption of radiation. This implies that the mechanism involved in the enhancement of the photo-thermal conversion depends largely on trapping and multiple reflections of radiation near the coating surface due to the morphological complexity produced by the addition of the ZrO2 and Fe particles. Inspection of the SEM images (Fig. 5) supported this interpretation, as the Fe/HRP coating exhibited a higher surface roughness than the ZrO_2/HRP coating.

Comparison of the UV–Vis spectra further showed that the area under the absorption curve, which represents the total absorbed radiation, was larger for the Fe/HRP composite coating. To

validate this observation, the total absorbance of the substrates was determined from total reflectance measurements performed using the pyrheliometer-like setup. Table 4 lists the absorbance values for the four substrates investigated. The calculations showed that the Fe/HRP-coated substrate absorbed 97.81% of the total incident radiation, which was the highest among all coatings studied. This high absorbance was consistent with the elevated substrate temperature of 382.65 K observed during photothermal conversion measurements (Fig. 8).

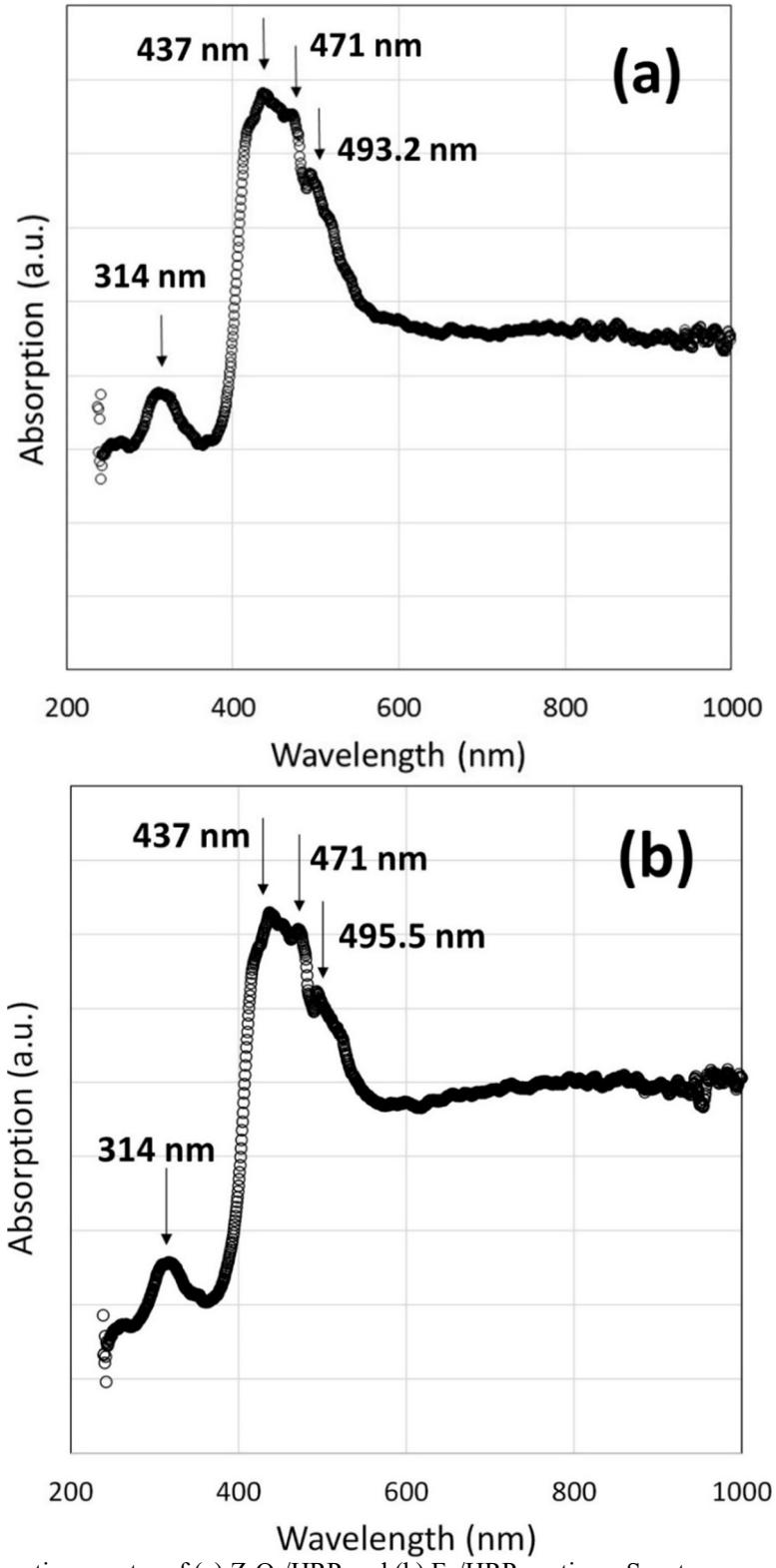

FIG. 9. UV-Vis absorption spectra of (a) ZrO_2/HRP and (b) Fe/HRP coatings. Spectra were determined from the reflection spectra measured experimentally.

TABLE 4. Absorbance of the uncoated and coated substrates, determined using the pyrheliometer-like setup.

Coating	Irradiance (W/m^2)	Total Reflected Intensity (W/m^2)	Absorbance (%)
Uncoated Al-substrate	1186	760	35.91
HRP	1186	67	94.32
ZrO_2/HRP	1188	43	96.38
Fe/HRP	1145	25	97.81

4. Conclusions

In this work, the photothermal conversion characteristics of a selective coating designed for flat-plate collector applications were investigated. ZrO_2 and Fe particles were incorporated into a heat-resistant paint (HRP) to enhance its solar-to-thermal conversion performance. The coating thicknesses were 323.5 and 837 μm for the ZrO_2/HRP and Fe/HRP coatings, respectively. The addition of ZrO_2 and Fe particles led to a decrease in coating density from 1.67 g/cm^3 to 0.31 and 0.5 g/cm^3 for the ZrO_2//HRP and Fe/HRP coatings, respectively. The solar-to-thermal conversion of the coatings was successfully improved due to the addition of these particles. A maximum absorbance of 97.81% of the incident radiation was achieved using the Fe/HRP composite coating. The maximum substrate temperature of the flat-plate collector setup was 382.65 K after 40 minutes of exposure to solar radiation. The high photothermal conversion characteristics and the ease of preparation and application of the Fe/HRP coating make it superior to other coating systems with varying structural, compositional, and morphological properties.

Declaration of interests

The authors declare that they have no known competing financial interests or personal relationships that could have appeared to influence the work reported in this paper.

Data availability

Data will be made available on request.

References

[1] Omer, K.A., Sameer, A., Raid, W.D., Hawazen, N.S., and Enas, F.A., Int. J. Renew. Ene. Dev., 12 (1) (2022) 166.

[2] Noc, L., Jerman, I., Sol. Energy Mater. Sol. Cells, 238 (2022) 111625.

[3] Gao, M., Zhu, L., Peh, C.K., and Ho, G.W., Energy Environ. Sci., 12 (2019) 841.

[4] Bhowmik, H. and Amin, R., Energy Rep., 3 (2017) 119.

[5] Vikas, Kumar, R., and Soni, S., Beilstein J. Nanotechnol., 14 (2023) 205.

[6] El-Mahallawy, N., Atia, M.R.A., Khaled, A., and Shoeib, M., Mater. Res. Express, 5 (2018) 046402.

[7] Wasim, M., M.Sc., Thesis, University of Eastern Finland, Faculty of Science and Forestry, (2024).

[8] Cheng, P., Wang, D., and Schaaf, P., Adv. Sust. Syst., 6 (2022) 2200115.

[9] Rubin, E.B., Chen, Y., and Chen, R., Solar Energy Mater. Sol. Cells, 195 (2019) 81.

[10] Atchuta, S.R., Sakthivel, S., and Barshilia, H.C., Sol. Energy Mater. Sol. Cells, 200 (2019) 109917.

[11] Sivakumar, S., Velmurugan, C., Ebenezer Jacob Dhas, D.S., Brusly Solomon, A., and Leo Dev Wins, K., Renew. Energy, 155 (2020) 1165e1172.

[12] Zerouali, M., Bouras, D., Daïra, R., Fellah, M., Boudjema, B., Barille, R., Sakherf, E., Bellucci, S., and El-Hiti, G.A., Ceram. Int., 51 (2025) 473.

[13] Bouras, D., Fellah, M., Barille, R., Zerouali, M., Hambli, N., and El-Hiti, G.A., Inorg. Chem. Commun., 171 (2025) 113561.

[14] Sadia, A., Ifra, S., Farzana, M., Ismat, B., Ijaz-ul-Mohsin, Kashif, J., Yassine, S., and Munawar, I., Z. Phys. Chem., 2020 (2020) 1.

[15] Elangbam, C.D. and Ibetombi, S., Adv. Mater. Process., 2 (2) (2017) 93.

[16] Jasim, R.H. and Al-Tabbakh, A.A., Jordan J. Phys., 15 (3) (2022) 323.

[17] Jasim, R.H., Al-Tabbakh, A.A., and Hasan, S.M., Al-Nahrain J. Sci., 24 (1) (2021) 24.

[18] Kohli, R., Develop. Surf. Cont. Clean., 2015 (2015) 71.

[19] Petersson, L., Meier, P., Kornmann, X., and Hillborg, H., J. Phys.: Appl. Phys., 44 (3) (2011) 34011.

[20] Kadlečková, M., Minařík, A., Smolka, P., Mráček, A., Wrzecionko, E., Novák, L., Musilová, L., and Gajdošík, R., Mater. (Basel), 12 (1) (2018) 109.

[21] https://www.bruker.com/en/landingpages/bna/technology/what-is-eds.html.

[22] Xie, Z., Wang, H., Li, M., Tian, Y., Deng, Q., Chen, R., Zhu, X., and Liao, Q., Chem. Eng. J., 435 (3) (2022) 135025.

[23] Abdelkader, T.K., Zhang, Y., Gaballah, E.S., Wang, S., Wan, Q., and Fan, Q., J. Clean. Prod., 2019 (2019) 119501.

[24] Al-Shamaileh, E., Sol. Energy, 84 (9) (2010) 1637.

[25] https://chem.libretexts.org.

[26] Tomovska, R., Agirre, A., Veloso, A., and Leiza, J.R., "Reference Module in Chemistry, Molecular Sciences and Chemical Engineering", (Elsevier, 2014).

[27] Masahiko, T. and Jonathan S.L., Digit. Discov., 4 (2025) 21.

Volume 18, Number 5, 2025. pp. 643-658

Jordan Journal of Physics

ARTICLE

Hadron Therapy with Nanoparticles for Dose Enhancement and Estimation of DNA Damage Using GEANT4

Fatemeh Habibi[a], **Zohreh Parang**[a], **S N Hosseinimotlagh**[a] and **Alireza Keshavarz**[b]

[a] *Department of Physics, Shi.C., Islamic Azad University, Shiraz, Iran.*
[b] *Department of Physics, Shiraz University of Technology, Shiraz, Iran.*

Doi: **https://doi.org/10.47011/18.5.7**

Received on: 02/11/2024; *Accepted on: 20/01/2025*

Abstract: Proton therapy is one of the most promising treatments for several types of tumors, such as those of the eye, brain, and breast, as it benefits from a sharp Bragg peak as well as a spread-out Bragg peak (SOBP) in the tumor region. The Bragg peak helps to deliver the maximum dose to the tumor and the minimum dose to the sensitive organs near the tumor. It has been shown that the addition of nanoparticles to the tumor can improve the treatment gain in radiation therapy. In this study, the microscopic dose enhancement ratio as well as the DNA damage frequency caused by 62.8 MeV protons with the presence of 3000 ppm (i.e., 30 mg/g) Au, Pt, C, ^{11}B, and Fe_3O_4 nanoparticles were investigated using the Geant4-DNA Monte Carlo toolkit. In addition, the cell survival curves were obtained and compared for the condition with and without nanoparticles. All simulations were performed at different locations along the proton range: at the beginning, in the middle, and at the end of the SOBP. The highest dose enhancement in the fibroblast cell was observed for Pt nanoparticles (up to 4%), followed by Au nanoparticles (up to 2.4%), while the lowest dose enhancement was observed for C nanoparticles (up to 0.32%). At the end of the proton range, higher levels of DNA damage were observed than at the beginning of the path and at the center of the SOBP. Unlike some previous studies, this work simulated more realistic clinical conditions, and the obtained results are in good agreement with some experimental results reported in the literature. In conclusion, the combination of Au and Pt nanoparticles with proton therapy has a superiority over C, ^{11}B, and Fe_3O_4 nanoparticles.

Keywords: Hadron therapy, Dose, Nanoparticles, DNA damage, Geant4-DNA.

1. Introduction

Proton therapy is used to treat some common cancerous tumors (such as those of the eye, brain, and lung) with promising clinical outcomes, although it is not yet widespread worldwide [1]. Proton is an interesting radiation source for cancer treatment. At the beginning of its path, a proton leaves relatively low energy in a human phantom, while they deposit the highest amount of energy at the end of its range. This results in the Bragg peak, which is obtained at the end of the proton range when the deposited dose is plotted versus range [2]. The consequence is the delivery of a maximum dose to the tumor with good sparing of sensitive organs and tissues near the tumor. This advantage is not present in conventional X-ray and gamma radiation therapy. It has been shown that gold nanoparticles (Au NPs) can be used to increase the tumor dose in radiation therapy [3-5]. In an in vitro study, Smith et al. [6] showed that the Au NP dose enhancement resulting from a spread-out Bragg peak (SOBP) of 150 MeV protons is less than 5%, which is within experimental uncertainties. Sisin *et al*. [7] measured an Au NP dose enhancement of about 9% (±3%) for 150 MeV proton irradiation using EBT3 radiochromic films. Studies have also been conducted in the field of radiobiology for

Corresponding Author: S N Hosseinimotlagh **Email**: nasrinhosseini_motlagh@iau.ir

proton therapy, one of whose goals is to calculate the relative biological effectiveness (RBE) for protons with different linear energy transfer (LET). Another goal of such studies is to calculate the number and spatial distribution of DNA double-strand breaks (DSBs) caused by protons and then to model cell repair mechanisms and obtain cell survival curves. In general, it has been demonstrated that, from a radiobiological standpoint, proton therapy is more effective in the presence of Au NPs in the tumor [8-14]. Considering laboratory limitations and the lack of easy access to proton therapy facilities, Monte Carlo (MC) simulations have greatly assisted researchers and physicists in dosimetry calculations and treatment planning. Numerous simulation studies have been conducted on Au NP dose enhancement in proton therapy. Some studies have been performed at a macroscopic scale (i.e., the tumor scale), while others have focused on a microscopic scale (i.e., the cellular and DNA scales) [15-21]. Heuskin *et al*. [22] showed that low-energy protons, on the order of 1.3 MeV, can generate up to 32% more secondary electrons around a single Au NP than in the absence of the Au NP. However, they did not report a significant dose enhancement for a mammalian cell model containing a large number of Au NPs. Furthermore, some studies have investigated the effects of Au NP size and distribution on the dose enhancement factor (DEF) in proton therapy [18, 23]. An important point is that, more recently, nanoparticles other than Au, such as superparamagnetic iron oxide (Fe_3O_4),^{11}B, C, Pt, Ag, and Bi NPs, have been investigated for proton therapy [24-28]. Although many interesting simulation studies have been carried out so far, there is an evident discrepancy among some results, which can be attributed to differences in the definition and distribution of Au NPs. In addition, the definition of the proton beam is also important and varies among the relevant studies. In many articles, the proton beam is defined without an accelerator as a monoenergetic radiation source, which differs from the clinical situation, where an SOBP is used to cover the entire tumor. For MC simulations at the microscopic scale, the radiation source has been defined either in the conventional manner (i.e., primary protons) or as a phase space (PS), representing the emission of secondary particles at specific points along the proton range, particularly at the Bragg peak location. One of the problems in some previous simulation studies was that they limited the transport of primary protons to a single NP, such that the incident protons were emitted from the inner surface of an NP and terminated at the opposite surface. This type of source definition appears to suffer from a lack of charged particle equilibrium. A more appropriate approach is to simulate a cell nucleus and consider nanoparticles in large numbers, which has the advantage of allowing the use of a specific mass concentration for nanoparticles (in mg/g or ppm).

Multiscale MC simulations (i.e., simulations at both macroscopic and microscopic scales) have attracted considerable interest in numerous studies [29-34]. Since there is a lack of data in the literature comparing these different simulation models, the present study aims to calculate the microscopic DEF for a therapeutic SOBP proton beam (62.8 MeV) using a multiscale MC simulation. The 62.8 MeV proton beam was chosen because it is a common therapeutic energy for the treatment of ocular tumors [35]. At the macroscopic stage, a phase space (PS) was defined in the middle of the SOBP, and information on the generated secondary particles, along with the primary protons, was stored. These particles were then used as the primary radiation source at the microscopic stage. At the microscopic stage, after defining a mammalian fibroblast cell, various nanoparticles (Au, Pt, C, ^{11}B, and Fe_3O_4) with a concentration of 30 mg/g were randomly implanted in the cytoplasm of the cell [17]. In addition to calculating the DEF induced by nanoparticles in proton therapy, the resulting DNA damage was calculated and compared for the different nanoparticles. Since cancer cell death is ultimately related to radiation-induced DNA damage, cell survival curves were plotted for SOBP irradiation with and without the presence of Au, Pt, C, ^{11}B, and Fe_3O_4 nanoparticles, using a mathematical model of survival and repair implemented in the Geant4-DNA code.

2. Material and Methods

2.1. Simulation Code, Physics, and Chemistry

In this study, the Geant4.11.1.3 MC simulation toolkit [36] with the QGSP_BIC reference physics list was used to obtain the PS

file in a large water phantom. The QGSP_BIC reference physics list has been introduced as an appropriate physics list for proton and hadron therapy simulations [37, 38]. It includes hadronic physics for elastic and inelastic nuclear interactions (i.e., the G4HadronElasticPhysics and G4HadronPhysicsQGSP_BIC classes), electromagnetic standard physics (i.e., the G4EmStandardPhysics class), decay physics (i.e., the G4DecayPhysics class), and other physics related to ions, neutrons, etc. (i.e., the G4EmExtraPhysics, G4StoppingPhysics, G4IonElasticPhysics, G4IonPhysics, and G4NeutronTrackingCut classes). For details on reference physics lists, see [39].

The Geant4-DNA extension [40] was used for the cell-scale simulation for microscopic DEF calculations. It is based on a track-structure algorithm and provides a high accuracy in macroscopic scale simulations. The Geant4-DNA extension includes physics data for the interactions of electrons up to 1 MeV and protons up to 300 MeV energy in liquid water [41-43]. We used the G4EmDNAPhysics_option4 class, which is a recommended class for DNA damage calculations. A detailed overview of the physics models implemented in the Geant4-DNA code for different particles and energy ranges can be found in Refs. [42, 44, 45]. The range cut for the production of secondary particles was set to 1 μm in the phantom (i.e., at the macroscopic stage) and 0.001 μm in the cell (i.e., at the microscopic stage). One of the advantages of the Geant4-DNA code is its capability to model the production, diffusion, and interaction of chemical species (i.e., free radicals) following water radiolysis [46, 47]. In this study, the updated "G4EmDNAChemistry_option3" chemistry constructor, embedded in version 11.1 of the Geant4-DNA code, was used to simulate the pre-chemical and chemical stages. This constructor is based on the synchronous Independent Reaction Times algorithm and includes the most common free radicals, along with their chemical interactions, reaction radii, and reaction rates [48]. For more details on the Independent Reaction Times algorithm, the reader is referred to [48-50]. This capability was used to calculate the indirect DNA damage caused by hydroxyl radicals following water radiolysis, resulting from proton interactions both with and without the presence of various nanoparticles in the cell. The simulation time for the chemical stage was set to 2.5 ns, following the study of Meylan *et al.* [51].

2.2. Cell Modelling and NPs

The cell geometry was defined using the *molecularDNA* example [52] of the Geant4 Monte Carlo toolkit. This model is based on the Hilbert curve, which is a continuous fractal space-filling curve [53]. The fractal geometry is constructed such that a small segment of DNA is continuously repeated in three dimensions in a specific arrangement without overlap. The full DNA chain consists of three types of base voxels: straight, turned, and turned with a 90° twist, and includes histone proteins. The smallest unit of DNA is a base pair (bp), also referred to as a nucleotide pair. Six spheres were modeled as DNA molecules and assembled to construct a nucleotide pair: two bases, two phosphates, and two sugars. Each nucleotide consists of three volumes: 2-deoxyribose, phosphoric acid, and a base, namely adenine ($C_5H_5N_5$), thymine ($C_5H_6N_2O_2$), cytosine ($C_4H_5N_3O$), or guanine ($C_5H_5N_5O$). The histone protein was modeled as a cylinder with a radius of 3.75 nm and a height of 5.75 nm. A histone surrounded by a 216 bp-long DNA helical segment forms a nucleosome. The continuous DNA chain has a total length of 6.4GbP. An ellipsoidal mask was created to confine the DNA chain within an ellipsoidal volume with dimensions of 14.2 × 5.0 × 14.2 μm^3. The effective nucleus density is approximately 0.015 bp per nm^3. Detailed descriptions of the geometrical levels are provided in the relevant publications [54-55]. The nucleus cell geometry is illustrated in Fig. 1. The DNA molecules are not shown in Fig. 1, and the scale of the histones is larger than the actual scale. For visualization purposes, a small number of histones are displayed in Fig. 1. Moreover, eight base boxes with a side length of 75 nm, including straight, turned, and turned-twisted sections, as well as a zoomed-in view of a single histone, are illustrated in Fig. 1.

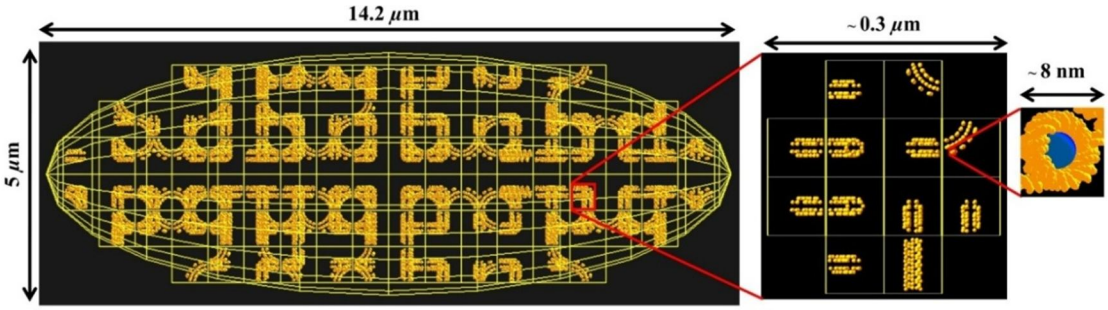

FIG. 1. The nucleus cell geometry taken from the "molecular DNA" example of the Geant4 toolkit.

To define NPs in the cell, an ellipsoid shell of water with a thickness of 1 μm was defined as the cytoplasm around the cell nucleus. So, the whole cell dimensions were 15.2 × 6.0 × 15.2 μm^3 (See Fig. 3). Au, Pt, C, ^{11}B, and Fe_3O_4 NPs, with a radius of 25 nm and a concentration of 30 mg/g (i.e., 3% weight percentage), were randomly distributed in the cytoplasm. Due to the different densities of NP's materials, the number of NPs required for the concentration of 30 mg/g was 17239, 15547, 151227, 144652, and 64352 for Au, Pt, C, ^{11}B, and Fe_3O_4 NPs, respectively.

2.3. Radiation Source

To generate the SOBP and obtain a PS in that region, we used the advanced example "Hadron therapy" [37, 56] of the Geant4 toolkit. This example provides the simulation of several proton and carbon accelerators according to some famous accelerator systems in the world [56-58]. We used the 62.8 MeV proton passive transport beam line in line installed at Laboratori Nazionali del Sud (INFN) in Catania, Italy, which is used for the treatment of eye tumors [56].

In this study, a cube of liquid water with a density of 1 g/cm^3 with dimensions of 25 × 25 × 25 cm^3 was defined as a phantom in front of the proton accelerator. Protons with an energy of 62.8 MeV were then emitted towards the phantom as a beam (with a radius of 2 mm) through the accelerator system. By implementing the default weight factors according to the thickness of the proton range shifter, a~10 mm SOBP was produced using a range modulator wheel and 12 Bragg peaks as 12 initial steps. These default weight factors and the corresponding range shifter thicknesses in the "Hadron therapy" example are listed in Table 1. Details on the design of an SOBP using a range modulator wheel can be found in [35]. Figure 2 shows the SOBP obtained using "Hadron therapy" example with a 62.8 MeV proton beam in a passive transport beam line. The PS was obtained at three locations along the SOBP by defining three virtual detectors with dimensions of 25 × 25 × 0.1 cm³ at the beginning (0.5 mm), middle (26.5 mm), and end (31.5 mm depth) of the SOBP. Information on the primary and secondary particles reaching each detector was recorded and stored in a text file as a PS. The data in each PS file were subsequently used as the primary radiation source for irradiating the fibroblast cell model (see Figure 3). At the cellular scale, the radiation source was defined as a circular planar source with a radius of 7.6 μm to fully cover the cell nucleus and cytoplasm.

TABLE 1. Default weight factors and corresponding range shifter thicknesses used to produce a SOBP from a 62.8 MeV proton beam in the "Hadron therapy" example of the Geant4 Monte Carlo toolkit.

Step Numbers	Step Thickness (mm)	Relative Wight factor
1	0.0	0.28215
2	0.84	0.06864
3	1.68	0.09704
4	2.52	0.05974
5	3.36	0.07385
6	4.20	0.05965
7	5.04	0.06518
8	5.88	0.05708
9	6.72	0.06055
10	7.56	0.05762
11	8.40	0.05942
12	9.24	0.05908

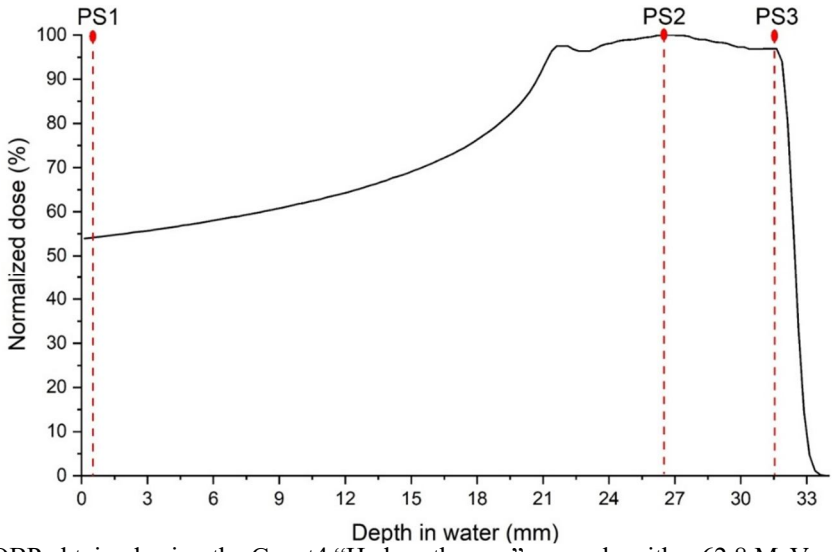

FIG. 2. The SOBP obtained using the Geant4 "Hadron therapy" example with a 62.8 MeV proton beam in a passive transport beam line. The locations of obtaining the phase-space (PS) are indicated by three dashed lines at depths of 0.5 mm (at the beginning), 26.5 mm (at the middle), and 31.5 mm (at the end).

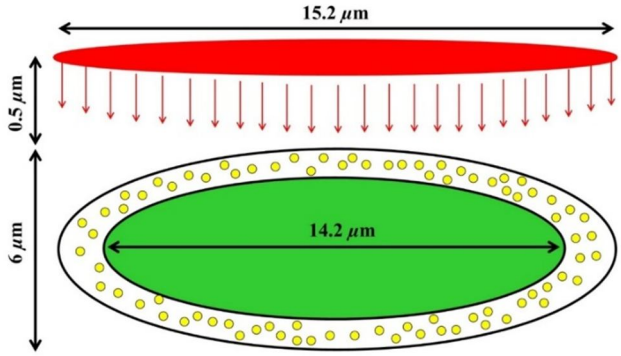

FIG. 3. The cell model irradiated by a circular plane source with a radius of 7.6 μm, emitting particles from a phase-space file.

2.4. DEF and DNA Damage Calculation

If D_{NP} and D_0 are the doses deposited in the cell with and without NPs in its cytoplasm, respectively, the DEF is calculated using Eq. (1):

$$DEF = D_{NP}/D_0 \quad (1)$$

According to the study of Nikjoo *et al*. [59], DNA damage has two general categories: single- and double-strand breaks (SSBs and DSBs). DNA damage can also be classified as direct (caused by the radiation), indirect (caused by free radicals), or hybrid. Figure 4 displays the classification of DNA damage that is the result of physical and chemical stages [60]. Two types of complex DSBs, i.e., DSB+ and DSB++, are also shown in Fig. 4. These complex lesions are essential for a mathematical model of cell repair and survival.

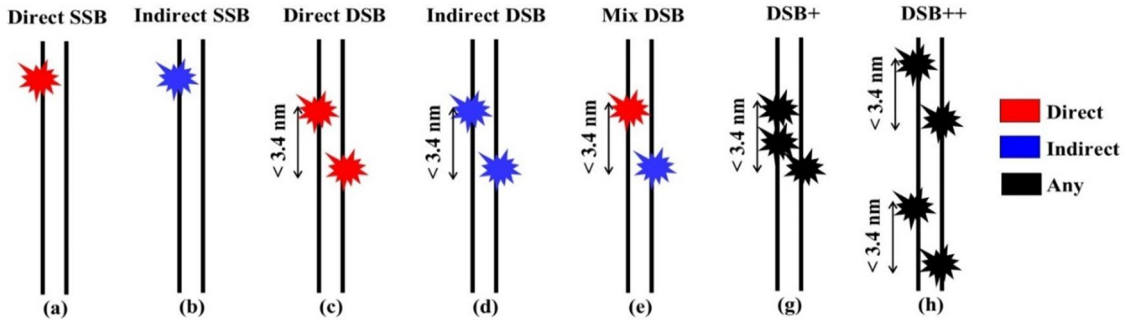

FIG. 4. Categorization of DNA damage: (a) direct and (b) indirect single-strand break (SSB); (c) direct and (b) indirect, and (c) mixed double-strand break (DSB). Two types of complex DSBs are also shown as DSB+ and DSB++.

SSB may be recorded when an energy deposition of 5 eV or greater occurs in the backbone of the DNA (i.e., sugar-phosphate volumes). It is the minimum energy threshold for the SSB occurrence, and the probability of SSB occurrence increases linearly with the deposited energy. The maximum energy threshold for the SSB occurrence is 37.5 eV, which means the probability of an SSB will be 100% when an energy deposition of 37.5 eV or greater occurs in the backbone of the DNA [61]. Two SSBs located on opposite DNA strands with a distance of less than ~3.4 nm (or 10 bps) lead to a DSB. To consider the quasi-direct effect, a radial distance of 0.6 nm beyond each sugar-phosphate molecule was determined as the hydration shell. This effect refers to the damage caused by charge transfers following ionization of the hydration shell around the DNA molecules [62]. In the case of indirect DNA damage, the presence of the chemical species in the sugar-phosphate molecules may lead to SSB. Only the hydroxyl radical ($OH^{\bullet}$) was taken into account for calculating indirect DNA damage, since it is the most reactive radical. Furthermore, only a proportion of $OH^{\bullet}$ radicals lead to indirect SSB. A probability of 40% was set for each $OH^{\bullet}$ radical reaching to the sugar-phosphate molecule to result in an indirect SSB [52, 54, 63]. Note that all chemical species that diffuse more than 4 nm from the DNA molecules were killed, as their effective diffusion range is roughly 4 nm for DNA damage calculation [59]. An 80 CPU-core computing system with 180 GB of RAM was used for this study. A statistical error of less than 1% was obtained for dose calculation with 2, 1, and 0.5 million initial particles for PS1, PS2, and PS3 files, respectively.

2.5. Cell Survival Calculation

The DNA damage yields induced by ionizing radiation increase during irradiation. A proportion of DNA damages are repaired over time. The freely available Python codes provided in the "molecularDNA" example of the Geant4 toolkit were used to obtain the cell survival fraction. Two mathematical models have been integrated with the Geant4-DNA code to estimate the cell survival fraction [64, 65]: the Two-Lesion Kinetic (TLK) model [66] and the Local Effect model (LEM) [67]. In this study, the TLK model was employed to estimate the cell survival fraction. The TLK model establishes a link between double-strand breaks (DSBs) and cell death, based on the complexity of DNA damage. It assumes that DSB repair depends on the complexity of the damage, with DSB+ and DSB++ considered as complex and lethal DNA lesions. The TLK model incorporates both slow and fast DNA repair mechanisms, which account for first-order (single-lesion) and second-order (multiple-lesion) repair processes. The first- and second-order repairs are represented by the parameters L(t) and $L^2(t)$, respectively, at time t after the irradiation. These repair mechanisms consider both the correct rejoining of the free ends of damaged DNA base pairs at their original locations and the incorrect rejoining at different positions. The second-order repair can therefore lead to fatal chromosomal aberrations. The TLK model calculates the cell survival fraction using the following equations [66]:

$$\frac{dL_1(t)}{dt} = \dot{D}(t)Y\Sigma_1 - \lambda_1 L_1(t) - \eta L_1[L_1(t) + L_2(t)] \quad (2)$$

$$\frac{dL_2(t)}{dt} = \dot{D}(t)Y\Sigma_2 - \lambda_2 L_2(t) - \eta L_2[L_1(t) + L_2(t)] \quad (3)$$

$$\frac{dL_f(t)}{dt} = \beta_1\lambda_1 L_1(t) + \beta_2\lambda_2 L_2(t) + \gamma\eta[L_1(t) + L_2(t)]^2 \quad (4)$$

Here, $L_1(t)$ and $L_2(t)$ are the frequencies of simple DSBs (fast repair) and complex DSBs (slow repair), respectively, per irradiated cell at time t. $L_f(t)$ represents the number of lethal DNA damages that may lead to cell death. Y is the genome length in Gbps, and $\dot{D}(t)$ is the dose rate. Σ_1 and Σ_2 are the frequencies of simple and complex DSBs, respectively. Simple (Σ_1) DSBs are equal to the number of isolated DSBs, i.e., DSBs other than DSB+ and DSB++. Complex (Σ_2) DSBs are considered to be $N_{DSB+} + 2N_{DSB++}$ [52, 64]. Simple and complex DNA damages are repaired by fast and slow repair processes, respectively. η and λ are repair probability factors that describe the rate of damage rejoining (h^{-1}). β and γ are the lethality probability factors that describe the likelihood that residual damage may lead to cell death. The subscripts 1 and 2 for λ and β parameters correspond to simple and complex lesions, respectively. All parameters were set for a fibroblast cell nucleus according to Chatzipapas *et al.* [52]. The cell survival fraction was then calculated by Eq. (5):

$$\text{Survival Fraction} = e^{-L_f} \quad (5)$$

Figure 5 shows the time variations of (a) $L_1(t)$, (b) $L_2(t)$, (c) $L_f(t)$, and (d) the survival fraction, calculated using Eqs. (2)-(5) with the fourth-order Runge-Kutta method.

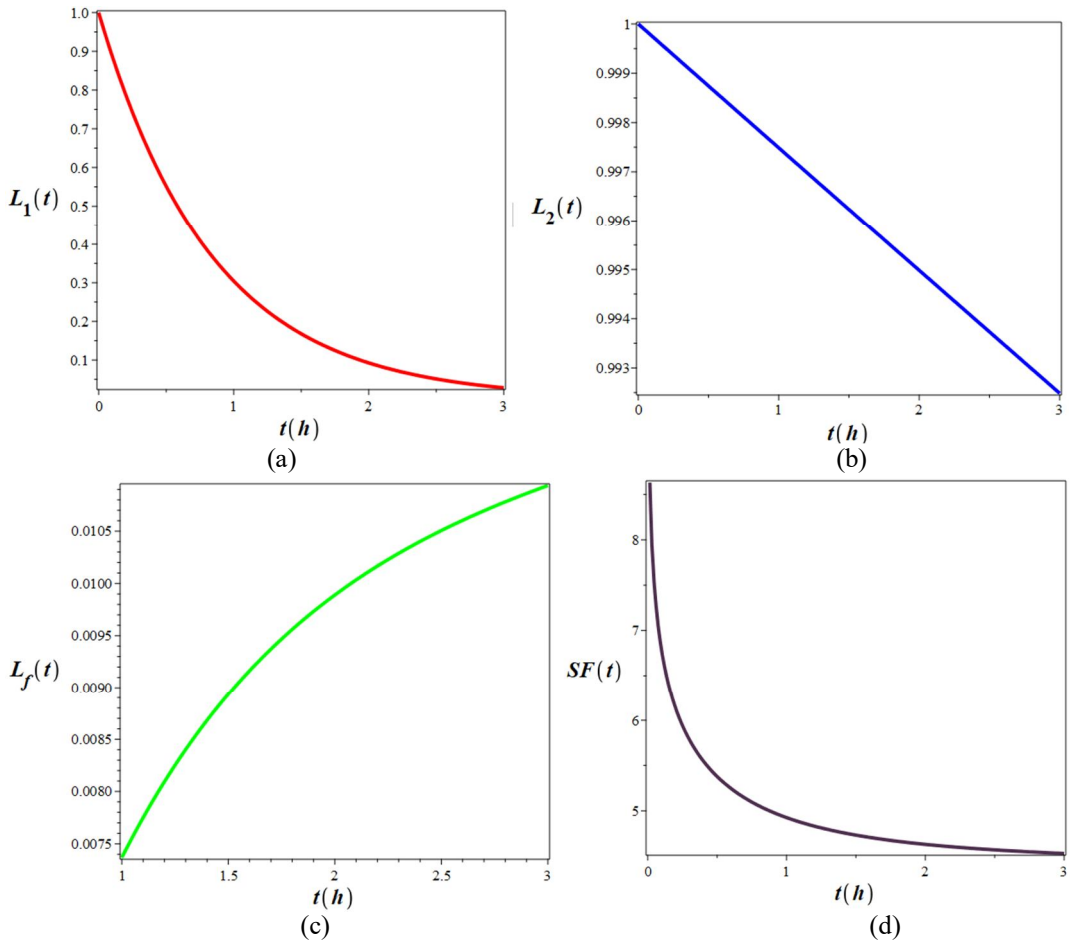

FIG. 5. Time variations of (a) $L_1(t)$, (b) $L_2(t)$, (c) $L_f(t)$, and (d) survival fraction.

The fraction of activity released (FAR), measured using gel-electrophoresis methods, is used to quantify the number and size of DNA fragments resulting from DNA fiber breakage, such as that induced by DSBs. By calculating the ratio between FAR and the initial FAR, it is possible to estimate the fraction of un-rejoined DSBs. According to the random-breakage model, the relationship between FAR and the number of un-rejoined DSBs ($(L_1(t) + L_2(t))/Y$) can be calculated using the following equation:

$$FRA(t) = F_{max}\{1 - [1 + K(L_1(t) + L_2(t))/Y(1 - \frac{K}{M_0})]\exp(-K(L_1(t) + L_2(t))/Y)\} \quad (6)$$

In Fig. 6, we plotted the time variations of $FRA(t)$ using Eq. (6).

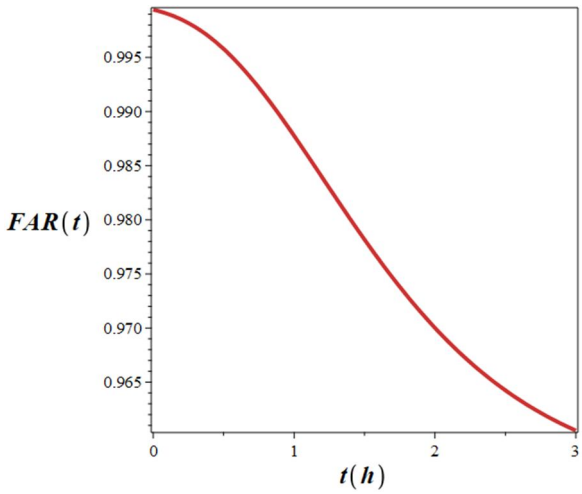

FIG. 6. Time variations of $FRA(t)$.

3. Results

For validating the simulation, the Bragg peak curve of 62.8 MeV protons in water obtained using Geant4 in this study was compared with experimental data (obtained with an ion chamber) provided by the example "Hadron therapy" [37, 56]. As can be seen in Fig. 7, good agreement is obtained between the simulation and the reference data.

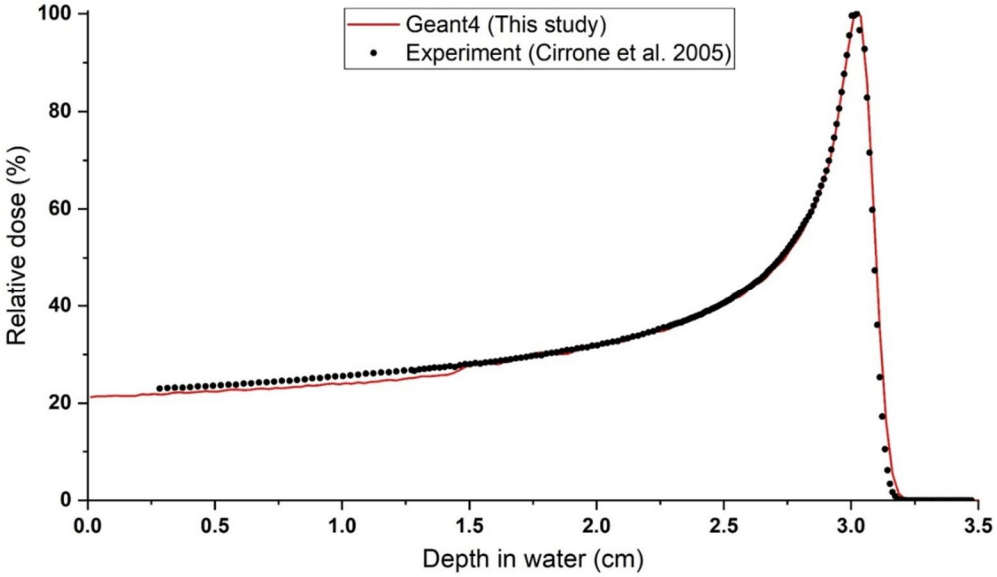

FIG. 7. Comparison of Bragg peak curves obtained using the Geant4 toolkit and experimental data obtained with an ion chamber [37, 56].

Figure 8 shows the DEF (%) for Au, Pt, C, ^{11}B, and Fe_3O_4 NPs at a concentration of 30 mg/g distributed in the cytoplasm of the cell. Figure 9 shows the DNA damage enhancement (SSBs and DSBs) caused by the presence of 30 mg/g Au, Pt, C, ^{11}B, and Fe_3O_4 NPs in the cell cytoplasm. The ratio of direct to indirect total DNA damages (D_{dir}/D_{ind}) and the ratio of DSB/SSB for 30 mg/g Au, Pt, C, ^{11}B, and Fe_3O_4 NPs in the cell cytoplasm are listed in Table 2. The ratios are presented for three PSs shown in Fig. 2.

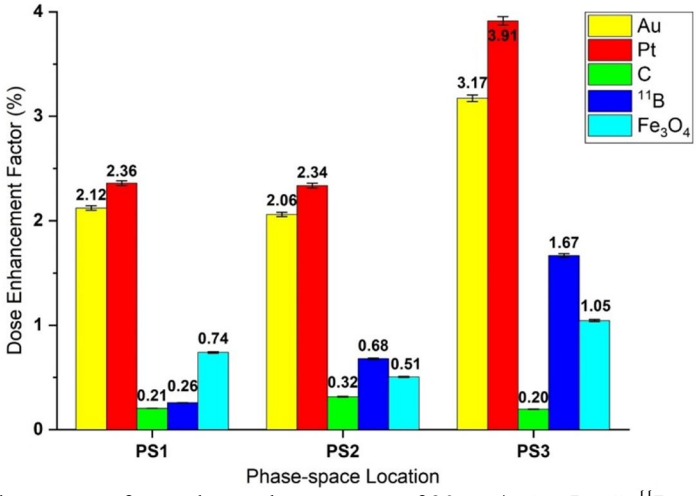

FIG. 8. The dose enhancement factor due to the presence of 30 mg/g Au, Pt, C, ^{11}B, and Fe_3O_4 NPs in the cytoplasm of the cell.

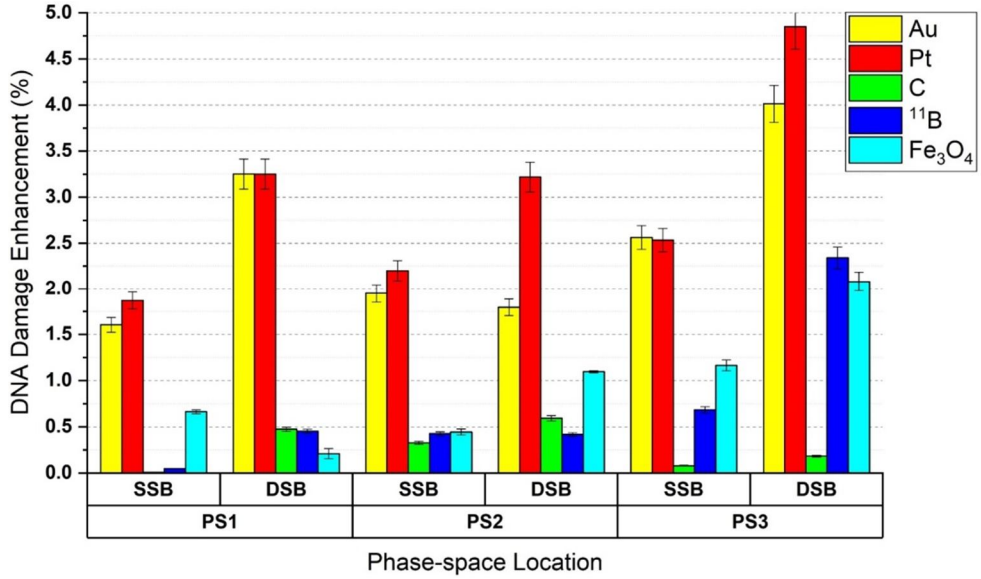

FIG. 9. Enhancement in the single- and double-strand DNA breaks (SSBs and DSBs) due to the presence of 30 mg/g Au, Pt, C, ^{11}B, and Fe_3O_4 NPs in the cytoplasm of the cell.

TABLE 3. Ratios of single- to double-strand breaks (DSB/SSB) and direct- to indirect-DNA damage (D_{dir}/D_{ind}) for various NPs in the cell irradiated by particles in three phase-spaces.

NP material	D_{dir}/D_{ind}			DSB/SSB		
	PS1	PS2	PS3	PS1	PS2	PS3
Au	1.346	1.491	1.655	0.0667	0.0833	0.1132
Pt	1.349	1.484	1.652	0.0665	0.0842	0.1169
C	1.341	1.485	1.649	0.0660	0.0836	0.1116
^{11}B	1.340	1.488	1.656	0.0659	0.0834	0.1135
Fe_3O_4	1.341	1.487	1.649	0.0661	0.0830	0.1127

The numbers of repairable and irreparable DSBs per primary particle induced in the cell nucleus, with and without the presence of 30 mg/g Au, Pt, C, ^{11}B, and Fe_3O_4 NPs are listed in Table 3. Figure 10 shows a comparison of the cell survival curves obtained from the TLK model with and without 30 mg/g Pt nanoparticles in the cell cytoplasm. The error bars are small and fall within the marker size. According to Table 3, Pt nanoparticles produced the highest DNA damage among the tested NPs; therefore, only the cell survival curves for Pt are shown.

TABLE 3. The frequency of repairable and irreparable DSBs per primary particle induced in the cell nucleus with and without different NPs (30 mg/g).

NP material (30 mg/g)	PS1 (0.5 mm)		PS2 (26.5 mm)		PS3 (31.5 mm)	
	Repairable DSBs/event	Irreparable DSBs/event	Repairable DSBs/event	Irreparable DSBs/event	Repairable DSBs/event	Irreparable DSBs/event
H_2O (No NP)	0.09041	0.04085	0.13415	0.06905	0.16982	0.09893
Au	0.09316	0.04215	0.13594	0.07134	0.17598	0.10439
Pt	0.09294	0.04250	0.13824	0.07179	0.18324	0.11218
C	0.09049	0.04143	0.13459	0.07001	0.17015	0.10029
^{11}B	0.09045	0.04153	0.13472	0.06921	0.17332	0.10273
Fe_3O_4	0.09109	0.04165	0.13419	0.06934	0.17339	0.10155

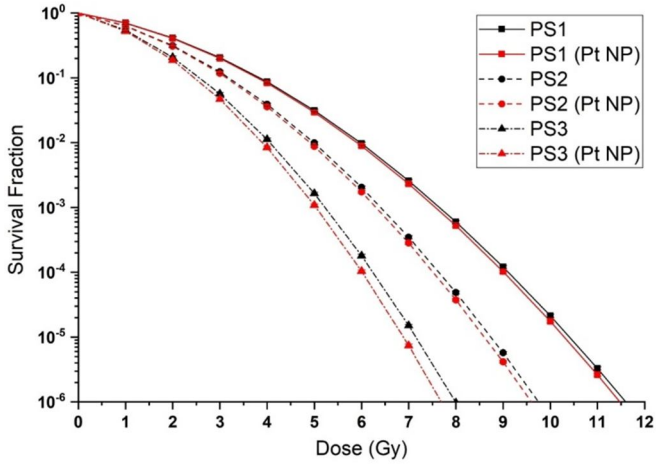

FIG. 10. Cell survival curves obtained from the TLK model with and without 30 mg/g Au, Pt, C, ^{11}B, and Fe_3O_4 NPs in the cell cytoplasm.

Figures 11 and 12 show the numerical values of the calculated dose and DEF, respectively, for selected NPs in terms of proton beam energy at the phantom cell.

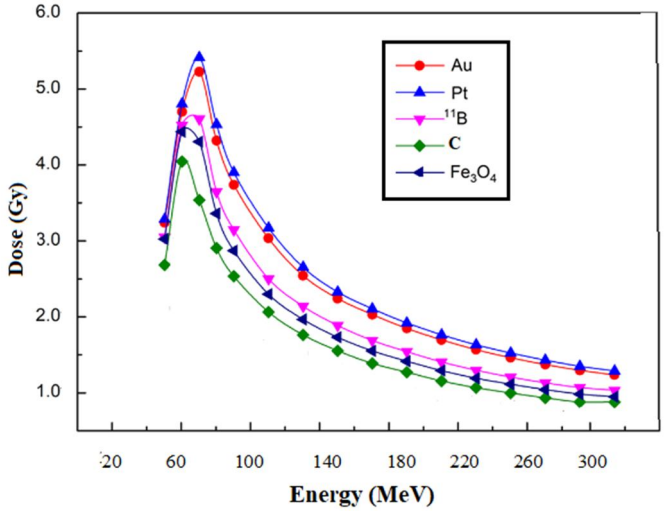

FIG. 11. Calculated dose for five different nanoparticles as a function of proton beam energy at the cell phantom.

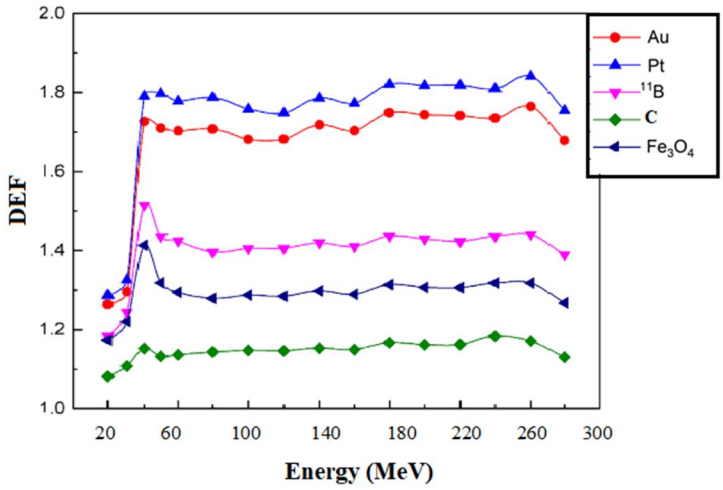

FIG. 12. Calculated DEF values for five different nanoparticles as a function of proton beam energy in the phantom.

Figure 13 presents a three-dimensional plot to show the dependency of DEF on the size and concentration of distributed NPs in the phantom irradiated with 62.5 MeV protons.

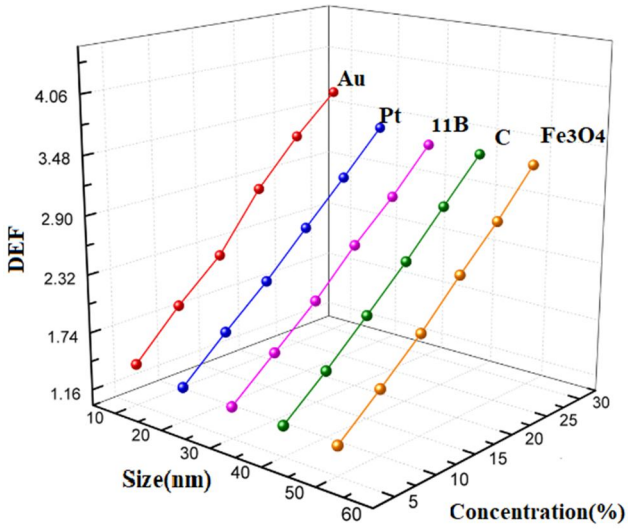

FIG. 13. Three-dimensional variations of DEF in terms of the size and concentration of selected NPs distributed in the phantom.

4. Discussion

Figure 6 shows that Pt NPs have the highest DEF in the cell nucleus among the studied NPs. At the beginning and middle of the proton range (i.e., for PS1 and PS2, respectively), the DEF difference between Pt and Au NPs is up to 13.5%, while at the end of the SOBP (i.e., for PS3), this difference reaches about 23.3%. For all PSs, Pt and Au NPs showed significant differences in DEF compared to other studied NPs. After Pt and Au, ^{11}B NPs seem to show a better effect. At the end of the range, ^{11}B NPs showed an increase of 101% and 427% in the DEF relative to the beginning and center of the SOBP, respectively. At that location, Fe_3O_4 NPs showed an increase of 41.9% and 106% in the DEF compared to the beginning and center of the SOBP, respectively. Among the studied NPs, C NPs had the lowest DEF in the cell. C and B elements have close atomic numbers and almost similar density (about 2.3 g/cm^3 at standard conditions) and can both produce alpha particles via nuclear interactions with protons [26, 68]:

$$p + {}^{12}C \rightarrow 3\alpha + p \quad (7)$$

$$p + {}^{11}B \rightarrow 3\alpha \quad (8)$$

Nevertheless, the observed differences in DEF arise from the cross sections of these nuclear interactions. The probability of such reactions is very low; for example, in the proton energy range of 50–60 MeV, the reaction cross section with carbon is only 400 mb (i.e., 10^{-27} cm^2). This means that the majority of transported particles are primary protons, secondary electrons, and photons, whereas alpha particles have a very small contribution in dose calculations. For 5×10^5 incident protons, only 3 alpha particles were recorded in the PS at the Bragg peak, i.e., only a single interaction occurred. In the case of PS1 and PS2 locations, there were zero alpha particles in the PS file for 2×10^6 and 10^6 incident protons, respectively. However, if we consider only certain nuclear interactions or only secondary particles, the DEF results will be completely different, but this does not correspond to the real conditions. The fact that by approaching the end of the SOBP, the effectiveness of ^{11}B NPs becomes higher than the previous positions is consistent with the results of Cirrone *et al*. [68] and Beni et al. [69]. The reason is that the cross-section of the above-mentioned interactions is greater at the Bragg peak, i.e., in the energy range of 0.1-10 MeV.

Although previous studies reported a large dose increase with C nanoparticles, the discrepancy with our results arises from differences in simulation methodology [20, 21, 25, 70]. In those studies, a single NP was simulated, and all primary particles directly hit that NP. In such cases, the probability of nuclear interactions is much higher, and secondary particles directly enter the target volume, which is considered a uniform water volume without DNA details. Furthermore, some studies assumed mono-energetic incident protons, unlike the realistic SOBP used clinically. These differences in simulation setup are the main reasons for the discrepancies in DEF between our results and previous studies. In this work, we aimed to simulate a more realistic scenario by incorporating the full energy spectrum of protons

in the center of the SOBP a detailed nucleus cell model, and a realistic distribution of nanoparticles at a defined concentration in the cytoplasm. The DEF of approximately 3% with Au nanoparticles obtained in our simulation is in good agreement with experimental data, which report increases of up to 9 % [6,7].

McKinnon *et al*. [70] reported a 27% increase in dose for Au nanoparticles using the Geant4 toolkit. In that study, as in many other simulation studies, only a single NP was considered, and all primary particles directly hit that NP, with the dose calculated in ring detectors up to a radius of 2 μm from the NP center. Other studies using the same single-NP approach reported DEF values of up to 1600% for Au and Pt nanoparticles [20, 21]. However, experimental studies indicate that such dose increases are inconsistent with real conditions, a finding confirmed by our simulation study.

Our results are consistent with the simulation study of Sotiropoulos *et al*. [17], which considered a whole-cell model with Au nanoparticles in the cytoplasm. However, they did not observe a significant increase in direct DNA damage for a concentration of 7 mg/g Au NPs when irradiating cells with 10 and 50 MeV protons. In contrast, as shown in Fig. 7, the present study demonstrates a 24% increase in DNA damage across different PS files. This difference arises because Sotiropoulos *et al*. [17] considered only direct DNA damages, whereas we accounted for both direct and indirect damages, highlighting the importance of including indirect damages resulting from water radiolysis.

The higher DEF of Pt nanoparticles compared to Au nanoparticles at the center of the SOBP, as well as at the other two PS locations (Fig. 6), is in good agreement with experimental results reported in the literature [71-73].

This superiority of Pt NPs over Au NPs, for the same size and concentration, is attributed to the physicochemical properties of Pt that enhance the production of chemical species following irradiation [73]. As the end of the SOBP is approached, the amount of DNA damage per incident particle increases compared to the previous PS locations, which aligns with other published studies [17,74]. This effect is due to the higher linear energy transfer (LET) at the end of the Bragg peak.

According to Table 3, the observed increase in the D_{dir}/D_{ind} ratio with increasing LET (corresponding to greater depth in water) is consistent with the findings of other studies [75-77]. Furthermore, the enhancement of the DSB/SSB ratio with increasing LET agrees with the results reported by Chattaraj and Selvam [78] and Rafiepour *et al*. [79].

Table 3 shows that as the atomic number of the NPs increases, the normalized DSB damages per event, which include repairable (simple DSBs) and irreparable (complex DSBs) damages, increase. Therefore, the calculated DSBs are higher for Au and Pt NPs, which explains the higher DEF in the cell compared to other NPs. However, this increase is negligible for protons compared to low-energy photons, because low-energy photons have an extremely high cross-section with materials of high atomic number [4, 6, 17]. Needless to say, atomic number is not the only main factor; other factors also play a role in this dose increase. For instance, higher density increases collisions with target molecules, and specific physicochemical properties of the NPs, demonstrated experimentally, can also influence dose enhancement. DSBs are used as input for the TLK mathematical model, the results of which are shown in the cell survival curves in Fig. 8. As illustrated, the cell survival curves with and without Pt NPs show no significant difference at the beginning and middle of the SOBP (two PSs), but the difference is significant at the end of the SOBP. Although the choice of mathematical model and parameter values can strongly affect the final shape of the survival curves, the observed difference between the curves with and without NPs is the key finding in this study. The variation in cell survival curves with different LETs, i.e., at different PS locations, is consistent with other relevant studies [8, 79-81]. Figure 9 presents the calculated dose in the phantom volume resulting from irradiation with monoenergetic protons ranging from 20 to 320 MeV. The dose plot for Pt NPs shows a superior curve compared to other NPs, indicating the greater efficacy of Pt in enhancing dose. The maximum dose for Pt NPs is approximately 5.34 Gy at 60 MeV protons. Figure 10 shows that the calculated DEF values strongly depend on the proton beam energy. The peak positions are similar for all five NPs, with maximum DEF values occurring in the energy range of 30-280 MeV. The results indicate that

Pt NPs outperform other nanoparticles in increasing dose rate, with DEF increasing 1.8 times over this energy range, resulting in a significant dose enhancement.

Therefore, further studies were performed using Pt NPs to investigate different parameters. Although DEF varies linearly with NP concentration, it is relatively insensitive to NP size. For concentrations of 5% and 30%, the DEFs for different NP sizes vary by approximately 8% and 13%, respectively. Based on these results, the size of Pt NPs distributed in the phantom is not a critical factor in predicting or controlling dose and DEF in the tumor volume.

5. Conclusion

A multiscale simulation was performed to study the dose enhancement factor (DEF) resulting from the presence of Au, Pt, C, ^{11}B, and Fe_3O_4 nanoparticles at a concentration of 30 mg/g in a fibroblast cell model under SOBP irradiation with 62.8 MeV protons. The results showed that high atomic number NPs, such as Au and Pt, are promising agents for 62.8 MeV proton therapy, as they can enhance the cell dose by up to 4%. The radiobiological impact of Au and Pt NPs, assessed through cell survival curves, also confirmed this conclusion. Although the results differ significantly from some previous simulation studies, this study highlights the importance of considering realistic clinical conditions. In summary, the Geant4 toolkit was used to perform a comparative study of NP properties and proton beam energy. Nanoparticles of different concentrations and sizes were distributed throughout the selected cell, and the DEF in the nucleus was calculated for various energies and materials. This study concludes that dose enhancement depends both on the incident proton energy and on the type of nanoparticle material.

References

[1] Mohan R., Precis. Radiat. Oncol., 6 (2) (2022) 164.

[2] Newhauser, W.D. and Zhang, R., Phys. Med. Biol., 60 (8) (2015) R155.

[3] Hainfeld, J.F., Dilmanian, F.A., Slatkin, D.N., and Smilowitz, H.M., J. Pharm. Pharmacol., 60 (8) (2008) 977.

[4] Rudek, B., McNamara, A., Ramos-Méndez, J., Byrne, H., Kuncic, Z., and Schuemann, J., Phys. Med. Biol., 64 (17) (2019) 175005.

[5] Cunningham, C., de Kock, M., Engelbrecht, M., Miles, X., Slabbert, J., and Vandevoorde, C., Front. Public Health, 9 (2021) 699822.

[6] Smith, C.L., Best, S.P., Gagliardi, F., Tominaga, T., and Geso, M., Radiat. Meas., 106 (2017) 352.

[7] Sisin, N.N.T. et al., Radiat., 2 (1) (2022) 130.

[8] Polf, J.C., Bronk, L.F., Driessen, W.H., Arap, W., Pasqualini, R., and Gillin, M., Appl. Phys. Lett., 98 (19) (2011) 193702.

[9] Kim, J.K., Seo, S.J., Kim, H.T., Kim, K.H., Chung, M.H., Kim, K.R., and Ye, S.J., Phys. Med. Biol., 57 (24) (2012) 8309.

[10] Hojo, H., Dohmae, T., Hotta, K., Kohno, R., Motegi, A., Yagishita, A., Makinoshima, H., Tsuchihara, K., and Akimoto, T., Radiat. Oncol., 12 (1) (2017) 111.

[11] Li, S., Bouchy, S., Penninckx, S., Marega, R., Fichera, O., Gallez, B., Feron, O., Martinive, P., Heuskin, A.C., Michiels, C., and Lucas, S., Nanomedicine, 14 (3) (2019) 317.

[12] Torrisi, L., Davidkova, M., Havranek, V., Cutroneo, M., and Torrisi, A., Radiat. Eff. Defects Solids, 175 (9-10) (2020) 863.

[13] Lo, C.Y., Tsai, S.W., Niu, H., Chen, F.H., Hwang, H.C., Chao, T.C., Hsiao, I.T., and Liaw, J.W., ACS Omega, 8 (20) (2023) 17922.

[14] Velten, C. and Tomé, W.A., Biomed. Phys. Eng. Express, 9 (4) (2023) 045004.

[15] Martínez-Rovira, I. and Prezado, Y., Med. Phys., 42 (11) (2015) 6703.

[16] McNamara, A.L., Kam, W.W., Scales, N., McMahon, S.J., Bennett, J.W., Byrne, H.L., Schuemann, J., Paganetti, H., Banati, R., and Kuncic, Z., Phys. Med. Biol., 61 (16) (2016) 5993.

[17] Sotiropoulos, M., Taylor, M.J., Henthorn, N.T., Warmenhoven, J.W., Mackay, R.I., Kirkby, K.J., and Merchant, M.J., Biomed. Phys. Eng. Express, 3 (2) (2017) 025025.

[18] Peukert, D., Kempson, I., Douglass, M., and Bezak, E., Med. Phys., 47 (2) (2020) 651.

[19] Huynh, N.H. and Chow, J.C., Appl. Sci., 11 (22) (2021) 10856.

[20] Rajabpour, S., Saberi, H., Rasouli, J., and Jabbari, N., Sci. Rep., 12 (1) (2022) 1779.

[21] Mansouri, E., Almisned, G., Tekin, H.O., Rajabpour, S., and Mesbahi, A., Radiat. Environ. Biophys., 63 (2024) 537.

[22] Heuskin, A.C., Gallez, B., Feron, O., Martinive, P., Michiels, C., and Lucas, S., Med. Phys., 44 (8) (2017) 4299.

[23] Lin, Y., McMahon, S.J., Paganetti, H., and Schuemann, J., Phys. Med. Biol., 60 (10) (2015) 4149.

[24] Ahn, S.H., Lee, N., Choi, C., Shin, S.W., Han, Y., and Park, H.C., Phys. Med. Biol., 63 (11) (2018) 114001.

[25] Tabbakh, F., Hosmane, N.S., Tajudin, S.M., Ghorashi, A.H., and Morshedian, N., Sci. Rep., 12 (1) (2022) 17404.

[26] Tabbakh, F. and Hosmane, N.S., Eur. Phys. J. Plus, 138 (6) (2023) 538.

[27] Zavestovskaya, I.N., Popov, A.L., Kolmanovich, D.D., Tikhonowski, G.V., Pastukhov, A.I., Savinov, M.S., Shakhov, P.V., Babkova, J.S., Popov, A.A., Zelepukin, I.V., Grigoryeva, M.S., Shemyakov, A.E., Klimentov, S.M., Ryabov, V.A., Prasad, P.N., Deyev, S.M., and Kabashin, A.V., Nanomaterials, 13 (15) (2023) 2167.

[28] Zavestovskaya, I.N. et al., Mater. Today, Nano, 27 (2024). 100508.

[29] Lin, Y., McMahon, S.J., Scarpelli, M., Paganetti, H., and Schuemann, J., Phys. Med. Biol., 59 (24) (2014) 7675.

[30] Klapproth, A.P., Schuemann, J., Stangl, S., Xie, T., Li, W.B., and Multhoff, G., Cancer Nanotech., 12 (2021) 27.

[31] Martinov, M.P., Fletcher, E.M., and Thomson, R.M., Med. Phys., 50 (9) (2023) 5853.

[32] Martinov, M.P., Fletcher, E.M., and Thomson, R.M., Med. Phys., 50 (9) (2023) 5842.

[33] Rafiepour P., Sina S., and Mortazavi S.M.J., Radiat. Phys. Chem., 212 (2023) 111016.

[34] Ganjeh, Z.A. and Mosleh-Shirazi, M.A., Radiat. Phys. Chem., 214 (2024) 111289.

[35] Jia, S.B., Romano, F., Cirrone, G.A., Cuttone, G., Hadizadeh, M.H., Mowlavi, A.A., and Raffaele, L., Nucl. Instrum. Methods Phys. Res. A, 806 (2016) 101.

[36] Agostinelli, S. et al., Nucl. Instrum. Methods Phys. Res. A, 506 (2003) 250.

[37] Cirrone, G.P. et al., IEEE Trans. Nucl. Sci., 52 (1) (2005) 262.

[38] Allison, J. et al., Nucl. Instrum. Methods Phys. Res. A, 835 (2016) 186.

[39] Geant4 Collaboration, Guide for Physics Lists (Geant4 version 11.1), (2023).

[40] Incerti, S. et al., Int. J. Model. Simul. Sci. Comput., 01 (02) (2010) 157.

[41] Bernal, M.A. et al., Phys. Med., 31 (8) (2015) 861.

[42] Incerti, S., Kyriakou, I., Bernal, M.A., Bordage, M.C., Francis, Z., Guatelli, S., Ivanchenko, V., Karamitros, M., Lampe, N., Lee, S.B., Meylan, S., Min, C.H., Shin, W.G., Nieminen, P., Sakata, D., Tang, N., Villagrasa, C., Tran, H.N., and Brown, J.M.C., Med. Phys., 45 (8) (2018) e722.

[43] Domínguez-Muñoz, A.D., Gallardo, M.I., Bordage, M.C., Francis, Z., Incerti, S., and Cortés-Giraldo, M.A., Radiat. Phys. Chem., 199 (2022) 110363.

[44] Incerti, S., Ivanchenko, A., Karamitros, M., Mantero, A., Moretto, P., Tran, H.N., Mascialino, B., Champion, C., Ivanchenko, V.N., Bernal, M.A., Francis, Z., Villagrasa, C., Baldacchin, G., Guèye, P., Capra, R., Nieminen, P., and Zacharatou, C., Med. Phys., 37 (9) (2010) 4692.

[45] Kyriakou, I., Sakata, D., Tran, H.N., Perrot, Y., Shin, W.G., Lampe, N., Zein, S., Bordage, M.C., Guatelli, S., Villagrasa, C., Emfietzoglou, D., and Incerti, S., Cancers, 14 (1) (2021) 35.

[46] Karamitros, M., Incerti, S., and Mantero, A., Prog. Nucl. Sci. Technol., 2 (2011) 503.

[47] Karamitros, M. et al., J. Comput. Phys., 274 (2014) 841.

[48] Tran, H.N., Ramos-Méndez, J., Shin, W.G., Perrot, Y., Faddegon, B., Okada, S., Karamitros, M., Davídková, M., Štěpán, V., Incerti, S., and Villagrasa, C., Med. Phys., 48 (2) (2021) 890.

[49] Plante, I. and Devroye, L., Radiat. Phys. Chem., 139 (2017) 157.

[50] Ramos-Méndez, J., Shin, W.G., Karamitros, M., Domínguez-Kondo, J., Tran, N.H., Incerti, S., Villagrasa, C., Perrot, Y., Štěpán, V., Okada, S., Moreno-Barbosa, E., and Faddegon, B., Med. Phys., 47 (11) (2020) 5919.

[51] Meylan, S., Incerti, S., Karamitros, M., Tang, N., Bueno, M., Clairand, I., and Villagrasa, C., Sci. Rep., 7 (1) (2017) 11923.

[52] Chatzipapas, K.P. et al., Precis. Radiat. Oncol., 7 (2023) 4.

[53] Hilbert, D. and Hilbert, D., "Über die stetige Abbildung einer Linie auf ein Flächenstück", In: "Dritter Band: Analysis·Grundlagen der Mathematik·Physik Verschiedenes", (Nebst Einer Lebensgeschichte, 1-2, 1935)

[54] Sakata, D. et al., Phys. Med., 62 (2019) 152.

[55] Shin, W.G., Sakata, D., Lampe, N., Belov, O., Tran, N.H., Petrovic, I., Ristic-Fira, A., Dordevic, M., Bernal, M.A., Bordage, M.C., Francis, Z., Kyriakou, I., Perrot, Y., Sasaki, T., Villagrasa, C., Guatelli, S., Breton, V., Emfietzoglou, D., and Incerti, S., Cancers, 13 (19) (2021) 4940.

[56] Cirrone, G.A.P. et al., Prog. Nucl. Sci. Technol., 2 (2011) 207.

[57] Tramontana, A. et al., Proc. 6th Int. Particle Accel. Conf. (IPAC'15), Richmond, VA, USA, May 3-8, 2015 (pp. 2515-2518). JACOW, Geneva, Switzerland.

[58] Tommasino, F. et al., Phys. Med., 58 (2019) 99.

[59] Nikjoo, H., O'Neill, P., Goodhead, D.T., and Terrissol, M., Int. J. Radiat. Biol., 71 (5) (1997) 467.

[60] Mortazavi, S.M.J., Rafiepour, P., Mortazavi, S.A.R., Razavi Toosi, S.M.T., Shomal, P.R., and Sihver, L., Med. Phys., 34 (1) (2024) 166.

[61] Francis, Z., Villagrasa, C., and Clairand, I., Com. Methods Programs Biomed., 101 (3) (2011) 265.

[62] Bertolet, A., Ramos-Méndez, J., McNamara, A., Yoo, D., Ingram, S., Henthorn, N., Warmenhoven, J.W., Faddegon, B., Merchant, M., McMahon, S.J., Paganetti, H., and Schuemann, J., Radiat. Res., 198 (3) (2022) 207.

[63] Lampe, N. et al., Phys. Med., 48 (2018) 135.

[64] Sakata, D., Belov, O., Bordage, M.C., Emfietzoglou, D., Guatelli, S., Inaniwa, T., Ivanchenko, V., Karamitros, M., Kyriakou, I., Lampe, N., Petrovic, I., Ristic-Fira, A., Shin, W.G., and Incerti, S., Sci. Rep., 10 (1) (2020) 20788.

[65] Sakata, D. et al., Phys. Med., 105 (2023) 102508.

[66] Stewart, R.D., Radiat. Res., 156 (4) (2001) 365.

[67] Elsässer, T., Weyrather, W.K., Friedrich, T., Durante, M., Iancu, G., Krämer, M., Kragl, G., Brons, S., Winter, M., Weber, K.J., and Scholz, M., Int. J. Radiat. Oncol. Biol. Phys., 78 (4) (2010) 1177.

[68] Cirrone, G.A.P., Manti, L., Margarone, D., Petringa, G., Giuffrida, L., Minopoli, A., Picciotto, A., Russo, G., Cammarata, F., Pisciotta, P., Perozziello, F.M., Romano, F., Marchese, V., Milluzzo, G., Scuderi, V., Cuttone, G., and Korn, G., Sci. Rep., 8 (1) (2018) 1141.

[69] Shahmohammadi Beni, M., Islam, M.R., Kim, K.M., Krstic, D., Nikezic, D., Yu, K.N., and Watabe, H., Sci. Rep., 12 (1) (2022) 18098.

[70] McKinnon, S., Guatelli, S., Incerti, S., Ivanchenko, V., Konstantinov, K., Corde, S., Lerch, M., Tehei, M., and Rosenfeld, A., Phys. Med., 32 (12) (2016) 1584.

[71] Ahmad, R., Royle, G., Lourenço, A., Schwarz, M., Fracchiolla, F., and Ricketts, K., Phys. Med. Biol., 61 (12) (2016) 4537.

[72] Rashid, R.A. et al., OpenNano, 4, (2019) 100027.

[73] Zwiehoff, S., Johny, J., Behrends, C., Landmann, A., Mentzel, F., Bäumer, C., Kröninger, K., Rehbock, C., Timmermann, B., and Barcikowski, S., Small, 18 (9) (2022) e2106383.

[74] Ganjeh, Z.A., Eslami-Kalantari, M., Loushab, M.E., and Mowlavi, A.A., Radiat. Phys. Chem., 179 (2021) 109249.

[75] Roots, R., Holley, W., Chatterjee, A., Irizarry, M., and Kraft, G., Int. J. Radiat. Biol., 58 (1) (1990) 55.

[76] Hirayama, R., Ito, A., Tomita, M., Tsukada, T., Yatagai, F., Noguchi, M., Matsumoto, Y., Kase, Y., Ando, K., Okayasu, R., and Furusawa, Y., Radiat. Res., 171 (2) (2009) 212.

[77] Ito, A., Nakano, H., Kusano, Y., Hirayama, R., Furusawa, Y., Murayama, C., Mori, T., Katsumura, Y., and Shinohara, K., Radiat. Res., 165 (6) (2006) 703.

[78] Chattaraj, A. and Selvam, T.P., Biomed. Phys. Eng. Express, 10 (4) (2024) 045059.

[79] Rafiepour, P., Sina, S., Amoli, Z.A., Shekarforoush, S.S., Farajzadeh, E., and Mortazavi, S.M.J., Phys. Eng. Sci. Med., 47 (3) (2024) 1015.

[80] Jeynes, J.C., Merchant, M.J., Spindler, A., Wera, A.C., and Kirkby, K.J., Phys. Med. Biol., 59 (21) (2014) 6431.

[81] Li, S., Penninckx, S., Karmani, L., Heuskin, A.C., Watillon, K., Marega, R., Zola, J., Corvaglia, V., Genard, G., Gallez, B., Feron, O., Martinive, P., Bonifazi, D., Michiels, C., and Lucas, S., Nanotechnology, 27 (45) (2016) 455101.

Volume 18, Number 5, 2025. pp. 659-667

Jordan Journal of Physics

ARTICLE

Gas Sensing Performance of ZnO/Si Nanostructured Thin Films Synthesis by Spin-Coating

Ahmad Z. Al-Jenaby, Othman A. Fahad, Saadallah F. Hasan and **Abubaker. S. Mohammed**

Ministry of Education, Directorate of Education in Al-Anbar, Al-Anbar, Iraq.

Doi: **https://doi.org/10.47011/18.5.8**

Received on: 11/01/2025; *Accepted on: 23/04/2025*

Abstract: In this work, ethanol, ammonium hydroxide, and a zinc acetate-containing precursor solution were used to create zinc oxide (ZnO) nanostructured films on silicon substrates using the spin-coating technique. The study also investigated how several layers affect structural, optical, and sensing properties. X-ray revealed that ZnO nanoparticles had a hexagonal structure phase and were polycrystalline, with the (002) plane as the preferred orientation parallel to the substrate surface. According to AFM analysis, as the number of layers increased, the grain size decreased, and the surface roughness increased. The energy gap increased from 3.31 to 3.39 eV as the number of layers increased, according to UV-visible analysis. Sensitivity of the films to ammonia gas in a 50 ppm concentration range was assessed at working temperatures ranging from room temperature to 150 °C. Nanostructured ZnO thin films must be produced for efficient and reasonably priced gas sensing applications. A synergistic effect was observed in this study: reducing grain size, increasing operating temperature, and enhancing surface roughness improved sensitivity, reaching up to 140.7% when seven layers were applied.

Keywords: ZnO nanoparticles, Sensitivity, Grain size, Roughness, NH3 gas sensor.

1. Introduction

Current solid-state device technologies have a wide range of applications. Among the materials that have received extensive investigation in recent years are transparent conductive oxides (TCOs) in thin films [1]. Zinc oxide (ZnO) is one of the most significant semiconductor materials, exhibiting a hexagonal crystal structure (wurtzite) and belonging to group II–VI compounds [2]. The compound has a direct band gap of 3.2–3.4 eV, is abundant, cheap, non-toxic, and has n-type conductivity [3]. Its visible range optical transmission is good, making it suitable for the solar spectrum [4, 5]. It has a variety of uses in optoelectronic devices due to its structural, electrical, and optical properties [4, 6]. By increasing the number of layers, zinc oxide films can be used to improve sensing and electrical properties, among other things, to increase ammonia gas sensitivity [7]. Gas sensing is influenced not only by structural properties, including grain size, grain boundaries, and surface-to-volume ratio, but also by surface states and oxygen adsorption rates [8–11]. Multilayered ZnO thin films can be deposited using a variety of techniques, including PLD [12], sputtering [13, 14], and spray pyrolysis [15]. The spin coating method is the most straightforward, economical, and suitable for large-area deposition. A straightforward and affordable sol-gel deposition method was used to apply the characteristics of stacked ZnO thin film layers [16]. Reasonably priced optoelectronic device manufacturing will be made easier by the ongoing work. The novelty of this work lies in fabricating ZnO thin films with three, five, and seven layers on silicon substrates that operate at room temperature. By producing nanostructured films, the resulting gas sensor can function within broadband in different temperatures.

Corresponding Author: Othman Abed Fahad **Email**: Othmanabad2@gmail.com

The current work has examined structural, morphological, sensing, and optical properties of 3-, 5-, and 7-layer thin films made using a straightforward technique (sol-gel spin coating).

2. Experimental

The sol-gel spin coating method was used to prepare ZnO films for growth on silicon substrates. Zinc dehydrate [Zn $(CH_3COO)_2$-$2H_2O$] was dissolved in isopropanol [$(CH_3)_2CHOH$]. Monoethanolamide was used to stabilize the solution (MEA) [NH2 CH2CH2OH]. It was incorporated into a 25 mL solution at a rate of 1, in order to make a con. of 0.2 mol/l. To create uniformity, the solutions were stirred for one hour at 65 °C. Clear solutions were then allowed to age at room temperature for a full day. The silicon substrates were cleaned with ethanol and acetone for ten minutes each using an ultrasonic cleaner, and then dried following a cleaning with deionized water prior to the deposition process. A small amount of the prepared coating material in liquid form was applied by dropper to the center of the substrate fixed in the spin coating machine at 2500 rpm. This process was repeated several times to obtain multiple layers (3, 5, and 7). The films were heated in an oven at 250 °C for 5 minutes to remove organic residues and evaporate the solvent. Then, the films are annealed for 1 hour at 500 °C in air. The thickness of the deposited film was measured using an optical interferometer method based on interference between a He-Ne laser (632 nm) reflected from the substrate and the film surface. We call this the Fizeau approach. The thickness was computed using the formula. The films had thicknesses of roughly 100, 200, and 300 nm. The films were measured using a profilometer, in which part of the film is scratched to expose the substrate, and the device measures the height difference between the film surface and the exposed substrate.

3. Results and Discussion

Figure 1 shows probes of XRD patterns that provided information about film structure and were used to study the crystal structure of ZnO, recorded in the range between 20° and 80°. The observed peaks at (010), (002), and (011) appear in XRD patterns along with other peaks, demonstrating the hexagonal polycrystalline (wurtzite) structure of the ZnO thin films, as indicated on the card with the number [17]. The (002) peak was the most noticeable, suggesting a preferred growth direction along the c-axis. This proved that the surface free energy of the (002) planes was the most stable when compared to other planes. Among other things, the crystals' position, intensity, and preferred orientation can reveal details about their size, tension, and strain [18, 19]. For the three-layer ZnO film, the peak intensity was incredibly low. Increasing the number of layers from five to seven caused a steady increase in the density of the ZnO film. The figure illustrates how the number of layers increases from three to seven, resulting in a gradual increase in peak intensity, indicating higher film density. As the number of layers increased, the (002) peak also became sharper, suggesting improved crystallinity with increasing film thickness [20].

This behavior can be explained by competitive growth among adjacent crystallites based on their orientation. Crystals with energetically favorable orientations grow at the expense of others, leading to a dominant crystallographic orientation and improved overall crystallinity [21, 22]. This competitive growth mechanism likely accounts for the observed increase in crystallinity as the film thickness increased, as supported by the decreasing FWHM values [23,24]. The average crystallite sizes were calculated using Scherrer's equation. The crystallite size of the ZnO films decreased from 13.23 nm to 9.86 nm as the film thickness increased.

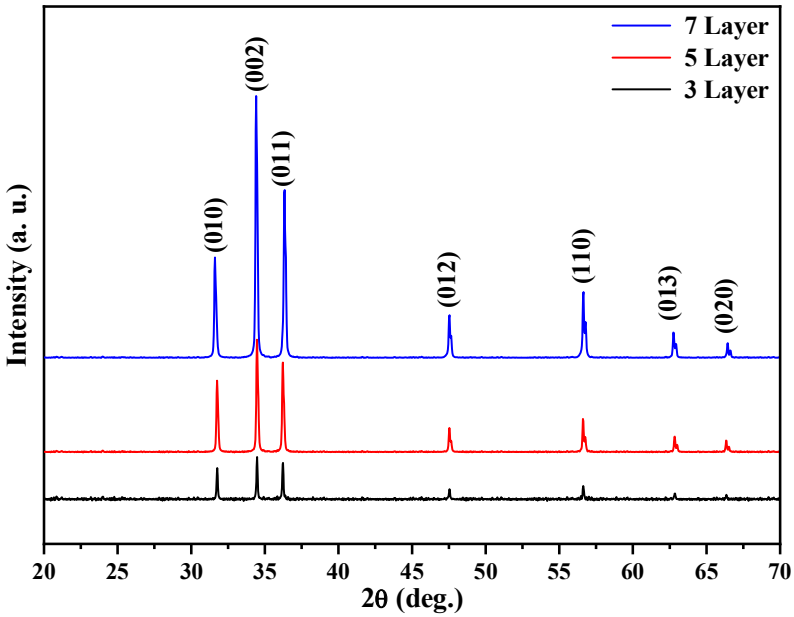

FIG. 1. XRD analysis of the generated ZnO for all films.

Figure 2 presents the surface topography of the annealed ZnO films, analyzed using AFM. The topographical analysis of surface roughness in two and three dimensions is displayed in Fig. 2(a). A 2.0 × 2.0 μm region was scanned from the AFM images of ZnO films. This indicates that the surface morphology is dominated by hexagonally faceted columnar granules. It is clear that the surface roughness of the films increased with their thickness. The 3L film thickness had a grain size of 99.41 nm and a root mean square (RMS) roughness of 2.17 nm; this suggests excellent homogeneity and good crystal regularity. As the number of layers increased to five and seven, the grain size decreased to 86.31 and 73.23 nm, while roughness progressively increased to 3.82 and 4.37 nm, respectively. The roughness increased as the ZnO thickness increased due to the decreasing grain size and the increased number of grains that formed [25, 26]. The high surface roughness of ZnO films makes them useful for gas sensors [27]. The sensitivity and response time of ZnO-based gas sensors are significantly impacted by the degree of roughness of the thin films. As thickness increased, so did the peak-to-peak and ten-point heights, according to Table 1, demonstrating the regularity of the generated films and the viability of using them as sensors, as improved absorption is achieved by surface uniformity [28]. Film roughness influences the sensor response by increasing the surface area specifically suited for gas adsorption [29]. To improve the gas sensor device, this increase is essential.

TABLE 1. AFM parameters of ZnO films with 3, 5, and 7 layers.

Sample ZnO layers	Ave. diameter (nm)	Roughness (nm)	R.M.S (nm)	Peak-peak (nm)	Ten-point hight (nm)
3 La.	99.41	2.17	2.36	11.48	6.28
5 La	86.31	3.82	4.22	14.29	12.77
7La.	75.23	4.37	4.83	18.32	12.57

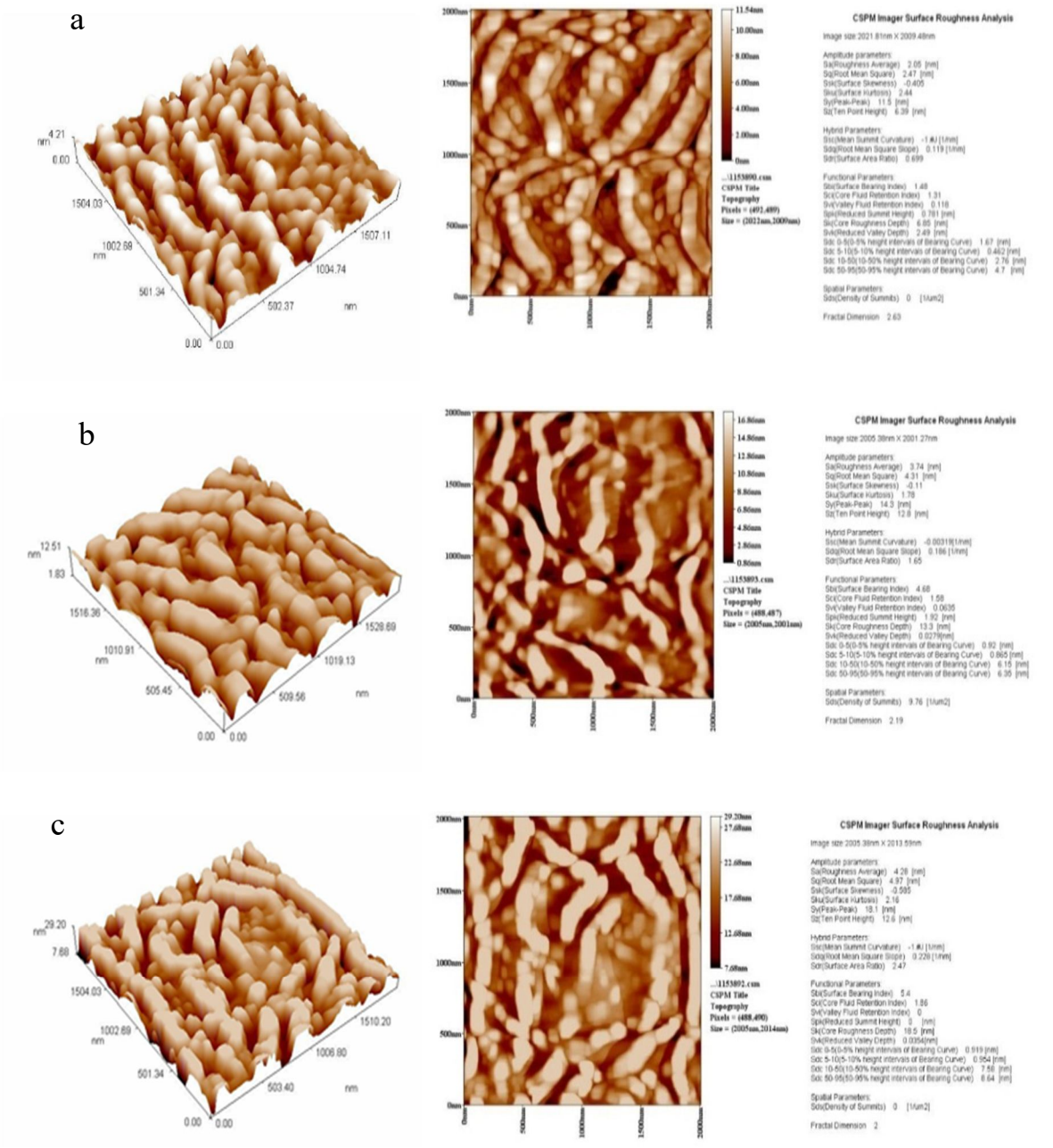

FIG. 2. AFM images of ZnO thin films with 3, 5, and 7 layers.

Figure 3 shows the transmittance spectra of ZnO films measured over the wavelength range of 200–1100 nm. The impact of layer count on ZnO film optical characteristics, including transmittance and band gap, was examined. The transmittance curves of ZnO films at different film thicknesses are shown in Fig 3. All of the samples exhibited good transparency, exceeding 84%. As the film thickness and surface roughness increased, the transmittance changed. This result was expected since when the thickness of a material increases, photons are absorbed into it in greater quantities. Additionally, the spectra revealed a shift in the absorption edge toward higher energies, which is associated with the thickness values. As the film thickness increased, the free spectral range decreased, resulting in more oscillations with the substrate [30]. Therefore, oscillations increased toward longer wavelengths. Interferences in the substrate are generally not observable in the incoherent formulation. However, it is well known that below the radiation wavelength of 500 nm (toward higher energy side of visible spectrum), the absorption coefficient of TCOs increases gradually and peaks at the ultraviolet (UV) region, resulting in the disappearance of interference patterns of the transmission

spectrum in this region (i.e., higher energy-side of the spectrum) [31, 32]. Since the absorbance increases with increasing thickness, the absorption coefficient decreases. Therefore, the phenomenon of optical quantum confinement is not achieved [24, 33]. Figure 4 shows the Tauc's plot for ZnO films as a function of film thickness. The band gap grew from 3.31 to 3.39 eV as the film thickness increased. As layer thickness increases, the optical band gap rises because of other lattice defects and a decreasing trend in strain. This is consistent with what Ennaceri, Houda, *et al.* found [34, 35]. The reduction in nanosize, which supports the charge carrier quantum confinement, may also be the cause of this [36, 37] and determines the band gap of the film (Fig. 4).

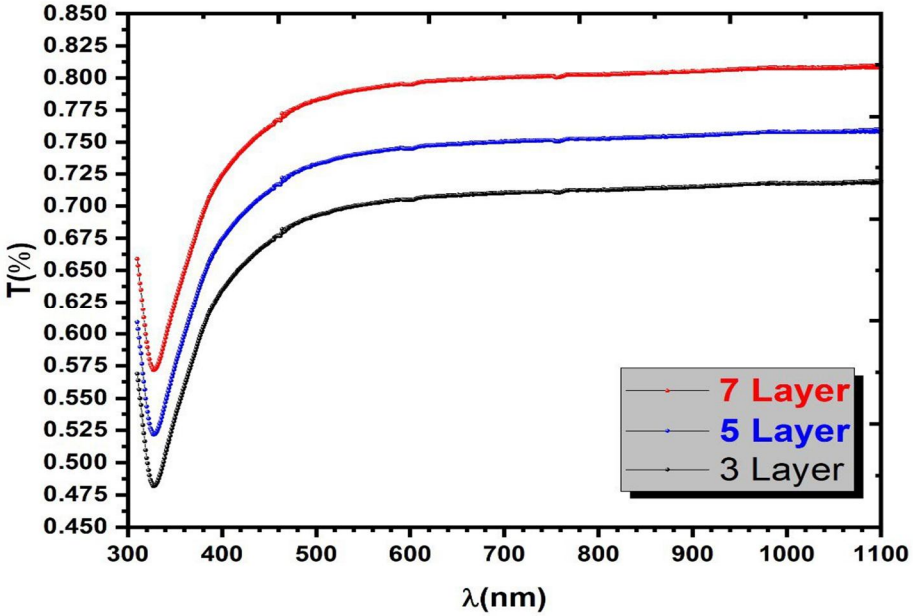

FIG. 3. The ZnO transmittance of all layers.

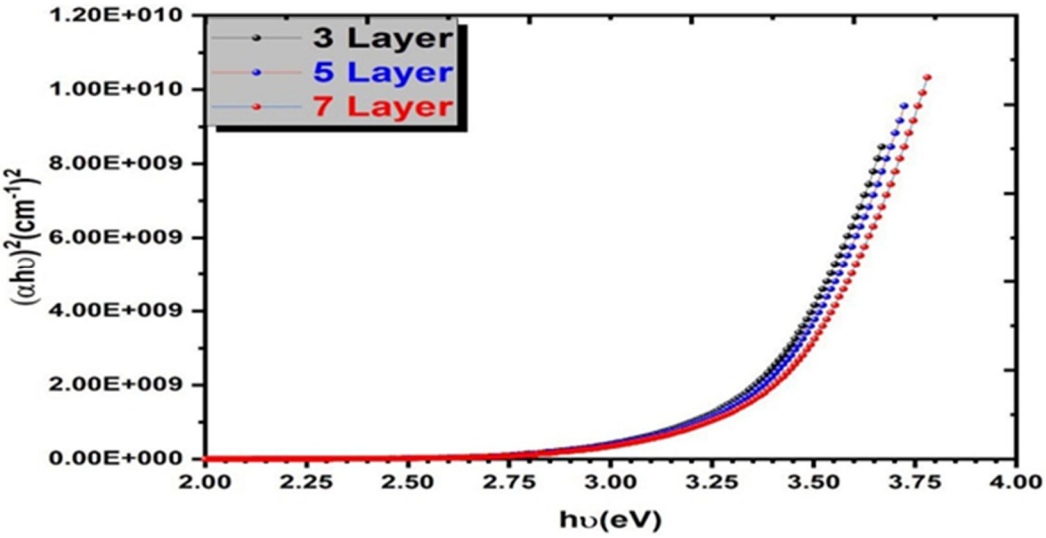

FIG. 4. The ZnO energy gap of all layers.

Figure 5 shows FE-SEM images of the surface for ZnO films on silicon papered by spin-coated with 3, 5, and 7 layers. Nanoparticles were formed on structure thin films. The image for FE-SEM shows height difference possibility in structures. As shown in Fig. 5(a), the ZnO film spin-coated with three layers shows less dense structure compared to the ZnO thin film spin-coated with five layers, depicted in Fig. 5(b). The ZnO thin film with seven layers, shown in Fig. 5(c), displays a more compact and uniform morphology with larger grains after annealing. This enhances the sensitivity characteristics of the gas sensor.

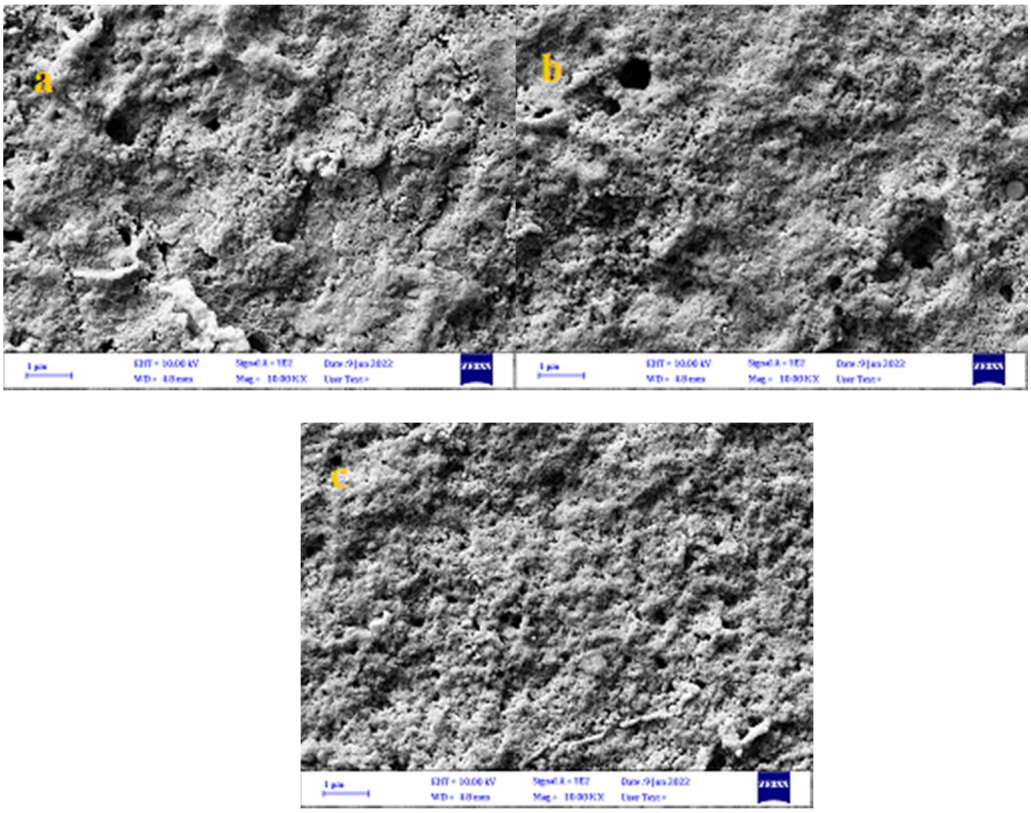

FIG. 5. The FESEM image of the surface for ZnO all layers.

Figures 6, 7, and 8 show the gas sensing properties when the thin films were exposed to the surrounding air. The conduction band electrons on the film's surface were grabbed by oxygen molecules that were adsorbed there [38]. Consequently, a depletion zone developed close to the surface, increasing the film's resistance [39]. Eqs. (1) and (2) show that when reducing gases, such as ammonia, were added to all layers of thin ZnO, they reacted with the adsorbed oxygen species.

$$O_2 + e^- \rightarrow O_{2(ads)} \quad (1)$$

$$NH_3 + 3O^-_{2(ads)} \rightarrow 2N_2 + 6H_2O + 6e^- \quad (2)$$

Due to the reducing nature of NH_3, the ZnO film's surface resistance was reduced by the interaction of ammonia molecules with the oxygen-adsorbed ZnO surface. When NH_3 entered the detecting chamber, the resistance of the thin ZnO film quickly decreased, leading to a quick rise in sensor response. When the NH_3 flow was stopped, the resistance increased, causing the response sensor to progressively return to its initial levels. Figures 6-8 show how resistance affected sensitivity for thin ZnO films with three, five, and seven layers at a 50 ppm ammonia concentration. The sensitivity (S%) of the ZnO films was calculated using Eq. (3) [40]:

$$S\% = \frac{R_a - R_g}{R_g} * 100\% \quad (3)$$

where R_a and R_g are resistances in air and testing gas, respectively.

The increased number of layers led to a higher sensor response, as shown in Figs. 6-8. Table 2 indicates that the maximum sensor response (35.81%) was attained at room temperature when there were seven layers. This is caused by a decrease in grain size and an increase in surface roughness of the thin film, with a response time of 14.4 s and a recovery time of 9.4 s, as indicated in Table 2. Additionally, we observed that throughout all samples, the sensitivity increased as the operating temperature rose, peaking at 140.7 at 150℃ for the seven-layer film. The reason for this is that the grain size has decreased and the surface roughness has increased, as shown in Fig. 8. This is crucial for determining how surface roughness and grain size affect the development of highly sensitive ZnO ammonia sensors.

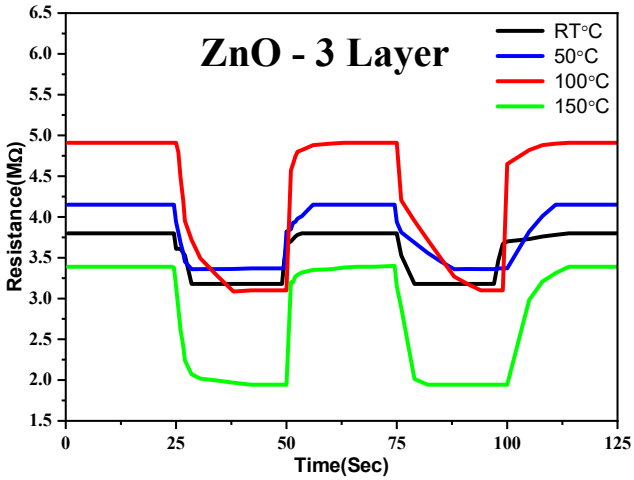

FIG. 6. Sensitivity of 3 layers of ZnO nanoparticles to 50 ppm ammonia as a function of resistance.

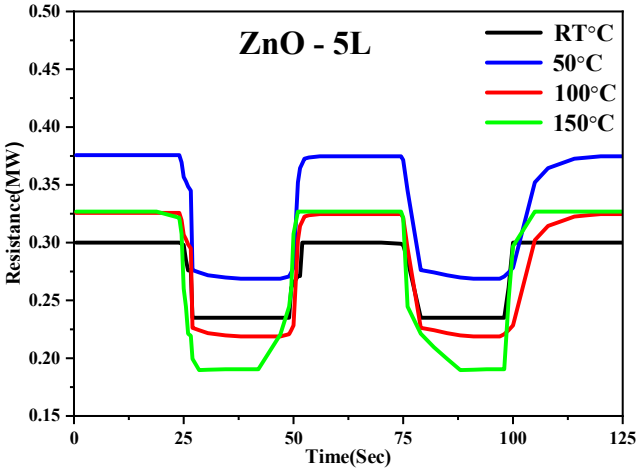

FIG. 7. Sensitivity of 5 layers of ZnO nanoparticles to 50 ppm ammonia as a function of resistance.

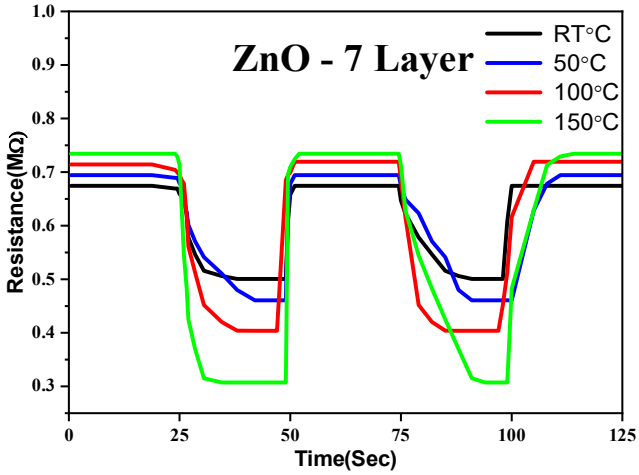

FIG. 8. Sensitivity of 7 layers of ZnO nanoparticles to 50 ppm ammonia as a function of resistance.

TABLE 2. ZnO sensitivity, response, and recovery time at layers 3, 5, and 7.

Samples	response time (s)				recovery time (s)				sensitivity (S%)			
	RT	50	100	150	RT	50	100	150	RT	50	100	150
3 La.	12.21	11.9	11.44	14.95	13.88	16.54	15.5	10.44	19.6	23.4	58.7	75.3
5 La.	8.43	12.7	11.6	9.65	13.76	13.34	12.7	14.95	27.8	39.9	47.6	76.7
7 La.	14. 4	13.9	12.22	9.6	9.4	8.53	8.32	9.56	35.8	51.7	73.3	140.7

Conclusions

Using the spin coating technique, ZnO thin films were produced for use as NH_3 gas sensors at room temperature and at operating temperatures of 50, 100, and 150 °C. The study examined how surface roughness and grain size affect ZnO films by varying the number of layers and concentration (50 ppm). The ZnO films with 3, 5, and 7 layers had the highest sensitivity small grains exhibited, which rose with an increase in working temperature. At 150 °C, the created sensor can be used to gas monitoring concentrations below 50 ppm. Films with small grains recovered faster than those with larger grains, even though they reacted to ammonia exposure more slowly. The recovery time and response time were both within 10 s. The outcomes showed that the synthesis of ZnO ammonia sensors using room-temperature spin-coating deposition was feasible, and that ZnO capacity to detect ammonia is significantly impacted by adjusting grain size to operating temperature. Consequently, it is thought that results could offer useful direction for upcoming industrial applications in the development of high-performance gas sensors.

Acknowledgements

The electronics laboratory at the College of Education of Pure Science, University of Anbar.

Funding Declaration

No funding was received for this work

Data Availability Statement

All data are available if requested by the reviewers. External data inferred within the manuscript are cited in the references.

Conflict of interest:

The authors have no conflicts to disclose.

Ethics Approval:

Ethics approval not required.

Author Contribution Declaration:

Ahmad Z. Al-Jenaby: Conceptualization, data duration, formal analysis, investigation, methodology, software, supervision, validation, visualization, writing – original draft, writing review & editing. Othman. A. Fahad: investigation, methodology، supervision, validation, and writing – original draft. Saadallah F. Hasan: writing– review & editing.

References

[1] Kuo, S.-Y., Chen, W.-C., and Cheng, C.-P., Superlattices Microstruct., 39 (1-4) (2006) 162.

[2] Banerjee, A. et al., Thin Solid Films, 496 (1) (2006) 112.

[3] Sivaramakrishnan, K. and Alford, T., Appl. Phys. Lett., 96 (20) (2010).

[4] Rwenyagila, E.R. et al., J. Mater. Res., 29 (24) (2014) 2912.

[5] Alzamzoum, T. et al., Jordan J. Phys., 17 (5) (2024) 577.

[6] Minami, T., Semicond. Sci. Technol., 20 (4) (2005) S35.

[7] Basyooni, M.A., Eker, Y.R., and Yilmaz, M., Superlattices Microstruct., 140 (2020) 106465.

[8] Korotcenkov, G., Mater. Sci. Eng. R Rep., 61 (1-6) (2008) 1.

[9] Xu, C. et al., Sens. Actuators B Chem., 3 (2) (1991) 147.

[10] Wang, X., Yee, S.S., and Carey, W.P., Sens. Actuators B Chem., 25 (1-3) (1995) 454-457.

[11] Bezy, N.A. et al., Jordan J. Phys., 17 (2) (2024) 245.

[12] Villanueva, Y.Y., Liu, D.-R., and Cheng, P.T., Thin Solid Films, 501 (1-2) (2006) 366.

[13] Fahad, O.A., Ramizy, A., and Al-Rawi, B.K., J. Mater. Sci. Mater. Electron., 35 (27) (2024) 1822.

[14] Al-Rashid, S.N.T., Nanosci. Technol. Int. J., 15 (3) (2024).

[15] Fahad, O.A., J. Opt., 2024 (2024) 1.

[16] Tamil Illakkiya, J. et al., Emerg. Mater. Res., 5 (1) (2016) 57.

[17] Rao, T.P. and Santhoshkumar, M., Appl. Surf. Sci., 255 (8) (2009) 4579.

[18] Tang, H. et al., J. Mater. Sci., 44 (2) (2009) 563.

[19] Al-Jenaby, A.Z., Al-Samarai, A.-M.E., and Ramizy, A., Mater. Today Proc., 42 (2021) 2840.

[20] Seto, J.Y., J. Electrochem. Soc., 122 (5) (1975) 701.

[21] Knuyt, G. et al., Phys. Status Solidi B, 195 (1) (1996) 179.

[22] Barna, P. and Adamik, M., Thin Solid Films, 317 (1-2) (1998) 27.

[23] Hasan, S.F. et al., IOP Conf. Ser. Mater. Sci. Eng., IOP Publishing, (2021).

[24] Fahad, O.A. et al., Sens. Actuators A Phys., 383 (2025) 116198.

[25] Kakati, N. et al., Thin Solid Films, 519 (1) (2010) 494.

[26] Al-Jenaby, A.Z., Ramizy, A., and Al-Samarai, A.-M.E., AIP Conf. Proc., AIP Publishing, (2022).

[27] Lee, J.H. et al., Nanotechnology, 20 (39) (2009) 395704.

[28] Hasan, S.F. et al., J. Opt., 2024 (2024) 1.

[29] Roy, S. and Basu, S., Bull. Mater. Sci., 25 (2002) 513.

[30] Mustafa, A. and Al-Rashid, S., Chalcogenide Lett., 21 (5) (2024) 407.

[31] Abdalameer, N.K., Fahad, O.A., and Khalaph, K.A., Int. J. Nanosci., 21 (01) (2022) 2150062.

[32] Fahad, O.A. et al., Int. J. Nanosci., 20 (06) (2021) 2150055.

[33] Al-Rawi, B.K. and Mazhir, S.N., Int. J. Nanosci., 22 (05) (2023) 2350044.

[34] Ennaceri, H. et al., Sol. Energy Mater. Sol. Cells, 201 (2019) 110058.

[35] Pankove, J.I., "Optical processes in semiconductors", (Courier Corporation, 1975).

[36] Hasan, S.F. et al., AIP Conf. Proc., AIP Publishing, (2022).

[37] Abed, H.A., Al Rashid, S.N., and Mazhir, S.N., Int. J. Nanosci., 22 (06) (2023) 2330005.

[38] Mohammed, A.S. and Fahad, O.A., AAIP Conf. Proc., AIP Publishing, (2021).

[39] Al-Jenaby, A.Z., Ramizy, A., and Al-Samarai, A.-M.E., IOP Conf. Ser. Mater. Sci. Eng., IOP Publishing, (2021).

[40] Barsan, N. and Weimar, U., J. Electroceram., 7 (2001) 143.

Volume 18, Number 5, 2025. pp. 669-693

Jordan Journal of Physics

ARTICLE

Derivation of the Lorentz Transformation Equations for Determination of their Matrix Form

Chandra Bahadur Khadka

Department of Physics, Tri-Chandra Multiple Campus, Tribhuvan University, Kathmandu-44600, Nepal.

Doi: **https://doi.org/10.47011/18.5.9**

Received on: 16/01/2025; *Accepted on: 23/02/2025*

Abstract: This article introduces a modified version of the Lorentz transformation equations that transform spacetime coordinates between two inertial frames when the relative motion between them occurs along the X-, Y-, and Z-directions, and represents an extension of the one-dimensional Lorentz transformation equations to three spatial dimensions. Making use of the invariance of the spacetime interval, the paper demonstrates that an event in the spacetime continuum can be represented by six coordinates, of which the first three represent the spatial coordinates, and the remaining three represent the time coordinates. By employing the notion of a position six-vector, the correct matrix form of the Lorentz transformation equations of order 6 × 6 has been thoroughly developed. In addition, the D'Alembert operator, the basic ingredient of the wave equation, is shown to be form-invariant under the modified Lorentz transformation equations. Furthermore, the relativistic velocity addition formulas, as well as the Lorentz transformations of linear momentum and energy, have been theoretically analyzed on the basis of the extended Lorentz transformations. Finally, the particular purpose of this work is to present equal and opposite relativistic spacetime coordinate transformation equations between inertial frames, which properly allow for the formulation of the correct matrix form of the Lorentz transformation equations in terms of the position six-vector.

Keywords: Four-vector, Lorentz transformation equations, Minkowski space, Special relativity.

Introduction

This paper presents the matrix form of the three-dimensional (3D) Lorentz transformation equations; therefore, it is recommended to read Ref. [1] in advance, which discusses spacetime coordinate transformations when the motion between inertial frames takes place in 3D space.

The Lorentz transformation, which is considered the backbone of the special theory of relativity, is a well-known and powerful theoretical tool for providing an accurate explanation of spatial and temporal phenomena occurring in the realm of relativistic mechanics. The Lorentz transformation equations were invented by Voigt [2] in 1887, adopted by Lorentz [3] in 1904, and further analyzed by Poincaré [4] in 1905. Einstein [5] likely derived them directly from Voigt's work. The contemporary version of the Lorentz transformation equations, when the motion between inertial frames is one-dimensional (1D) along a single X-axis, is defined as follows:

$$\left.\bar{x}=\frac{x-vt}{\sqrt{1-\frac{v^2}{c^2}}},\bar{t}=\frac{t-\frac{vx}{c^2}}{\sqrt{1-\frac{v^2}{c^2}}},\bar{y}=y,\bar{z}=z\right\}, \quad (1)$$

Here, (x,y,z,t) and $(\bar{x},\bar{y},\bar{z},\bar{t})$ are the spacetime coordinates measured in the rest and moving frames of reference, respectively. Equation (1) in four-vector form can be represented as follows:

$$\left.\bar{x}_1=\gamma(x_1+i\rho x_4),\bar{x}_4=\gamma(x_4-i\rho x_1),\bar{x}_2=x_2,\bar{x}_3=x_3\right\}, \quad (2)$$

Here, $(\bar{x}_1,\bar{x}_2,\bar{x}_3,\bar{x}_4)=(\bar{x},\bar{y},\bar{z},ic\bar{t})$, $(x_1,x_2,x_3,x_4)=(x,y,z,ict)$, $\rho=v/c$, $\gamma=1/\sqrt{1-\rho^2}$.

Corresponding Author: Chandra Bahadur Khadka **Email**: chandrabahadur9988@gmail.com

Various derivations of Eqs. (1) and (2) can be found in the literature, such as in the works of Feynman *et al.* [6] and Landau and Lifshitz [7]. If we examine Eq. (1) carefully, it becomes evident that the transformation of time $\bar{t}$ depends only on a single spatial coordinate, x. Thus, Eq. (1) clearly fails to relate y and z space coordinates to the time coordinate ict, as it is formulated on the basis of one-dimensional motion between inertial frames. Fortunately, a recently published article [1] formulates the correct Lorentz transformation equations, also known as 3D Lorentz transformations, for the case in which the motion between inertial frames takes place along the X-, Y-, and Z-directions. These transformations are of the following form [1]:

$$\left.\begin{aligned} \bar{x} &= \frac{x-\frac{vtx}{\sqrt{x^2+y^2+z^2}}}{\sqrt{1-\frac{v^2}{c^2}}}, \bar{y} = \frac{y-\frac{vty}{\sqrt{x^2+y^2+z^2}}}{\sqrt{1-\frac{v^2}{c^2}}} \\ \bar{z} &= \frac{z-\frac{vtz}{\sqrt{x^2+y^2+z^2}}}{\sqrt{1-\frac{v^2}{c^2}}}, \bar{t} = \frac{t-\frac{v\sqrt{x^2+y^2+z^2}}{c^2}}{\sqrt{1-\frac{v^2}{c^2}}} \end{aligned}\right\}, \quad (3)$$

Equation (3) above represents an extended version of the one-dimensional Lorentz transformation equations to three spatial dimensions when there is simultaneous relative motion along the X-, Y-, and Z-axes. These three-dimensional transformations treat each spatial coordinate on equal footing, and the transformation of time $\bar{t}$ depends equally on the X-, Y-, and Z-coordinates. In Ref. [1], the 3D transformations were formulated to explain the phenomenon of space contraction; however, in the present work, the same 3D transformations are retrieved to construct the correct matrix form of the Lorentz transformation equations. Based on the contents of our work, an event in the spacetime continuum can be represented by six-vectors $(x_1, x_2, x_3, x_4, x_5, x_6)$ out of which the first three denote the space coordinates and the last three denote the time coordinates. The 3D Lorentz transformation given in Eq. (3), expressed in terms of six-vectors, takes the following form:

$$\left.\begin{aligned} \bar{x}_1 &= \gamma(x_1 + i\rho x_4), \\ \bar{x}_2 &= \gamma(x_2 + i\rho x_5), \\ \bar{x}_3 &= \gamma(x_3 + i\rho x_6) \\ \bar{x}_4 &= \gamma(x_4 - i\rho x_1), \\ \bar{x}_5 &= \gamma(x_5 - i\rho x_2), \\ \bar{x}_6 &= \gamma(x_6 - i\rho x_3) \end{aligned}\right\}, \quad (4)$$

It should be noted that Eqs. (1) and (2) represent spacetime coordinate transformations when the relative motion between inertial frames is aligned along a single X-axis, whereas Eqs. (3) and (4) represent spacetime coordinate transformations when the relative motion between inertial frames takes place along the X-, Y-, and Z-directions. In concise terms, this work develops the three-dimensional Lorentz transformations, namely Eq. (3), by considering simultaneous relative motion along the X-, Y-, and Z-directions, and also presents their formulation in terms of six-vectors, namely Eq. (4).

Albert Einstein and Henri Poincaré considered the concept of three-dimensional time many years ago, such that space and time would possess the same dimensionality. At present, many authors in works [8–12] introduce multidimensional time in order to provide better explanations of quantum mechanics and spin. Some time ago, Recami and Mignani [13], Pappas [14], Guy [15], and Weinberg [16] added two extra time coordinates to the four-dimensional spacetime coordinates to interpret imaginary quantities in superluminal Lorentz transformations. In Ref. [17], three-dimensional time is also proposed, along with the replacement of the Lorentz transformation by vector Lorentz transformations. The author of Article [18] obtained a general subluminal Lorentz transformation in six-dimensional spacetime. Paper [19] explains the phenomenon of time dilation on the basis of a special theory of ether. In Work [20], it was shown that the existence of a universal frame of reference in which light propagates remains an unresolved problem in physics. Paper [21] presents a method for parameterizing new Lorentz spacetime coordinates based on coupled parameters. Article [22] introduces an innovative method for deriving infinitely many dynamics in relativistic mechanics. The author of Article [23] describes a Lorentz-invariant extension of Newton's second law. The authors of Works [24, 25] propose an original method for deriving transformation equations for kinematics with a universal reference system. The author of Work [26] provides a mathematical interpretation of the Lorentz transformation equations between inertial frames of reference moving in two spatial dimensions. Reference [27] demonstrates the phenomenon of space contraction along the X-, Y-, and Z-directions by introducing relative

motion between inertial frames in three-dimensional space. Reference [28] gives a detailed explanation of time dilation and the relativity of simultaneity in two- and three-dimensional space.

The structure of this paper is organized as follows. In the next Section, we introduce the transformation equations along the X-, Y-, and Z-axes when the motion between coordinate systems takes place in three-dimensional space. In the subsequent Section, we develop new modified three-dimensional spacetime transformation equations for the X-, Y-, and Z-axes. In the Section that follows, we formulate the exact matrix form of the Lorentz transformations by introducing the notion of six-vectors. Next, we discuss the invariance of the spacetime interval and the D'Alembert operator under the six new Lorentz transformation equations. In the following Section, we develop formulas for relativistic velocity addition and for the transformation of momentum and energy on the basis of the extended three-dimensional Lorentz transformation equations. The conclusion is presented in the final Section.

2. Methods

2.1 Transformation Equations between Inertial Frames

Consider two inertial reference frames, K and K', with relative velocity v between them along the radius vector r in 3D space, as shown in Fig. 1. The Cartesian space coordinates of a point P are (x, y, z) and $(\bar{x}, \bar{y}, \bar{z})$ in frames K and K' respectively while the respective corresponding polar coordinates of the same point are (r, α, β) and $(\bar{r}, \alpha, \beta)$. Here, the angles α and β are the same for observers in both the K and K' systems due to symmetric space contraction in the X-, Y-, and Z-directions. If the motion between the frames of reference occurs in three dimensions of space, then simultaneous space contraction takes place in the X-, Y-, and Z-directions by the same Lorentz factor, which consequently keeps the angles α and β identical in both frames of reference. For further details, it is strongly recommended to consult Ref. [1].

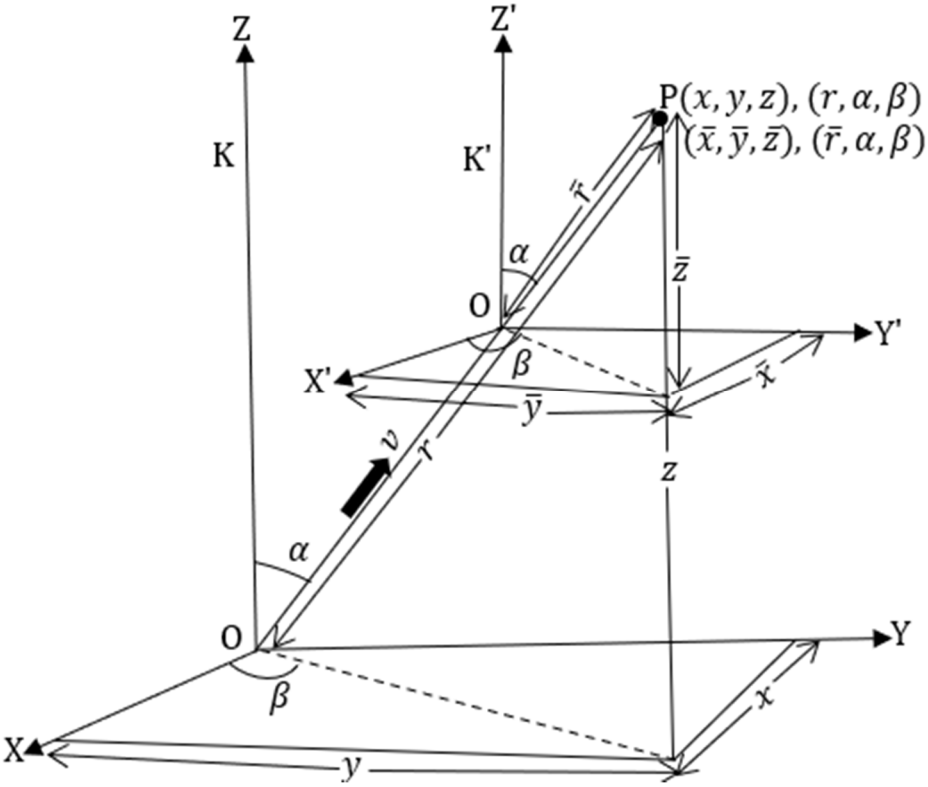

FIG. 1. Motion between inertial frames in three-dimensional space.

Consider time measured in the rest frame by the variable t and in the moving frame by the variable $\bar{t}$. The coordinate axes in the two frames are parallel and oriented such that frame K' is moving in three-dimensional space with speed v, as viewed from frame K. For simplicity, let the origins of the coordinates in K and K' be coincident at $t = \bar{t} = 0$. If a light source at rest

at the origin in K is flashed on and off rapidly at $t = \bar{t} = 0$, then Einstein's second postulate implies that observers in both K and K' will see a spherical shell of radiation expanding outward from the respective origins with speed c along the radius vector r. Breaking up the resultant velocity of light c into X-component $c_x = c\sin\alpha\cos\beta$, Y-component $c_y = c\sin\alpha\sin\beta$, and Z-component $c_z = c\cos\alpha$ allows us to deal with each direction separately (see Fig. 1). Hence, the equation of the wavefront of light along the X-axis in the frame K is given by the equation:

$$x^2 - (c_x t)^2 = 0,$$

$$x^2 - c^2t^2\sin^2\alpha\cos^2\beta = 0. \quad (5)$$

where $c_x = c\sin\alpha\cos\beta$ be the component of the velocity of light along the X-axis. According to the constancy of the speed of light, the component of velocity of light along the X-, Y-, and Z-directions in the K' frame should be the same as in the K frame of reference. Therefore, in frame K', the equation of wavefront light along the X-axis is specified by the equation:

$$\bar{x}^2 - (c_x\bar{t})^2 = 0,$$

$$\bar{x}^2 - c^2\bar{t}^2\sin^2\alpha\cos^2\beta = 0. \quad (6)$$

Since both the frames are at the center of the expanding wavefront at $t = \bar{t} = 0$, Eqs. (5) and (6) must be equal.

$$x^2 - c^2t^2\sin^2\alpha\cos^2\beta = \bar{x}^2 - c^2\bar{t}^2\sin^2\alpha\cos^2\beta. \quad (7)$$

Equation (7) represents the wavefront of light along the X-axis when motion between inertial frames is in three-dimensional space. Similarly, the equation of the wavefront of light along the Y-axis in the frame K is given by the equation:

$$y^2 - \left(c_y t\right)^2 = 0,$$

$$y^2 - c^2t^2\sin^2\alpha\sin^2\beta = 0. \quad (8)$$

where $c_y = c\sin\alpha\sin\beta$ be the component of the velocity of light along the Y-axis. Also, in frame K', the equation of the wavefront of light along the Y-axis is specified by the equation:

$$\bar{y}^2 - \left(c_y\bar{t}\right)^2 = 0,$$

$$\bar{y}^2 - c^2\bar{t}^2\sin^2\alpha\sin^2\beta = 0. \quad (9)$$

Since both the frames are at the center of the expanding wavefront at $t = \bar{t} = 0$, Eqs. (8) and (9) must be equal.

$$y^2 - c^2t^2\sin^2\alpha\sin^2\beta = \bar{y}^2 - c^2\bar{t}^2\sin^2\alpha\sin^2\beta. \quad (10)$$

Equation (10) represents the wavefront of light along the Y-axis when motion between inertial frames is in three-dimensional space. Similarly, the equation of the wavefront of light along the Z-axis in the frame K is given by the equation:

$$z^2 - (c_z t)^2 = 0,$$

$$z^2 - c^2t^2\cos^2\alpha = 0. \quad (11)$$

where $c_z = c\cos\alpha$ be the component of the velocity of light along the Z-axis. Also, in frame K', the equation of the wavefront of light along the Z-axis is specified by the equation:

$$\bar{z}^2 - (c_z\bar{t})^2 = 0,$$

$$\bar{z}^2 - c^2\bar{t}^2\cos^2\alpha = 0. \quad (12)$$

Since both the frames are at the center of the expanding wavefront at $t = \bar{t} = 0$, Eqs. (11) and (12) must be equal.

$$z^2 - c^2t^2\cos^2\alpha = \bar{z}^2 - c^2\bar{t}^2\cos^2\alpha. \quad (13)$$

Equation (13) represents the wavefront of light along the Z-axis when motion between inertial frames is in three-dimensional space. The frame K' is moving away from the rest frame K in such a way that there is relative motion along the X-, Y-, and Z-directions simultaneously, as shown in Fig. 1. Let v denote the velocity of the moving frame along the radius vector r in 3D space. Breaking up the resultant velocity v into X-component $v_x = v\sin\alpha\cos\beta$, Y-component $v_y = v\sin\alpha\sin\beta$, and Z-component $v_z = v\cos\alpha$ allows us to deal with each direction separately. Hence, the respective transformation equations from frame K to K' along the X-, Y-, and Z-axes are as follows:

$$\bar{x} = x - v_x t = x - vt\sin\alpha\cos\beta,$$

$$\bar{y} = y - v_y t = y - vt\sin\alpha\sin\beta,$$

$$\bar{z} = z - v_z t = z - vt\cos\alpha.$$

The three equations above are valid only in classical mechanics, but not in relativistic mechanics. Therefore, multiplying them by the Lorentz coefficient γ, we get:

$$\bar{x} = \gamma(x - vt\sin\alpha\cos\beta), \quad (14)$$

$$\bar{y} = \gamma(y - vt\sin\alpha\sin\beta), \quad (15)$$

$$\bar{z} = \gamma(z - vt\cos\alpha). \quad (16)$$

Similarly, the respective inverse transformation equations from frame K' to K along the X-, Y-, and Z-directions are as follows:

$$x = \bar{x} + v_x\bar{t} = \bar{x} + v\bar{t}\sin\alpha\cos\beta,$$

$$y = \bar{y} + v_y\bar{t} = \bar{y} + v\bar{t}\sin\alpha\sin\beta,$$

$$z = \bar{z} + v_z\bar{t} = \bar{z} + v\bar{t}\cos\alpha.$$

where $v_x = v\sin\alpha\cos\beta$, $v_y = v\sin\alpha\sin\beta$ and $v_z = v\cos\alpha$ are the components of velocity along the X-, Y-, and Z-directions, respectively. The above three equations are valid only in classical mechanics, but not in relativistic mechanics. Therefore, multiplying them by the Lorentz coefficient $\bar{\gamma}$, we get:

$$x = \bar{\gamma}(\bar{x} + v\bar{t}\sin\alpha\cos\beta), \quad (17)$$

$$y = \bar{\gamma}(\bar{y} + v\bar{t}\sin\alpha\sin\beta), \quad (18)$$

$$z = \bar{\gamma}(\bar{z} + v\bar{t}\cos\alpha). \quad (19)$$

Furthermore, the following equations show the mathematical relationship between Cartesian coordinates (x, y, z) and polar coordinates (r, α, β) of point P measured from the K frame of reference (see Fig. 1).

$$x = r\sin\alpha\cos\beta, \quad (20)$$

$$y = r\sin\alpha\sin\beta, \quad (21)$$

$$z = r\cos\alpha. \quad (22)$$

Squaring both sides of Eqs. (20)-(22) and then adding them, we get:

$$r^2\sin^2\alpha\cos^2\beta + r^2\sin^2\alpha\sin^2\beta + r^2\cos^2\alpha = x^2 + y^2 + z^2,$$

$$r^2\sin^2\alpha(\cos^2\beta + \sin^2\beta) + r^2\cos^2\alpha = x^2 + y^2 + z^2,$$

$$r^2\sin^2\alpha + r^2\cos^2\alpha = x^2 + y^2 + z^2,$$

$$r^2 = x^2 + y^2 + z^2,$$

$$r = \sqrt{x^2 + y^2 + z^2}. \quad (23)$$

Also, the following equations show the mathematical relationship between Cartesian coordinates $(\bar{x}, \bar{y}, \bar{z})$ and polar coordinates $(\bar{r}, \alpha, \beta)$ of point P measured from the K' frame of reference (see Fig. 1).

$$\bar{x} = \bar{r}\sin\alpha\cos\beta, \quad (24)$$

$$\bar{y} = \bar{r}\sin\alpha\sin\beta, \quad (25)$$

$$\bar{z} = \bar{r}\cos\alpha. \quad (26)$$

Squaring both sides of Eqs. (24)-(26) and then adding them, we get:

$$\bar{r}^2\sin^2\alpha\cos^2\beta + \bar{r}^2\sin^2\alpha\sin^2\beta + \bar{r}^2\cos^2\alpha = \bar{x}^2 + \bar{y}^2 + \bar{z}^2,$$

$$\bar{r}^2\sin^2\alpha(\cos^2\beta + \sin^2\beta) + \bar{r}^2\cos^2\alpha = \bar{x}^2 + \bar{y}^2 + \bar{z}^2,$$

$$\bar{r}^2\sin^2\alpha + \bar{r}^2\cos^2\alpha = \bar{x}^2 + \bar{y}^2 + \bar{z}^2,$$

$$\bar{r}^2 = \bar{x}^2 + \bar{y}^2 + \bar{z}^2,$$

$$\bar{r} = \sqrt{\bar{x}^2 + \bar{y}^2 + \bar{z}^2}. \quad (27)$$

2.2 Lorentz Transformation Equations Along the X-axis

From Eq. (17), the relativistic transformation equation along the X-axis is given by the equation:

$$x = \bar{\gamma}(\bar{x} + v\bar{t}\sin\alpha\cos\beta),$$

Substituting Eq. (14) into the above expression leads to

$$x = \bar{\gamma}[\gamma(x - vt\sin\alpha\cos\beta) + v\bar{t}\sin\alpha\cos\beta],$$

$$x = \bar{\gamma}\gamma x - \bar{\gamma}\gamma vt\sin\alpha\cos\beta + \bar{\gamma}v\bar{t}\sin\alpha\cos\beta,$$

$$\bar{\gamma}v\bar{t}\sin\alpha\cos\beta = \bar{\gamma}\gamma vt\sin\alpha\cos\beta - \bar{\gamma}\gamma x + x,$$

$$\bar{t}\sin\alpha\cos\beta = \gamma t\sin\alpha\cos\beta - \frac{\gamma x}{v} + \frac{x}{\bar{\gamma}v},$$

$$\bar{t} = \frac{\gamma}{\sin\alpha\cos\beta}\left[t\sin\alpha\cos\beta - \frac{x}{v}\left(1 - \frac{1}{\bar{\gamma}\gamma}\right)\right]. \quad (28)$$

Now, substituting Eqs. (28) and (14) into Eq. (7) leads to

$$x^2 - c^2t^2\sin^2\alpha\cos^2\beta = \bar{x}^2 - c^2\bar{t}^2\sin^2\alpha\cos^2\beta, \quad (29)$$

$$x^2 - c^2t^2\sin^2\alpha\cos^2\beta = [\gamma(x - vt\sin\alpha\cos\beta)]^2 - c^2\sin^2\alpha\cos^2\beta\frac{\gamma^2}{\sin^2\alpha\cos^2\beta}\left[t\sin\alpha\cos\beta - \frac{x}{v}\left(1 - \frac{1}{\bar{\gamma}\gamma}\right)\right]^2,$$

$$x^2 - c^2t^2\sin^2\alpha\cos^2\beta = \gamma^2x^2 - 2\gamma^2xvt\sin\alpha\cos\beta + \gamma^2v^2t^2\sin^2\alpha\cos^2\beta - c^2\gamma^2t^2\sin^2\alpha\cos^2\beta + 2c^2\gamma^2t\sin\alpha\cos\beta\frac{x}{v}\left(1 - \frac{1}{\bar{\gamma}\gamma}\right) - \gamma^2c^2\frac{x^2}{v^2}\left(1 - \frac{1}{\bar{\gamma}\gamma}\right)^2,$$

$$x^2 - c^2t^2\sin^2\alpha\cos^2\beta = x^2\left[\gamma^2 - \frac{c^2\gamma^2}{v^2}\left(1 - \frac{1}{\bar{\gamma}\gamma}\right)^2\right] + xt\sin\alpha\cos\beta\left[-2\gamma^2v + \frac{2c^2\gamma^2}{v}\left(1 - \frac{1}{\bar{\gamma}\gamma}\right)\right] + t^2\sin^2\alpha\cos^2\beta(\gamma^2v^2 - c^2\gamma^2),$$

After comparing the corresponding coefficients of $x^2, xt, and\ t^2$ on both sides, the following expressions are obtained:

$$\gamma^2 - \frac{c^2\gamma^2}{v^2}\left(1-\frac{1}{\bar{\gamma}\gamma}\right)^2 = 1, \quad (30)$$

$$\sin\alpha\cos\beta\left[-2\gamma^2 v + \frac{2c^2\gamma^2}{v}\left(1-\frac{1}{\bar{\gamma}\gamma}\right)\right] = 0, \quad (31)$$

$$\sin^2\alpha\cos^2\beta\,(\gamma^2v^2 - c^2\gamma^2) = -c^2\sin^2\alpha\cos^2\beta. \quad (32)$$

Now, Eq. (32) gives

$$-\gamma^2(c^2-v^2) = -c^2,$$

$$\gamma^2 = \frac{c^2}{c^2-v^2} = \frac{1}{1-\frac{v^2}{c^2}},$$

$$\gamma = \frac{1}{\sqrt{1-\frac{v^2}{c^2}}}. \quad (33)$$

And further mathematical calculation results in

$$\gamma^2 = \frac{1}{1-\frac{v^2}{c^2}},$$

$$\frac{v^2}{c^2} = 1 - \frac{1}{\gamma^2}. \quad (34)$$

Again, Eq. (31) yields

$$-v + \frac{c^2}{v}\left(1-\frac{1}{\bar{\gamma}\gamma}\right) = 0,$$

$$\frac{-v^2 + c^2\left(1-\frac{1}{\bar{\gamma}\gamma}\right)}{v} = 0,$$

$$\frac{v^2}{c^2} = \left(1-\frac{1}{\bar{\gamma}\gamma}\right). \quad (35)$$

Substituting Eq. (34) into Eq. (35) leads to

$$1 - \frac{1}{\gamma^2} = \left(1-\frac{1}{\bar{\gamma}\gamma}\right),$$

$$\frac{1}{\gamma} = \frac{1}{\bar{\gamma}},$$

$$\gamma = \bar{\gamma} = \frac{1}{\sqrt{1-\frac{v^2}{c^2}}}.$$

Now, substituting Eq. (33) into (14) leads to

$$\bar{x} = \frac{x - vt\sin\alpha\cos\beta}{\sqrt{1-\frac{v^2}{c^2}}}, \quad (36)$$

Substituting the value of $\sin\alpha\cos\beta$ from Eq. (20) into Eq. (36), and then inserting the value of r from Eq. (23) into the resulting expression, yields

$$\bar{x} = \frac{x-\frac{vtx}{r}}{\sqrt{1-\frac{v^2}{c^2}}} = \frac{x-\frac{vtx}{\sqrt{x^2+y^2+z^2}}}{\sqrt{1-\frac{v^2}{c^2}}}. \quad (37)$$

Equation (37) represents the Lorentz transformation along the X-axis for the case of simultaneous relative motion between inertial frames in three-dimensional space. To obtain the transformation equation for the time coordinate, Eq. (35) is substituted into Eq. (28):

$$\bar{t} = \gamma\left[t - \frac{x}{v\sin\alpha\cos\beta}\left(1-\frac{1}{\bar{\gamma}\gamma}\right)\right],$$

$$\bar{t} = \gamma\left(t - \frac{vx}{c^2\sin\alpha\cos\beta}\right), \quad (38)$$

Using the value of r from Eq. (20) and then substituting Eq. (23), the above expression takes the form

$$\bar{t} = \gamma\left(t - \frac{vr}{c^2}\right) = \gamma\left(t - \frac{v\sqrt{x^2+y^2+z^2}}{c^2}\right),$$

$$\bar{t} = \frac{t-\frac{v\sqrt{x^2+y^2+z^2}}{c^2}}{\sqrt{1-\frac{v^2}{c^2}}}. \quad (39)$$

The inverse space-time coordinates along the X-axis in 3D space can be achieved by exchanging space-time coordinates and replacing v by $-v$ in Eqs. (37) and (39) as follows:

$$x = \frac{\bar{x}+\frac{v\bar{t}\bar{x}}{\sqrt{\bar{x}^2+\bar{y}^2+\bar{z}^2}}}{\sqrt{1-\frac{v^2}{c^2}}}, \quad (40)$$

$$t = \frac{\bar{t}+\frac{v\sqrt{\bar{x}^2+\bar{y}^2+\bar{z}^2}}{c^2}}{\sqrt{1-\frac{v^2}{c^2}}}. \quad (41)$$

2.3 Lorentz Transformation Equations Along the Y-axis

From Eq. (18), the relativistic transformation equation along the Y-axis is:

$$y = \bar{\gamma}(\bar{y} + v\bar{t}\sin\alpha\sin\beta),$$

Substituting Eq. (15) into the above expression leads to

$$y = \bar{\gamma}[\gamma(y - vt\sin\alpha\sin\beta) + v\bar{t}\sin\alpha\sin\beta],$$

$$y = \bar{\gamma}\gamma y - \bar{\gamma}\gamma vt\sin\alpha\sin\beta + \bar{\gamma}v\bar{t}\sin\alpha\sin\beta,$$

$$\bar{\gamma}v\bar{t}\sin\alpha\sin\beta = \bar{\gamma}\gamma vt\sin\alpha\sin\beta - \bar{\gamma}\gamma y + y,$$

$$\bar{t}\sin\alpha\sin\beta = \gamma t\sin\alpha\sin\beta - \frac{\gamma y}{v} + \frac{y}{\bar{\gamma}v},$$

$$\bar{t} = \frac{\gamma}{\sin\alpha\sin\beta}\left[t\sin\alpha\sin\beta - \frac{y}{v}\left(1-\frac{1}{\bar{\gamma}\gamma}\right)\right], \quad (42)$$

Now, substituting Eqs. (42) and (15) into Eq. (10), we get:

$$y^2 - c^2t^2\sin^2\alpha\sin^2\beta = \bar{y}^2 - c^2\bar{t}^2\sin^2\alpha\sin^2\beta, \quad (43)$$

$$y^2 - c^2t^2\sin^2\alpha\sin^2\beta = [\gamma(y - vt\sin\alpha\sin\beta)]^2 - c^2\sin^2\alpha\sin^2\beta\frac{\gamma^2}{\sin^2\alpha\sin^2\beta}\left[t\sin\alpha\sin\beta - \frac{y}{v}\left(1 - \frac{1}{\bar{\gamma}\gamma}\right)\right]^2,$$

$$y^2 - c^2t^2\sin^2\alpha\sin^2\beta = \gamma^2y^2 - 2\gamma^2yvt\sin\alpha\sin\beta + \gamma^2v^2t^2\sin^2\alpha\sin^2\beta - c^2\gamma^2t^2\sin^2\alpha\sin^2\beta + 2c^2\gamma^2t\sin\alpha\sin\beta\frac{y}{v}\left(1 - \frac{1}{\bar{\gamma}\gamma}\right) - \gamma^2c^2\frac{y^2}{v^2}\left(1 - \frac{1}{\bar{\gamma}\gamma}\right)^2,$$

$$y^2 - c^2t^2\sin^2\alpha\sin^2\beta = y^2\left[\gamma^2 - \frac{c^2\gamma^2}{v^2}\left(1 - \frac{1}{\bar{\gamma}\gamma}\right)^2\right] + yt\sin\alpha\sin\beta\left[-2\gamma^2v + \frac{2c^2\gamma^2}{v}\left(1 - \frac{1}{\bar{\gamma}\gamma}\right)\right] + t^2\sin^2\alpha\sin^2\beta\,(\gamma^2v^2 - c^2\gamma^2),$$

After comparing the corresponding coefficients of $y^2, yt\ and\ t^2$ on both sides, the following expressions are obtained

$$\gamma^2 - \frac{c^2\gamma^2}{v^2}\left(1 - \frac{1}{\bar{\gamma}\gamma}\right)^2 = 1, \quad (44)$$

$$\sin\alpha\sin\beta\left[-2\gamma^2v + \frac{2c^2\gamma^2}{v}\left(1 - \frac{1}{\bar{\gamma}\gamma}\right)\right] = 0, \quad (45)$$

$$\sin^2\alpha\sin^2\beta\,(\gamma^2v^2 - c^2\gamma^2) = -c^2\sin^2\alpha\sin^2\beta. \quad (46)$$

On solving the above three equations as done in Section 2.2, we obtain:

$$\gamma = \bar{\gamma} = \frac{1}{\sqrt{1 - \frac{v^2}{c^2}}}, \quad (47)$$

$$\frac{v^2}{c^2} = \left(1 - \frac{1}{\bar{\gamma}\gamma}\right). \quad (48)$$

Substituting Eq. (47) into Eq. (15) leads to

$$\bar{y} = \frac{y - vt\sin\alpha\sin\beta}{\sqrt{1 - \frac{v^2}{c^2}}}, \quad (49)$$

Substituting the value of $\sin\alpha\sin\beta$ from Eq. (21) into Eq. (49), and then putting the value of r from Eq. (23) into the resulting equation, leads to

$$\bar{y} = \frac{y - \frac{vty}{r}}{\sqrt{1 - \frac{v^2}{c^2}}} = \frac{y - \frac{vty}{\sqrt{x^2+y^2+z^2}}}{\sqrt{1 - \frac{v^2}{c^2}}}. \quad (50)$$

Equation (50) is the Lorentz transformation equation along the Y-axis when there is the simultaneous relative motion between inertial systems in 3D space. To find the equation of time coordinates, let us use Eq. (48) in Eq. (42):

$$\bar{t} = \gamma\left[t - \frac{y}{v\sin\alpha\sin\beta}\left(1 - \frac{1}{\bar{\gamma}\gamma}\right)\right],$$

$$\bar{t} = \gamma\left(t - \frac{vy}{c^2\sin\alpha\sin\beta}\right), \quad (51)$$

Using the value of r from Eq. (21) and then substituting Eq. (23), the above expression takes the form

$$\bar{t} = \gamma\left(t - \frac{vr}{c^2}\right) = \gamma\left(t - \frac{v\sqrt{x^2+y^2+z^2}}{c^2}\right),$$

$$\bar{t} = \frac{t - \frac{v\sqrt{x^2+y^2+z^2}}{c^2}}{\sqrt{1 - \frac{v^2}{c^2}}}. \quad (52)$$

Here, it should be noted that the transformation equation of time, namely Eq. (52), is exactly the same as Eq. (39). Hence, the transformation equation of time is the same for X- and Y-directions. The inverse space coordinates along the Y-axis in 3D space can be achieved by exchanging space-time coordinates and replacing v by $-v$ in Eq. (50) as follows:

$$y = \frac{\bar{y} + \frac{v\bar{t}\bar{y}}{\sqrt{\bar{x}^2+\bar{y}^2+\bar{z}^2}}}{\sqrt{1 - \frac{v^2}{c^2}}}. \quad (53)$$

2.4 Lorentz Transformation Equations Along the Z-axis

From Eq. (19), the relativistic transformation equation along the Z-axis is given by the equation:

$$z = \bar{\gamma}(\bar{z} + v\bar{t}\cos\alpha),$$

Substituting Eq. (16) into the above expression leads to

$$z = \bar{\gamma}[\gamma(z - vt\cos\alpha) + v\bar{t}\cos\alpha],$$
$$z = \bar{\gamma}\gamma z - \bar{\gamma}\gamma vt\cos\alpha + \bar{\gamma}v\bar{t}\cos\alpha,$$
$$\bar{\gamma}v\bar{t}\cos\alpha = \bar{\gamma}\gamma vt\cos\alpha - \bar{\gamma}\gamma z + z,$$
$$\bar{t}\cos\alpha = \gamma t\cos\alpha - \frac{\gamma z}{v} + \frac{z}{\bar{\gamma}v},$$

$$\bar{t} = \frac{\gamma}{\cos\alpha}\left[t\cos\alpha - \frac{z}{v}\left(1 - \frac{1}{\bar{\gamma}\gamma}\right)\right]. \quad (54)$$

Now, substituting Eqs. (54) and (16) into Eq. (13) leads to

$$z^2 - c^2t^2\cos^2\alpha = \bar{z}^2 - c^2\bar{t}^2\cos^2\alpha \quad (55)$$
$$z^2 - c^2t^2\cos^2\alpha = [\gamma(z - vt\cos\alpha)]^2 - c^2\cos^2\alpha\frac{\gamma^2}{\cos^2\alpha}\left[t\cos\alpha - \frac{z}{v}\left(1 - \frac{1}{\bar{\gamma}\gamma}\right)\right]^2$$

$$z^2 - c^2t^2\cos^2\alpha = \gamma^2z^2 - 2\gamma^2zvt\cos\alpha + \gamma^2v^2t^2\cos^2\alpha - c^2\gamma^2t^2\cos^2\alpha + 2c^2\gamma^2t\cos\alpha\frac{z}{v}\left(1-\frac{1}{\bar{\gamma}\gamma}\right) - \gamma^2c^2\frac{z^2}{v^2}\left(1-\frac{1}{\bar{\gamma}\gamma}\right)^2$$

$$z^2 - c^2t^2\cos^2\alpha = z^2\left[\gamma^2 - \frac{c^2\gamma^2}{v^2}\left(1-\frac{1}{\bar{\gamma}\gamma}\right)^2\right] + zt\cos\alpha\left[-2\gamma^2v + \frac{2c^2\gamma^2}{v}\left(1-\frac{1}{\bar{\gamma}\gamma}\right)\right] + t^2\cos^2\alpha\,(\gamma^2v^2 - c^2\gamma^2)$$

After comparing the corresponding coefficients of $z^2, zt \text{ and } t^2$ on both sides, the following expressions are obtained:

$$\gamma^2 - \frac{c^2\gamma^2}{v^2}\left(1-\frac{1}{\bar{\gamma}\gamma}\right)^2 = 1, \tag{56}$$

$$\cos\alpha\left[-2\gamma^2v + \frac{2c^2\gamma^2}{v}\left(1-\frac{1}{\bar{\gamma}\gamma}\right)\right] = 0, \tag{57}$$

$$\cos^2\alpha\,(\gamma^2v^2 - c^2\gamma^2) = -c^2\cos^2\alpha. \tag{58}$$

On solving the above three equations as done in Section 2.2, we obtain:

$$\gamma = \bar{\gamma} = \frac{1}{\sqrt{1-\frac{v^2}{c^2}}}, \tag{59}$$

$$\frac{v^2}{c^2} = \left(1-\frac{1}{\bar{\gamma}\gamma}\right). \tag{60}$$

Substituting Eq. (59) into Eq. (16) leads to

$$\bar{z} = \frac{z - vt\cos\alpha}{\sqrt{1-\frac{v^2}{c^2}}}, \tag{61}$$

Substituting the value of $\cos\alpha$ from Eq. (22) into Eq. (61) and then putting the value of r from Eq. (23) into the obtained equation leads to

$$\bar{z} = \frac{z - \frac{vtz}{r}}{\sqrt{1-\frac{v^2}{c^2}}} = \frac{z - \frac{vtz}{\sqrt{x^2+y^2+z^2}}}{\sqrt{1-\frac{v^2}{c^2}}}. \tag{62}$$

Equation (62) is the Lorentz transformation equation along the Y-axis when there is the simultaneous relative motion between inertial systems in 3D space. To find the equation of time coordinates, let us substitute Eq. (60) into Eq. (54):

$$\bar{t} = \gamma\left[t - \frac{z}{v\cos\alpha}\left(1-\frac{1}{\bar{\gamma}\gamma}\right)\right],$$

$$\bar{t} = \gamma\left(t - \frac{vz}{c^2\cos\alpha}\right), \tag{63}$$

Using the value of r from Eq. (22) and then substituting Eq. (23), the above expression takes the form

$$\bar{t} = \gamma\left(t - \frac{vr}{c^2}\right) = \gamma\left(t - \frac{v\sqrt{x^2+y^2+z^2}}{c^2}\right),$$

$$\bar{t} = \frac{t - \frac{v\sqrt{x^2+y^2+z^2}}{c^2}}{\sqrt{1-\frac{v^2}{c^2}}}. \tag{64}$$

Here, it should be noted that the transformation equation of time, namely Eq. (64), is exactly the same as Eq. (39) and Eq. (52). Hence, the transformation equation of time is the same for the X-, Y-, and Z-directions. The inverse space coordinates along the Y-axis in 3D space can be achieved by exchanging space-time coordinates and replacing v by $-v$ in Eq. (62) as follows.

$$z = \frac{\bar{z} + \frac{v\bar{t}\bar{z}}{\sqrt{\bar{x}^2+\bar{y}^2+\bar{z}^2}}}{\sqrt{1-\frac{v^2}{c^2}}}. \tag{65}$$

2.5 Lorentz Transformation Equations Along Radial Line

In previous sections, we have derived the Lorentz transformation equations along the X-, Y-, and Z-directions. Now we wish to find the relativistic space-time transformation formulas relating radius vectors r and $\bar{r}$ along the radial line OP. In Fig. 1, the moving frame K' and the emitted pulse of light are moving along the radial line OP with the velocity v and c respectively. Now, the equation of the wavefront of light along the radius vector r in the frame K is given by the equation:

$$r^2 - c^2t^2 = 0, \tag{66}$$

Also, the corresponding equation of the wavefront of light along the radius vector $\bar{r}$ in frame K' is specified by the equation:

$$\bar{r}^2 - c^2\bar{t}^2 = 0, \tag{67}$$

Since both the frames are at the center of the expanding wavefront at $t = \bar{t} = 0$, Eqs. (66) and (67) must be equal.

$$r^2 - c^2t^2 = \bar{r}^2 - c^2\bar{t}^2. \tag{68}$$

Equation (68) represents the wavefront of light along the radial line OP. Also, frame K' is moving along the radial line OP with the uniform velocity v as shown in Fig. 1. Hence, it is obvious that radius vectors r and $\bar{r}$ are related by the equation:

$$O'P = OP - OO',$$

$$\bar{r} = r - vt,$$

Hence, the corresponding relativistic transformation equation relating radius vectors r

and $\bar{r}$ with Lorentz coefficient γ should be in the following form:

$$\bar{r} = \gamma(r - vt). \tag{69}$$

Also, the corresponding inverse relativistic transformation equation relating radius vectors r and $\bar{r}$ should be in the following form:

$$r = \bar{\gamma}(\bar{r} + v\bar{t}\,), \tag{70}$$

Substituting Eq. (69) into Eq. (70) leads to

$$r = \bar{\gamma}[\gamma(r - vt) + v\bar{t}\,],$$
$$r = \bar{\gamma}\gamma r - \bar{\gamma}\gamma vt + \bar{\gamma}v\bar{t},$$
$$\bar{\gamma}v\bar{t} = \bar{\gamma}\gamma vt - \bar{\gamma}\gamma r + r,$$
$$\bar{t} = \gamma\left[t - \frac{r}{v}\left(1 - \frac{1}{\bar{\gamma}\gamma}\right)\right]. \tag{71}$$

Now, substituting Eqs. (71) and (69) into Eq. (68) leads to

$$r^2 - c^2t^2 = \bar{r}^2 - c^2\bar{t}^2,$$
$$r^2 - c^2t^2 = [\gamma(r - vt)]^2 - c^2\gamma^2\left[t - \frac{r}{v}\left(1 - \frac{1}{\bar{\gamma}\gamma}\right)\right]^2,$$
$$r^2 - c^2t^2 = \gamma^2r^2 - 2\gamma^2rvt + \gamma^2v^2t^2 - c^2\gamma^2t^2 + \frac{2c^2\gamma^2tr}{v}\left(1 - \frac{1}{\bar{\gamma}\gamma}\right) - \frac{\gamma^2c^2r^2}{v^2}\left(1 - \frac{1}{\bar{\gamma}\gamma}\right)^2,$$
$$r^2 - c^2t^2 = r^2\left[\gamma^2 - \frac{c^2\gamma^2}{v^2}\left(1 - \frac{1}{\bar{\gamma}\gamma}\right)^2\right] + rt\left[-2\gamma^2v + \frac{2c^2\gamma^2}{v}\left(1 - \frac{1}{\bar{\gamma}\gamma}\right)\right] + t^2(\gamma^2v^2 - c^2\gamma^2),$$

After comparing the corresponding coefficients of $r^2, rt\ and\ t^2$ on both sides, the following expressions are obtained

$$\gamma^2 - \frac{c^2\gamma^2}{v^2}\left(1 - \frac{1}{\bar{\gamma}\gamma}\right)^2 = 1, \tag{72}$$

$$-2\gamma^2v + \frac{2c^2\gamma^2}{v}\left(1 - \frac{1}{\bar{\gamma}\gamma}\right) = 0, \tag{73}$$

$$\gamma^2v^2 - c^2\gamma^2 = -c^2. \tag{74}$$

On solving the above three equations as done in Section 2.2, we obtain:

$$\gamma = \bar{\gamma} = \frac{1}{\sqrt{1 - \frac{v^2}{c^2}}}, \tag{75}$$

$$\frac{v^2}{c^2} = \left(1 - \frac{1}{\bar{\gamma}\gamma}\right). \tag{76}$$

Substituting Eq. (75) into Eq. (69) leads to

$$\bar{r} = \frac{r - vt}{\sqrt{1 - \frac{v^2}{c^2}}}. \tag{77}$$

This Eq. (77) is the Lorentz transformation equation along the radial line. To find the equation of time coordinates, let us substitute Eqs. (76) and (75) into Eq. (71),

$$\bar{t} = \gamma\left[t - \frac{r}{v}\left(1 - \frac{1}{\bar{\gamma}\gamma}\right)\right],$$
$$\bar{t} = \frac{t - \frac{vr}{c^2}}{\sqrt{1 - \frac{v^2}{c^2}}} = \frac{t - \frac{v\sqrt{x^2+y^2+z^2}}{c^2}}{\sqrt{1 - \frac{v^2}{c^2}}}. \tag{78}$$

Here, it should be noted that the transformation equation of time, namely Eq. (78), is exactly the same as Eqs. (39), (52), and (64). Hence, the transformation equation of time is the same for all directions. The inverse space coordinates along a radial line can be achieved by exchanging space-time coordinates and replacing v by $-v$ in Eq. (77) as follows.

$$r = \frac{\bar{r} + v\bar{t}}{\sqrt{1 - \frac{v^2}{c^2}}}, \tag{79}$$

Using Eqs. (23) and (27), Eq. (79) takes the following form:

$$\sqrt{x^2 + y^2 + z^2} = \frac{\sqrt{\bar{x}^2 + \bar{y}^2 + \bar{z}^2} + v\bar{t}}{\sqrt{1 - \frac{v^2}{c^2}}}. \tag{80}$$

This Eq. (80) represents the inverse transformation equation along the radial line when the relative motion between inertial frames occurs in 3D space. If the motion between inertial frames is aligned along a single X-axis only, then we need to substitute $y = \bar{y} = 0$ and $z = \bar{z} = 0$ in Eq. (80), which exactly gives the former 1D inverse Lorentz transformation equation along the X-axis as follows:

$$\sqrt{x^2 + 0^2 + 0^2} = \frac{\sqrt{\bar{x}^2 + 0^2 + 0^2} + v\bar{t}}{\sqrt{1 - \frac{v^2}{c^2}}},$$
$$x = \frac{\bar{x} + v\bar{t}}{\sqrt{1 - \frac{v^2}{c^2}}}.$$

3. Results and Discussion

3.1 Lorentz Transformation Equations in 3D Space

In Section "Methods", we have derived the Lorentz transformation equations along radial line, the X-, Y-, and Z-directions when the motion between inertial frames takes place in 3D space. These 3D transformation equations, namely Eqs. (37), (50), (62), and (64) represent the extended version of the 1D Lorentz

transformation to three dimensions of space, and these equations exactly take the form of the 1D Lorentz transformation when the relative motion between inertial frames is reduced from 3D to 1D along the X-axis, as discussed in Table 1.

TABLE 1. Inverse Lorentz transformation equations in 3D space

Motion between frames	Transformation of time	Space coordinate transformation equations		
		Along the X-direction	Along Y-direction	Along Z-direction
Along X-, Y-, and Z-axes	From Eq. (41), $t=\frac{\bar{t}+\frac{v\sqrt{\bar{x}^2+\bar{y}^2+\bar{z}^2}}{c^2}}{\sqrt{1-\frac{v^2}{c^2}}}$	From Eq. (40), $x=\frac{\bar{x}+\frac{v\bar{t}\bar{x}}{\sqrt{\bar{x}^2+\bar{y}^2+\bar{z}^2}}}{\sqrt{1-\frac{v^2}{c^2}}}$	From Eq. (53), $y=\frac{\bar{y}+\frac{v\bar{t}\bar{y}}{\sqrt{\bar{x}^2+\bar{y}^2+\bar{z}^2}}}{\sqrt{1-\frac{v^2}{c^2}}}$	From Eq. (65), $z=\frac{\bar{z}+\frac{v\bar{t}\bar{z}}{\sqrt{\bar{x}^2+\bar{y}^2+\bar{z}^2}}}{\sqrt{1-\frac{v^2}{c^2}}}$
Along X- and Y-axes only ($\bar{z}=0$)	$t=\frac{\bar{t}+\frac{v\sqrt{\bar{x}^2+\bar{y}^2+0^2}}{c^2}}{\sqrt{1-\frac{v^2}{c^2}}}$ $t=\frac{\bar{t}+\frac{v\sqrt{\bar{x}^2+\bar{y}^2}}{c^2}}{\sqrt{1-\frac{v^2}{c^2}}}$	$x=\frac{\bar{x}+\frac{v\bar{t}\bar{x}}{\sqrt{\bar{x}^2+\bar{y}^2+0^2}}}{\sqrt{1-\frac{v^2}{c^2}}}$ $x=\frac{\bar{x}+\frac{v\bar{t}\bar{x}}{\sqrt{\bar{x}^2+\bar{y}^2}}}{\sqrt{1-\frac{v^2}{c^2}}}$	$y=\frac{\bar{y}+\frac{v\bar{t}\bar{y}}{\sqrt{\bar{x}^2+\bar{y}^2+0^2}}}{\sqrt{1-\frac{v^2}{c^2}}}$ $y=\frac{\bar{y}+\frac{v\bar{t}\bar{y}}{\sqrt{\bar{x}^2+\bar{y}^2}}}{\sqrt{1-\frac{v^2}{c^2}}}$	$z=\frac{0+\frac{v\bar{t}0}{\sqrt{\bar{x}^2+\bar{y}^2+0^2}}}{\sqrt{1-\frac{v^2}{c^2}}}$ $z=0$
Along X -axis only $\bar{z}=0,\bar{y}=0$	$t=\frac{\bar{t}+\frac{v\sqrt{\bar{x}^2+0^2+0^2}}{c^2}}{\sqrt{1-\frac{v^2}{c^2}}}$ $t=\frac{\bar{t}+\frac{v\bar{x}}{c^2}}{\sqrt{1-\frac{v^2}{c^2}}}$	$x=\frac{\bar{x}+\frac{v\bar{t}\bar{x}}{\sqrt{\bar{x}^2+0^2+0^2}}}{\sqrt{1-\frac{v^2}{c^2}}}$ $x=\frac{\bar{x}+v\bar{t}}{\sqrt{1-\frac{v^2}{c^2}}}$	$y=\frac{0+\frac{v\bar{t}0}{\sqrt{\bar{x}^2+0^2+0^2}}}{\sqrt{1-\frac{v^2}{c^2}}}$ $y=0$	$z=\frac{0+\frac{v\bar{t}0}{\sqrt{\bar{x}^2+0^2+0^2}}}{\sqrt{1-\frac{v^2}{c^2}}}$ $z=0$

From the last row of Table 1, it is clearly seen that modified Lorentz transformation equations achieve the exact form of the former 1D Lorentz transformation equations when the motion between inertial frames takes place along a single X-axis only. These transformation equations are exactly the same transformation equations as derived in Ref. [1]. In Ref. [1], the equations were obtained to demonstrate the simultaneous space contraction along the X-, Y-, and Z-directions, whereas in the present work, the same equations are recovered in order to formulate the matrix representation of the three-dimensional Lorentz transformation.

3.2 Invariance of Space-time Interval

One of the important properties of the Lorentz transformation equations is that the space-time interval must be invariant under these transformation equations. The equation of the space-time interval in a moving frame of reference is given by,

$$\bar{\tau}^2=\bar{x}^2+\bar{y}^2+\bar{z}^2-c^2\bar{t}^2,$$

The corresponding equation of the space-time interval in the rest frame of reference is given by

$$\tau^2=x^2+y^2+z^2-c^2t^2.$$

Substituting the values of x,y,z,t from Eqs. (40), (41), (53), and (65) into the formula of space-time interval, i.e.,

$$x^2+y^2+z^2-c^2t^2,$$

$$=\left(\frac{\bar{x}+\frac{v\bar{t}\bar{x}}{\sqrt{\bar{x}^2+\bar{y}^2+\bar{z}^2}}}{\sqrt{1-\frac{v^2}{c^2}}}\right)^2+\left(\frac{\bar{y}+\frac{v\bar{t}\bar{y}}{\sqrt{\bar{x}^2+\bar{y}^2+\bar{z}^2}}}{\sqrt{1-\frac{v^2}{c^2}}}\right)^2+\left(\frac{\bar{z}+\frac{v\bar{t}\bar{z}}{\sqrt{\bar{x}^2+\bar{y}^2+\bar{z}^2}}}{\sqrt{1-\frac{v^2}{c^2}}}\right)^2-c^2\left(\frac{\bar{t}+\frac{v\sqrt{\bar{x}^2+\bar{y}^2+\bar{z}^2}}{c^2}}{\sqrt{1-\frac{v^2}{c^2}}}\right)^2,$$

$$\bar{x}^2+\bar{y}^2+\bar{z}^2+2v\bar{t}\left(\frac{\bar{x}^2+\bar{y}^2+\bar{z}^2}{\sqrt{\bar{x}^2+\bar{y}^2+\bar{z}^2}}\right)+(v\bar{t})^2\frac{\bar{x}^2+\bar{y}^2+\bar{z}^2}{\bar{x}^2+\bar{y}^2+\bar{z}^2}-c^2\bar{t}^2$$

$$=\frac{-2\bar{t}v\sqrt{\bar{x}^2+\bar{y}^2+\bar{z}^2}-\frac{v^2(\bar{x}^2+\bar{y}^2+\bar{z}^2)}{c^2}}{1-\frac{v^2}{c^2}},$$

$$=\frac{\bar{x}^2+\bar{y}^2+\bar{z}^2+(v\bar{t})^2-c^2\bar{t}^2-\frac{v^2(\bar{x}^2+\bar{y}^2+\bar{z}^2)}{c^2}}{1-\frac{v^2}{c^2}},$$

$$= \frac{(\bar{x}^2+\bar{y}^2+\bar{z}^2)\left(1-\frac{v^2}{c^2}\right)-c^2\bar{t}^2\left(1-\frac{v^2}{c^2}\right)}{1-\frac{v^2}{c^2}},$$

$$= \bar{x}^2 + \bar{y}^2 + \bar{z}^2 - c^2\bar{t}^2.$$

Thus, we have clearly proved that $x^2 + y^2 + z^2 - c^2t^2 = \bar{x}^2 + \bar{y}^2 + \bar{z}^2 - c^2\bar{t}^2$. Hence, the space-time interval equation is invariant under the 3D Lorentz transformation equations.

3.3 Matrix Form of 3D Lorentz Transformation Equations

In former 1D Lorentz transformations, the relative motion between inertial frames is constrained along a single axis (say X-axis). Hence, we take the account of single space coordinates and the transformation of time coordinate depends only upon X coordinates [see Eq. (1)]. Unlike it, in 3D Lorentz transformations, we have simultaneous relative motion between inertial frames along the X-, Y-, and Z-directions. Hence, we need to have the transformation equations for all X, Y, and Z space coordinates, and the transformation of the time coordinate should depend upon all space coordinates [see Eq. (4)]. For that, let's write the corresponding values of space coordinates from Eqs. (20)-(22) as follows:

$$x = x_1 = r\sin\alpha\cos\beta, \tag{81}$$

$$y = x_2 = r\sin\alpha\sin\beta, \tag{82}$$

$$z = x_3 = r\cos\alpha. \tag{83}$$

Equations (81)-(83) represent the value of space coordinates along the X-, Y-, and Z-axes in the rest frame of reference. The corresponding expression of space coordinates in a moving frame can be written from Eqs. (24)-(26) as follows:

$$\bar{x} = \bar{x}_1 = \bar{r}\sin\alpha\cos\beta, \tag{84}$$

$$\bar{y} = \bar{x}_2 = \bar{r}\sin\alpha\sin\beta, \tag{85}$$

$$\bar{z} = \bar{x}_3 = \bar{r}\cos\alpha. \tag{86}$$

In fact, the above equations represent the three components of the resultant radius vector $\bar{r}$. Now, we wish to find the components of the time coordinate, or more conveniently ict, under the 3D Lorentz transformation equations. For that, let us write the equation of the wavefront of light along the X-axis from Eq. (29) in the following form:

$$x^2 - (ct\sin\alpha\cos\beta)^2 = \bar{x}^2 - (c\bar{t}\sin\alpha\cos\beta)^2,$$

$$\left.\begin{aligned} x^2 + (ict\sin\alpha\cos\beta)^2 &= \\ \bar{x}^2 + (ic\bar{t}\sin\alpha\cos\beta)^2 &\\ {x_1}^2 + {x_4}^2 = {\bar{x}_1}^2 + {\bar{x}_4}^2 &\end{aligned}\right\}. \tag{87}$$

Equation (87) shows the invariance of the space-time interval along the X-direction. Hence, it is obvious that $x_4 = ict\sin\alpha\cos\beta$ must represent the time coordinate corresponding to the space coordinate $x_1 = r\sin\alpha\cos\beta$. Similarly, let us write the equation of the wavefront of light along the Y-axis from Eq. (43) in the following form:

$$y^2 - (ct\sin\alpha\sin\beta)^2 = \bar{y}^2 - (c\bar{t}\sin\alpha\sin\beta)^2,$$

$$\left.\begin{aligned} y^2 + (ict\sin\alpha\sin\beta)^2 &= \\ \bar{y}^2 + (ic\bar{t}\sin\alpha\sin\beta)^2 &\\ {x_2}^2 + {x_5}^2 = {\bar{x}_2}^2 + {\bar{x}_5}^2 &\end{aligned}\right\}. \tag{88}$$

Equation (88) shows the invariance of the space-time interval along the Y-direction. Hence, it is obvious that $x_5 = ict\sin\alpha\sin\beta$ must represent the time coordinate corresponding to the space coordinate $x_2 = r\sin\alpha\sin\beta$. Similarly, let us write the equation of the wavefront of light along the Z-axis from Eq. (55) in the following form:

$$z^2 - (ct\cos\alpha)^2 = \bar{z}^2 - (c\bar{t}\cos\alpha)^2,$$

$$\left.\begin{aligned} z^2 + (ict\cos\alpha)^2 = \bar{z}^2 + (ic\bar{t}\cos\alpha)^2 \\ {x_3}^2 + {x_6}^2 = {\bar{x}_3}^2 + {\bar{x}_6}^2 \end{aligned}\right\}. \tag{89}$$

Equation (89) shows the invariance of the space-time interval along the Z-direction. Hence, it is obvious that $x_6 = ict\cos\alpha$ must represent the time coordinate corresponding to the space coordinate $x_3 = r\cos\alpha$. Thus, the time coordinates, namely the components of ict, under the 3D Lorentz transformation equations in the rest frame, can be written from Eqs. (87)-(89) in the following form:

$$x_4 = ict\sin\alpha\cos\beta, \tag{90}$$

$$x_5 = ict\sin\alpha\sin\beta, \tag{91}$$

$$x_6 = ict\cos\alpha. \tag{92}$$

The corresponding expression of components of $ic\bar{t}$ in a moving frame can be written from Eqs. (87)-(89) as follows:

$$\bar{x}_4 = ic\bar{t}\sin\alpha\cos\beta, \tag{93}$$

$$\bar{x}_5 = ic\bar{t}\sin\alpha\sin\beta, \tag{94}$$

$$\bar{x}_6 = ic\bar{t}\cos\alpha. \tag{95}$$

From the above mathematical manipulations, it is obvious that time has three coordinates,

namely (x_4, x_5, x_6), like space has three coordinates, namely (x_1, x_2, x_3). Hence, an event in the spacetime continuum should be represented by six coordinates (let's name them six-vectors), out of which the first three represent the space coordinates and the remaining three represent the time coordinates. Now, our main task is to write the 3D Lorentz transformation in terms of six-vectors. For this, let's write the Lorentz transformation equation along the X-axis with $\rho = v/c$ from Eq. (36) as follows:

$$\bar{x} = \gamma(x - vt\sin\alpha\cos\beta),$$
$$\bar{x} = \gamma\left(x - \frac{v}{c}ct\sin\alpha\cos\beta\right),$$
$$\bar{x} = \gamma(x - \rho ct\sin\alpha\cos\beta),$$
$$\bar{x} = \gamma(x + i^2\rho ct\sin\alpha\cos\beta),$$

Substituting Eqs. (81), (84), and (90) into the above expression results in

$$\bar{x}_1 = \gamma(x_1 + i\rho x_4). \quad (96)$$

Similarly, let's write the Lorentz transformation equation along the Y-axis with $\rho = v/c$ from Eq. (49) as follows:

$$\bar{y} = \gamma(y - vt\sin\alpha\sin\beta),$$
$$\bar{y} = \gamma\left(y - \frac{v}{c}ct\sin\alpha\sin\beta\right),$$
$$\bar{y} = \gamma(y - \rho ct\sin\alpha\sin\beta),$$
$$\bar{y} = \gamma(y + i^2\rho ct\sin\alpha\sin\beta),$$

Substituting Eqs. (82), (85), and (91) into the above expression results in

$$\bar{x}_2 = \gamma(x_2 + i\rho x_5). \quad (97)$$

Similarly, let us write the Lorentz transformation equation along the Z-axis with $\rho = v/c$ from Eq. (61) as follows:

$$\bar{z} = \gamma(z - vt\cos\alpha),$$
$$\bar{z} = \gamma\left(z - \frac{v}{c}ct\cos\alpha\right),$$
$$\bar{z} = \gamma(z - \rho ct\cos\alpha),$$
$$\bar{z} = \gamma(z + i^2\rho ct\cos\alpha),$$

Substituting Eqs. (83), (86), and (92) into the above expression results in

$$\bar{x}_3 = \gamma(x_3 + i\rho x_6). \quad (98)$$

Equations (96)-(98) are the 3D Lorentz transformations of space coordinates in terms of six-vectors. To find the transformation equations of time in terms of six-vectors, let us write Eq. (38) with $\rho = v/c$ in the following form:

$$\bar{t} = \gamma\left(t - \frac{vx}{c^2\sin\alpha\cos\beta}\right),$$
$$\bar{t} = \gamma\left(t - \frac{\rho x}{c\sin\alpha\cos\beta}\right),$$
$$c\bar{t}\sin\alpha\cos\beta = \gamma(ct\sin\alpha\cos\beta - \rho x),$$
$$ic\bar{t}\sin\alpha\cos\beta = \gamma(ict\sin\alpha\cos\beta - i\rho x),$$

Substituting Eqs. (81), (90), and (93) into the above expression results in

$$\bar{x}_4 = \gamma(x_4 - i\rho x_1). \quad (99)$$

Similarly, let us write Eq. (51) with $\rho = v/c$ in the following form:

$$\bar{t} = \gamma\left(t - \frac{vy}{c^2\sin\alpha\sin\beta}\right),$$
$$\bar{t} = \gamma\left(t - \frac{\rho y}{c\sin\alpha\sin\beta}\right),$$
$$c\bar{t}\sin\alpha\sin\beta = \gamma(ct\sin\alpha\sin\beta - \rho y),$$
$$ic\bar{t}\sin\alpha\sin\beta = \gamma(ict\sin\alpha\sin\beta - i\rho y),$$

Substituting Eqs. (82), (91), and (94) into the above expression results in

$$\bar{x}_5 = \gamma(x_5 - i\rho x_2). \quad (100)$$

Similarly, let us write Eq. (63) with $\rho = v/c$ in the following form:

$$\bar{t} = \gamma\left(t - \frac{vz}{c^2\cos\alpha}\right),$$
$$\bar{t} = \gamma\left(t - \frac{\rho z}{c\cos\alpha}\right),$$
$$c\bar{t}\cos\alpha = \gamma(ct\cos\alpha - \rho z),$$
$$ic\bar{t}\cos\alpha = \gamma(ict\cos\alpha - i\rho z),$$

Substituting Eqs. (82), (92), and (95) into the above expression results in

$$\bar{x}_6 = \gamma(x_6 - i\rho x_3). \quad (101)$$

Equations (99)-(101) are the transformation formulas for three coordinates of time, i.e., $(\bar{x}_4, \bar{x}_5, \bar{x}_6)$. Equations (96)-(98) represent the Lorentz transformation equations of the first three space coordinates of six-vectors, while Eqs. (99)-(101) represent the Lorentz transformation equations of the remaining three time coordinates of the six-vectors. Equations (96)-(101) can be written in the following form:

$$\left.\begin{array}{c}\bar{x}_1 = \gamma.x_1 + 0.x_2 + 0.x_3 \\ +i\rho\gamma.x_4 + 0.x_5 + 0.x_6 \\ \bar{x}_2 = 0.x_1 + \gamma.x_2 + 0.x_3 \\ +0.x_4 + i\rho\gamma.x_5 + 0.x_6 \\ \bar{x}_3 = 0.x_1 + 0.x_2 + \gamma.x_3 \\ +0.x_4 + 0.x_5 + i\rho\gamma.x_6 \\ \bar{x}_4 = -i\rho\gamma.x_1 + 0.x_2 + 0.x_3 \\ +\gamma.x_4 + 0.x_5 + 0.x_6 \\ \bar{x}_5 = 0.x_1 - i\rho\gamma.x_2 + 0.x_3 \\ +0.x_4 + \gamma.x_5 + 0.x_6 \\ \bar{x}_6 = 0.x_1 + 0.x_2 - i\rho\gamma.x_3 \\ +0.x_4 + 0.x_5 + \gamma.x_6 \end{array}\right\}, \quad (102)$$

In matrix form above equations can be written as:

$$\begin{bmatrix}\bar{x}_1\\ \bar{x}_2\\ \bar{x}_3\\ \bar{x}_4\\ \bar{x}_5\\ \bar{x}_6\end{bmatrix} = \begin{bmatrix}\gamma & 0 & 0 & i\rho\gamma & 0 & 0\\ 0 & \gamma & 0 & 0 & i\rho\gamma & 0\\ 0 & 0 & \gamma & 0 & 0 & i\rho\gamma\\ -i\rho\gamma & 0 & 0 & \gamma & 0 & 0\\ 0 & -i\rho\gamma & 0 & 0 & \gamma & 0\\ 0 & 0 & -i\rho\gamma & 0 & 0 & \gamma\end{bmatrix}\begin{bmatrix}x_1\\ x_2\\ x_3\\ x_4\\ x_5\\ x_6\end{bmatrix}. \quad (103)$$

Equation (103) represents the matrix form of the three-dimensional Lorentz transformation equations in terms of six-vectors. The inverse of this equation that transforms coordinates from a moving frame to a rest frame can be achieved by exchanging space-time coordinates and replacing ρ with $-\rho$ in Eq. (103) as follows:

$$\begin{bmatrix}x_1\\ x_2\\ x_3\\ x_4\\ x_5\\ x_6\end{bmatrix} = \begin{bmatrix}\gamma & 0 & 0 & -i\rho\gamma & 0 & 0\\ 0 & \gamma & 0 & 0 & -i\rho\gamma & 0\\ 0 & 0 & \gamma & 0 & 0 & -i\rho\gamma\\ i\rho\gamma & 0 & 0 & \gamma & 0 & 0\\ 0 & i\rho\gamma & 0 & 0 & \gamma & 0\\ 0 & 0 & i\rho\gamma & 0 & 0 & \gamma\end{bmatrix}\begin{bmatrix}\bar{x}_1\\ \bar{x}_2\\ \bar{x}_3\\ \bar{x}_4\\ \bar{x}_5\\ \bar{x}_6\end{bmatrix}. \quad (104)$$

Equations (103) and (104) represent the matrix form of 3D direct and inverse Lorentz transformation equations, respectively, when the motion between inertial frames takes place along the X-, Y-, and Z-directions simultaneously. However, when the motion between inertial frames takes place along a single X-axis, we should have $\alpha = \frac{\pi}{2}$ and $\beta = 0$ (see Fig. 1), and Eqs. (81), (82) and (83) achieve the following form under such one-dimensional conditions.

$$x = x_1 = r\sin\frac{\pi}{2}\cos 0 = r, \quad (105)$$

$$y = x_2 = r\sin\frac{\pi}{2}\sin 0 = 0, \quad (106)$$

$$z = x_3 = r\cos\frac{\pi}{2} = 0. \quad (107)$$

Equations (90)-(92) take the following form when $\alpha = \frac{\pi}{2}$ and $\beta = 0$.

$$x_4 = ict\sin\frac{\pi}{2}\cos 0 = ict, \quad (108)$$

$$x_5 = ict\sin\frac{\pi}{2}\sin 0 = 0, \quad (109)$$

$$x_6 = ict\cos\frac{\pi}{2} = 0. \quad (110)$$

Substituting Eqs. (105)-(110) into six Lorentz transformations, namely Eq. (102) results in

$$\left.\begin{array}{c}\bar{x}_1 = \gamma.x_1 + 0.0 + 0.0 + \\ i\rho\gamma.x_4 + 0.0 + 0.0 \\ \bar{x}_2 = 0.x_1 + \gamma.0 + 0.0 + \\ 0.x_4 + i\rho\gamma.0 + 0.0 = 0 \\ \bar{x}_3 = 0.x_1 + 0.0 + \gamma.0 + \\ 0.x_4 + 0.0 + i\rho\gamma.0 = 0 \\ \bar{x}_4 = -i\rho\gamma.x_1 + 0.0 + 0.x_3 + \\ \gamma.x_4 + 0.0 + 0.0 \\ \bar{x}_5 = 0.x_1 - i\rho\gamma.0 + 0.x_3 + \\ 0.x_4 + \gamma.0 + 0.0 = 0 \\ \bar{x}_6 = 0.x_1 + 0.0 - i\rho\gamma.0 + \\ 0.x_4 + 0.0 + \gamma.0 = 0 \end{array}\right\}. \quad (111)$$

From the above mathematical calculations, it is clear that the value of Y and Z space-time coordinates drops out ($\bar{x}_2 = \bar{x}_3 = \bar{x}_5 = \bar{x}_6 = 0$) when the motion between inertial frames takes place along a single X-axis only. If we remove the coordinates having zero values from Eq. (111), then we get:

$$\left.\begin{array}{l}\bar{x}_1 = \gamma.x_1 + +0.0 + 0.0 + i\rho\gamma.x_4 + 0.0 + 0.0 \\ \bar{x}_4 = -i\rho\gamma.x_1 + 0.0 + 0.0 + \gamma.x_4 + 0.0 + 0.0 \end{array}\right\}, \quad (112)$$

In matrix form above equations can be written as:

$$\begin{bmatrix}\bar{x}_1\\ \bar{x}_4\end{bmatrix} = \begin{bmatrix}\gamma & i\rho\gamma\\ -i\rho\gamma & \gamma\end{bmatrix}\begin{bmatrix}x_1\\ x_4\end{bmatrix}. \quad (113)$$

Equation (113) represents the matrix form of the one-dimensional Lorentz transformation equations. Also, Eqs. (84) and (93) achieve the following form under one-dimensional conditions, i.e., $\alpha = \frac{\pi}{2}$ and $\beta = 0$:

$$\bar{x} = \bar{x}_1 = \bar{r}\sin\frac{\pi}{2}\cos 0 = \bar{r}, \quad (114)$$

$$\bar{x}_4 = ic\bar{t}\sin\frac{\pi}{2}\cos 0 = ic\bar{t}. \quad (115)$$

Substituting Eqs. (105), (108), (114), and (115) into Eq. (113) results in

$$\begin{bmatrix}\bar{x}\\ ic\bar{t}\end{bmatrix} = \begin{bmatrix}\gamma & i\rho\gamma\\ -i\rho\gamma & \gamma\end{bmatrix}\begin{bmatrix}x\\ ict\end{bmatrix}. \quad (116)$$

Solution of the above matrix Eq. (116) gives exact one-dimensional Lorentz transformation equations as follows:

$$\bar{x} = \gamma x + i^2\gamma\rho ct = \frac{x-vt}{\sqrt{1-\frac{v^2}{c^2}}}.$$

and,

$$ic\bar{t} = -i\rho\gamma x + ict\gamma = \frac{ict-\frac{ivx}{c}}{\sqrt{1-\frac{v^2}{c^2}}},$$

$$\bar{t} = \frac{t-\frac{vx}{c^2}}{\sqrt{1-\frac{v^2}{c^2}}}.$$

For the invariance of the space-time interval in terms of the six-vector, let us add the Eqs. (87)-(89):

$$x_1{}^2 + x_2{}^2 + x_3{}^2 + x_4{}^2 + x_5{}^2 + x_6{}^2 = \bar{x}_1{}^2 + \bar{x}_2{}^2 + \bar{x}_3{}^2 + \bar{x}_4{}^2 + \bar{x}_5{}^2 + \bar{x}_6{}^2. \quad (117)$$

This equation represents the invariance of the spacetime interval under the extended new six Lorentz transformation equations.

3.4 Invariance of the Wave Equation

In Fig. 1, frame K' is moving with velocity v relative to frame K along the radius vector r in 3D space. If an electromagnetic wave is travelling in frame K, then the propagation equation for such a wave is of the form,

$$\left\{\nabla^2 - \frac{\partial^2}{\partial(ct)^2}\right\}\Phi = \left\{\frac{\partial^2}{\partial r^2} + \frac{\partial^2}{\partial(ict)^2}\right\}\Phi = 0,$$

Here, r denotes the resultant vector, which has three components, namely $x_1 = x$, $x_2 = y$, and $x_3 = z$, as discussed in Eqs. (81)-(83). Hence, the above expression can be extended in terms of components of r as follows,

$$\left\{\frac{\partial^2}{\partial x^2} + \frac{\partial^2}{\partial y^2} + \frac{\partial^2}{\partial z^2} + \frac{\partial^2}{\partial(ict)^2}\right\}\Phi = \left\{\frac{\partial^2}{\partial x_1{}^2} + \frac{\partial^2}{\partial x_2{}^2} + \frac{\partial^2}{\partial x_3{}^2} + \frac{\partial^2}{\partial(ict)^2}\right\}\Phi = 0,$$

Similarly, ict has three components, namely, x_4, x_5, and x_6 as discussed in Eqs. (90)-(92). Hence, the above expression can be extended in terms of components of ict as follows,

$$\left\{\frac{\partial^2}{\partial x_1{}^2} + \frac{\partial^2}{\partial x_2{}^2} + \frac{\partial^2}{\partial x_3{}^2} + \frac{\partial^2}{\partial x_4{}^2} + \frac{\partial^2}{\partial x_5{}^2} + \frac{\partial^2}{\partial x_6{}^2}\right\}\Phi = 0. \quad (118)$$

Equation (118) represents the equation of an electromagnetic wave in a six-dimensional space-time continuum. Now, the propagation equation of the same wave in frame K' is given by

$$\left\{\frac{\partial^2}{\partial \bar{x}_1{}^2} + \frac{\partial^2}{\partial \bar{x}_2{}^2} + \frac{\partial^2}{\partial \bar{x}_3{}^2} + \frac{\partial^2}{\partial \bar{x}_4{}^2} + \frac{\partial^2}{\partial \bar{x}_5{}^2} + \frac{\partial^2}{\partial \bar{x}_6{}^2}\right\}\Phi = 0. \quad (119)$$

Here Φ is a function of $\bar{x}_1, \bar{x}_2, \bar{x}_3, \bar{x}_4, \bar{x}_5$ and $\bar{x}_6$ and thus it may be written as $\Phi(\bar{x}_1, \bar{x}_2, \bar{x}_3, \bar{x}_4, \bar{x}_5, \bar{x}_6)$. Hence, we can write the following differential operator:

$$\frac{\partial\Phi}{\partial x_1} = \frac{\partial\Phi}{\partial\bar{x}_1}\frac{\partial\bar{x}_1}{\partial x_1} + \frac{\partial\Phi}{\partial\bar{x}_2}\frac{\partial\bar{x}_2}{\partial x_1} + \frac{\partial\Phi}{\partial\bar{x}_3}\frac{\partial\bar{x}_3}{\partial x_1} + \frac{\partial\Phi}{\partial\bar{x}_4}\frac{\partial\bar{x}_4}{\partial x_1} + \frac{\partial\Phi}{\partial\bar{x}_5}\frac{\partial\bar{x}_5}{\partial x_1} + \frac{\partial\Phi}{\partial\bar{x}_6}\frac{\partial\bar{x}_6}{\partial x_1},$$

$$\frac{\partial}{\partial x_1} = \frac{\partial}{\partial\bar{x}_1}\frac{\partial\bar{x}_1}{\partial x_1} + \frac{\partial}{\partial\bar{x}_2}\frac{\partial\bar{x}_2}{\partial x_1} + \frac{\partial}{\partial\bar{x}_3}\frac{\partial\bar{x}_3}{\partial x_1} + \frac{\partial}{\partial\bar{x}_4}\frac{\partial\bar{x}_4}{\partial x_1} + \frac{\partial}{\partial\bar{x}_5}\frac{\partial\bar{x}_5}{\partial x_1} + \frac{\partial}{\partial\bar{x}_6}\frac{\partial\bar{x}_6}{\partial x_1},$$

Substituting Eqs. (96)-(101) into the above expression results in

$$\frac{\partial}{\partial x_1} = \frac{\partial}{\partial\bar{x}_1}\frac{\partial\{\gamma(x_1+i\rho x_4)\}}{\partial x_1} + \frac{\partial}{\partial\bar{x}_2}\frac{\partial\{\gamma(x_2+i\rho x_5)\}}{\partial x_1} + \frac{\partial}{\partial\bar{x}_3}\frac{\partial\{\gamma(x_3+i\rho x_6)\}}{\partial x_1} + \frac{\partial}{\partial\bar{x}_4}\frac{\partial\gamma(x_4-i\rho x_1)}{\partial x_1} + \frac{\partial}{\partial\bar{x}_5}\frac{\partial\gamma(x_5-i\rho x_2)}{\partial x_1} + \frac{\partial}{\partial\bar{x}_6}\frac{\partial\gamma(x_6-i\rho x_3)}{\partial x_1},$$

$$\frac{\partial}{\partial x_1} = \frac{\partial}{\partial\bar{x}_1}\gamma + \frac{\partial}{\partial\bar{x}_2}0 + \frac{\partial}{\partial\bar{x}_3}0 - \frac{\partial}{\partial\bar{x}_4}i\gamma\rho + \frac{\partial}{\partial\bar{x}_5}0 + \frac{\partial}{\partial\bar{x}_6}0,$$

$$\frac{\partial}{\partial x_1} = \gamma\frac{\partial}{\partial\bar{x}_1} - i\gamma\rho\frac{\partial}{\partial\bar{x}_4},$$

Multiplying the above equation by itself, we get:

$$\frac{\partial^2}{\partial x_1{}^2} = \left(\gamma\frac{\partial}{\partial\bar{x}_1} - i\gamma\rho\frac{\partial}{\partial\bar{x}_4}\right)\left(\gamma\frac{\partial}{\partial\bar{x}_1} - i\gamma\rho\frac{\partial}{\partial\bar{x}_4}\right),$$

$$\frac{\partial^2}{\partial x_1{}^2} = \gamma^2\frac{\partial^2}{\partial\bar{x}_1{}^2} - 2i\rho\gamma^2\frac{\partial}{\partial\bar{x}_1}\frac{\partial}{\partial\bar{x}_4} - \rho^2\gamma^2\frac{\partial^2}{\partial\bar{x}_4{}^2}. \quad (120)$$

Similarly, we can write the following differential operator:

$$\frac{\partial\Phi}{\partial x_4} = \frac{\partial\Phi}{\partial\bar{x}_1}\frac{\partial\bar{x}_1}{\partial x_4} + \frac{\partial\Phi}{\partial\bar{x}_2}\frac{\partial\bar{x}_2}{\partial x_4} + \frac{\partial\Phi}{\partial\bar{x}_3}\frac{\partial\bar{x}_3}{\partial x_4} + \frac{\partial\Phi}{\partial\bar{x}_4}\frac{\partial\bar{x}_4}{\partial x_4} + \frac{\partial\Phi}{\partial\bar{x}_5}\frac{\partial\bar{x}_5}{\partial x_4} + \frac{\partial\Phi}{\partial\bar{x}_6}\frac{\partial\bar{x}_6}{\partial x_4},$$

$$\frac{\partial}{\partial x_4} = \frac{\partial}{\partial\bar{x}_1}\frac{\partial\bar{x}_1}{\partial x_4} + \frac{\partial}{\partial\bar{x}_2}\frac{\partial\bar{x}_2}{\partial x_4} + \frac{\partial}{\partial\bar{x}_3}\frac{\partial\bar{x}_3}{\partial x_4} + \frac{\partial}{\partial\bar{x}_4}\frac{\partial\bar{x}_4}{\partial x_4} + \frac{\partial}{\partial\bar{x}_5}\frac{\partial\bar{x}_5}{\partial x_4} + \frac{\partial}{\partial\bar{x}_6}\frac{\partial\bar{x}_6}{\partial x_4},$$

Substituting Eqs. (96)-(101) into the above expression results in

$$\frac{\partial}{\partial x_4} = \frac{\partial}{\partial\bar{x}_1}\frac{\partial\{\gamma(x_1+i\rho x_4)\}}{\partial x_4} + \frac{\partial}{\partial\bar{x}_2}\frac{\partial\{\gamma(x_2+i\rho x_5)\}}{\partial x_4} + \frac{\partial}{\partial\bar{x}_3}\frac{\partial\{\gamma(x_3+i\rho x_6)\}}{\partial x_4} + \frac{\partial}{\partial\bar{x}_4}\frac{\partial\gamma(x_4-i\rho x_1)}{\partial x_4} + \frac{\partial}{\partial\bar{x}_5}\frac{\partial\gamma(x_5-i\rho x_2)}{\partial x_4} + \frac{\partial}{\partial\bar{x}_6}\frac{\partial\gamma(x_6-i\rho x_3)}{\partial x_4},$$

$$\frac{\partial}{\partial x_4} = \frac{\partial}{\partial \bar{x}_1} i\gamma\rho + \frac{\partial}{\partial \bar{x}_2} 0 + \frac{\partial}{\partial \bar{x}_3} 0 + \frac{\partial}{\partial \bar{x}_4} \gamma + \frac{\partial}{\partial \bar{x}_5} 0 + \frac{\partial}{\partial \bar{x}_6} 0,$$

$$\frac{\partial}{\partial x_4} = \gamma \frac{\partial}{\partial \bar{x}_4} + i\gamma\rho \frac{\partial}{\partial \bar{x}_1},$$

Multiplying the above equation by itself, we get:

$$\frac{\partial^2}{\partial {x_4}^2} = \left(\gamma \frac{\partial}{\partial \bar{x}_4} + i\gamma\rho \frac{\partial}{\partial \bar{x}_1}\right)\left(\gamma \frac{\partial}{\partial \bar{x}_4} + i\gamma\rho \frac{\partial}{\partial \bar{x}_1}\right),$$

$$\frac{\partial^2}{\partial {x_4}^2} = \gamma^2 \frac{\partial^2}{\partial {\bar{x}_4}^2} + 2i\rho\gamma^2 \frac{\partial}{\partial \bar{x}_1}\frac{\partial}{\partial \bar{x}_4} - \rho^2\gamma^2 \frac{\partial^2}{\partial {\bar{x}_1}^2}. \quad (121)$$

Adding Eqs. (121) and (120) results in

$$\frac{\partial^2}{\partial {x_1}^2} + \frac{\partial^2}{\partial {x_4}^2} = \gamma^2 \frac{\partial^2}{\partial {\bar{x}_1}^2} - 2i\rho\gamma^2 \frac{\partial}{\partial \bar{x}_1}\frac{\partial}{\partial \bar{x}_4} - \rho^2\gamma^2 \frac{\partial^2}{\partial {\bar{x}_4}^2} + \gamma^2 \frac{\partial^2}{\partial {\bar{x}_4}^2} + 2i\rho\gamma^2 \frac{\partial}{\partial \bar{x}_1}\frac{\partial}{\partial \bar{x}_4} - \rho^2\gamma^2 \frac{\partial^2}{\partial {\bar{x}_1}^2},$$

$$\frac{\partial^2}{\partial {x_1}^2} + \frac{\partial^2}{\partial {x_4}^2} = \gamma^2 \left(\frac{\partial^2}{\partial {\bar{x}_1}^2} - \rho^2 \frac{\partial^2}{\partial {\bar{x}_4}^2} + \frac{\partial^2}{\partial {\bar{x}_4}^2} - \rho^2 \frac{\partial^2}{\partial {\bar{x}_1}^2}\right),$$

$$\frac{\partial^2}{\partial {x_1}^2} + \frac{\partial^2}{\partial {x_4}^2} = \frac{1}{1-\frac{v^2}{c^2}}\left(\frac{\partial^2}{\partial {\bar{x}_1}^2} - \frac{v^2}{c^2}\frac{\partial^2}{\partial {\bar{x}_1}^2} + \frac{\partial^2}{\partial {\bar{x}_4}^2} - \frac{v^2}{c^2}\frac{\partial^2}{\partial {\bar{x}_4}^2}\right),$$

$$\frac{\partial^2}{\partial {x_1}^2} + \frac{\partial^2}{\partial {x_4}^2} = \frac{1}{1-\frac{v^2}{c^2}}\left[\left(1-\frac{v^2}{c^2}\right)\frac{\partial^2}{\partial {\bar{x}_1}^2} + \left(1-\frac{v^2}{c^2}\right)\frac{\partial^2}{\partial {\bar{x}_4}^2}\right],$$

$$\frac{\partial^2}{\partial {x_1}^2} + \frac{\partial^2}{\partial {x_4}^2} = \frac{\partial^2}{\partial {\bar{x}_1}^2} + \frac{\partial^2}{\partial {\bar{x}_4}^2}. \quad (122)$$

Similarly, we can write the following differential operator:

$$\frac{\partial}{\partial x_2} = \frac{\partial}{\partial \bar{x}_1}\frac{\partial \bar{x}_1}{\partial x_2} + \frac{\partial}{\partial \bar{x}_2}\frac{\partial \bar{x}_2}{\partial x_2} + \frac{\partial}{\partial \bar{x}_3}\frac{\partial \bar{x}_3}{\partial x_2} + \frac{\partial}{\partial \bar{x}_4}\frac{\partial \bar{x}_4}{\partial x_2} + \frac{\partial}{\partial \bar{x}_5}\frac{\partial \bar{x}_5}{\partial x_2} + \frac{\partial}{\partial \bar{x}_6}\frac{\partial \bar{x}_6}{\partial x_2},$$

Substituting Eqs. (96)-(101) into the above expression results in

$$\frac{\partial}{\partial x_2} = \frac{\partial}{\partial \bar{x}_1}\frac{\partial\{\gamma(x_1+i\rho x_4)\}}{\partial x_2} + \frac{\partial}{\partial \bar{x}_2}\frac{\partial\{\gamma(x_2+i\rho x_5)\}}{\partial x_2} + \frac{\partial}{\partial \bar{x}_3}\frac{\partial\{\gamma(x_3+i\rho x_6)\}}{\partial x_2} + \frac{\partial}{\partial \bar{x}_4}\frac{\partial\gamma(x_4-i\rho x_1)}{\partial x_2} + \frac{\partial}{\partial \bar{x}_5}\frac{\partial\gamma(x_5-i\rho x_2)}{\partial x_2} + \frac{\partial}{\partial \bar{x}_6}\frac{\partial\gamma(x_6-i\rho x_3)}{\partial x_2},$$

$$\frac{\partial}{\partial x_2} = \frac{\partial}{\partial \bar{x}_1} 0 + \frac{\partial}{\partial \bar{x}_2}\gamma + \frac{\partial}{\partial \bar{x}_3} 0 + \frac{\partial}{\partial \bar{x}_4} 0 - \frac{\partial}{\partial \bar{x}_5} i\gamma\rho + \frac{\partial}{\partial \bar{x}_6} 0,$$

$$\frac{\partial}{\partial x_2} = \gamma \frac{\partial}{\partial \bar{x}_2} - i\gamma\rho \frac{\partial}{\partial \bar{x}_5},$$

Multiplying the above equation by itself, we get:

$$\frac{\partial^2}{\partial {x_2}^2} = \left(\gamma \frac{\partial}{\partial \bar{x}_2} - i\gamma\rho \frac{\partial}{\partial \bar{x}_5}\right)\left(\gamma \frac{\partial}{\partial \bar{x}_2} - i\gamma\rho \frac{\partial}{\partial \bar{x}_5}\right),$$

$$\frac{\partial^2}{\partial {x_2}^2} = \gamma^2 \frac{\partial^2}{\partial {\bar{x}_2}^2} - 2i\rho\gamma^2 \frac{\partial}{\partial \bar{x}_2}\frac{\partial}{\partial \bar{x}_5} - \rho^2\gamma^2 \frac{\partial^2}{\partial {\bar{x}_5}^2}. \quad (123)$$

Similarly, we can write the following differential operator:

$$\frac{\partial}{\partial x_5} = \frac{\partial}{\partial \bar{x}_1}\frac{\partial \bar{x}_1}{\partial x_5} + \frac{\partial}{\partial \bar{x}_2}\frac{\partial \bar{x}_2}{\partial x_5} + \frac{\partial}{\partial \bar{x}_3}\frac{\partial \bar{x}_3}{\partial x_5} + \frac{\partial}{\partial \bar{x}_4}\frac{\partial \bar{x}_4}{\partial x_5} + \frac{\partial}{\partial \bar{x}_5}\frac{\partial \bar{x}_5}{\partial x_5} + \frac{\partial}{\partial \bar{x}_6}\frac{\partial \bar{x}_6}{\partial x_5},$$

Substituting Eqs. (96)-(101) into the above expression results in

$$\frac{\partial}{\partial x_5} = \frac{\partial}{\partial \bar{x}_1}\frac{\partial\{\gamma(x_1+i\rho x_4)\}}{\partial x_5} + \frac{\partial}{\partial \bar{x}_2}\frac{\partial\{\gamma(x_2+i\rho x_5)\}}{\partial x_5} + \frac{\partial}{\partial \bar{x}_3}\frac{\partial\{\gamma(x_3+i\rho x_6)\}}{\partial x_5} + \frac{\partial}{\partial \bar{x}_4}\frac{\partial\gamma(x_4-i\rho x_1)}{\partial x_5} + \frac{\partial}{\partial \bar{x}_5}\frac{\partial\gamma(x_5-i\rho x_2)}{\partial x_5} + \frac{\partial}{\partial \bar{x}_6}\frac{\partial\gamma(x_6-i\rho x_3)}{\partial x_5},$$

$$\frac{\partial}{\partial x_5} = \frac{\partial}{\partial \bar{x}_1} 0 + \frac{\partial}{\partial \bar{x}_2} i\gamma\rho + \frac{\partial}{\partial \bar{x}_3} 0 + \frac{\partial}{\partial \bar{x}_4} 0 + \frac{\partial}{\partial \bar{x}_5}\gamma + \frac{\partial}{\partial \bar{x}_6} 0,$$

$$\frac{\partial}{\partial x_5} = \gamma \frac{\partial}{\partial \bar{x}_5} + i\gamma\rho \frac{\partial}{\partial \bar{x}_2},$$

Multiplying the above equation by itself, we get:

$$\frac{\partial^2}{\partial {x_5}^2} = \left(\gamma \frac{\partial}{\partial \bar{x}_5} + i\gamma\rho \frac{\partial}{\partial \bar{x}_2}\right)\left(\gamma \frac{\partial}{\partial \bar{x}_5} + i\gamma\rho \frac{\partial}{\partial \bar{x}_2}\right),$$

$$\frac{\partial^2}{\partial {x_5}^2} = \gamma^2 \frac{\partial^2}{\partial {\bar{x}_5}^2} + 2i\rho\gamma^2 \frac{\partial}{\partial \bar{x}_2}\frac{\partial}{\partial \bar{x}_5} - \rho^2\gamma^2 \frac{\partial^2}{\partial {\bar{x}_2}^2}. \quad (124)$$

Adding Eqs. (123) and (124) results in

$$\frac{\partial^2}{\partial {x_2}^2} + \frac{\partial^2}{\partial {x_5}^2} = \gamma^2 \frac{\partial^2}{\partial {\bar{x}_2}^2} - 2i\rho\gamma^2 \frac{\partial}{\partial \bar{x}_2}\frac{\partial}{\partial \bar{x}_5} - \rho^2\gamma^2 \frac{\partial^2}{\partial {\bar{x}_5}^2} + \gamma^2 \frac{\partial^2}{\partial {\bar{x}_5}^2} + 2i\rho\gamma^2 \frac{\partial}{\partial \bar{x}_2}\frac{\partial}{\partial \bar{x}_5} - \rho^2\gamma^2 \frac{\partial^2}{\partial {\bar{x}_2}^2},$$

$$\frac{\partial^2}{\partial {x_2}^2} + \frac{\partial^2}{\partial {x_5}^2} = \gamma^2 \left(\frac{\partial^2}{\partial {\bar{x}_2}^2} - \rho^2 \frac{\partial^2}{\partial {\bar{x}_5}^2} + \frac{\partial^2}{\partial {\bar{x}_5}^2} - \rho^2 \frac{\partial^2}{\partial {\bar{x}_2}^2}\right),$$

$$\frac{\partial^2}{\partial {x_2}^2} + \frac{\partial^2}{\partial {x_5}^2} = \gamma^2 \left(\frac{\partial^2}{\partial {\bar{x}_2}^2} - \rho^2 \frac{\partial^2}{\partial {\bar{x}_5}^2} + \frac{\partial^2}{\partial {\bar{x}_5}^2} - \rho^2 \frac{\partial^2}{\partial {\bar{x}_2}^2}\right),$$

$$\frac{\partial^2}{\partial {x_2}^2} + \frac{\partial^2}{\partial {x_5}^2} = \frac{1}{1-\frac{v^2}{c^2}}\left(\frac{\partial^2}{\partial {\bar{x}_2}^2} - \frac{v^2}{c^2}\frac{\partial^2}{\partial {\bar{x}_2}^2} + \frac{\partial^2}{\partial {\bar{x}_5}^2} - \frac{v^2}{c^2}\frac{\partial^2}{\partial {\bar{x}_5}^2}\right),$$

$$\frac{\partial^2}{\partial {x_2}^2}+\frac{\partial^2}{\partial {x_5}^2}=\frac{1}{1-\frac{v^2}{c^2}}\left[\left(1-\frac{v^2}{c^2}\right)\frac{\partial^2}{\partial {\bar{x}_2}^2}+\left(1-\frac{v^2}{c^2}\right)\frac{\partial^2}{\partial {\bar{x}_5}^2}\right],$$

$$\frac{\partial^2}{\partial {x_2}^2}+\frac{\partial^2}{\partial {x_5}^2}=\frac{\partial^2}{\partial {\bar{x}_2}^2}+\frac{\partial^2}{\partial {\bar{x}_5}^2}. \quad (125)$$

Similarly, we can write the following differential operator:

$$\frac{\partial}{\partial x_3}=\frac{\partial}{\partial \bar{x}_1}\frac{\partial \bar{x}_1}{\partial x_3}+\frac{\partial}{\partial \bar{x}_2}\frac{\partial \bar{x}_2}{\partial x_3}+\frac{\partial}{\partial \bar{x}_3}\frac{\partial \bar{x}_3}{\partial x_3}+\frac{\partial}{\partial \bar{x}_4}\frac{\partial \bar{x}_4}{\partial x_3}+\frac{\partial}{\partial \bar{x}_5}\frac{\partial \bar{x}_5}{\partial x_3}+\frac{\partial}{\partial \bar{x}_6}\frac{\partial \bar{x}_6}{\partial x_3},$$

Substituting Eqs. (96)-(101) into the above expression results in

$$\frac{\partial}{\partial x_3}=\frac{\partial}{\partial \bar{x}_1}\frac{\partial\{\gamma(x_1+i\rho x_4)\}}{\partial x_3}+\frac{\partial}{\partial \bar{x}_2}\frac{\partial\{\gamma(x_2+i\rho x_5)\}}{\partial x_3}+\frac{\partial}{\partial \bar{x}_3}\frac{\partial\{\gamma(x_3+i\rho x_6)\}}{\partial x_3}+\frac{\partial}{\partial \bar{x}_4}\frac{\partial\gamma(x_4-i\rho x_1)}{\partial x_3}+\frac{\partial}{\partial \bar{x}_5}\frac{\partial\gamma(x_5-i\rho x_2)}{\partial x_3}+\frac{\partial}{\partial \bar{x}_6}\frac{\partial\gamma(x_6-i\rho x_3)}{\partial x_3},$$

$$\frac{\partial}{\partial x_3}=\frac{\partial}{\partial \bar{x}_1}0+\frac{\partial}{\partial \bar{x}_2}0+\frac{\partial}{\partial \bar{x}_3}\gamma+\frac{\partial}{\partial \bar{x}_4}0+\frac{\partial}{\partial \bar{x}_5}0-\frac{\partial}{\partial \bar{x}_6}i\gamma\rho,$$

$$\frac{\partial}{\partial x_3}=\gamma\frac{\partial}{\partial \bar{x}_3}-i\gamma\rho\frac{\partial}{\partial \bar{x}_6},$$

Multiplying the above equation by itself, we get

$$\frac{\partial^2}{\partial {x_3}^2}=\left(\gamma\frac{\partial}{\partial \bar{x}_3}-i\gamma\rho\frac{\partial}{\partial \bar{x}_6}\right)\left(\gamma\frac{\partial}{\partial \bar{x}_3}-i\gamma\rho\frac{\partial}{\partial \bar{x}_6}\right),$$

$$\frac{\partial^2}{\partial {x_3}^2}=\gamma^2\frac{\partial^2}{\partial {\bar{x}_3}^2}-2i\rho\gamma^2\frac{\partial}{\partial \bar{x}_3}\frac{\partial}{\partial \bar{x}_6}-\rho^2\gamma^{\,2}\frac{\partial^2}{\partial {\bar{x}_6}^2}. \quad (126)$$

Similarly, we can write the following differential operator:

$$\frac{\partial}{\partial x_6}=\frac{\partial}{\partial \bar{x}_1}\frac{\partial \bar{x}_1}{\partial x_6}+\frac{\partial}{\partial \bar{x}_2}\frac{\partial \bar{x}_2}{\partial x_6}+\frac{\partial}{\partial \bar{x}_3}\frac{\partial \bar{x}_3}{\partial x_6}+\frac{\partial}{\partial \bar{x}_4}\frac{\partial \bar{x}_4}{\partial x_6}+\frac{\partial}{\partial \bar{x}_5}\frac{\partial \bar{x}_5}{\partial x_6}+\frac{\partial}{\partial \bar{x}_6}\frac{\partial \bar{x}_6}{\partial x_6},$$

Substituting Eqs. (96)-(101) into the above expression results in

$$\frac{\partial}{\partial x_6}=\frac{\partial}{\partial \bar{x}_1}\frac{\partial\{\gamma(x_1+i\rho x_4)\}}{\partial x_6}+\frac{\partial}{\partial \bar{x}_2}\frac{\partial\{\gamma(x_2+i\rho x_5)\}}{\partial x_6}+\frac{\partial}{\partial \bar{x}_3}\frac{\partial\{\gamma(x_3+i\rho x_6)\}}{\partial x_6}+\frac{\partial}{\partial \bar{x}_4}\frac{\partial\gamma(x_4-i\rho x_1)}{\partial x_6}+\frac{\partial}{\partial \bar{x}_5}\frac{\partial\gamma(x_5-i\rho x_2)}{\partial x_6}+\frac{\partial}{\partial \bar{x}_6}\frac{\partial\gamma(x_6-i\rho x_3)}{\partial x_6},$$

$$\frac{\partial}{\partial x_6}=\frac{\partial}{\partial \bar{x}_1}0+\frac{\partial}{\partial \bar{x}_2}0+\frac{\partial}{\partial \bar{x}_3}i\gamma\rho+\frac{\partial}{\partial \bar{x}_4}0+\frac{\partial}{\partial \bar{x}_5}0+\frac{\partial}{\partial \bar{x}_6}\gamma,$$

$$\frac{\partial}{\partial x_6}=\gamma\frac{\partial}{\partial \bar{x}_6}+i\gamma\rho\frac{\partial}{\partial \bar{x}_3},$$

Multiplying the above equation by itself, we get,

$$\frac{\partial^2}{\partial {x_6}^2}=\left(\gamma\frac{\partial}{\partial \bar{x}_6}+i\gamma\rho\frac{\partial}{\partial \bar{x}_3}\right)\left(\gamma\frac{\partial}{\partial \bar{x}_6}+i\gamma\rho\frac{\partial}{\partial \bar{x}_3}\right),$$

$$\frac{\partial^2}{\partial {x_6}^2}=\gamma^2\frac{\partial^2}{\partial {\bar{x}_6}^2}+2i\rho\gamma^2\frac{\partial}{\partial \bar{x}_3}\frac{\partial}{\partial \bar{x}_6}-\rho^2\gamma^{\,2}\frac{\partial^2}{\partial {\bar{x}_3}^2}. \quad (127)$$

Adding Eqs. (126) and (127) results in

$$\frac{\partial^2}{\partial {x_3}^2}+\frac{\partial^2}{\partial {x_6}^2}=\gamma^2\frac{\partial^2}{\partial {\bar{x}_3}^2}-2i\rho\gamma^2\frac{\partial}{\partial \bar{x}_3}\frac{\partial}{\partial \bar{x}_6}-\rho^2\gamma^{\,2}\frac{\partial^2}{\partial {\bar{x}_6}^2}+\gamma^2\frac{\partial^2}{\partial {\bar{x}_6}^2}+2i\rho\gamma^2\frac{\partial}{\partial \bar{x}_3}\frac{\partial}{\partial \bar{x}_6}-\rho^2\gamma^{\,2}\frac{\partial^2}{\partial {\bar{x}_3}^2},$$

$$\frac{\partial^2}{\partial {x_3}^2}+\frac{\partial^2}{\partial {x_6}^2}=\gamma^2\left(\frac{\partial^2}{\partial {\bar{x}_3}^2}-\rho^2\frac{\partial^2}{\partial {\bar{x}_6}^2}+\frac{\partial^2}{\partial {\bar{x}_6}^2}-\rho^2\frac{\partial^2}{\partial {\bar{x}_3}^2}\right),$$

$$\frac{\partial^2}{\partial {x_3}^2}+\frac{\partial^2}{\partial {x_6}^2}=\gamma^2\left(\frac{\partial^2}{\partial {\bar{x}_3}^2}-\rho^2\frac{\partial^2}{\partial {\bar{x}_6}^2}+\frac{\partial^2}{\partial {\bar{x}_6}^2}-\rho^2\frac{\partial^2}{\partial {\bar{x}_3}^2}\right),$$

$$\frac{\partial^2}{\partial {x_3}^2}+\frac{\partial^2}{\partial {x_6}^2}=\frac{1}{1-\frac{v^2}{c^2}}\left(\frac{\partial^2}{\partial {\bar{x}_3}^2}-\frac{v^2}{c^2}\frac{\partial^2}{\partial {\bar{x}_3}^2}+\frac{\partial^2}{\partial {\bar{x}_6}^2}-\frac{v^2}{c^2}\frac{\partial^2}{\partial {\bar{x}_6}^2}\right),$$

$$\frac{\partial^2}{\partial {x_3}^2}+\frac{\partial^2}{\partial {x_6}^2}=\frac{1}{1-\frac{v^2}{c^2}}\left[\left(1-\frac{v^2}{c^2}\right)\frac{\partial^2}{\partial {\bar{x}_3}^2}+\left(1-\frac{v^2}{c^2}\right)\frac{\partial^2}{\partial {\bar{x}_6}^2}\right],$$

$$\frac{\partial^2}{\partial {x_3}^2}+\frac{\partial^2}{\partial {x_6}^2}=\frac{\partial^2}{\partial {\bar{x}_3}^2}+\frac{\partial^2}{\partial {\bar{x}_6}^2}. \quad (128)$$

Adding Eqs. (122), (125), and (128), we get,

$$\frac{\partial^2}{\partial {x_1}^2}+\frac{\partial^2}{\partial {x_2}^2}+\frac{\partial^2}{\partial {x_3}^2}+\frac{\partial^2}{\partial {x_4}^2}+\frac{\partial^2}{\partial {x_5}^2}+\frac{\partial^2}{\partial {x_6}^2}=\frac{\partial^2}{\partial {\bar{x}_1}^2}+\frac{\partial^2}{\partial {\bar{x}_2}^2}+\frac{\partial^2}{\partial {\bar{x}_3}^2}+\frac{\partial^2}{\partial {\bar{x}_4}^2}+\frac{\partial^2}{\partial {\bar{x}_5}^2}+\frac{\partial^2}{\partial {\bar{x}_6}^2}. \quad (129)$$

From Eqs. (118), (119), and (129), we can conclude that the propagation equation of the electromagnetic wave or D'Alembert operator is invariant under the six new relativistic Lorentz transformation equations.

3.5 Transformation of Energy and Momentum

Let us suppose once again that the frame K' moves relative to the frame k with velocity v in three dimensions of space as indicated in Fig. 2. Here, the symbols u and $\bar{u}$ will be used for velocities of the particle measured from the inertial frames K and K', respectively. Symbol v will only be used for the relative velocity between inertial frames (see Fig. 2), and symbol

γ will always represent $1/\sqrt{1-v^2/c^2}$. Symbol m_0 will be used to represent the rest mass of the particle so that the relativistic mass of the particle measured from the frames K and K' isgiven by the following:

$$m = \frac{m_0}{\sqrt{1-\frac{u^2}{c^2}}}, \bar{m} = \frac{m_0}{\sqrt{1-\frac{\bar{u}^2}{c^2}}}.$$

Here, m and $\bar{m}$ represent the relativistic mass of the particle measured from the inertial frames K and K', respectively.

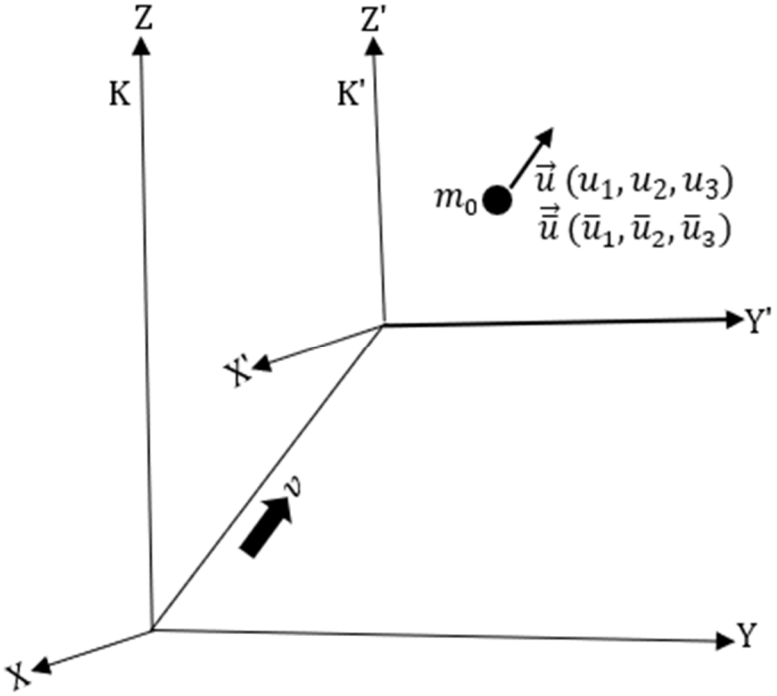

FIG. 2. Velocity of a moving particle observed from frames K and K'.

The position vector of a particle measured from frame K at any instant of time t can be written as follows:

$$\vec{r} = x\vec{\imath} + y\vec{\jmath} + z\vec{k},$$

Differentiating this equation with respect to t, we get:

$$\left.\begin{aligned} \frac{d\vec{r}}{dt} &= \frac{dx}{dt}\vec{\imath} + \frac{dy}{dt}\vec{\jmath} + \frac{dz}{dt}\vec{k} \\ \vec{u} &= u_1\vec{\imath} + u_2\vec{\jmath} + u_3\vec{k} \end{aligned}\right\}. \quad (130)$$

Multiplying both sides by the relativistic mass $m = m_0/\sqrt{1-u^2/c^2}$ of the particle as measured in frame K we get:

$$\left.\begin{aligned} m\vec{u} &= mu_1\vec{\imath} + mu_2\vec{\jmath} + mu_3\vec{k} \\ \vec{p} &= p_1\vec{\imath} + p_2\vec{\jmath} + p_3\vec{k} \end{aligned}\right\}. \quad (131)$$

Here, p_1, p_2, and p_3 represent the component of linear momentum along the X-, Y-, and Z-directions in the K frame of reference. Also, using Eqs. (20)-(22), the position of the same particle in the form of polar coordinates can be written as follows:

$$\vec{r} = x\vec{\imath} + y\vec{\jmath} + z\vec{k},$$

$$\vec{r} = r\sin\alpha\cos\beta\,\vec{\imath} + r\sin\alpha\sin\beta\,\vec{\jmath} + r\cos\alpha\,\vec{k},$$

Differentiating this equation with respect to t, we get:

$$\frac{d\vec{r}}{dt} = \frac{d(r\sin\alpha\cos\beta)}{dt}\vec{\imath} + \frac{d(r\sin\alpha\sin\beta)}{dt}\vec{\jmath} + \frac{d(r\cos\alpha)}{dt}\vec{k},$$

$$\frac{d\vec{r}}{dt} = \frac{dr}{dt}\sin\alpha\cos\beta\,\vec{\imath} + \frac{dr}{dt}\sin\alpha\sin\beta\,\vec{\jmath} + \frac{dr}{dt}\cos\alpha\,\vec{k},$$

$$\vec{u} = u\sin\alpha\cos\beta\,\vec{\imath} + u\sin\alpha\sin\beta\,\vec{\jmath} + u\cos\alpha\,\vec{k}, \quad (132)$$

Multiplying both sides by the relativistic mass $m = m_0/\sqrt{1-u^2/c^2}$ of the particle as measured in frame K, we get:

$$m\vec{u} = mu\sin\alpha\cos\beta\,\vec{\imath} + mu\sin\alpha\sin\beta\,\vec{\jmath} + mu\cos\alpha\,\vec{k},$$

$$\vec{p} = p\sin\alpha\cos\beta\,\vec{\imath} + p\sin\alpha\sin\beta\,\vec{\jmath} + p\cos\alpha\,\vec{k}, \quad (133)$$

Now, comparing the corresponding coefficients of Eqs. (130) and (132), we get:

$u_1 = u\sin\alpha\cos\beta\,, u_2 = u\sin\alpha\sin\beta\,, u_3 = u\cos\alpha,$ (134)

Also, comparing the corresponding coefficients of Eqs. (131) and (133), we get:

$p_1 = p\sin\alpha\cos\beta\,, p_2 = p\sin\alpha\sin\beta\,, p_3 = p\cos\alpha,$ (135)

Similarly, the position vector of the same particle measured from frame K' at any instant of time $\bar{t}$ can be written as follows:

$\vec{\bar{r}} = \bar{x}\vec{\imath} + \bar{y}\vec{\jmath} + \bar{z}\vec{k},$

Differentiating this equation with respect to $\bar{t}$, we get:

$$\left.\begin{aligned}\frac{d\vec{\bar{r}}}{d\bar{t}} &= \frac{d\bar{x}}{d\bar{t}}\vec{\imath} + \frac{d\bar{y}}{d\bar{t}}\vec{\jmath} + \frac{d\bar{z}}{d\bar{t}}\vec{k}\\ \vec{\bar{u}} &= \bar{u}_1\vec{\imath} + \bar{u}_2\vec{\jmath} + \bar{u}_3\vec{k}\end{aligned}\right\}. \quad (136)$$

Multiplying both sides by the relativistic mass $\bar{m} = m_0/\sqrt{1-\bar{u}^2/c^2}$ of the particle as measured in frame K', we get:

$$\left.\begin{aligned}\bar{m}\vec{\bar{u}} &= \bar{m}\bar{u}_1\vec{\imath} + \bar{m}\bar{u}_2\vec{\jmath} + \bar{m}\bar{u}_3\vec{k}\\ \vec{\bar{p}} &= \bar{p}_1\vec{\imath} + \bar{p}_2\vec{\jmath} + \bar{p}_3\vec{k}\end{aligned}\right\}. \quad (137)$$

Here, $\bar{p}_1$, $\bar{p}_2$, and $\bar{p}_3$ represent the component of linear momentum along the X-, Y-, and Z-directions in the K' frame of reference. Also, using Eqs. (24)-(26), the position of the same particle in the form of polar coordinates can be written as follows:

$\vec{\bar{r}} = \bar{x}\vec{\imath} + \bar{y}\vec{\jmath} + \bar{z}\vec{k},$

$\vec{\bar{r}} = \bar{r}\sin\alpha\cos\beta\,\vec{\imath} + \bar{r}\sin\alpha\sin\beta\,\vec{\jmath} + \bar{r}\cos\alpha\,\vec{k},$

Differentiating this equation with respect to $\bar{t}$, we get:

$\frac{d\vec{\bar{r}}}{d\bar{t}} = \frac{d(\bar{r}\sin\alpha\cos\beta)}{d\bar{t}}\vec{\imath} + \frac{d(\bar{r}\sin\alpha\sin\beta)}{d\bar{t}}\vec{\jmath} + \frac{d(\bar{r}\cos\alpha)}{d\bar{t}}\vec{k},$

$\frac{d\vec{\bar{r}}}{d\bar{t}} = \sin\alpha\cos\beta\frac{d\bar{r}}{d\bar{t}}\vec{\imath} + \sin\alpha\sin\beta\frac{d\bar{r}}{d\bar{t}}\vec{\jmath} + \cos\alpha\frac{d\bar{r}}{d\bar{t}}\vec{k},$

$\vec{\bar{u}} = \bar{u}\sin\alpha\cos\beta\,\vec{\imath} + \bar{u}\sin\alpha\sin\beta\,\vec{\jmath} + \bar{u}\cos\alpha\,\vec{k},$ (138)

Multiplying both sides by the relativistic mass $\bar{m} = m_0/\sqrt{1-\bar{u}^2/c^2}$ of the particle as measured in frame K', we get:

$m\vec{\bar{u}} = m\bar{u}\sin\alpha\cos\beta\,\vec{\imath} + m\bar{u}\sin\alpha\sin\beta\,\vec{\jmath} + m\bar{u}\cos\alpha\,\vec{k},$

$\vec{\bar{p}} = \bar{p}\sin\alpha\cos\beta\,\vec{\imath} + \bar{p}\sin\alpha\sin\beta\,\vec{\jmath} + \bar{p}\cos\alpha\,\vec{k},$ (139)

Now, comparing the corresponding coefficients of Eqs. (136) and (138), we get:

$\bar{u}_1 = \bar{u}\sin\alpha\cos\beta\,, \bar{u}_2 = \bar{u}\sin\alpha\sin\beta\,, \bar{u}_3 = \bar{u}\cos\alpha,$ (140)

Similarly, comparing the corresponding coefficients of Eqs. (137) and (139) we get:

$\bar{p}_1 = \bar{p}\sin\alpha\cos\beta\,, \bar{p}_2 = \bar{p}\sin\alpha\sin\beta\,, \bar{p}_3 = \bar{p}\cos\alpha,$ (141)

Now we find formulas relating the velocity of the particle in one inertial frame to its velocity in a second inertial frame. From Eqs. (78), (77), (61), (49), and (36), we can write the following relativistic space-time coordinates transformation equations in differential form with the Lorentz factor $\gamma = 1/\sqrt{1-v^2/c^2}$.

$d\bar{t} = \gamma\left(dt - \frac{v}{c^2}dr\right),$ (142)

$d\bar{r} = \gamma(dr - vdt)$ (143)

$d\bar{x} = \gamma(dx - v\sin\alpha\cos\beta\,dt),$ (144)

$d\bar{y} = \gamma(dy - v\sin\alpha\sin\beta\,dt),$ (145)

$d\bar{z} = \gamma(dz - v\cos\alpha\,dt),$ (146)

From Eq. (136), the total resultant velocity of the particle as measured in frame K' can be written as follows:

$\bar{u} = \frac{d\bar{r}}{d\bar{t}},$

After the substitution of Eqs. (142) and (143), the following is obtained

$\bar{u} = \frac{\gamma(dr - vdt)}{\gamma\left(dt - \frac{v}{c^2}dr\right)} = \frac{\frac{dr}{dt} - v}{1 - \frac{v\,dr}{c^2\,dt}},$

$\bar{u} = \frac{u - v}{1 - \frac{uv}{c^2}}.$ (147)

Equation (147) determines the transformation of the velocity of the particle along the radial line. To determine the velocity transformation formulas for the X-, Y-, and Z-components, let's write the X-component of velocity of the particle from Eq. (136) as follows:

$\bar{u}_1 = \frac{d\bar{x}}{d\bar{t}},$

After the substitution of the Eqs. (142) and (144), the following is obtained:

$\bar{u}_1 = \frac{\gamma(dx - v\sin\alpha\cos\beta\,dt)}{\gamma\left(dt - \frac{v}{c^2}dr\right)} = \frac{\frac{dx}{dt} - v\sin\alpha\cos\beta}{1 - \frac{v\,dr}{c^2\,dt}},$

$$\bar{u}_1 = \frac{u_1 - v\sin\alpha\cos\beta}{1-\frac{uv}{c^2}}. \quad (148)$$

Similarly, let's write the Y-component of velocity of the particle from Eq. (136) as follows:

$$\bar{u}_2 = \frac{d\bar{y}}{d\bar{t}},$$

After the substitution of the Eqs. (142) and (145), the following is obtained:

$$\bar{u}_2 = \frac{\gamma(dy - v\sin\alpha\sin\beta\, dt)}{\gamma\left(dt - \frac{v}{c^2}dr\right)} = \frac{\frac{dy}{dt} - v\sin\alpha\sin\beta}{1-\frac{v\,dr}{c^2\,dt}},$$

$$\bar{u}_2 = \frac{u_2 - v\sin\alpha\sin\beta}{1-\frac{uv}{c^2}}. \quad (149)$$

Similarly, let's write the Z-component of velocity of the particle from Eq. (136) as follows:

$$\bar{u}_3 = \frac{d\bar{z}}{d\bar{t}},$$

After the substitution of the Eqs. (142) and (146), the following is obtained:

$$\bar{u}_3 = \frac{\gamma(dz - v\cos\alpha\, dt)}{\gamma\left(dt - \frac{v}{c^2}dr\right)} = \frac{\frac{dz}{dt} - v\cos\alpha}{1-\frac{v\,dr}{c^2\,dt}},$$

$$\bar{u}_3 = \frac{u_3 - v\cos\alpha}{1-\frac{uv}{c^2}}. \quad (150)$$

Equation (147) represents the transformation of the resultant velocity along the radial line, whereas Eqs. (148), (149), and (150) give the relativistic velocity-addition formulas for the Z-components, respectively. The corresponding inverse velocity-transformation equations along the radial direction and the X-, Y-, and Z-axes are obtained by interchanging the coordinates and replacing v with $-v$ in Eqs. (147)-(150). These inverse transformations take the following forms:

$$u = \frac{\bar{u}+v}{1+\frac{\bar{u}v}{c^2}}, \quad (151)$$

$$u_1 = \frac{\bar{u}_1 + v\sin\alpha\cos\beta}{1+\frac{\bar{u}v}{c^2}}, \quad (152)$$

$$u_2 = \frac{\bar{u}_2 + v\sin\alpha\sin\beta}{1+\frac{\bar{u}v}{c^2}}, \quad (153)$$

$$u_3 = \frac{\bar{u}_3 + v\cos\alpha}{1+\frac{\bar{u}v}{c^2}}. \quad (154)$$

In the inertial frame K, the total resultant linear momentum of the particle along the radial line [see also Eq. (131)] is given by the relation:

$$p = mu = \frac{m_0 u}{\sqrt{1-\frac{u^2}{c^2}}},$$

And total energy is defined by the relation:

$$E = mc^2 = \frac{m_0 c^2}{\sqrt{1-\frac{u^2}{c^2}}},$$

The corresponding quantities in frame K' are defined as:

$$\bar{p} = \bar{m}\bar{u} = \frac{m_0\bar{u}}{\sqrt{1-\frac{\bar{u}^2}{c^2}}}, \quad (155)$$

$$\bar{E} = \bar{m}c^2 = \frac{m_0 c^2}{\sqrt{1-\frac{\bar{u}^2}{c^2}}}, \quad (156)$$

From Eq. (147), the velocity transformation formula along the radial line is given by the equation:

$$\bar{u} = \frac{u-v}{1-\frac{uv}{c^2}}, \quad (157)$$

$$\frac{\bar{u}^2}{c^2} = \frac{\left(\frac{u}{c}-\frac{v}{c}\right)^2}{\left(1-\frac{uv}{c^2}\right)^2},$$

$$1-\frac{\bar{u}^2}{c^2} = \frac{\left(1-\frac{uv}{c^2}\right)^2 - \left(\frac{u}{c}-\frac{v}{c}\right)^2}{\left(1-\frac{uv}{c^2}\right)^2} = \frac{1+\frac{u^2v^2}{c^4}-\frac{u^2}{c^2}-\frac{v^2}{c^2}}{\left(1-\frac{uv}{c^2}\right)^2},$$

$$1-\frac{\bar{u}^2}{c^2} = \frac{\left(1-\frac{u^2}{c^2}\right)-\frac{v^2}{c^2}\left(1-\frac{u^2}{c^2}\right)}{\left(1-\frac{uv}{c^2}\right)^2} = \frac{\left(1-\frac{u^2}{c^2}\right)\left(1-\frac{v^2}{c^2}\right)}{\left(1-\frac{uv}{c^2}\right)^2},$$

$$\sqrt{1-\frac{\bar{u}^2}{c^2}} = \frac{\sqrt{\left(1-\frac{u^2}{c^2}\right)\left(1-\frac{v^2}{c^2}\right)}}{1-\frac{uv}{c^2}}, \quad (158)$$

Substituting this value in Eq. (155) and also using Eq. (157), one obtains

$$\bar{p} = \frac{m_0\bar{u}}{\sqrt{1-\frac{\bar{u}^2}{c^2}}} = \frac{m_0\bar{u}\left(1-\frac{uv}{c^2}\right)}{\sqrt{\left(1-\frac{u^2}{c^2}\right)\left(1-\frac{v^2}{c^2}\right)}},$$

$$\bar{p} = \frac{m_0(u-v)}{1-\frac{uv}{c^2}} \times \frac{\left(1-\frac{uv}{c^2}\right)}{\sqrt{\left(1-\frac{u^2}{c^2}\right)\left(1-\frac{v^2}{c^2}\right)}},$$

$$\bar{p} = \frac{m_0}{\sqrt{1-\frac{u^2}{c^2}}} \times \frac{(u-v)}{\sqrt{1-\frac{v^2}{c^2}}} = \frac{mu-mv}{\sqrt{1-\frac{v^2}{c^2}}},$$

But, $p = mu$ and $m = \frac{E}{c^2}$. Hence,

$$\bar{p} = \frac{p-\frac{Ev}{c^2}}{\sqrt{1-\frac{v^2}{c^2}}} = \gamma\left(p - \frac{Ev}{c^2}\right), \quad (159)$$

Now, from Eqs. (156) and (158) we get:

$$\bar{E} = \frac{m_0 c^2}{\sqrt{1-\frac{\bar{u}^2}{c^2}}} = \frac{m_0 c^2\left(1-\frac{uv}{c^2}\right)}{\sqrt{\left(1-\frac{u^2}{c^2}\right)\left(1-\frac{v^2}{c^2}\right)}},$$

$$\bar{E} = \frac{m_0}{\sqrt{1-\frac{u^2}{c^2}}} \times \frac{(c^2-uv)}{\sqrt{1-\frac{v^2}{c^2}}} = \gamma(mc^2 - muv),$$

$$\bar{E} = \gamma(E - pv). \tag{160}$$

Similarly, one has the inverse relations:

$$p = \gamma\left(\bar{p} + \frac{\bar{E}v}{c^2}\right), \tag{161}$$

$$E = \gamma(\bar{E} + \bar{p}v). \tag{162}$$

Equations (159) and (161) represent the transformation of total resultant linear momentum along the radial line. Now we wish to determine the transformation equations for the X-, Y-, and Z-components of linear momentum. The components of momentum along the X-, Y-, and Z-directions in frame S are defined by the relations [see also Eq. (131)]:

$$p_1 = mu_1 = \frac{m_0 u_1}{\sqrt{1-\frac{u^2}{c^2}}}, \tag{163}$$

$$p_2 = mu_2 = \frac{m_0 u_1}{\sqrt{1-\frac{u^2}{c^2}}}, \tag{164}$$

$$p_2 = mu_2 = \frac{m_0 u_1}{\sqrt{1-\frac{u^2}{c^2}}}. \tag{165}$$

The corresponding quantities in frame K' are defined as [see also Eq. (137)]:

$$\overline{p_1} = \bar{m}\overline{u_1} = \frac{m_0\overline{u_1}}{\sqrt{1-\frac{\bar{u}^2}{c^2}}}, \tag{166}$$

$$\overline{p_2} = \bar{m}\overline{u_2} = \frac{m_0\overline{u_2}}{\sqrt{1-\frac{\bar{u}^2}{c^2}}}, \tag{167}$$

$$\overline{p_3} = \bar{m}\overline{u_3} = \frac{m_0\overline{u_3}}{\sqrt{1-\frac{\bar{u}^2}{c^2}}}. \tag{168}$$

Substituting Eqs. (148) and (158) into Eq. (166), one obtains

$$\overline{p_1} = \frac{m_0\overline{u_1}}{\sqrt{1-\frac{\bar{u}^2}{c^2}}} = \frac{m_0\overline{u_1}\left(1-\frac{uv}{c^2}\right)}{\sqrt{\left(1-\frac{u^2}{c^2}\right)\left(1-\frac{v^2}{c^2}\right)}},$$

$$\overline{p_1} = \frac{m_0(u_1 - v\sin\alpha\cos\beta)}{1-\frac{uv}{c^2}} \times \frac{\left(1-\frac{uv}{c^2}\right)}{\sqrt{\left(1-\frac{u^2}{c^2}\right)\left(1-\frac{v^2}{c^2}\right)}},$$

$$\overline{p_1} = \frac{m_0}{\sqrt{1-\frac{u^2}{c^2}}} \times \frac{(u_1 - v\sin\alpha\cos\beta)}{\sqrt{1-\frac{v^2}{c^2}}} = \frac{mu_1 - mv\sin\alpha\cos\beta}{\sqrt{1-\frac{v^2}{c^2}}},$$

$$\overline{p_1} = \frac{p_1 - \frac{Ev\sin\alpha\cos\beta}{c^2}}{\sqrt{1-\frac{v^2}{c^2}}} = \gamma\left(p_1 - \frac{Ev\sin\alpha\cos\beta}{c^2}\right). \tag{169}$$

Similarly, substituting Eqs. (149) and (158) into Eqs (167), one obtains

$$\overline{p_2} = \frac{m_0\overline{u_2}}{\sqrt{1-\frac{\bar{u}^2}{c^2}}} = \frac{m_0\overline{u_2}\left(1-\frac{uv}{c^2}\right)}{\sqrt{\left(1-\frac{u^2}{c^2}\right)\left(1-\frac{v^2}{c^2}\right)}},$$

$$\overline{p_2} = \frac{m_0(u_2 - v\sin\alpha\sin\beta)}{1-\frac{uv}{c^2}} \times \frac{\left(1-\frac{uv}{c^2}\right)}{\sqrt{\left(1-\frac{u^2}{c^2}\right)\left(1-\frac{v^2}{c^2}\right)}},$$

$$\overline{p_2} = \frac{m_0}{\sqrt{1-\frac{u^2}{c^2}}} \times \frac{(u_2 - v\sin\alpha\sin\beta)}{\sqrt{1-\frac{v^2}{c^2}}} = \frac{mu_2 - mv\sin\alpha\sin\beta}{\sqrt{1-\frac{v^2}{c^2}}},$$

$$\overline{p_2} = \frac{p_2 - \frac{Ev\sin\alpha\sin\beta}{c^2}}{\sqrt{1-\frac{v^2}{c^2}}} = \gamma\left(p_2 - \frac{Ev\sin\alpha\sin\beta}{c^2}\right). \tag{170}$$

Similarly, substituting Eqs. (150) and (158) into Eq. (168), one obtains

$$\overline{p_3} = \frac{m_0\overline{u_3}}{\sqrt{1-\frac{\bar{u}^2}{c^2}}} = \frac{m_0\overline{u_3}\left(1-\frac{uv}{c^2}\right)}{\sqrt{\left(1-\frac{u^2}{c^2}\right)\left(1-\frac{v^2}{c^2}\right)}},$$

$$\overline{p_3} = \frac{m_0(u_3 - v\cos\alpha)}{1-\frac{uv}{c^2}} \times \frac{\left(1-\frac{uv}{c^2}\right)}{\sqrt{\left(1-\frac{u^2}{c^2}\right)\left(1-\frac{v^2}{c^2}\right)}},$$

$$\overline{p_3} = \frac{m_0}{\sqrt{1-\frac{u^2}{c^2}}} \times \frac{(u_3 - v\cos\alpha)}{\sqrt{1-\frac{v^2}{c^2}}} = \frac{mu_3 - mv\cos\alpha}{\sqrt{1-\frac{v^2}{c^2}}},$$

$$\overline{p_3} = \frac{p_3 - \frac{Ev\cos\alpha}{c^2}}{\sqrt{1-\frac{v^2}{c^2}}} = \gamma\left(p_3 - \frac{Ev\cos\alpha}{c^2}\right). \tag{171}$$

Equations (169), (170), and (171) represent the relativistic momentum transformation formulas for the X-, Y-, and Z-components, respectively. The respective inverse momentum transformation equations along the X-, Y-, and Z-axes are obtained by interchanging the coordinates and replacing v with $-v$ in Eqs. (169)-(171). These inverse transformations take the following forms:

$$p_1 = \gamma\left(\overline{p_1} + \frac{\bar{E}v\sin\alpha\cos\beta}{c^2}\right), \tag{172}$$

$$p_2 = \gamma\left(\overline{p_2} + \frac{\bar{E}v\sin\alpha\sin\beta}{c^2}\right), \tag{173}$$

$$p_3 = \gamma\left(\overline{p_3} + \frac{\bar{E}v\cos\alpha}{c^2}\right). \tag{174}$$

These equations represent the transformation relations for the first three spatial components of the four-momentum vector $(p_1, p_2, p_3, iE/c)$ in ordinary four-dimensional Minkowski space. However, in the extended space–time continuum considered in this work, it will be shown in the derivation presented in the forthcoming Section 3.6 that the time part of the momentum also yields three distinct components. This leads naturally to the concept of a six-momentum. The six-momentum vector thus defined has six components, of which the first three represent the spatial momenta (p_1, p_2, p_3) i.e., momentum components along the X, Y and Z-directions, while the remaining three represent the time components of momentum, which are of the following form (see the forthcoming Section 3.6 for the explicit derivation):

$$p_4 = \frac{iE\sin\alpha\cos\beta}{c}, p_5 = \frac{iE\sin\alpha\sin\beta}{c}, p_6 = \frac{iE\cos\alpha}{c}, \quad (175)$$

These time components of the six-momentum are defined for the frame K; however, they must be defined for the frame K' in the following way (see the forthcoming Section 3.6 for the explicit derivation):

$$\bar{p}_4 = \frac{i\bar{E}\sin\alpha\cos\beta}{c}, \bar{p}_5 = \frac{i\bar{E}\sin\alpha\sin\beta}{c}, \bar{p}_6 = \frac{i\bar{E}\cos\alpha}{c}. \quad (176)$$

Using Eq. (175) in Eqs. (169), (170), and (171), the following expressions are obtained with the factor $\rho = v/c$:

$$\overline{p_1} = \gamma\left(p_1 - \rho\frac{E\sin\alpha\cos\beta}{c}\right) = \gamma\left(p_1 + \rho\frac{i^2E\sin\alpha\cos\beta}{c}\right) = \gamma(p_1 + i\rho p_4), \quad (178)$$

$$\overline{p_2} = \gamma\left(p_2 - \rho\frac{E\sin\alpha\sin\beta}{c}\right) = \gamma\left(p_2 + \rho\frac{i^2E\sin\alpha\sin\beta}{c}\right) = \gamma(p_2 + i\rho p_5), \quad (179)$$

$$\overline{p_3} = \gamma\left(p_3 - \rho\frac{E\cos\alpha}{c}\right) = \gamma\left(p_3 + \rho\frac{i^2E\cos\alpha}{c}\right) = \gamma(p_3 + i\rho p_6). \quad (180)$$

Now, multiplying both sides of Eq. (160) by $i\sin\alpha\cos\beta/c$, we get:

$$\bar{E} = \gamma(E - pv),$$

$$\frac{i\bar{E}\sin\alpha\cos\beta}{c} = \gamma\left(\frac{iE\sin\alpha\cos\beta}{c} - \frac{ipv\sin\alpha\cos\beta}{c}\right),$$

After the substitution of Eqs. (135), (175), and (176), the following is obtained with factor $\rho = v/c$:

$$\frac{i\bar{E}\sin\alpha\cos\beta}{c} = \gamma\left(\frac{iE\sin\alpha\cos\beta}{c} - \frac{ivp_1}{c}\right),$$

$$\bar{p}_4 = \gamma(p_4 - i\rho p_1). \quad (181)$$

Similarly, let us multiply both sides of Eq. (160) by $i\sin\alpha\sin\beta/c$ to get:

$$\bar{E} = \gamma(E - pv),$$

$$\frac{i\bar{E}\sin\alpha\sin\beta}{c} = \gamma\left(\frac{iE\sin\alpha\sin\beta}{c} - \frac{ipv\sin\alpha\sin\beta}{c}\right),$$

After the substitution of Eqs. (135), (175), and (176), the following is obtained with factor $\rho = v/c$:

$$\frac{i\bar{E}\sin\alpha\sin\beta}{c} = \gamma\left(\frac{iE\sin\alpha\sin\beta}{c} - \frac{ivp_2}{c}\right),$$

$$\bar{p}_5 = \gamma(p_5 - i\rho p_2). \quad (182)$$

Similarly, let us multiply both sides of Eq. (160) by $i\cos\alpha/c$ to get:

$$\bar{E} = \gamma(E - pv),$$

$$\frac{i\bar{E}\cos\alpha}{c} = \gamma\left(\frac{iE\cos\alpha}{c} - \frac{ipv\cos\alpha}{c}\right),$$

After the substitution of Eqs. (135), (175), and (176), the following is obtained with factor $\rho = v/c$:

$$\frac{i\bar{E}\cos\alpha}{c} = \gamma\left(\frac{iE\cos\alpha}{c} - \frac{ivp_3}{c}\right),$$

$$\bar{p}_6 = \gamma(p_6 - i\rho p_3). \quad (183)$$

Equations (178)-(183) represent the Lorentz transformation equations for the six-momentum. These transformation relations have been obtained using the extended three-dimensional Lorentz transformation equations. The same six-momentum transformation equations can also be derived directly by employing the matrix formulation of the three-dimensional Lorentz transformation, as discussed in the forthcoming Section 3.6.

3.6 Six-Velocity and Six-momentum

Based on the matrix form of the extended Lorentz transformation equations, namely Eq. (103), an event in the space-time continuum should be represented by six coordinates $(x_1, x_2, x_3, x_4, x_5, x_6)$, out of which the first three represent the spatial coordinates and the last three represent the temporal coordinates. As a result of these six space-time coordinates, we need to extend the notion of the ordinary four-vector analysis to a six-vector. Now, the components of the six-velocity in the rest frame K can be defined as:

$$w_i = \frac{dx_i}{dt_0},$$

where $x_i = (x_1, x_2, x_3, x_4, x_5, x_6)$ denote the space-time six-vector coordinates of a particle moving with velocity u with respect to the rest frame K, and $dt_0 = dt\sqrt{1-\frac{u^2}{c^2}}$ is the proper time. Now, the components of the six-velocity in the rest frame are:

$$w_1 = \frac{dx_1}{dt_0} = \frac{d(r\sin\alpha\cos\beta)}{dt\sqrt{1-\frac{u^2}{c^2}}} = \frac{\sin\alpha\cos\beta}{\sqrt{1-\frac{u^2}{c^2}}}\frac{dr}{dt} = \frac{u\sin\alpha\cos\beta}{\sqrt{1-\frac{u^2}{c^2}}},$$

$$w_2 = \frac{dx_2}{dt_0} = \frac{d(r\sin\alpha\sin\beta)}{dt\sqrt{1-\frac{u^2}{c^2}}} = \frac{\sin\alpha\sin\beta}{\sqrt{1-\frac{u^2}{c^2}}}\frac{dr}{dt} = \frac{u\sin\alpha\sin\beta}{\sqrt{1-\frac{u^2}{c^2}}},$$

$$w_3 = \frac{dx_3}{dt_0} = \frac{d(r\cos\alpha)}{dt\sqrt{1-\frac{u^2}{c^2}}} = \frac{\cos\alpha}{\sqrt{1-\frac{u^2}{c^2}}}\frac{dr}{dt} = \frac{u\cos\alpha}{\sqrt{1-\frac{u^2}{c^2}}},$$

$$w_4 = \frac{dx_4}{dt_0} = \frac{d(ict\sin\alpha\cos\beta)}{dt\sqrt{1-\frac{u^2}{c^2}}} = ic\frac{\sin\alpha\cos\beta}{\sqrt{1-\frac{u^2}{c^2}}}\frac{dt}{dt} = \frac{ic\sin\alpha\cos\beta}{\sqrt{1-\frac{u^2}{c^2}}},$$

$$w_5 = \frac{dx_5}{dt_0} = \frac{d(ict\sin\alpha\sin\beta)}{dt\sqrt{1-\frac{u^2}{c^2}}} = ic\frac{\sin\alpha\sin\beta}{\sqrt{1-\frac{u^2}{c^2}}}\frac{dt}{dt} = \frac{ic\sin\alpha\sin\beta}{\sqrt{1-\frac{u^2}{c^2}}},$$

$$w_6 = \frac{dx_6}{dt_0} = \frac{d(ict\cos\alpha)}{dt\sqrt{1-\frac{u^2}{c^2}}} = ic\frac{\cos\alpha}{\sqrt{1-\frac{u^2}{c^2}}}\frac{dt}{dt} = \frac{ic\cos\alpha}{\sqrt{1-\frac{u^2}{c^2}}},$$

The components of six-momentum can be defined as

$$p_i = m_0 w_i,$$

where m_0 is the rest mass, and w_i denotes the components of the six-velocity. Now, the components of the six-momentum are:

$$p_1 = m_0 w_1 = \frac{m_0}{\sqrt{1-\frac{u^2}{c^2}}} \times u\sin\alpha\cos\beta = mu\sin\alpha\cos\beta = p\sin\alpha\cos\beta,$$

$$p_2 = m_0 w_2 = \frac{m_0}{\sqrt{1-\frac{u^2}{c^2}}} \times u\sin\alpha\sin\beta = mu\sin\alpha\sin\beta = p\sin\alpha\sin\beta,$$

$$p_3 = m_0 w_3 = \frac{m_0}{\sqrt{1-\frac{u^2}{c^2}}} \times u\cos\alpha = mu\cos\alpha = p\cos\alpha,$$

$$p_4 = m_0 w_4 = \frac{m_0}{\sqrt{1-\frac{u^2}{c^2}}} \times ic\sin\alpha\cos\beta = imc\sin\alpha\cos\beta = \frac{iE}{c}\sin\alpha\cos\beta,$$

$$p_5 = m_0 w_5 = \frac{m_0}{\sqrt{1-\frac{u^2}{c^2}}} \times ic\sin\alpha\sin\beta = imc\sin\alpha\sin\beta = \frac{iE}{c}\sin\alpha\sin\beta,$$

$$p_6 = m_0 w_6 = \frac{m_0}{\sqrt{1-\frac{u^2}{c^2}}} \times ic\cos\alpha = imc\cos\alpha = \frac{iE}{c}\cos\alpha,$$

Thus, we can write the following expression of the six-momentum for the frame K.

$$\left.\begin{array}{l} p_1 = p\sin\alpha\cos\beta\,, p_2 = p\sin\alpha\sin\beta\,, p_3 = p\cos\alpha \\ p_4 = \frac{iE}{c}\sin\alpha\cos\beta\,, p_5 = \frac{iE}{c}\sin\alpha\sin\beta\,, p_6 = \frac{iE}{c}\cos\alpha \end{array}\right\}. \quad (184)$$

These expressions represent the components of the six-momentum of a particle as measured in the rest frame K, relative to which the particle moves with velocity u. Next, we aim to determine the six-momentum in the moving frame K', with respect to which the particle moves with velocity $\bar{u}$. The components of the six-velocity in frame K' can now be defined as

$$\bar{w}_i = \frac{d\bar{x}_i}{dt_0},$$

where $\bar{x}_i = (\bar{x}_1, \bar{x}_2, \bar{x}_3, \bar{x}_4, \bar{x}_5, \bar{x}_6)$ denote the space-time six-vector coordinates of a particle moving with velocity $\bar{u}$ with respect to the moving frame K' and $dt_0 = d\bar{t}\sqrt{1-\frac{\bar{u}^2}{c^2}}$ be the proper time. Now, the components of the six-velocity in the moving frame are:

$$\bar{w}_1 = \frac{d\bar{x}_1}{dt_0} = \frac{d(\bar{r}\sin\alpha\cos\beta)}{d\bar{t}\sqrt{1-\frac{\bar{u}^2}{c^2}}} = \frac{\sin\alpha\cos\beta}{\sqrt{1-\frac{\bar{u}^2}{c^2}}}\frac{d\bar{r}}{d\bar{t}} = \frac{\bar{u}\sin\alpha\cos\beta}{\sqrt{1-\frac{\bar{u}^2}{c^2}}},$$

$$\bar{w}_2 = \frac{d\bar{x}_2}{dt_0} = \frac{d(\bar{r}\sin\alpha\sin\beta)}{d\bar{t}\sqrt{1-\frac{\bar{u}^2}{c^2}}} = \frac{\sin\alpha\sin\beta}{\sqrt{1-\frac{\bar{u}^2}{c^2}}}\frac{d\bar{r}}{d\bar{t}} = \frac{\bar{u}\sin\alpha\sin\beta}{\sqrt{1-\frac{\bar{u}^2}{c^2}}},$$

$$\bar{w}_3 = \frac{d\bar{x}_3}{dt_0} = \frac{d(\bar{r}\cos\alpha)}{d\bar{t}\sqrt{1-\frac{\bar{u}^2}{c^2}}} = \frac{\cos\alpha}{\sqrt{1-\frac{\bar{u}^2}{c^2}}}\frac{d\bar{r}}{d\bar{t}} = \frac{\bar{u}\cos\alpha}{\sqrt{1-\frac{\bar{u}^2}{c^2}}},$$

$$\bar{w}_4 = \frac{d\bar{x}_4}{dt_0} = \frac{d(ic\bar{t}\sin\alpha\cos\beta)}{d\bar{t}\sqrt{1-\frac{\bar{u}^2}{c^2}}} = ic\frac{\sin\alpha\cos\beta}{\sqrt{1-\frac{\bar{u}^2}{c^2}}}\frac{d\bar{t}}{d\bar{t}} = \frac{ic\sin\alpha\cos\beta}{\sqrt{1-\frac{\bar{u}^2}{c^2}}},$$

$$\bar{w}_5 = \frac{d\bar{x}_5}{dt_0} = \frac{d(ic\bar{t}\sin\alpha\sin\beta)}{d\bar{t}\sqrt{1-\frac{\bar{u}^2}{c^2}}} = ic\frac{\sin\alpha\sin\beta}{\sqrt{1-\frac{\bar{u}^2}{c^2}}}\frac{d\bar{t}}{d\bar{t}} = \frac{ic\sin\alpha\sin\beta}{\sqrt{1-\frac{\bar{u}^2}{c^2}}},$$

$$\bar{w}_6 = \frac{d\bar{x}_6}{dt_0} = \frac{d(ic\bar{t}\cos\alpha)}{d\bar{t}\sqrt{1-\frac{\bar{u}^2}{c^2}}} = ic\frac{\cos\alpha}{\sqrt{1-\frac{\bar{u}^2}{c^2}}}\frac{d\bar{t}}{d\bar{t}} = \frac{ic\cos\alpha}{\sqrt{1-\frac{\bar{u}^2}{c^2}}},$$

The components of the six-momentum in the moving frame K' can be defined as

$$\bar{p}_i = m_0\bar{w}_i,$$

where m_0 is the rest mass, and $\bar{w}_i$ denotes the components of the six-velocity in frame K'. Now, the components of the six-momentum are:

$$\bar{p}_1 = m_0\bar{w}_1 = \frac{m_0}{\sqrt{1-\frac{\bar{u}^2}{c^2}}} \times \bar{u}\sin\alpha\cos\beta = \bar{m}\bar{u}\sin\alpha\cos\beta = \bar{p}\sin\alpha\cos\beta,$$

$$\bar{p}_2 = m_0\bar{w}_2 = \frac{m_0}{\sqrt{1-\frac{\bar{u}^2}{c^2}}} \times \bar{u}\sin\alpha\sin\beta = \bar{m}\bar{u}\sin\alpha\sin\beta = \bar{p}\sin\alpha\sin\beta,$$

$$\bar{p}_3 = m_0\bar{w}_3 = \frac{m_0}{\sqrt{1-\frac{\bar{u}^2}{c^2}}} \times \bar{u}\cos\alpha = \bar{m}\bar{u}\cos\alpha = \bar{p}\cos\alpha,$$

$$\bar{p}_4 = m_0\bar{w}_4 = \frac{m_0}{\sqrt{1-\frac{\bar{u}^2}{c^2}}} \times ic\sin\alpha\cos\beta = i\bar{m}c\sin\alpha\cos\beta = \frac{i\bar{E}}{c}\sin\alpha\cos\beta,$$

$$\bar{p}_5 = m_0\bar{w}_5 = \frac{m_0}{\sqrt{1-\frac{\bar{u}^2}{c^2}}} \times ic\sin\alpha\sin\beta = i\bar{m}c\sin\alpha\sin\beta = \frac{i\bar{E}}{c}\sin\alpha\sin\beta,$$

$$\bar{p}_6 = m_0\bar{w}_6 = \frac{m_0}{\sqrt{1-\frac{\bar{u}^2}{c^2}}} \times ic\cos\alpha = i\bar{m}c\cos\alpha = \frac{i\bar{E}}{c}\cos\alpha,$$

Thus, we can write the following expression for the six-momentum in the frame K'.

$$\left.\begin{matrix}\bar{p}_1 = \bar{p}\sin\alpha\cos\beta, \bar{p}_2 = \bar{p}\sin\alpha\sin\beta, \bar{p}_3 = \bar{p}\cos\alpha \\ \bar{p}_4 = \frac{i\bar{E}}{c}\sin\alpha\cos\beta, \bar{p}_5 = \frac{i\bar{E}}{c}\sin\alpha\sin\beta, \bar{p}_6 = \frac{i\bar{E}}{c}\cos\alpha\end{matrix}\right\}. \quad (185)$$

These expressions represent the components of the six-momentum of a particle as measured in the moving frame K', relative to which the particle has velocity $\bar{u}$. The transformation of this six-momentum from frame K to K' follows the same rules as the transformation of space-time coordinates, as discussed in Eq. (103). Hence, based on the transformation in Eq. (103), the six-momentum transforms as:

$$\begin{bmatrix}\bar{p}_1\\ \bar{p}_2\\ \bar{p}_3\\ \bar{p}_4\\ \bar{p}_5\\ \bar{p}_6\end{bmatrix} = \begin{bmatrix}\gamma & 0 & 0 & i\rho\gamma & 0 & 0\\ 0 & \gamma & 0 & 0 & i\rho\gamma & 0\\ 0 & 0 & \gamma & 0 & 0 & i\rho\gamma\\ -i\rho\gamma & 0 & 0 & \gamma & 0 & 0\\ 0 & -i\rho\gamma & 0 & 0 & \gamma & 0\\ 0 & 0 & -i\rho\gamma & 0 & 0 & \gamma\end{bmatrix}\begin{bmatrix}p_1\\ p_2\\ p_3\\ p_4\\ p_5\\ p_6\end{bmatrix},$$

Solution of the above matrix gives the following equations:

$$\overline{p_1} = \gamma(p_1 + i\rho p_4),$$
$$\overline{p_2} = \gamma(p_2 + i\rho p_5),$$
$$\overline{p_3} = \gamma(p_3 + i\rho p_6),$$
$$\bar{p}_4 = \gamma(p_4 - i\rho p_1),$$
$$\bar{p}_5 = \gamma(p_5 - i\rho p_2),$$
$$\bar{p}_6 = \gamma(p_6 - i\rho p_3).$$

These six transformation equations are identical to Eqs. (178)–(183) from Section 3.5. In Section 3.5, they were derived using the extended 3D Lorentz transformations; here, in Section 3.6, we obtain the same results directly using the matrix form of the 3D Lorentz transformation. An important property of a six-vector is that the square of its magnitude remains invariant under Lorentz transformations. Now we wish to prove that the square of the length of the six-momentum is also invariant under the Lorentz transformation. In relativistic mechanics, it is well known that the quantity $p^2 - E^2/c^2$ remains unchanged in any frame of reference, i.e.,

$$p^2 - \frac{E^2}{c^2} = \bar{p}^2 - \frac{\bar{E}^2}{c^2}. \quad (186)$$

Now from L.H.S. of Eq. (186),

$$p^2 - \frac{E^2}{c^2} = p^2(\sin^2\alpha + \cos^2\alpha) - \frac{E^2}{c^2}(\sin^2\alpha + \cos^2\alpha),$$
$$= p^2[\sin^2\alpha(\cos^2\beta + \sin^2\beta) + \cos^2\alpha] - \frac{E^2}{c^2}[\sin^2\alpha(\cos^2\beta + \sin^2\beta) + \cos^2\alpha],$$
$$= (p\sin\alpha\cos\beta)^2 + (p\sin\alpha\sin\beta)^2 + (p\cos\alpha)^2 + \left(\frac{iE}{c}\sin\alpha\cos\beta\right)^2 + \left(\frac{iE}{c}\sin\alpha\sin\beta\right)^2 + \left(\frac{iE}{c}\cos\alpha\right)^2,$$

After the substitution of Eq. (184), the following is obtained:

$$p^2 - \frac{E^2}{c^2} = (p_1)^2 + (p_2)^2 + (p_3)^2 + (p_4)^2 + (p_5)^2 + (p_6)^2. \quad (187)$$

Similarly, from R.H.S. of Eq. (186),

$$\bar{p}^2 - \frac{\bar{E}^2}{c^2} = \bar{p}^2(\sin^2\alpha + \cos^2\alpha) - \frac{\bar{E}^2}{c^2}(\sin^2\alpha + \cos^2\alpha),$$

$$= \bar{p}^2[\sin^2\alpha\,(\cos^2\beta + \sin^2\beta) + \cos^2\alpha] - \frac{\bar{E}^2}{c^2}[\sin^2\alpha\,(\cos^2\beta + \sin^2\beta) + \cos^2\alpha],$$

$$= (\bar{p}\sin\alpha\cos\beta)^2 + (\bar{p}\sin\alpha\sin\beta)^2 + (\bar{p}\cos\alpha)^2 + \left(\frac{i\bar{E}}{c}\sin\alpha\cos\beta\right)^2 + \left(\frac{i\bar{E}}{c}\sin\alpha\sin\beta\right)^2 + \left(\frac{i\bar{E}}{c}\cos\alpha\right)^2,$$

After the substitution of Eq. (185), the following is obtained:

$$\bar{p}^2 - \frac{\bar{E}^2}{c^2} = (\bar{p}_1)^2 + (\bar{p}_2)^2 + (\bar{p}_3)^2 + (\bar{p}_4)^2 + (\bar{p}_5)^2 + (\bar{p}_6)^2. \quad (188)$$

Now, after the substitution of Eqs. (187) and (188) into Eq. (186), the following is obtained:

$$(p_1)^2 + (p_2)^2 + (p_3)^2 + (p_4)^2 + (p_5)^2 + (p_6)^2 = (\bar{p}_1)^2 + (\bar{p}_2)^2 + (\bar{p}_3)^2 + (\bar{p}_4)^2 + (\bar{p}_5)^2 + (\bar{p}_6)^2.$$

From the above expression, one can conclude that the square of the length of the six-momentum vector remains unchanged in any frame of reference.

4. Conclusion

In this investigation, we have derived extended relativistic Lorentz transformation equations for three-dimensional motion between inertial frames of reference. Both polar and Cartesian coordinate systems were introduced to specify the position of a point in 3D space. The Lorentz transformation equations along the X-, Y-, and Z-directions were thoroughly obtained for the case where the relative motion between inertial frames occurs in three dimensions. To formulate the matrix representation of these 3D transformations, namely Eqs. (37), (39), (50), and (62), we first expressed the X-, Y-, and Z-coordinates as given in Eqs. (81)-(83), which take the following form:

$$x_1 = r\sin\alpha\cos\beta,$$
$$x_2 = r\sin\alpha\sin\beta,$$
$$x_3 = r\cos\alpha.$$

In fact, these equations represent the components of the radius vector r along the X-, Y-, and Z-directions. In the same way, we considered that the time coordinate ict must have three components, like space coordinate r has. For that, we have first analyzed invariance of the space-time interval equations along the X-, Y-, and Z-directions [see Eqs. (87)-(89)] and these invariance equations explicitly clarify that the temporal coordinate ict has three components in following form [see Eqs. (90)-(92)]:

$$x_4 = ict\sin\alpha\cos\beta,$$
$$x_5 = ict\sin\alpha\sin\beta,$$
$$x_6 = ict\cos\alpha.$$

Based on the concept of six-vectors, an event in the space-time continuum should be represented by six coordinates $(x_1, x_2, x_3, x_4, x_5, x_6)$, of which the first three represent spatial coordinates, and the last three represent temporal coordinates. Using these six-vectors, we obtained six new Lorentz transformation equations, including their 6×6 matrix form [see Eq. (103)]. Furthermore, the D'Alembert operator, the fundamental component of the wave equation, is shown to be form-invariant under these six Lorentz transformations [see Eq. (129)]. Correct transformation equations of linear momentum between inertial frames were also theoretically interpreted using the matrix form of the six-vector Lorentz transformations, as discussed in Sections 3.5 and 3.6. To the best of our knowledge, this is the first study to formulate Lorentz transformation equations in terms of six-vectors. This work could serve as a milestone, providing a potential new framework to explore further consequences of relativistic mechanics using the obtained six-vector Lorentz transformations.

Data availability: Data sharing not applicable – no new data generated, or the article describes entirely theoretical research.

Conflict of interest: As the author of this work, I declare that I have no conflicts of interest.

Funding: This research received no external funding.

References

[1] Khadka, C.B., St. Petersburg State Polytech. Univ. J., Phys. Math., 17 (2024) 160.

[2] Voigt, W., Nachr. Königl. Ges. Wiss. Göttingen, 2 (1887) 42.

[3] Lorentz, H.A., Proc. R. Netherlands Acad. Arts Sci., 6 (1904) 809.

[4] Poincare, H., C. R. Acad. Sci., 140 (1905) 1504.

[5] Einstein, A., Ann. Phys., 17 (1905) 891.

[6] Feynman, R.P., Leighton, R.B., and Sands, M., "The Feynman Lectures on Physics", (Addison-Wesley, USA, 1964).

[7] Landau, L.D. and Lifshitz, E.M., "Course of Theoretical Physics", (Addison-Wesley, USA, 1951).

[8] Cole, E.A.B., J. Phys. A, 13 (1980) 109.

[9] Strnad, J., Phys. Lett. A, 96 (1983) 231.

[10] Dattoli, G. and Mingani, R., Lett. Nuovo Cimento, 22 (1978) 65.

[11] Trencevski, K., Kragujevac J. Math., 35 (2011) 327.

[12] Brody, D.C. and Graefe, E.M., Phys. Rev. D, 84 (2011) 125016.

[13] Recami, E. and Mignani, R., Riv. Nuovo Cimento, 4 (1974) 209.

[14] Pappas, P., Nuovo Cimento Lett., 22 (1987) 601.

[15] Guy, B., J. New Energy, 6 (2002) 46.

[16] Weinberg, S., Phys. Rev. D, 82 (2010) 045031.

[17] Franco, R. and Jorge, A., Electron. J. Theor. Phys., 3 (2006) 35.

[18] Teli, M.T., Phys. Lett. A, 122 (1987) 447.

[19] Szostek, R., Appl. Sci., 12 (2022) 1.

[20] Szostek, K. and Szostek, R., Jordan J. Phys., 15 (2022) 457.

[21] Akintsov, N.S., Nevecheria, A.P., Kopytov, G.F., Yang Y., and Cao, T., Symmetry, 16 (2024) 357.

[22] Szostek, R., Open Phys., 17 (2019) 153.

[23] Hill, J.M., Symmetry, 16 (2024) 1691.

[24] Szostek, R., J. Fiz. Malaysia, 43 (2022) 10244.

[25] Szostek, K. and Szostek, R., Results Phys., 8 (2018) 429.

[26] Khadka, C.B., Bibechana, 21 (2024) 103.

[27] Khadka, C.B., St. Petersburg State Polytech. Univ. J., Phys. Math., 16 (2023) 115.

[28] Khadka, C.B., Jordan J. Phys., 18 (2025) 225.

Volume 18, Number 5, 2025. pp. 695-703

Jordan Journal of Physics

ARTICLE

Soil Radioactivity Levels, Spatial Distribution and Radiation Hazard Assessment in Anambra and Imo States, Southeastern Nigeria

O. I. Agbelusi[a], P. S. Ayanlola[b], M. K. Lawal[c], S. O. Awokoya[b], O. O. Oloyede[b], A. Olatunji[d] and G. A. Isola[b]

[a] *Department of Physical Sciences, Chrisland University, Abeokuta, Nigeria.*

[b] *Department of Pure and Applied Physics, Ladoke Akintola University of Technology, Ogbomoso, Nigeria.*

[c] *Department of Science Laboratory Technology, Ladoke Akintola University of Technology, Ogbomoso, Nigeria..*

[d] *Department of Physics, Ajayi Crowther University, Oyo, Nigeria.*

Doi: **https://doi.org/10.47011/18.5.10**

Received on: 27/01/2025; *Accepted on: 07/04/2025*

Abstract: This study assessed the radioactivity levels in soil samples from Anambra and Imo States, two regions affected by the Nigerian Civil War. Using a thallium-activated sodium iodide detector, a total of 80 stratified, randomly collected soil samples were analyzed. The detected radionuclides included non-serial ^{40}K and decay series of ^{238}U and ^{232}Th, as well as trace levels of the anthropogenic ^{137}Cs. Their spatial variability and associated health implications were also evaluated. The average activity concentrations in Anambra State were 835.91 ± 7.40 Bq kg^{-1} for ^{40}K, 21.05 ± 3.65 Bq kg^{-1} for ^{238}U, 12.99 ± 0.85 Bq kg^{-1} for ^{232}Th, and 3.88 ± 0.10 Bq kg^{-1} for ^{137}Cs. In Imo State, the respective values were 761.29 ± 6.63, 19.19 ± 2.97, 9.29 ± 1.52, and 5.39 ± 0.25 Bq kg^{-1}. The estimated mean absorbed dose rates were 52.65 nGyh^{-1} for Anambra and 46.38 nGyh^{-1} for Imo, corresponding to annual effective dose equivalents of 0.06 mSvy^{-1} for both states, a value well below the global safety thresholds. Spatial analysis revealed that ^{40}K levels were influenced by potassium-rich soils and intensive agricultural practices, while geological formations governed the distribution of ^{238}U and ^{232}Th. This study confirms that current soil usage poses no immediate radiological risks. However, proactive monitoring is recommended to mitigate potential long-term radiological impacts.

Keywords: Soil radioactivity, Spatial distribution, Radiation hazard, Gamma spectrometry, Nigeria.

1. Introduction

Human exposure to naturally occurring radioactive materials (NORM) is an inevitable aspect of everyday life. Primordial radionuclides such as ^{238}U, ^{232}Th, along with radon isotopes (^{222}Rn) from the decay of these elements and the non-serial decay ^{40}K, are the primary sources of natural radiation. While the radiation from these sources is universal, the risks associated with ionizing radiation vary depending on the region's geological setting, human activities, and historical factors [1-4]. Therefore, global background radiation levels differ significantly. Thus, the understanding of these concentrations is essential in quantifying the absorbed dose and potential radiological hazards, which can have significant public health implications [5-9].

Several studies from various parts of the world have been carried out to assess the radionuclide levels of different environmental matrices, most especially soil. In the study conducted by Leal *et al.* [8], it was reported that the median values of the activity concentrations

Corresponding Author: P. S. Ayanlola **Email**: psayanlola28@lautech.edu.ng

of ^{226}Ra, ^{228}Ra, and ^{40}K in the soils of Pernambuco, Brazil, were consistent with values reported worldwide. In reporting their findings on the natural radioactivity in soil dust samples from Ketu, Ghana, Addo *et al.* [10] found that the soils in the studied area had normal levels of radiation and were therefore radiologically safe. In another study conducted by Nagathil *et al.* [11] to investigate the spatial analysis of radionuclide concentration in the high background radiation regions of Kerala, India, it was reported that the results obtained exceed the safe limits recommended by the [1]. Abu-Kharma *et al.* [12] reported that, with the exception of ^{40}K and ^{232}Th, the radioactivity levels obtained for ^{238}U in soils from Al-Lajjun, Jordan, were significantly higher than world average values.

In Southern Nigeria, Anambra and Imo states were among the regions severely affected by the Nigerian Civil War waged half a century ago (1967 - 1970). As radiation exposure is influenced by both natural and anthropogenic factors, the movement of contaminated soil and debris in the zones can contribute to elevated radiation levels. While examining the radioactivity levels and related radiological dangers of surface soils in Ore metropolis, Ondo state, Nigeria, a town located along the civil war track, Akinloye *et al.* [13] reported the presence of primordial radionuclides and detected ^{137}Cs at three places. Furthermore, after evaluating the radioactive contents in soil and food samples in Enugu state, southeastern Nigeria, Agbelusi *et al.* [14] found that the radioactivity levels and calculated radiological indices were above the prescribed limits. The results also revealed that ^{137}Cs were present in a small number of communities at low concentrations, which was linked to wartime activity.

Hence, the redistribution of artificial radionuclides during this period, in conjunction with natural radiation sources, has raised concerns about long-term exposure risks in other regions (specifically Anambra and Imo states) affected by the war. Soils, frequently used for construction and agricultural purposes, are a significant source of both external gamma radiation and internal radon exposure. The accumulation of the penetrative radiations in poorly ventilated buildings may further elevate internal radiation exposure, making this a public health concern. Epidemiological studies have linked prolonged exposure to natural radionuclides to severe health issues [15, 16]. The health risks associated with ionizing radiation include genetic damage and other conditions such as tumors, cataracts, and leukemia.

This study, therefore, focuses on evaluating the levels of radionuclides in Anambra and Imo states, offering a comprehensive assessment of the associated health impacts, as well as identifying and mapping radiation hotspots. Particular attention is given to areas where elevated radiation levels are influenced by both natural sources and the historical redistribution of radioactive materials. The study aims to contribute to public health initiatives by providing baseline data for radiation monitoring in the states, with emphasis on the spatial distribution of radionuclides. The findings are expected to support the development of radiation protection programs, inform policymakers about radiation-related risks, and aid efforts to mitigate exposure in both urban and rural areas. In addition, this research provides a foundation for future studies on radiation hazards in Anambra and Imo States. Overall, the study aligns with the United Nations Sustainable Development Goals by contributing to the promotion of healthy lives and well-being for all at all ages (SDG 3) and to the development of inclusive, safe, resilient, and sustainable cities and human settlements (SDG 11) [17].

2. Materials and Methods

2.1 Study Area

Anambra and Imo states, located in southeastern Nigeria (Fig. 1), are known for their rich cultural heritage and diverse socio-economic landscapes. Anambra State, nicknamed the Light of the Nation and one of the urbanized states in Nigeria, lies between latitudes 5°50'N and 7°10'N and longitudes 6°40'E and 7°25'E, with a land area of approximately 4,844 km². It is the eighth most populous state in the country and the second most densely populated after Lagos State, with a population exceeding 7.2 million. Anambra experiences a tropical wet-and-dry (savanna) climate, with an average annual temperature of about 28.99 °C, which is slightly lower than the national average. The state receives approximately 212.36 mm (8.36 inches) of rainfall annually and experiences rainfall on

about 243 days per year, corresponding to roughly 66.7% of the year.

Imo state, positioned between latitudes 4°45'N and 7°15'N and longitudes 6°50'E and 7°25'E, covers a total area of 5530 km^2. Although it is the third smallest state in Nigeria by area, Imo State is the fourteenth most populous, with an estimated population exceeding 6 million as of 2022 [18, 19]. Both states are adjacent to each other and have predominantly agrarian economies, with farming and trading as common occupations.

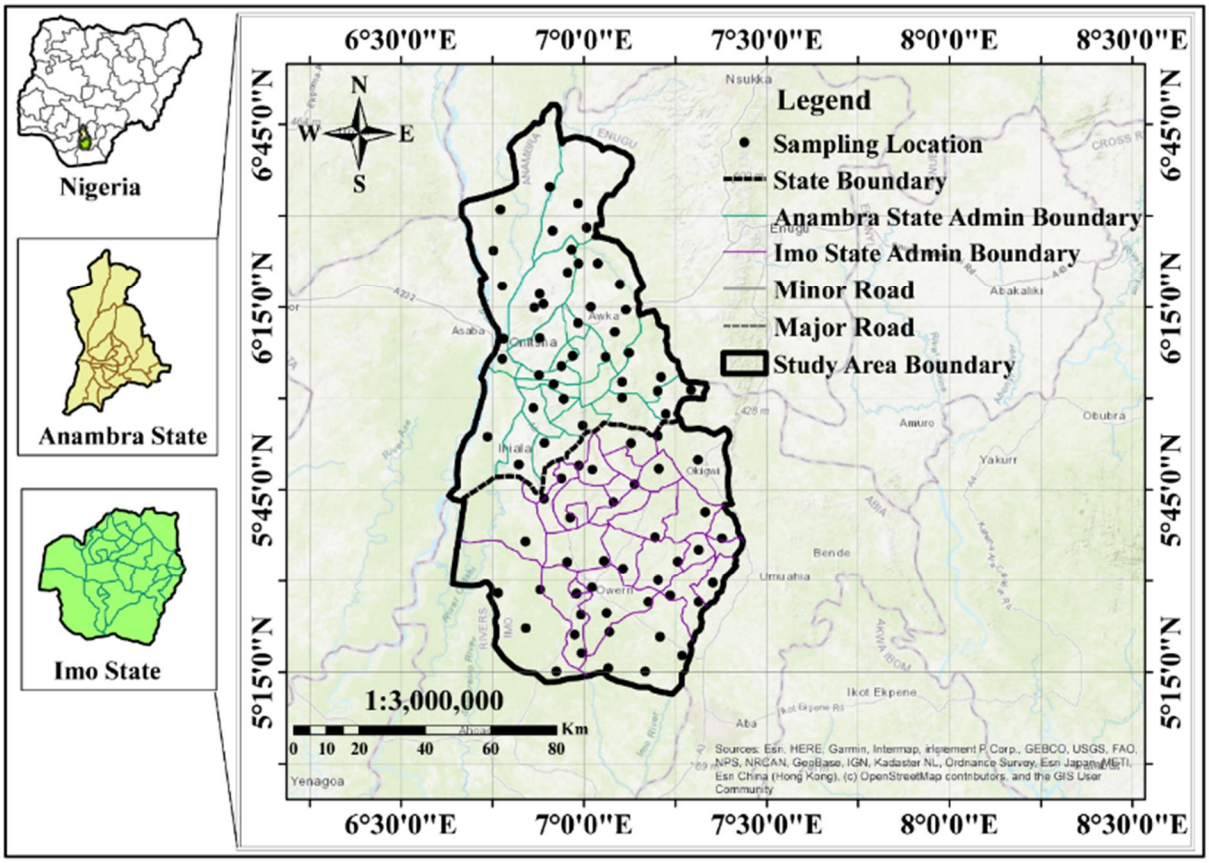

FIG. 1. Map of study area.

2.2 Sample Collection

An initial survey was conducted to identify representative sampling points across the study area. Subsequently, the study area was divided into four regions covering the northern and southern parts of each state, with random sampling points selected within each region to ensure spatial variability and adequate coverage of the entire area. Soil samples were collected using a hand auger to a depth of 10 cm. A total of 80 soil samples were collected from Anambra and Imo states and packaged in a black polypropylene bag pending laboratory preparation and spectrometry analysis.

2.3 Sample Preparation

The soil samples were air-dried at room temperature to a constant weight, ground up, and sieved through a 2 mm mesh. A 200 g portion of each sample was placed into a cylindrical polypropylene container that matched the detector's geometry and was tightly sealed to prevent ^{222}Rn from escaping. To ensure radioactive secular equilibrium between ^{238}U and its decay products, as well as between ^{232}Th and its progeny, all samples were stored for 28 days before being measured [2, 3].

2.4 Sample Measurement

The samples underwent gamma spectrometry analysis using a gamma spectrometry system that featured a 3" x 3" sodium iodide detector activated with thallium [NaI(Tl)], which was linked to a multichannel analyzer (MCA), specifically the GS-2000 Pro model. Acquisition and analysis of the gamma-ray spectra were carried out using Theremino software. The calibration of the system was accomplished using standard sources that contained known radionuclides, with an acquisition duration of 36000 s. Before measuring the samples, an

empty container identical in geometry to the detector was counted for 36000 s to determine the background gamma-ray distribution. After reaching secular equilibrium, the sealed samples were counted for the same period. The concentrations of radionuclides were estimated by analyzing the gamma energies of ^{214}Pb at 352.0 keV, ^{214}Bi at 609.3 keV for ^{238}U, ^{208}Tl at 583.2 keV, and ^{228}Ac at 911.1 keV for ^{232}Th, as well as ^{40}K at 1460.8 keV and ^{137}Cs at 661.6 keV [2, 3, 20]. The activity concentrations A (Bq kg^{-1}) of the samples were calculated using Eq. (1):

$$A\ (Bq\ kg^{-1}) = \frac{C_{net}}{\mathrm{P\gamma \times \varepsilon \times m \times t}} \quad (1)$$

where ε is the detector's full energy peak efficiency, t is the counting time, m is the sample mass, C_{net} is the net peak area, and P_γ is the absolute gamma-ray emission probability [2 - 4, 14, 20].

The minimum detectable activity (MDA) for each radionuclide was determined using Eq. (2):

$$MDA = \frac{2.71+4.66\ (\sigma)}{\mathrm{P\gamma \times \varepsilon \times m \times t}} \quad (2)$$

where Pγ, ε, m, and t remain as earlier defined, and σ is the standard deviation of the background recorded at time t over the energy range of interest. For ^{40}K, ^{238}U, ^{232}Th, and ^{137}Cs, the corresponding minimum detectable limit (MDA) is 7.79 Bq kg^{-1}, 5.68 Bq kg^{-1}, 4.59 Bq kg^{-1}, and 2.98 Bq kg^{-1}, respectively.

2.4.1 Calculation of Absorbed Dose Rate

Equation (3) was used to assess the contribution of the radionuclides found in the samples to the absorbed dose rate as a result of external exposure [1-4, 14, 20].

$$D\ (nGyh^{-1}) = 0.462\ A_u + (0.621\ A_{Th}) + (0.0417\ A_k) \quad (3)$$

where A_U, A_{Th}, and A_k are the activity concentrations of ^{238}U, ^{232}Th, and ^{40}K, respectively.

2.4.2 Calculation of Annual Effective Dose Equivalent

Equation (4) was used to estimate the annual effective dose equivalent caused by the radionuclides found in the soil samples:

$$AEDE\ (mSvy^{-1}) = D\ (nGyh^{-1}) \times 24hr \times 365.25days \times 0.2 \times 0.7(SvGy^{-1}) \times 10^{-6} \quad (4)$$

where 0.7 SvGy^{-1} is the conversion coefficient which transforms the absorbed dose rate in the air to an effective dose, and 10^{-6} is the factor converting nanosievert into millisievert [1-4, 14, 20].

2.4.3 Spatial Distribution of Soil Radioactivity Concentration

Using the spatial analyst extension in the geographic information system (GIS) environment, the spatial distribution of the radionuclide concentrations was carried out in ArcMap 10.8.2. Using the Kriging interpolation technique described by [21], a map of the distribution of activity concentration of detected radionuclides was created, offering a comprehensive view of the radionuclide distribution. This provides crucial insights into how local geological formations, agricultural activities, and historical events impact radionuclide concentrations.

3. Results and Discussion

Tables 1 and 2 present the results of the gamma spectrometry analysis of soil collected from Anambra and Imo states. In Anambra state, the activity concentrations of ^{40}K ranged from 42.44±6.72 to 2275.54±15.67 Bq kg^{-1}, with a mean of 835.91±7.40 Bq kg^{-1}. The activity concentrations of ^{238}U ranged from 9.09±3.67 to 57.56±3.52 Bq kg^{-1}, with a mean of 21.05±3.65 Bq kg^{-1}. For ^{232}Th, concentrations ranged from 4.78 ± 0.73 to 38.69±0.66 Bq kg^{-1}, with a mean of 12.99±0.85 Bq kg^{-1}. Additionally, the ^{137}Cs concentrations ranged from 3.66±0.10 to 4.16±0.20 Bq kg^{-1}, with a mean of 3.88±0.10 Bq kg^{-1}. In Imo state, the activity concentrations of ^{40}K ranged from 106.01 ± 1.76 to 2135.74±18.37 Bq kg^{-1}, with a mean of 761.29±6.63 Bq kg^{-1}. The concentrations of ^{238}U ranged from 10.01±1.92 to 34.44±1.37 Bq kg^{-1}, with a mean of 19.19±2.97. The concentrations of ^{232}Th ranged from 4.96±0.42 to 15.43±4.03 Bq kg^{-1} with a mean of 9.29±1.52. Similarly, ^{137}Cs concentrations ranged from 3.76±0.11 to 4.78±0.23 Bq kg^{-1}, with a mean of 5.39±0.25 Bq kg^{-1}. These values are significantly lower than the global average of 400.00, 35.00, 30.00, and 10.00 Bq kg^{-1} for ^{40}K, ^{238}U, ^{232}Th, and ^{137}Cs, respectively [1]. However, Anambra state recorded higher radionuclide levels than Imo State. These elevated levels can be attributed to a combination of the region's geological composition and significant industrial activities. Geologically, Anambra is characterized by formations rich in NORMs, such as granitic and

sedimentary rocks, which inherently contribute to higher radionuclide concentrations [22]. These formations act as natural sources, releasing radionuclides into the surrounding soil and environment. Industrial activities in Anambra state further amplify these concentrations. The state's industries, including mining, manufacturing, and construction, play a pivotal role in redistributing radionuclides through processes such as raw material extraction and processing. For instance, mining and quarrying activities disturb subsurface materials, mobilizing radionuclides such as ^{40}K, ^{238}U, and ^{232}Th. Additionally, industrial emissions, waste disposal, and the use of by-products in construction and land reclamation contribute to the elevated observed radionuclide activity levels [23].

In comparison with other studies, significantly higher ^{40}K activity levels were recorded in this study for Imo (761.29 Bq kg^{-1}) and Anambra (835.80 Bq kg^{-1}) states compared to previous studies (Table 3). This increase may be attributed to the agricultural practices of using potassium-rich fertilizers and the environmental legacy of the civil war, which could have redistributed potassium-bearing materials in these regions due to soil disturbances caused by explosives and other military activities. Interestingly, the present study recorded lower activity levels for Imo state (^{238}U: 19.19 Bq kg^{-1}, ^{232}Th: 9.30 Bq kg^{-1}), while Anambra had 21.05 Bq kg^{-1} (^{238}U) and 12.99 Bq kg^{-1} (^{232}Th). These values are lower than those reported in other southern Nigerian regions affected by the civil war, such as Ebonyi (^{238}U: 88.22 Bq kg^{-1}, ^{232}Th: 80.26 Bq kg^{-1}) and Abia (^{238}U: 52.64 Bq kg^{-1}, ^{232}Th: 97.68 Bq kg^{-1}) states. These lower values could be attributed to natural geological variability, as these areas may lack uranium and thorium-rich rocks or minerals. Over time, soil erosion and leaching, exacerbated by the post-war environmental recovery, might have further reduced the concentrations of these radionuclides. Previous studies largely did not report or detect ^{137}Cs at some locations, possibly due to its low concentrations being below detection limits (BDL) or minimal historical inputs. In the present study, the detection of ^{137}Cs (5.39 Bq kg^{-1} in Imo state and 3.88 Bq kg^{-1} in Anambra state) suggests anthropogenic contributions, likely from fallout associated with explosives used during the war [13]. The civil war may also have played a role in redistributing this radionuclide, as military activities could have introduced or concentrated cesium isotopes in localized areas.

TABLE 1. Activity concentrations of radionuclides in soil samples from Anambra.

Location	^{40}K (Bqkg^{-1})	^{238}U (Bqkg^{-1})	^{232}Th (Bqkg^{-1})	^{137}Cs (Bqkg^{-1})	D (nGyh^{-1})	AEDE (mSvy^{-1})
AN1	1223.98±5.62	27.16±5.42	5.95±0.67	BDL	67.28	0.08
AN2	1256.66±8.37	29.55±3.67	5.41±0.70	BDL	69.41	0.09
AN3	1435.33±8.33	29.73±2.93	38.69±0.53	BDL	97.62	0.12
AN4	1145.86±8.63	17.85±4.57	36.66±0.88	BDL	78.80	0.10
AN5	958.7±4.85	19.35±3.58	4.78±0.92	4.15±0.13	51.89	0.06
AN6	900.00±5.34	22.00±2.72	13.00±1.12	BDL	55.77	0.07
AN7	850.00±15.65	21.00±5.69	13.00±0.78	BDL	53.22	0.07
AN8	820±11.04	20.50±3.96	12.50±0.73	BDL	51.43	0.06
AN9	870.00±10.83	21.50±2.77	13.5.00±0.44	BDL	54.60	0.07
AN10	840.00±7.83	21.00±3.56	13.00±0.69	BDL	52.80	0.07
AN11	860.00±14.49	21.50±2.08	13.50±0.76	BDL	54.18	0.07
AN12	830.00±13.78	20.50±1.86	12.50±0.93	BDL	51.85	0.06
AN13	2135.74±15.67	57.56±3.52	8.26±1.44	3.66±0.62	120.78	0.15
AN14	880.00±14.98	22.00±3.52	13.50±1.32	BDL	55.24	0.07
AN15	810.00±6.33	20.50±3.77	12.50±0.76	BDL	51.01	0.06
AN16	890.00±6.72	22.00±1.99	13.50±0.56	BDL	55.66	0.07
AN17	800.00±5.84	20.00±1.07	12.00±0.34	BDL	50.05	0.06
AN18	870.00±3.07	21.50±1.92	13.50±0.39	BDL	54.56	0.07
AN19	850.00±11.88	21.00±2.44	13.00±0.66	BDL	53.22	0.07
AN20	820.00±10.62	20.50±2.38	12.50±0.43	BDL	51.43	0.06
AS21	763.45±6.07	9.09±1.67	9.16±0.39	BDL	41.73	0.05
AS22	664.64±14.79	10.01±3.85	5.16±0.74	BDL	35.54	0.04
AS23	566.44±7.27	29.34±2.17	7.16±0.42	BDL	41.62	0.05
AS24	567.44±8.05	20.30±1.75	8.16±0.31	BDL	38.11	0.05

Location	^{40}K ($Bqkg^{-1}$)	^{238}U ($Bqkg^{-1}$)	^{232}Th ($Bqkg^{-1}$)	^{137}Cs ($Bqkg^{-1}$)	D ($nGyh^{-1}$)	AEDE ($mSvy^{-1}$)
AS25	785.26±12.02	14.68±3.36	7.41±0.73	BDL	44.13	0.05
AS26	623.66±10.62	10.95±2.44	27.93±0.74	BDL	48.41	0.06
AS27	519.11±6.07	19.95±1.37	12.17±0.88	BDL	38.42	0.05
AS28	691.10±14.79	11.89±3.52	6.97±0.92	BDL	38.64	0.05
AS29	820.00±7.27	20.50±3.77	12.50±1.12	BDL	51.42	0.06
AS30	2084.04±8.05	28.05±1.99	14.45±1.32	BDL	108.84	0.13
AS31	860.00±4.85	21.50±1.85	13.50±0.43	BDL	54.18	0.07
AS32	2275.54±5.34	17.77±3.85	17.23±0.39	3.68±0.10	113.80	0.14
AS33	561.35±15.65	20.50±2.17	12.50±0.69	BDL	40.64	0.05
AS34	251.04±13.78	22.00±1.99	13.50±0.76	3.76±0.11	29.02	0.04
AS35	252.58±15.67	20.50±1.07	12.50±0.93	4.12±0.11	27.77	0.03
AS36	310.36±14.98	22.00±1.92	13.50±0.88	BDL	31.49	0.04
AS37	225.85±6.33	22.00±2.44	12.00±0.92	BDL	27.04	0.03
AS38	270.91±5.62	21.50±2.38	13.50±1.12	3.66±4.16	29.61	0.04
AS39	250.41±8.37	13.63±1.85	14.43±0.56	4.16±0.20	25.70	0.03
AS40	42.44±6.72	9.09±1.99	4.78±0.34	BDL	8.94	0.01
Mean	835.80±7.40	21.05±3.65	12.99±0.85	3.88±0.10	52.65	0.06

TABLE 2. Activity concentrations of radionuclides in soil samples from Imo.

Location	^{40}K ($Bqkg^{-1}$)	^{238}U ($Bqkg^{-1}$)	^{232}Th ($Bqkg^{-1}$)	^{137}Cs ($Bqkg^{-1}$)	D ($nGyh^{-1}$)	AEDE ($mSvy^{-1}$)
IN1	1435.32±6.72	27.16±5.42	8.69±0.48	BDL	77.80	0.10
IN2	1413.75±18.37	34.44±3.67	14.25±1.14	BDL	83.71	0.10
IN3	1289.09±3.07	13.63±2.93	13.2±0.84	BDL	68.25	0.08
IN4	1191.44±5.84	16.18±4.57	4.98±0.88	BDL	60.25	0.07
IN5	1145.86±10.62	14.68±3.58	6.66±0.82	BDL	58.70	0.07
IN6	1092.72±3.33	11.38±2.72	9.25±0.54	BDL	56.57	0.07
IN7	940.99±11.88	29.34±5.69	7.44±0.77	BDL	57.42	0.07
IN8	716.22±10.02	15.75±3.96	4.96±0.34	BDL	40.22	0.05
IN9	638.54±2.33	13.53±2.77	6.33±3.35	BDL	36.81	0.05
IN10	562.44±6.33	28.08±3.56	7.16±0.72	4.48±0.23	40.87	0.05
IN11	540.61±7.22	22.27±2.08	9.52±0.8	BDL	38.74	0.05
IN12	516.11±1.76	19.91±1.86	8.25±0.71	6.57±0.31	35.84	0.04
IN13	458.76±2.92	20.7±1.37	5.72±0.61	BDL	32.25	0.04
IN14	439.88±7.22	10.95±3.52	9.17±0.42	BDL	29.10	0.04
IN15	394.02±3.81	19.31±3.77	14.87±0.13	6.18±0.25	34.59	0.04
IN16	338.92±5.97	27.73±1.99	10.25±0.43	BDL	33.31	0.04
IN17	301.26±4.69	20.3±1.07	6.07±0.89	BDL	25.71	0.03
IN18	299.88±10.97	18.39±1.92	15.43±1.05	BDL	30.58	0.04
IN19	277.56±2.92	12.6±2.44	6.45±1.29	BDL	21.40	0.03
IN20	274.45±14.98	22.53±2.38	15.38±2.84	BDL	31.40	0.04
IS21	2135.74±18.37	34.44±1.85	15.43±3.73	BDL	114.56	0.14
IS22	243.96±2.17	11.86±3.85	14.43±4.72	4.97±0.29	24.61	0.03
IS23	106.01±11.02	28.05±2.17	6.63±3.03	BDL	21.50	0.03
IS24	106.01±2.97	10.01±1.92	4.96±4.03	BDL	12.13	0.02
IS25	623.66±3.77	10.01±3.36	7.93±3.54	3.89±0.11	35.56	0.04
IS26	2135.74±2.33	19.09±2.93	8.22±1.05	BDL	102.99	0.13
IS27	1614.74±6.33	11.88±4.57	11.25±1.29	BDL	79.81	0.10
IS28	277.56±3.07	12.6±3.58	6.45±2.84	BDL	21.40	0.03
IS29	716.22±5.84	15.75±2.72	4.96±1.29	BDL	40.22	0.05
IS30	439.88±10.62	10.95±5.69	9.17±2.84	BDL	29.10	0.04
IS31	550.61±10.87	22.27±3.96	9.52±0.34	7.12±0.42	39.16	0.05
IS32	516.11±10.02	22.36±1.85	8.25±3.35	3.76±0.11	36.98	0.05
IS33	1092.72±2.33	11.38±3.85	9.25±0.72	BDL	56.57	0.07
IS34	338.92±6.33	27.73±2.17	8.39±0.8	BDL	32.15	0.04
IS35	1614.74±2.33	11.88±1.99	11.25±0.71	BDL	79.81	0.10
IS36	1289.09±6.33	13.63±1.07	9.10±0.61	BDL	65.71	0.08
IS37	274.45±7.22	22.53±2.38	9.29±0.42	BDL	27.62	0.03

Location	^{40}K (Bqkg^{-1})	^{238}U (Bqkg^{-1})	^{232}Th (Bqkg^{-1})	^{137}Cs (Bqkg^{-1})	D (nGyh^{-1})	AEDE (mSvy^{-1})
IS38	1413.75±1.76	34.44±1.85	8.71±0.13	BDL	80.27	0.10
IS39	299.88±2.92	18.39±3.85	9.87±0.43	BDL	27.13	0.03
IS40	394.02±7.22	19.31±2.17	14.87±3.03	6.15±0.27	34.59	0.04
Mean	761.29±6.63	19.19±2.97	9.30±1.52	5.39±0.25	46.38	0.06

TABLE 3. Comparison of mean radioactivity levels and radiological parameters with previous studies.

Location	^{40}K (Bqkg^{-1})	^{238}U (Bqkg^{-1})	^{232}Th (Bqkg^{-1})	^{137}Cs (Bqkg^{-1})	D (nGyh^{-1})	AEDE (mSvy^{-1})	Reference
IMSU, Imo State	91.63	20.32	22.55	-	26.86	33.1	Eke *et al.* [24]
Ebonyi State	202.18	88.22	80.26	BDL	97.67	0.24	Ubgede *et al.* [25]
Abia State	179.15	52.64	97.68	-	92.45	0.11	Agbalagba *et al.* [26]
Imo State	761.29	19.19	9.30	5.39	46.38	0.06	Present Study
Anambra State	835.80	21.05	12.99	3.88	52.65	0.06	Present Study
World Average	400	35	30	59	55	1.00	UNSCEAR

Spatial distribution of radionuclide concentration within the study area, illustrated in Figs. 2(a)-2(d), revealed distinct patterns influenced by both natural and anthropogenic factors. ^{40}K concentrations ranged from 486.49 to 1205.51 Bq kg^{-1}, with the highest values observed in southern parts of Anambra and Imo states, as seen in Fig 2(a). This likely reflects the use of potassium-based fertilizers and naturally potassium-rich soils. Figure 2(b) shows that ^{238}U exhibited a narrower range (15.26–26.20 Bq kg^{-1}) and a more uniform distribution, suggesting minimal geological variability in uranium-rich materials. ^{232}Th concentrations, depicted in Fig. 2(c) varied from 8.79 to 27.97 Bq kg^{-1}, with higher levels concentrated in specific northern and central regions, likely due to thorium-rich mineral deposits. In contrast, ^{137}Cs [Fig. 2(d)] showed lower activity concentrations (0.19–6.90 Bq kg^{-1}) but notable hotspots in central regions, which may be linked to anthropogenic sources, including fallout from explosive weapons and redistribution during the civil war.

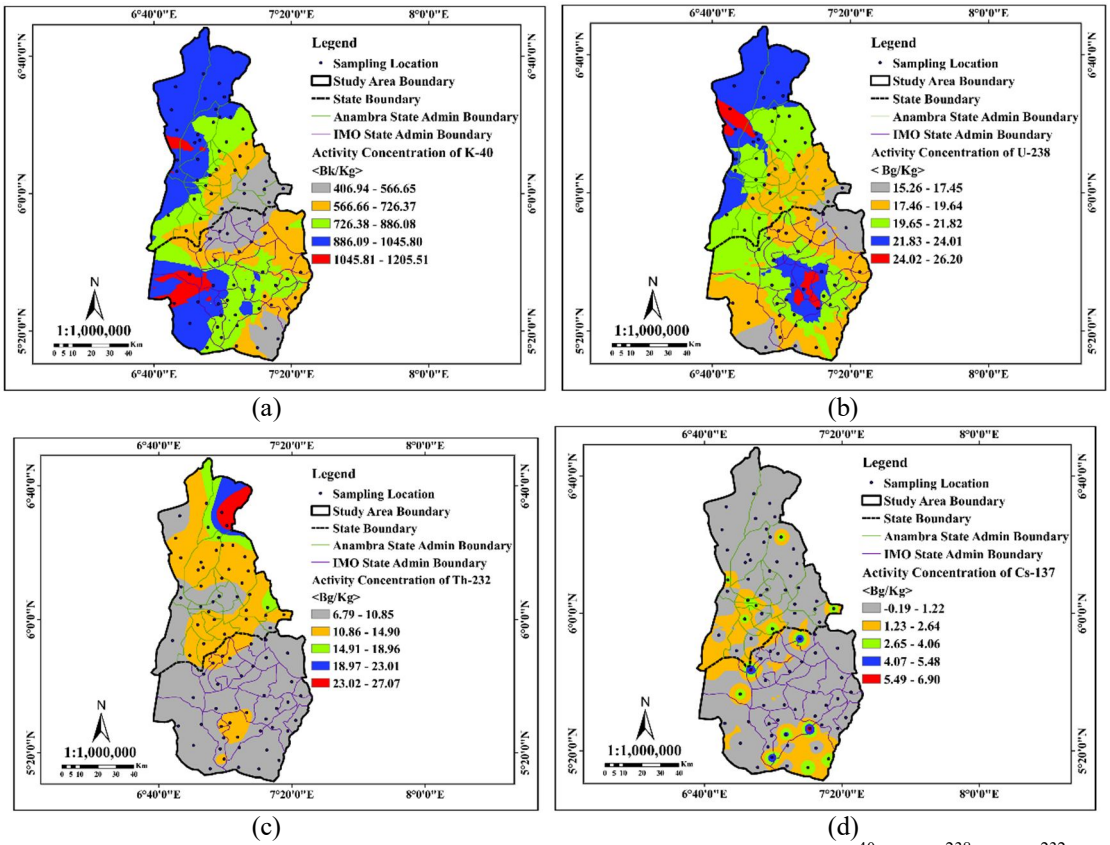

FIG. 2. Spatial distribution of radionuclide concentration within the study area: (a) ^{40}K, (b) ^{238}U, (c) ^{232}Th, (d) ^{137}Cs.

This highlights the distinct influence of human activities on cesium distribution compared with naturally occurring radionuclides. Among the radionuclides, ^{40}K showed the widest range and highest concentrations, reflecting significant variability, while ^{238}U exhibited the least spatial variability. The observed concentrations of ^{137}Cs emphasize the lingering impacts of historical events, contrasting with the geological control seen in ^{232}Th. These patterns not only highlight the environmental heterogeneity of the study area but also underscore the importance of monitoring radionuclides with both natural and anthropogenic origins for radiological safety. While the activity concentrations remain within global safety limits, elevated levels of ^{137}Cs in hotspots may require further investigation to assess localized risks.

In addition, as presented in Tables 1 and 2, the estimated average dose rate (D) values ranged from 25.431 to 120.78 nGyh^{-1} for Anambra and from 21.40 to 102.99 nGyh^{-1} for Imo, with an average of 52.65 and 46.38 nGyh^{-1}, respectively. Both mean values are below the global average of 55 nGyh^{-1} recommended by [1]. Similarly, the annual effective dose equivalent (AEDE) ranged from 0.03 to 0.15 mSvy^{-1} in Anambra and from 0.03 to 0.13 mSvy^{-1} in Imo, with mean values of 0.06 and 0.06 mSvy^{-1}, respectively. The mean values are significantly lower than the recommended 1.00 mSvy^{-1} [1]. These values indicate no significant health risks. When compared with previous studies (Table 3), the present study recorded lower absorbed dose rates, D, with corresponding AEDE values, than those reported for Ebonyi state (97.67 nGyh^{-1}, 0.24 mSvy^{-1}) and Ota, Ogun state (109.8 nGyh^{-1}, 0.135 mSvy^{-1}). This is consistent with the reduced ^{238}U and ^{232}Th activity concentrations observed in the present study areas. Furthermore, the low AEDE values are well below the global safety threshold of 1 mSvy^{-1}, indicating minimal radiological risk. The present study highlights elevated ^{40}K activity linked to agricultural and war-related soil disturbances, lower ^{238}U and ^{232}Th concentrations due to geological and environmental recovery factors, and the detection of ^{137}Cs, which was not accounted for in previous studies, likely due to its anthropogenic origins and redistribution from historical events. Despite these variations, radiological risks remain minimal in the studied regions.

4. Conclusion

Using gamma-ray spectrometry with a thallium-activated sodium iodide [NaI(Tl)] detector, the study analyzed 80 random soil samples collected from various locations within the Anambra and Imo states. The radionuclides measured include ^{40}K, ^{238}U, ^{232}Th, and ^{137}Cs, providing insight into both natural and anthropogenic radiation sources. The spatial distribution map created using ArcMap version 10.8.2 visualized the variability of radionuclide activity levels within the study area. In both states, the activity levels of the identified radionuclides, with the exception of ^{40}K, were found to be lower than the global average. The spatial distribution of the radionuclides within the study area revealed distinct patterns influenced by both natural and anthropogenic factors, with ^{40}K exhibiting the highest variability, driven by agricultural activities and naturally potassium-rich soils, while ^{238}U and ^{232}Th were predominantly influenced by geological conditions. Elevated ^{137}Cs concentrations in localized hotspots highlight anthropogenic sources such as explosive fallout and redistribution used during the civil war. Furthermore, the radiological indices estimated in lieu of the activity concentrations were lower than the permissible limit of 1.00 mSvy^{-1} recommended globally, indicating the safety of using these soil samples for their intended purposes and posed no radiological health risk. Based on the findings of the study, it is hereby recommended that other environmental matrices, such as water and plants, in the studied locations be investigated to ascertain their radiological status.

References

[1] United Nations Scientific Committee on the Effects of Atomic Radiation (UNSCEAR), "Report of UNSCEAR to the general assembly", (United Nations, New York, USA, 2000).

[2] Akinloye, M.K., Isola G.A., and Ayanlola, P.S., Int. J. Sci. Res. Pub., 8 (8) (2018) 628.

[3] Isola, G.A., Oni, O.M., Akinloye, M.K., and Ayanlola P.S., Int. J. Sci. Res. Pub., 8 (8) (2018) 618.

[4] Isola, G.A., Akinloye, M.K., Amuda, D.B., Ayanlola, P.S., and Fajuyigbe A., Int. J. Sci. Res. Pub., 10 (9) (2019) 1647.

[5] United Nations Scientific Committee on the Effects of Atomic Radiation, Sources and Effects of Ionizing Radiation, "Report to the General Assembly with Scientific Annexes". (New York, NY, USA, 2008).

[6] Manigandan, P.K. and Chandar, S.B., J. Rad. Res. Appl. Sci., 7 (2014) 310.

[7] Ekong, G., Akpa, T., Umaru, I., Lumbi, W., Akpanowo, M., and Benson, N., Int. J. Environ. Monit. Anal. 7 (2) (2019) 40.

[8] Leal, A. et al., J. Environ. Radioact., 211 (2020) 106046.

[9] Sirin, M., Microchem. J., 152 (2020) 104349.

[10] Addo, M.A., Lomotey, J.S., Osei, B., and Appiah, K., Radiat. Prot. Environ., 43 (2020) 6.

[11] Nagathil, N., Vadakkemattathil, V., Parambil, S.K., and Vamanan, P., Radiat. Prot. Dosimetry, 199 (20) (2023) 2554.

[12] Abu-Kharma, M., Rawashdeh, S., and El-Hasan, T., Int. J. Plant Anim. Environ. Sci., 14 (2024) 12.

[13] Akinloye, M.K., Isola, G.A., and Oladapo, O.O., Environ. Natl. Resour. Res., 2 (1) (2012) 140.

[14] Agbelusi, O.I., Ayanlola, P.S., Akinlabi, I.A., Amusat, T.A., Amuda, D.B., and Isola, G.A., Niger. J. Theor. Environ. Phys., 2 (2) (2024) 76.

[15] Xinwei, L., Lingquig, W., Xiaodan, J., and Leipengy, G.D., Chin. Rad. Prot. Dos., 118 (3) (2006) 352.

[16] Gao, J., Cao, C., Luo, Z., and Zhang, X., Indoor Built Environ., 23 (2014) 236.

[17] The 17 Goals of the United Nations Sustainable Development, https://sdgs.un.org/goals, Retrieved 3 September 2024.

[18] National Population Commission (NPC), "Nigeria Population 2022", (Demographics, Maps, Graphs), worldpopulationreview.com. Retrieved 3 September 2022.

[19] National Bureau of Statistics (NBS), (Demographic Statics Bulletin, 2020).

[20] Adeoje, E.A., Isola, G.A., Ayanlola, P.S., Lawal, M.K., Aremu, A.A., Oni, E.A., and Agbelusi, O.I., E-Proc. Int. Conf. Adv. Cem. Concr., 2023 (2023) 53.

[21] Awokoya, S.O., Ayanlola, P.S., Olatunji, A., Ojeniyi, F.A., Agbelusi, O.I., Orodiran, O.T, and Isola, G.A., Malays. J. Sci. Adv. Technol., 4 (4) (2024) 464.

[22] Ejeh, O.I., Heliyon, 7 (10) (2021) e08110.

[23] Onwuka, S.U., Duluora, J.O., and Amaechi, I.E., Albanian J. Agric. Sci., 12(2) (2013) 229.

[24] Eke, B.C., Akomolafe, I.R., Ukewuihe, U.M., and Onyenegecha, C.P., Environ. Health Inspect., 18 (2024).

[25] Ugbede, F.O., Osahon, O.D., and Akpolile, A.F., Environ. Forensics, 23 (1–2) (2021) 32.

[26] Agbalagba, E.O., Chaanda, M.S., and Egarievwe, S.U., Int. J. Env. Anal. Chem., 103 (17) (2021) 5539.

Volume 18, Number 5, 2025. pp. 705-724

Jordan Journal of Physics

ARTICLE

Proton Transmission through Magnetic Lenses for Characterizing Water and Human Tissues via Proton Radiography

Fatemeh Namdari and **Seyede Nasrin Hosseinimotlagh**

Department of Physics, Shiraz Branch, Islamic Azad University, Shiraz, Iran.

Doi: **https://doi.org/10.47011/18.5.11**

Received on: 29/01/2025; *Accepted on: 07/04/2025*

Abstract: Proton radiography (PR) is a new imaging method that allows direct measurement of the proton energy dissipation in different tissues. Proton radiography enables fast and effective high-precision lateral alignment of the proton beam and target volume in human irradiation experiments with limited dose exposure. The benefits of PR can be summarized as: 1) high image resolution, 2) the complete field of view can be measured with one short proton spill, 3) short data acquisition time, and 4) simple data processing. Enhancing image contrast can be achieved by substituting cuts on the scattering angle with the use of a magnetic lens (ML) system, resulting in optimal images of objects. The current study is primarily focusing on proton acceleration via target normal sheath acceleration (TNSA) using nanowire-coated foils as targets, followed by an investigation of the LET, range, and dose of protons. In this work, simplified physical models of proton transport, including Bethe–Bloch energy loss, energy straggling, and multiple Coulomb scattering (MCS), are used in the 0–300 MeV energy range of interest to analytically quantify the tradeoffs and scaling relationships between dose, spatial resolution, density resolution, and voxel size. We found that dose (D) is directly influenced by the size of voxel α and the necessary density resolution δ, which highlights a very strong dependence on voxel size. Our work shows that the average dose increases with increasing number of protons, while the average dose decreases with increasing proton beam energy, which is in good agreement with the other references. These studies demonstrate that the dose D of water, breast, brain, lung, and eye tissues is directly influenced by the size of voxel α and the necessary density resolution δ, adhering to the relationship $D \propto \alpha^{-5}\delta^{-2}$, which highlights a very strong dependence on voxel size.

Keywords: Magnetic lenses, PR, Tissue characterization, Radiation dose, Image blurring, Diagnostic imaging.

1. Introduction

A new diagnostic technique, high-energy proton radiography (PR), is being used to investigate the imaging of objects [1-3]. The three key events affecting protons as they pass via a material are absorption, energy dissipation, and multiple Coulomb scattering (MCS). PR has not been utilized for a prolonged time due to the MCS causing image blurring in radiography. A crucial method used in PR development involves a magnetic imaging lens system situated between the image and object, which focuses the proton beam (PB) point-to-point and achieves the resolution required across the full field of view for radiography [3–10].

More recently, it has been shown that many of the advantages of protons as a radiographic probe can be realized by using a magnetic lens to focus on the transmitted proton beam. Some potential advantages of protons over conventional X-ray techniques for flash radiography of thick, dense, dynamic systems include: 1) high penetrating power, 2) high detection efficiency, 3) small scattered background, 4) no need for a conversion target and the consequent phase-space broadening of the beam, 5) inherent multi-pulse capability, and 6) large stand-off distances from the test object and containment vessel to the detectors. Additionally, the use of a magnetic lens with thin

Corresponding Author: Seyede Nasrin Hosseinimotlagh **Email**: hosseinimotlagh@iaushiraz.ac.ir

detectors allows multiple images on a single axis, though progressively smaller apertures to be used to vary the magnitude and Z-dependence of the interaction, and can provide material identification. In addition, mono-energetic protons offer advantages over X-rays in the visualization of internal bodily structures. Thus, unlike X-rays and neutrons whose flux is exponentially attenuated with respect to absorber thickness, proton flux is only moderately attenuated before falling off steeply at the end of the particle range. This property may be used to advantage by placing a photographic film in the region of very steep attenuation, when radiographs of very high contrast may be obtained. A further advantage is that radiography based on proton transmission is relatively insensitive to variations in the chemical composition of the tissues [10-16]. This work utilizes a radiography technique that employs protons with high energy as probe particles. The effectiveness of this method relies on the use of magnetic lenses (MLs) to counteract the small MCS angle caused by the passage of charged protons through the object under investigation. Employing an ML renders the side effects of MCS perturbation a valuable and fulfilling endeavor. Protons exhibit distinct dependencies on material properties, influenced by a combination of Coulomb scattering at small angles, nuclear scattering, and energy dissipation processes, each with unique characteristics related to electron configuration, atomic number, density, and atomic weight. These tips enable the simultaneous estimation of the amount of matter and its identity [17-25].

However, protons suffer a significant amount of elastic scattering with nuclei through their trajectory in the form of multiple Coulomb scattering (MCS), which severely reduces the spatial resolution of proton imaging. Advanced trajectory estimation methods have successfully helped address the problem of MCS in proton imaging, ameliorating the spatial resolution. In PR, the images are blurred because of MCS. Thus, it is important to find the best way to reduce the impact of MCS on the extracted proton energy loss radiographic image to minimize the blurring and, consequently, to improve the accuracy of the energy-loss map. To suppress this kind of blurring, a magnetic structure called the Zumbro lens was developed by Mottershead and Zumbro [1], which is now the most important part of the PR system. The Zumbro lens is designed according to the momentum of the transmitted proton [8, 9]. As a result, the lens provides point-to-point focusing from the object to the image without blurring for protons whose momentum matches the reference value. The basic configuration of the PR system consists of three key parts: the diffuser, the matching lens, and a Zumbro lens. In the system, the proton beam propagates from left to right. A pencil monoenergetic proton beam is first scattered by a diffuser. After acquiring a broader angular distribution, it is transported into the matching lens. Both the angle and size of the beam are modified in the matching lens according to the coordinate-angle correlation required by the Zumbro lens. Then, the protons with this correlation can be imaged by the Zumbro lens upon reaching the image plane.

The multiphase interaction allows adjustments to be made to the sensitivity of the technique, thereby enhancing its utility across various material thicknesses. The magnetic optic enables unit magnification between the image and object and allows the detector planes and image to be moved away from the object being tested [26-27]. This significantly enhances the signal-to-background ratio. The ML system allows for adjustable angular acceptance, which is essential for material identification and enables the system to be sensitive to objects of varying thicknesses. Protons offer additional advantages as probe particles in radiography due to their high detection yield and the ability to be recorded repeatedly using a multilayer detector. In applications where dense objects require multiple rapid radiographs, consecutive velocities, protons are nearly an ideal solution due to their high penetration capabilities. This is because devices that accelerate protons produce long trains of high-intensity and short-duration beams, which are needed for these applications. Furthermore, advancements in technology have made available high-resolution, high-velocity proton data recordings, allowing for accurate results in energetic experiments, as well as in proton computed tomography (PCT). The range, as well as the transverse displacements and their angles, of the input protons can now be measured, for instance, by employing calorimeters and detectors.

This approach bears a strong resemblance to XRCT methods [1-8, 28-30]. 1) The average energy dissipation method involves gathering

statistics for a set of paths, with a focus on quantitatively assessing the average energy dissipation per path. Proton radiographs taken from multiple viewpoints can then be used to perform PCT in the same manner as X-ray computed tomography (XRCT) or PET, even when the paths of the protons are not completely straight. Many imaging methods can predictably quantify the dose-resolution relationship, as well as spatial and density resolution, in an ideal diagnostic system scenario. Two specific methods were chosen. Statistics for every category of proton path, not limited to a straight line, are compiled from within the imaged object. The proportion of protons transferred to each respective pathway is known as the "transfer efficiency" quantity. This method and XRCT are similar to each other. [1-8, 28-30]. 2) The mean energy dissipation method collects a set of statistical paths, but is qualitatively interested in determining the mean energy dissipation on every path. In fact, it turns out that the use of protons instead of X-rays for transmission imaging has some disadvantages. These include the need for large, expensive equipment to produce proton beams (e.g., a cyclotron or synchrotron) and the limitations on image quality arising from the multiple scattering of protons. However, the advantages of PR include a lower patient dose, higher soft-tissue contrast than X-rays, and real-time capability for tumor tracking within tissue [11–13]. PR also offers an improved contrast-to-noise ratio compared with standard X-ray imaging.

Verification of patient-specific proton stopping powers obtained in the patient's treatment position can be used to reduce the distal and proximal margins needed in particle beam planning. Proton radiography can be used as a pre-treatment instrument to verify integrated stopping power consistency with the treatment planning CT. Although a proton radiograph is a pixel-by-pixel representation of integrated stopping powers, the image may also be of high enough quality and contrast to be used for patient alignment. This investigation quantifies the accuracy and image quality of a prototype proton radiography system on a clinical proton delivery system. The highest level of spatial resolution can be attained by employing the most advanced methods to reconstruct the individual path, which is primarily constrained by the physical properties of the MCS phenomenon. This paper investigates ways to attain high image quality with high contrast in PR employing MLs in PCT. The structure of the paper is as follows. Section 2 presents a laser-driven proton accelerator based on target normal sheath acceleration (TNSA) using nanowire-coated foils as targets. Section 3 discusses the interaction of protons with matter. Section 4 examines proton imaging quality. Section 5 compares high-energy PR with other imaging techniques. Section 6 presents a theoretical investigation of PR along with numerical results. Finally, the discussion and conclusions are provided.

2. Laser-Driven Proton Accelerator

The higher flux and temperature of hot electrons that propagate into the target enable the use of nanostructured targets to accelerate protons or light ions via target normal sheath acceleration (TNSA) when a foil a few μm thick is used as the substrate for the nanostructures. According to the TNSA scheme (Fig.1), relativistic electrons produced during the interaction between an ultra-intense laser pulse and a thin foil cross the target and escape from its rear surface, generating a sheath electric field of several TV/m. Therefore, nearby ions, including protons adsorbed on the target surface as impurities, accelerated in the forward direction at energies of up to several tens of MeV per nucleon [31-33]. The capability of nanostructured targets to improve laser-target coupling and electron acceleration suggests the possibility of producing compact electron or proton beam sources using optimized structured targets and controlled irradiation conditions.
Since different target geometries are suitable for different scopes, it is important to achieve a deeper understanding of the interaction mechanisms and processes involved in this system in order to optimize the experimental conditions for various applications. Experimental and numerical studies suggest, for example, that the size of the gaps between nanostructures, such as the spacing between nanowires or the channel size in a nanotube, plays a key role in the interaction. Larger gaps seem in fact to favor the acceleration of high-energy electrons via plasmonic effects, whereas small gaps give rise to a stochastic heating that produces a hot, dense plasma [34-39].

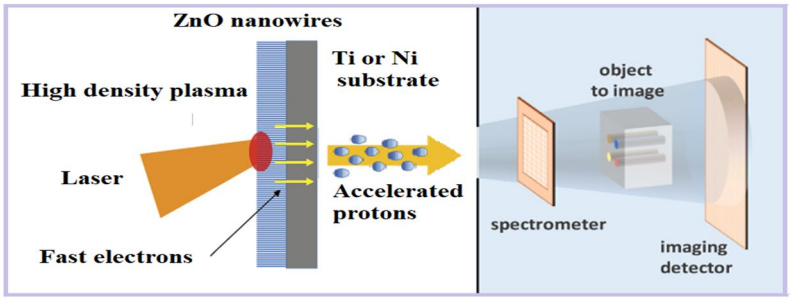

FIG. 1. Scheme showing proton acceleration via target normal sheath acceleration (TNSA) using nanowire-coated foils as targets with illustration of laser-driven PR.

3. Interaction of Protons with Matter

In PR, several interaction processes with matter have to be considered. These mainly include energy loss, nuclear interactions, and multiple Coulomb scattering.

3.1. Energy Loss

The energy loss of charged particles in matter is described by the Bethe-Bloch formula: $-dE/dx = \frac{4\pi k_0^2 z^2 e^4 n_e}{m_e c^2 \beta^2 \rho}[ln\frac{2m_e c^2\beta^2}{I(1-\beta^2)} - \beta^2 - \frac{\delta(\beta)}{2} - \frac{C(\beta)}{2}]$, where $k_0 = 8.99 \times 10^9 Nm^2C^{-2}$, z = atomic number of the projectile, e = electron charge, n_e = electron density of the medium, m_e = electron mass, c = speed of light, $\beta = v/c$ = relativistic beta factor, ρ = density of the medium, I = mean excitation energy in eV. It is dependent on the thickness, density, and composition of the target. The interaction in the target with the electrons of the target atoms leads to a non-uniform energy distribution of the exiting beam. This affects the point-to-point focusing as the Lorentz force, responsible for the bending of the particle trajectories, which is dependent on the particle velocity or beam direction, which is directly correlated to the particle energy. This causes dispersion in the magnets, leading to a z-shift of the focal spot x_i in the image plane. It is difficult to estimate the quantitative effect of the energy loss on the spatial resolution performance of a radiographic setup, mainly because of the unknown influence of the used collimator. Assuming that particles experiencing more energy loss also exit the target with a larger scattering angle due to more interactions, these particles will be the ones traveling further away from the beam axis at the location of the Fourier plane. The mid-plane collimator will sort out the particles; therefore, this effect can partly be canceled by choosing a different collimator.

3.2. Nuclear Interactions

In case of nuclear interactions, we have to differentiate between elastic nuclear collisions and inelastic nuclear interactions. The elastic collisions cause large scattering angles and possibly even a recoil of the proton. In this case, the interaction between the incident protons and the nuclei of the target happens through charge, as described in the following section on MCS. If the velocity of the incident proton is large enough to overcome the electrostatic potential of the nucleus, a nuclear reaction will happen. In this reaction, which is considered an inelastic interaction, the protons are first absorbed by the target nuclei, forming a new compound nucleus. These nuclei are mostly unstable and break up into various fragments, being ejected from the initial nucleus. The process is also called spallation and happens through strong interaction; it is dominant for the high energies used for PR. Although both types of interaction usually lead to a removal of the involved primary proton from the particle distribution, the total cross-section for the processes, and therefore the effect on the total particle distribution at the image plane of a radiographic setup, is very small. By integrating the differential cross-section for nuclear collisions outside of the angular acceptance of the utilized radiographic setup, the removal probability can be determined; however, this quantity is not measured continuously at the high energies required for PR. Therefore, a simple approximation can be introduced. For sufficiently high beam energies above 1 GeV, the probability for a scattering event is related to the nuclear collision length λ_{nc} [38]. Using the exponential attenuation law known as the Lambert-Beer law, the transmission can then be described by: $T_{nucl} = e^{-x/\lambda_{nc}}$. The corresponding nuclear collision lengths are tabulated by the particle data group [39]. Due to

the small cross-section, the influence of nuclear collisions on the total transmission is naturally very small, but will increase for thick or dense targets.

4. Image Quality

The image quality of a radiographic setup depends mainly on three factors: chromatic aberrations, scattering, and detector blur.

4.1. Chromatic Aberrations

Chromatic aberrations lead to the definition of the chromatic length. This effect is dependent on the properties and geometry of the object of interest, which directly affect the scattering φ and the energy loss straggling δ. This may lead to an effect known as limning, which particularly affects regions with steep density transitions.

4.2. Scattering

Scattering in the object, especially MCS, results in a non-zero scattering angle of the exiting proton but may also cause a shift of the trajectory. It is proportional to the square root of the target thickness and is also $\propto 1/p$, where p is the proton momentum.

4.3. Detector Blur

Protons interacting in the used scintillation generally do not travel on a trajectory parallel to the beam axis but rather traverse the material with an angle determined by the focusing properties of the lens system. This leads to a non-parallel emission of photons by a single proton track, an effect that can be partially reduced by selecting scintillators grown from columnar crystals capable of containing the produced photons in one column by total reflection. The effect can also be decreased by using thin scintillators, which in turn decreases the total yield of light [38-39]. Detector blur is also boosted by secondary particles, which are created during scattering processes of primary protons in the scintillation material. Summarizing the above findings, the detector blur is $\propto 1/p$ and decreases with increasing proton energy. All of the effects above tend to scale inversely with the proton energy, suggesting that an increase in the particle energy would lead to infinitely good spatial resolution performance. However, this is not the case for several reasons. Choosing higher proton energies will decrease the amount of scattering and therefore require longer collimators with smaller angular acceptances, which are not only complicated to handle in terms of alignment but also deliver worse results. This is obvious as the collimator has to be long or dense enough to at least deflect unwanted parts of the angular proton distribution so that those protons do not contribute to the final image.

5. High-Energy PR vs. Other Techniques

Currently, the most prominent candidates for future medical imaging alongside high-energy PR are single-tracking pCT and DECT. DECT is already clinically available and has been shown to deliver good results for treatment planning; however, its material separation capability is mainly used to improve image quality. This includes reducing artifacts originating from parasitic high-Z materials or enabling the visualization of contrast agents, for example, for the analysis of renal function or renal stones. Compared with conventional XCT, DECT neither offers increased data acquisition speed nor improves the spatial resolution performance of the system. In contrast, tracking pCT offers, compared with current high-energy PR, the possibility of simultaneously measuring both the density of the sample via scattering and the stopping power by employing a range telescope. As the requirements on the accelerator side are relatively low, a large number of research groups worldwide are addressing the challenges of this technique. Despite significant advancements in recent years, the major limitations of this method remain the speed of data acquisition, particularly for scattering data), as well as constraints on the size of the object being investigated. Both factors are critical for clinical adoption, since maintaining a patient in a fixed position is more difficult in a constricting environment, which may also cause stress. In terms of dose deposition and image quality, tracking PCT is quite similar to conventional XCT. The requirements for novel PCT scanners, and more generally for any new clinical imaging technique, were discussed in the early 2000s [38] and remain valid today, as the parameters of conventional XCT, which serve as baseline values, have not changed significantly since then.

When comparing high-energy PR with tracking PCT, the advantages of PR clearly include outstanding spatial resolution in the

micrometer range, extremely short data acquisition times limited only by the capabilities of the accelerator, and generous space constraints that allow easy patient placement and handling due to the long range of high-energy protons in air. The crucial factors that still need to be addressed are dose deposition, which remains too high in the performed measurements, but may be reduced as suggested by the investigations conducted on proton flux dependent density measurements.

The tracking PCT performance may increase further during the next few years due to more computing power and better detector systems; however, the outlined problem of the narrow space available for patient positioning will remain. Summing up those findings, high-energy PR presents a promising alternative to current imaging techniques. Several improvements and upgrades will be required, but these may become available in the coming years. The unique capability of real-time online imaging during the treatment procedure, as well as the outstanding spatial resolution performance, could significantly boost the accuracy of current hadron therapy and make this technique very useful for clinics.

6. Theoretical Investigation of PR

6.1. Desired Particle Attenuation Length

By setting a constant regulation for incoming particles, one can estimate the optimal attenuation length λ in order to inspect particles during radiography of an object with a specified thickness L. The attenuation length λ is minimized when there is a relative error in estimating the number of particles transferred between two regions of the object under consideration, which vary in L and are distinct from T in terms of size. We begin with the fundamental assumption that the exponential decay of the beam through the object is: $N(L) = N_0 exp(-L/\lambda)$. We assume that N_0 is the number of incident particles per pixel. Therefore, the net number of particles passing through the two areas is as follows:

$$N(L) - N(L+T) = N_0 exp\left(-\frac{L}{\lambda}\right) - N_0 exp\left(-\frac{(L+T)}{\lambda}\right) = N_0 exp\left(-\frac{L}{\lambda}\right)\left[1 - \exp(-\frac{T}{\lambda})\right] \quad (1)$$

If $T \to 0$, then $\exp\left(-\frac{T}{\lambda}\right) \to 1 - \frac{T}{\lambda}$, and Eq. (1) converts to $N(L) - N(L+T) = N_0 exp\left(-\frac{L}{\lambda}\right)\left[\frac{T}{\lambda}\right]$ .Research findings indicate that the maximum absorption distance is equivalent to half the object thickness, with a specific ratio of λ = L/2.

6.2. MCS Mechanism

Coulomb scattering describes the deflection of charged particles in the electromagnetic potential of the nucleus of target atoms. During the passage, this process does not happen only once, but several times; therefore, it is also called MCS. In certain cases, MCS can affect the reconstruction of the initial scattering event and, consequently, degrade image quality. For thin objects, MCS is the dominant interaction process, as the cross-section for nuclear collisions is considerably smaller.

Unlike X-rays, when proton beams enter an object, they undergo multiple collisions with charged particles in the atoms of the object. As a result, they are scattered at small angles and propagate through the material. At first glance, MCS appears to be a significant drawback for PR because protons do not travel in straight lines over long distances, leading to image blurring caused by angular dispersion immediately after exiting the object. The angular distribution of protons emerging from the object due to MCS follows a Gaussian distribution, which can be characterized by its root mean square (rms) value. The initial deflection angle $\theta_0$in the plane of projection is defined by: $\theta_0(z) = 0.0136GeV(\beta cp)^{-1}\left(\frac{z}{X_0}\right)^{\frac{1}{2}}\left[1 + 0.038\ln(\frac{z}{X_0})\right]$ [11].

In this equation, c represents the light velocity, the proton velocity is βc, p is the proton linear momentum, and z parameter is the object's thickness, which is measured in the same unit as the length, denoted as X_0. It is important to note that the proton beta value is close to unity, and the angle θ_0 depends inversely on the proton momentum, while increasing significantly with $\sqrt{L}$, where L is the object thickness. We plotted a three-dimensional variation of $\theta_0(z)$ as a function of z and the energy of the incident proton (E), for water and various tissues including breast, eyes, brain, and lung in Fig. 2.

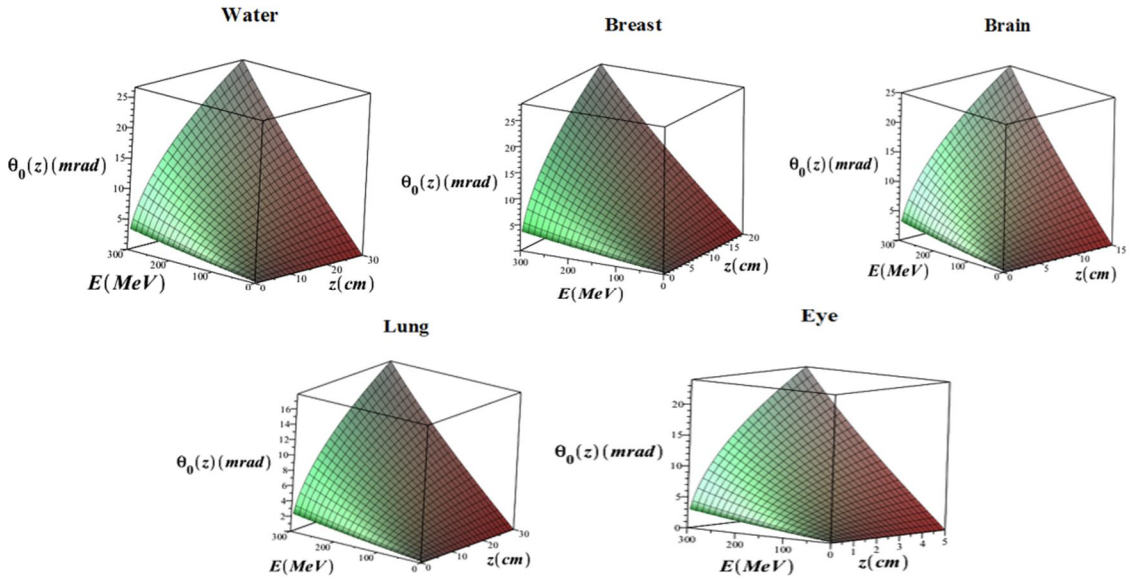

FIG. 2. 3-D diagram of $\theta_0(z)$ variations in terms of different values of z and E in water and in breast, eye, brain, and lung tissues.

MCS has two important effects on system performance. The first is a random effect that results in the limitation of object blurring, which is determined by the rms deviation of the image plane, y, upon the proton's arrival at the object's end from its non-scattered location. This deviation is expressed as: $y(z) = 3^{-1/2} z\theta_0(z)$. The 3-D diagram depicted in Fig. 3 illustrates variations of y (z) as a function of E and z in water and four distinct biological tissues, namely breast, eye, brain, and lung.

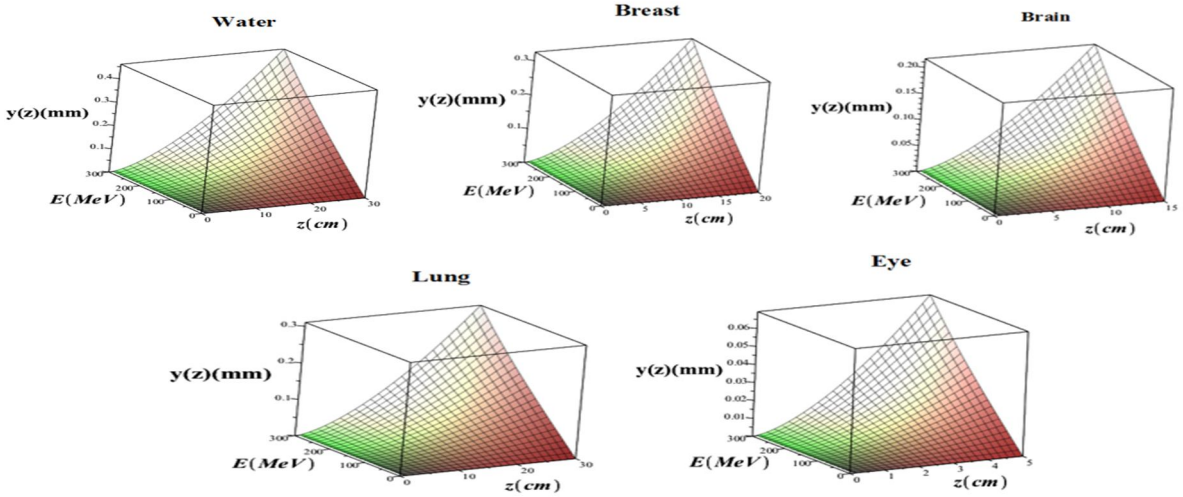

FIG. 3. The 3-D variations of $y\ (z)$ in terms of E and z in water and breast, eye, brain, and lung tissues.

The second factor contributing to blurring is the random proton trajectories emitted from the MCS when they depart the object and travel towards the detector, a distance greater than zero from the object. This effect can be studied by merely elevating the PB momentum. The initial effect can be readily examined by raising the PB's intensity. It is evident from $\theta_0(z)$ and $y(z)$ that the results become progressively better in a linear fashion, as the momentum of the beam is increased. Multiplying the linear thickness of an object by the square root of the object thickness as a function of radiation length leads to even greater growth. Choosing a high momentum can effectively reduce blur to any desired degree for radiography of thick objects. For observing moving objects, the detectors need to be positioned at a distance from the object. The second effect is characterized by different methods of operation. The current approach to solving this issue hinges on the fact that protons possess a charge and their paths can be altered by a B-field, which can be achieved using an ML, as discussed in the following section. This

is in addition to PR processes, where a facile exponential equation is used for the angular scattering distribution and the nuclear attenuation based on a Gaussian MCS [12–13]. The proton transmission process in this approximation is $T(L) = \exp\left(-\sum_i \frac{L_i}{\lambda_i}\right)\left[1 - exp\left(-\frac{\theta_{cut}^2}{2\theta_0^2}\right)\right]$. A three-dimensional diagram of the variations of T (L) is shown in Fig. 4, illustrating its relationship with different z values and the incident proton energy of E for both water and various human tissues, including breast, eye, brain, and lung.

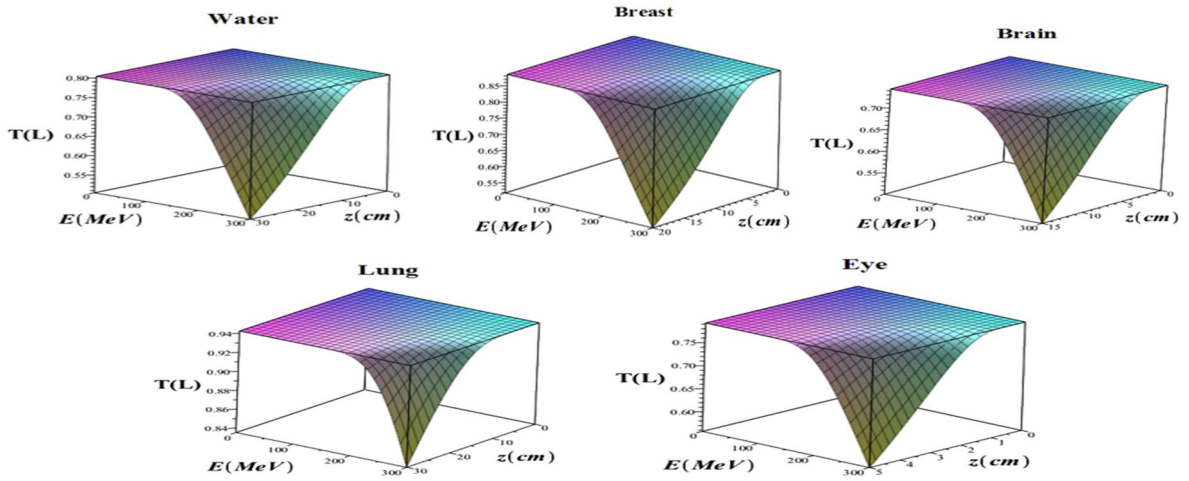

FIG. 4. 3-D diagram of $T(L)$ variations in terms of different values of z and incident proton kinetic energy of E in water and in breast, eye, brain, and lung tissues.

$\sum_i L_i$ is defined as the sum of L_i (the individual areal densities of each material), while λ_i is the factor of nuclear attenuation for i'th material: $\lambda_i = \frac{A_i}{N_A \sigma_i}$ .For the given expressions, the parameters can be defined as follows: N_A is equal to Avogadro's number; the absorption cross-section and atomic weight of the i'th material are shown by σ_i and A_i, respectively. θ_{cut} represents the angle-cut that includes the angular collimator. The X_{0i} (radiation length) parameter is defined as: $X_{0i} = \frac{716.4 A_i}{Z_i\,(Z_i+1)\ln(287/\sqrt{Z_i})}$. The initial component of T(L) pertains to attenuation, specifically nuclear attenuation, and is consistent with the X-ray attenuation process, whereas the second component is attributed to angular attenuation, a characteristic that distinguishes PR. Angular attenuation provides an alternative method for distinguishing material properties. The angular beam fraction broadening that forms the image for thick objects is determined by the material composition and the elastic scattering of proton-nucleon within the object itself [13]. The given equation should be accurate if the scattering angular distribution exhibits the same Gaussian momentum correlation spectrum. It is assumed that pixels a and b, which are crucial for observation in the lane of the image, are correlated with the quality of PR based on the contrast between them. The difference in transmission between these pixels is expressed as:

$$\Delta T = \exp\left(-\sum_i \frac{L_{ia}}{\lambda_i}\right)\left[1 - exp\left(-\frac{\theta_{cut}^2}{2\theta_{0a}^2}\right)\right] - \exp\left(-\sum_i \frac{L_{ib}}{\lambda_i}\right)\left[1 - exp\left(-\frac{\theta_{cut}^2}{2\theta_{0b}^2}\right)\right] \quad (2)$$

The cut-angle at its most favorable value can be found using Eq. (2). At high-energy, λ_i (the mean free path for the i'th material) parameter being roughly constant, the optimal cut-angle can be estimated by: $dT/d\theta_{cut} = 0$.

6.3. Magnetic Lens of PR System

The magnetic lens (ML) system, as illustrated in Fig.5, is designed in accordance with [14]. The two imaging lens cells have a magnification factor of negative one. Each cell contains four quadrupole magnets that operate under the same field strength, but they show alternating poles (+, –, +, –). The cell's configuration has a characteristic where protons are positioned radially around the midpoint between its two central magnets, based exclusively on their scattering angle in the object.

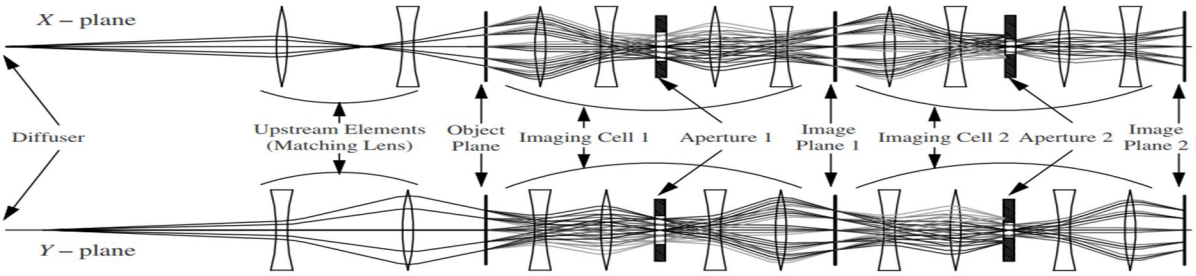

FIG. 5. Schematic illustration of the ML system, showing the X and Y planes.

Despite the fact that the appearance of the object's origin relates to a specific point in its plane, this topic enables the placement of a collimator in that specific location for making cuts on the MCS angle within the object. It was previously mentioned that the scattering distribution angle is in a Gaussian shape, with a width that can be calculated using the $\theta_0(z)$ relation. The collimator enables one to direct the particles at angles smaller than the cut angle (θ_{cut}), denoted by MCS. The number of transmitted particles N_C is given by: $N_C \approx N\left[1 - exp\left(-\frac{\theta_{cut}^2}{2\theta_0^2}\right)\right]$. In Error! Reference source not found., we plotted the 3D diagram of the $\frac{N_c}{N}$ variations in terms of different values of z and E in water and in breast, eye, brain, and lung tissues.

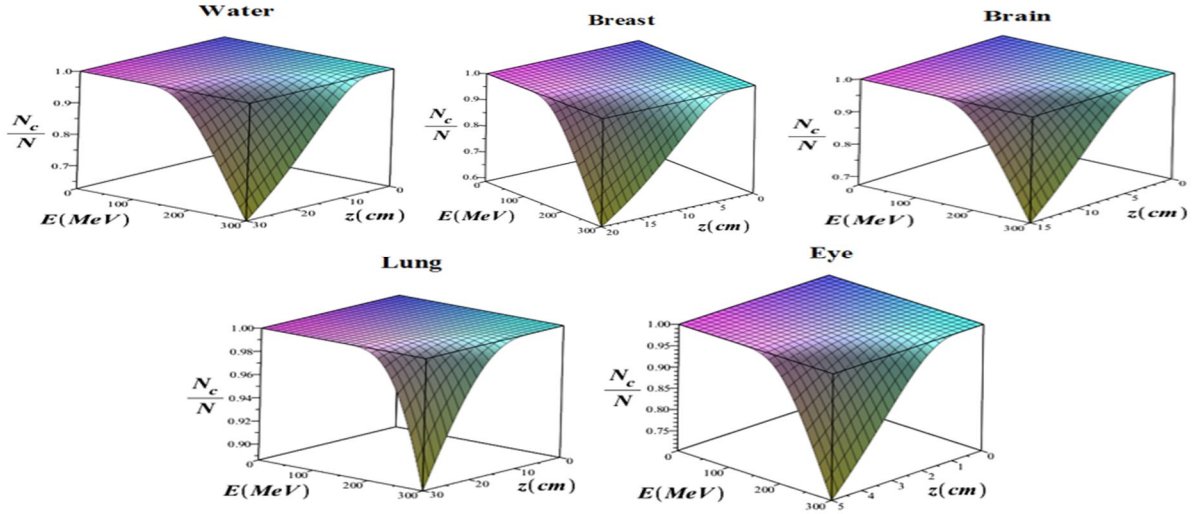

FIG. 6. 3-D diagram of $\frac{N_c}{N}$ variations in terms of different values of z and E in water and in breast, eye, brain, and lung tissues.

Here, the variable N represents the number of incident particles. When the value of θ_{cut} greatly exceeds θ_0 ,we anticipate that $N_c$will be equal to N. By substituting the $\theta_0(z)$ relation into the equation for θ_0 and simplifying, it can be found that $\frac{z}{X_0}$ is expressed as: $\frac{z}{X_0} \approx \frac{-\theta_c^2}{2\left(\frac{13.6MeV}{\beta cp}\right) ln\left(1-\frac{N_C}{N}\right)}$.

In Fig. 7, we depicted a three-dimensional diagram illustrating variations of $\frac{z}{X_0}$ with respect to z and E in water and in breast, eye, brain, and lung tissues.

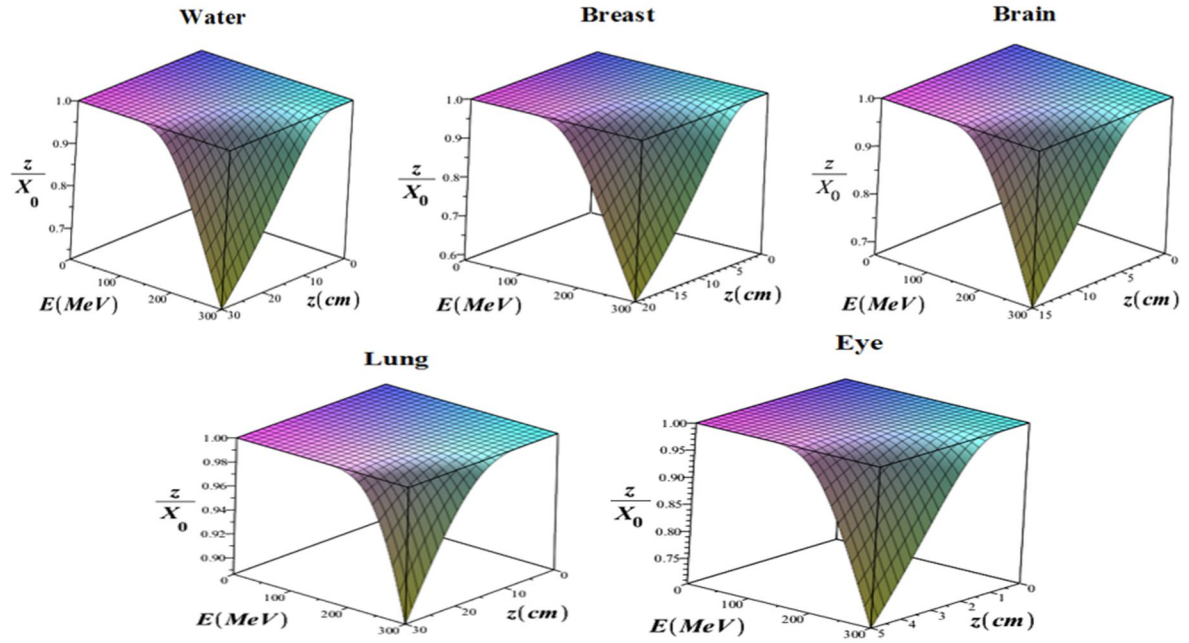

FIG. 7. 3D diagram of $\frac{z}{X_0}$ variations in terms of different values of z and E in water and in breast, eye, brain, and lung tissues.

When examining an ML system comprising two lenses (–I) mounted back-to-back, the first lens has an aperture that allows passage of all particles deflected by MCS, excluding those deflected by inelastic collisions. The second lens has its aperture set to cut into the MCS distribution. Detectors are then placed in the image plane of the two MLs and acquire two independent measurements. The first dependence is linked to the object's material in terms of nuclear interaction lengths, whereas the second dependence is related to the object's material in terms of radiation lengths. Because the values for nuclear interaction and radiation length have varying dependencies based on the type of material, we can thus determine both the quantity of existing material within the object and the type of material that exists in it. Using an ML with a single MCS cut angle can produce high-contrast PR, even when the object's thickness results in poor contrast through nuclear attenuation. For a thick object of a given thickness, an optimization cut-angle exists, which, as in the case of nuclear exponential beam attenuation, maximizes sensitivity to variations in object thickness when using pure MCS radiography. The optimal cut angle can be calculated using the same method that yielded equation λ=L/2, with the attenuation now expressed as $\frac{z}{X_0}$. The cut angle of MCS is generated by adjusting the aperture.

6.4. LET, Range, and Dose

The energy dissipation rate for a single proton with kinetic energy K that passes through the water is provided by $\left|\frac{dK}{d\lambda}\right|\left[MeV/(g/cm^2)\right] \approx \frac{1}{0.098k+0.0277}$. In medical applications, the relevant range for K is between 3 and 300 keV, which is expressed as κ = K / (100 [MeV]). The unit of λ is expressed as g.cm^{-2}, allowing consideration of its relationship with the thickness Δs (cm) of water, and $\Delta\lambda = \rho\Delta s$. The |dK/dλ| variations were graphed against the instantaneous kinetic energy K in the range 3 < K [MeV] < 300 for a single proton within the water, as shown in Fig. 8(a). The graph demonstrates a decrease in the average energy dissipation rate for the proton as K increases.

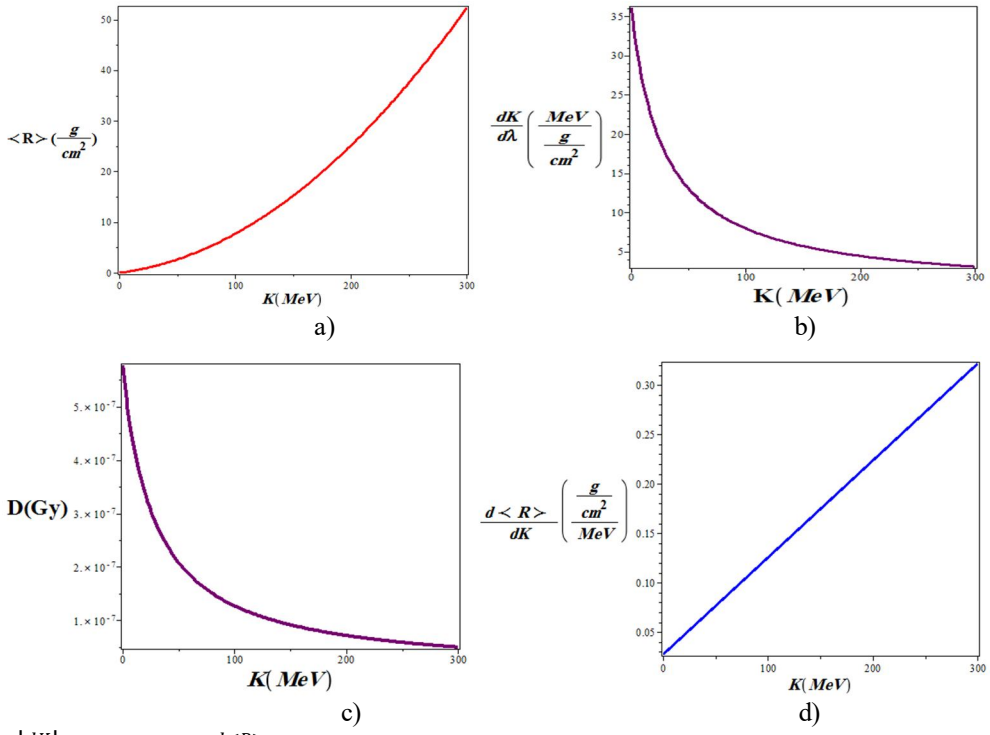

FIG. 8. a)$\left|\frac{dK}{d\lambda}\right|$, b) $< R >$, c) $\frac{d<R>}{dK}$, and d) average dose ($a = 0.1\ cm$) variations in terms of K in the interval $3 < K\ [MeV] < 300$ for a single proton in water.

The mean range ($R\ [gcm^{-2}]$) of a proton in water is: $< R > \approx 4.900\kappa^2 + 2.770\kappa$. Equations $\left|\frac{dK}{d\lambda}\right|$ and $< R >$ are not independent of each other. Hence, we have: $\frac{d<R>}{dK} = \left|\frac{dK}{d\lambda}\right|^{-1}$. In Fig. 8(b), the average range of proton variations versus K in water is plotted, with K being the variable of interest. The average number of protons in water exhibits a nonlinear increase with rising K levels, exhibiting the opposite trend compared to the average rate of energy dissipation caused by incident kinetic energy. In Error! Reference source not found.), the variations of $\frac{d<R>}{dK}$ in terms of the incident kinetic energy K of a single proton in water are shown, demonstrating a gradual nonlinear increase with increasing K. The instantaneous energy is maximized when K equals K_0, at which point λ is linked to the amplitude R. For example, a 200 MeV proton energy has a LET of about 4.47 $[MeV\ /\ (g\ /\ cm^2)]$ that exactly before it stops in the water at the end of its average range of about $226g\ /\ cm^2$, it increases significantly. Higher order approximations can be applied to Eq. (2) to improve the accuracy of low energy behavior, which is proportional to LET. The dose is expressed in grays, representing the total energy deposited per unit mass, measured in joules per kilogram. The average dose is obtained from the number of protons N passing through a square pixel of size a: $D \equiv \frac{N}{\rho a^2 \Delta s}\left|\frac{dK}{d\lambda}\right| \rho \Delta s = \frac{N}{a^2}\left|\frac{dK}{d\lambda}\right|$. Alternatively, it is simpler to write: $D[Gy] = 1.6 \times 10^{-10} \frac{N}{a^2[cm^2]}\left|\frac{dK}{d\lambda}\right| [MeV/({}^{g}/_{cm^2})]$. In Error! Reference source not found.), the average dose variations are plotted for the number of protons N passing through a square pixel of size a in terms of an incident kinetic energy of the proton, K. It is clear that the average dose declines as K increases. In Fig. 9, the 3D variations of the average dose are shown for N protons passing through a square pixel of size $a = 0.1\ cm$ in terms of the incident kinetic energy K in the range $3 < K\ [MeV] < 300$ and $10^5 < N < 10^6$. As seen in this figure, the average dose increases with increasing proton number, while it decreases with increasing proton beam energy, in good agreement with previous studies [40-41].

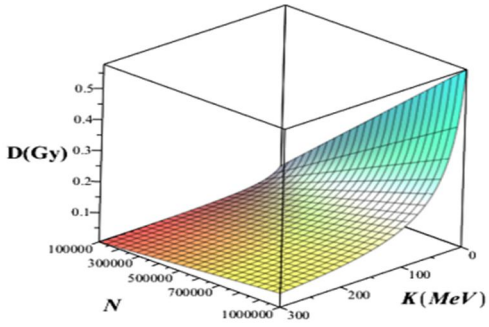

FIG. 9. 3D variations of the number of protons N passing through a square pixel with a size of 0.1 cm in terms of incident kinetic energy K in the range of $0 < K\,[MeV] < 300$ and $10^5 < N < 10^6$.

A proton with an energy of 200 MeV passing through a square pixel measuring 0.1 cm in size delivers an average dose of approximately 7.2×10^{-8}.

6.5. Adjustment

The loss of energy of protons in collisions with atomic electrons is governed by statistical principles. In addition to calculating the average, it is also necessary to verify the collection of dispersed RMS in energy dissipation and range [30-33]. A PB traversing a material with a thickness of Δλ can acquire the average square of the additional scattered energy: $\Delta\sigma_K^2 = 0.6\frac{Z}{A}(m_e c^2)^2\gamma\left(1-\frac{\beta^2}{2}\right)\Delta\lambda$. Here, m_e is the electron rest mass, Z and A are the atomic number and atomic weight of the element (pure) being traversed, and β and γ are the relativistic coefficients [15]. The three-dimensional diagram in Fig. 10 displays variations of $\Delta\sigma_K^2$ in relation to the kinetic energy of an incident proton (K) and the thickness (Δλ) for water and four distinct biological tissues: breast, brain, eye, and lung.

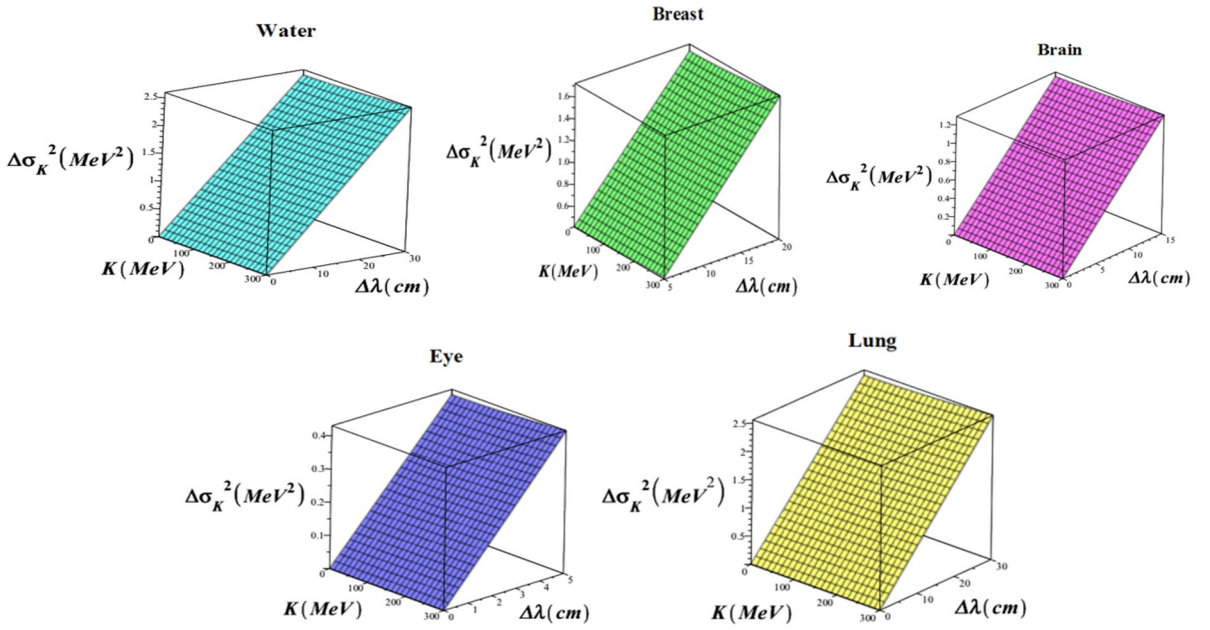

FIG. 1. 3D diagram of the variations of $\Delta\sigma_K^2$ in terms of the kinetic energy of an incident proton K and the thickness Δ for water and four different tissues: breast, brain, eye, and lung.

The growth rate is consistently uniform, and for water, it can be accurately approximated within the energy range relevant to medical applications as: $\sigma_K^2[MeV^2] \approx 0.089\lambda\left[{}^{g}/_{cm^2}\right]$. Immediately before stopping, the total RMS energy of a monochromatic proton beam can be expressed as: $\sigma_{KT}[MeV] = 0.30\sqrt{< R > [{}^{g}/_{cm^2}]}$. In Error! Reference source not found.(a), σ_{KT} variations are plotted as a function of the incident proton kinetic energy K in water. The figure clearly shows that σ_{KT} increases nonlinearly with increasing K.

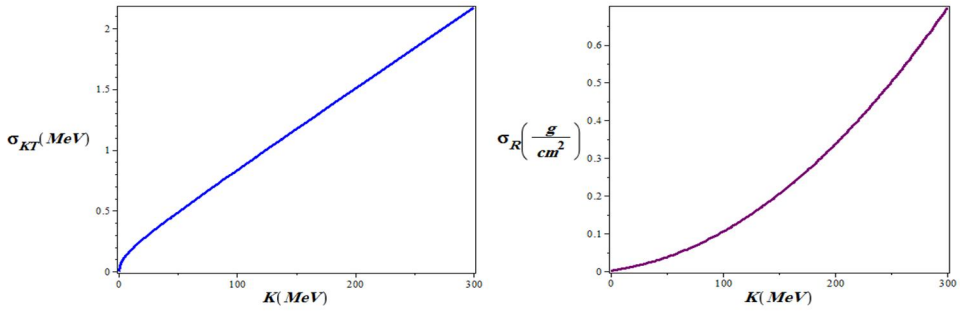

a) b)

FIG. 2. a) σ_{KT} and b) σ_R variations in terms of the kinetic energy of an incident proton K in water.

The phenomenon is linked to RMS range broadening: $\sigma_R = \frac{d<R>}{dK}\sigma_{KT}$, which can be approximated by: $\sigma_R\left[{}^{g}/_{cm^2}\right] \approx 0.300(0.0980\kappa + 0.0280)\,(4.900\kappa^2 + 2.770\kappa)^{1/2}$. For example, a monochromatic 200 MeV proton beam has an RMS kinetic energy spread of about 1.53 MeV at the end of its range of 26 g/cm^2, and an RMS range spread of about 0.34 g/cm^2 (0.34 cm in water). The spatial resolution of the radiographic image is defined by the RMS size of the beam on exit and, as a result, by the RMS range broadening if proton-by-proton track reconstruction is not possible or is not performed. In Error! Reference source not found.), we plotted σ_R variations in terms of the kinetic energy of an incident proton K in water. The data shown in this figure reveal an approximately nonlinear increase in the value of σ_R with rising K values in water (note that κ = K / (100 [MeV])). This is almost true for tissues, because, on average, approximately two-thirds of the human body is made up of water.

6.6. Mean Transmission Observation

The average transmission method, as depicted in Fig. 12 [16], is characterized by setting the incoming beam energy and bowtie filter properties such that the Bragg peak falls at the distal edge of the bowtie. This configuration optimizes the dose delivered to the patient while achieving maximum measurement sensitivity. The total linear density along a straight line is given by:

$$\lambda(x,y) = \int_A^B \rho(s)\,ds + \int_C^D \rho_{bowtie}\,ds \qquad (3)$$

$\lambda(x,y)$ is a function of the transverse coordinates x and y at the entrance. Bowtie filters are known to reduce the radiation dose at the periphery of the imaging field of view [1, 3], and they have also been shown to be effective in reducing scatter, a major source of image artifacts [1, 3, 4]. Additionally, they can help flatten the scatter distribution, which is beneficial for post-processing scatter correction strategies [7]. Typically, the thickness of a bowtie filter varies within the axial plane but remains constant along the third dimension, corresponding to the longitudinal field of view. Therefore, the material, thickness, and density of bowtie filters are important factors for image quality. From Eq. (3), $\lambda(x,y)$ depends on both the water density and the applied bowtie density. The value of $\lambda(x,y)$ influences the number of protons reaching the detector and, consequently, the resulting image quality. Simulation data indicate that the use of bowtie filters can reduce the ambient dose around the tissue. Furthermore, the bowtie filter design concepts are applied in this work to create a computational realization of a 3D human bowtie filter capable of achieving a constant effective attenuation coefficient across the entire field of view of human tissue.

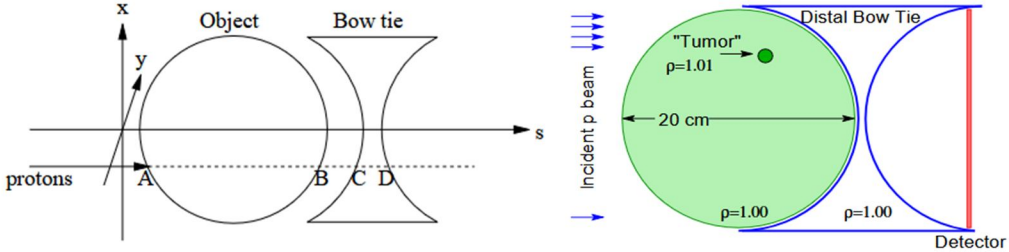

FIG. 3. Schematic design of the radiographed object with a "bowtie" compensator. The illustrated simple phantom can be used in initial reconstruction simulations [16].

The fraction of the transferred PB is a function of λ and an initial kinetic energy K_0, i.e., $T = T(\lambda, K_0)$. Transmission is measured for each square input pixel with a size of a: $T_{meas} = \frac{N_{out}}{N}$ .The number of input protons to each pixel is denoted as N, but only N_{out} is emitted from the bowtie and is subsequently transferred to a downstream detector. The accuracy of T_{meas} is indicated by the fact that T increases with the radiation proton number N: $T_{meas,\pm} = T \pm \frac{\sqrt{N_{out}}}{N} = T \pm \sqrt{\frac{T}{N}}$ .Note that in this relation, the quantity T is a function of λ and K_0. As a result, $T_{meas,\pm}$ becomes a function of K_0. In Figs. 13(a) and 13(b), we have plotted the 3D diagram of $T_{meas,+}$ and $T_{meas,-}$ variations for the $\pm$ signs in terms of T and N variations, respectively.

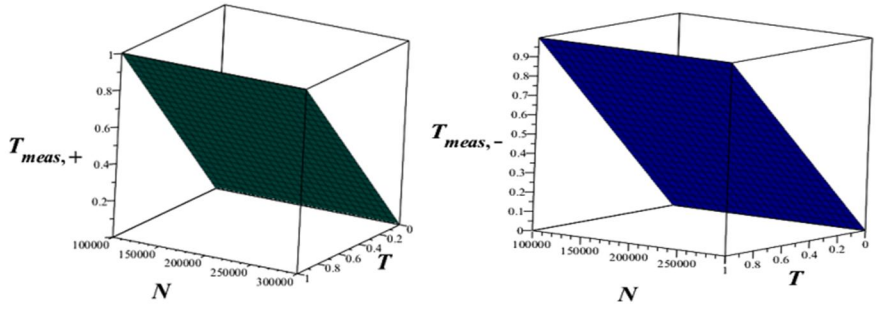

a) b)

FIG. 4. 3D diagram of a) $T_{meas,+}$ b) $T_{meas,-}$ variations in terms of changes of T and N.

The number of radiation protons required to alter the fractional change in density, expressed as $\delta \frac{\Delta\rho}{\rho_0}$, in a cubic voxel to a specific size 'a' needs to be determined. For the diagnosis of this kind of variation, the transmission T must be accurately quantified: $\Delta T = \frac{dT}{d\lambda}\Delta\lambda = \frac{dT}{d\lambda}\rho_0 a\delta$. $T_{meas,\pm}$ approximately shows that: $N \cong \frac{T}{\Delta T^2}$. Therefore, according to this relation, if the value of ΔT decreases, then the value of N increases, and as a result, according to $T_{meas,\pm} = T \pm \sqrt{\frac{T}{N}}$, the value of $T_{meas,\pm}$ increases.

Protons are necessary for each pixel's radiation. This outcome gives rise to a fundamental principle that yields a distinct radiography design: $N\delta^2 a^2 = \frac{T}{(\frac{dT}{d\lambda})^2 \rho_0^2}$. This expression can be applied straightforwardly to photons in X-ray imaging.

6.7. Sensitivity Response - Optimal Dose

Figure 14 implies that the right-hand side of the above relation can be minimized by adjusting the initial kinetic energy $K_0$to optimize the transfer gradient: $\frac{dT}{d\lambda}$, thereby maximizing sensitivity δ while minimizing dose D on the left-hand side. Studies in proton radiography indicate that the choice of analytical algorithms for more complex clinical imaging, such as lung or breast imaging, depends on the range distribution function. The range distribution φ(R) exhibits a substantial Landau tail. For practical purposes, a Gaussian approximation is reasonable: $\varphi(R) = \frac{1}{\sqrt{2\pi}\sigma_R}\exp\left(\frac{(R-<R>)^2}{2\sigma_R^2}\right)$. Note that the amount of beam spread is characterized by the quantity σ_R, which is an increasing function of the depth. Physically, this spread is due to the lateral scattering during the proton propagation. In addition, according to $< R > \approx 4.900\kappa^2 + 2.770\kappa$, this $\varphi(R)$ depends on the K.

Ignoring nuclear losses, we have: $\frac{dT}{d\lambda} = -\varphi(\lambda)$. and the maximum transfer gradient occurs when $\lambda =< R >$ and $T = 0.5$: $\left|\frac{dT}{d\lambda}\right|_{max} = \frac{1}{\sqrt{2\pi}\sigma_R}$. As a result, when the initial kinetic energy K_0 is altered so that half of the protons pass through into the object and the bowtie, we have: $N\delta^2 a^2 = \frac{\pi\sigma_R^2}{\rho_0^2}$. The local dose D that is delivered by this proton flux is a function of both the local energy of K and the initial energy K: $D\delta^2 a^4 = \frac{\pi\sigma_R^2}{\rho_0^2}\left|\frac{dK}{d\lambda}\right|$. When K equals$K_0$, at the patient's level, using equations $\frac{d<R>}{dK}$, σ_{KT}, and σ_R, we obtain: $D\delta^2 a^4 = \frac{0.089\pi}{\rho_0^2} < R > \frac{d<R>}{dK}$. Substituting $\left|\frac{dK}{d\lambda}\right|$ and σ_R yields the following suitable approximations:

$$N\delta^2 a^2[cm^2] \approx \frac{0.28}{\rho_0^2}(4.9k^2 + 2.8k)(0.10k + 0.03)^2 \quad (4)$$

and

$$Da^4\delta^2[Gy\ cm^4] \approx \frac{4.5\times10^{-11}}{\rho_0^2}(4.9k^2 + 2.8k)(0.10k + 0.03) \quad (5)$$

Here, $k \equiv {}^{K}/_{100}\,[MeV]$ and $\rho_0 \approx 1\,{}^{g}/_{cm^3}$. Note that, according to the above equations, both R and D are functions of $\varphi(R)$. In Error! Reference source not found., we plotted $N\delta^2 a^2$ and $D\delta^2 a^4$ variations in terms of the proton kinetic energy for water and for breast, brain, lung, and eye tissues. It is evident that as the kinetic energy of a proton rises, the values of $N\delta^2 a^2$ and $D\delta^2 a^4$ increase in a nonlinear fashion.

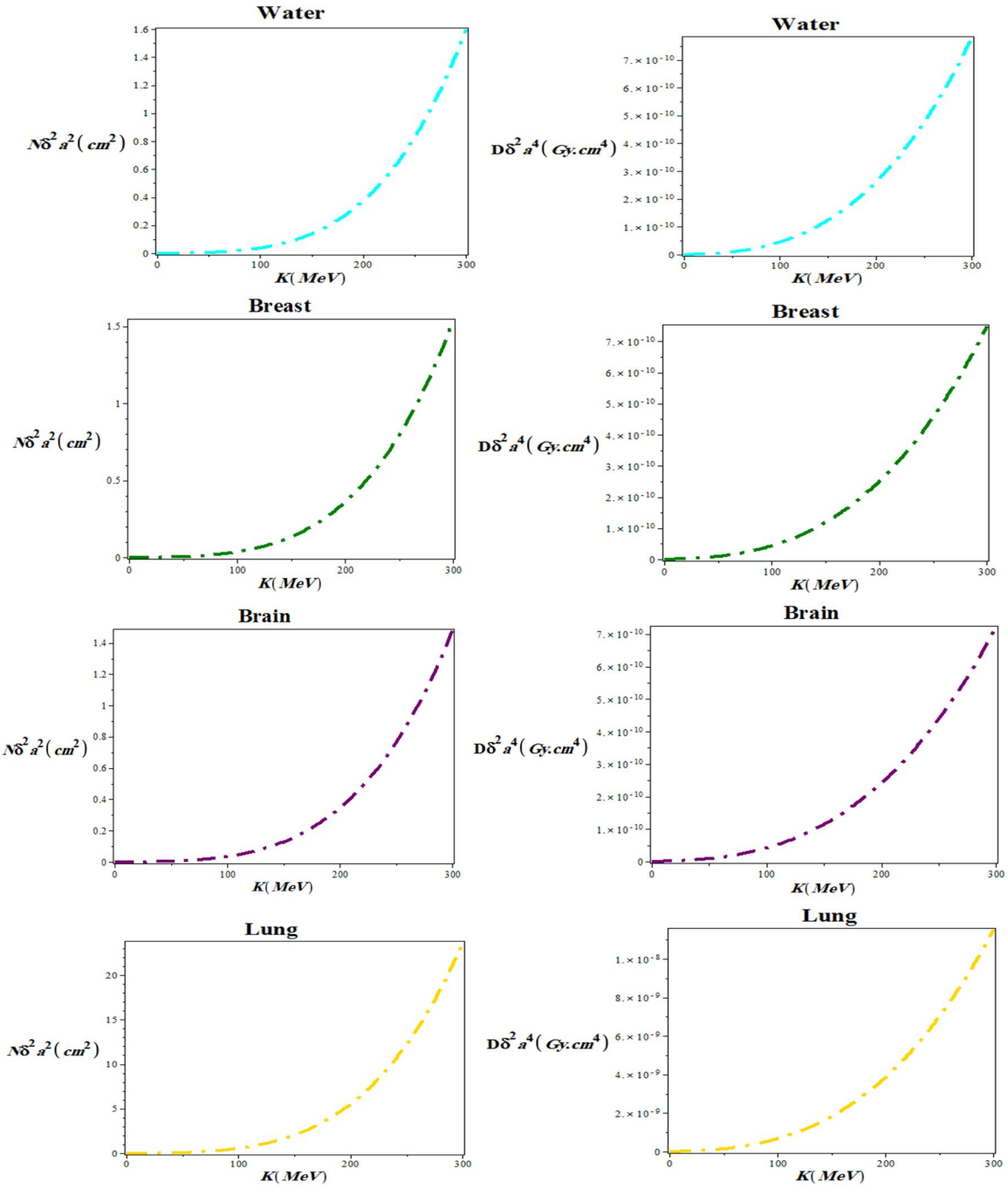

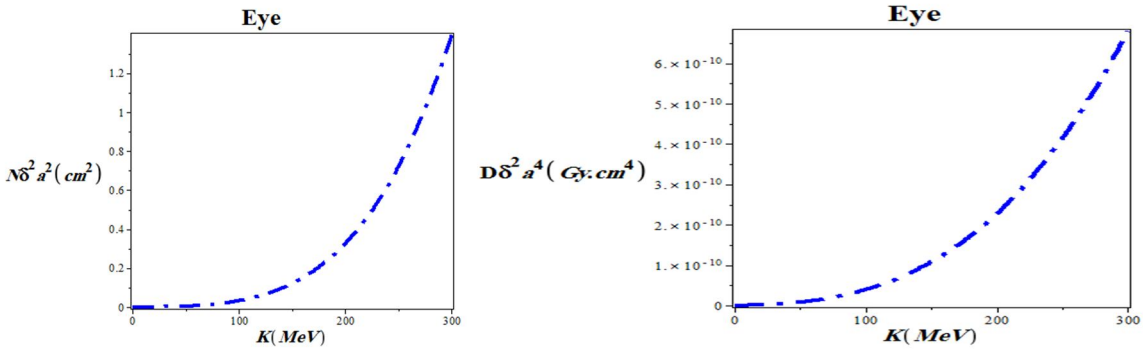

FIG. 5. $N\delta^2a^2$ and $D\delta^2a^4$ variations in terms of the kinetic energy of an incident proton in the range of $0 < K\,[MeV] < 300$ for water and breast, brain, lung, and eye tissues.

A PB with an energy of 200MeV is used in water for identifying density fluctuations, where the fluctuations, denoted as δ, are measured at a resolution of 0.01 in voxels with dimensions of a = 0.1 cm. In this case, N δ^2a^2 = 0.37, and the number of $N_0 = 3700000$ protons per pixel is required, resulting in a surface dose of $D = 26mGy$ for $K = 200\,MeV$. Eqs. (4) and (5) specify the dosage for a single radiographic image. In a computed tomography scan, for a field of view with a width of w, we have approximately: $M = \frac{W}{a}$. Accordingly, the total dose for CT scanning is scaled as: $D \sim \frac{W}{a^5\delta^2}$ .The relationship is heavily influenced by the voxel's size to the fifth power. In summary, results show that the nonlinear increase in Nδ^2a^2 and Dδ^2a^4 with increasing kinetic energy (K) are: transmission, $T(\lambda, K_0)$, the total linear density of a straight line, λ, initial kinetic energyK_0, number of input protons to each pixel, N, and σ_R parameter. Two factors are particularly important for proton radiography: (1) image resolution improves with accumulated proton shots (dose), but beyond a certain dose, further increases do not enhance resolution; (2) spatial resolution is higher for higher-energy protons due to their smaller scattering angle caused by MCS.

Studies indicate that CR39 detectors provide better resolution than RCF but are suitable only for low proton flux. Image blurring is mainly caused by MCS and represents out-of-focus blur. Applying non-blind image deblurring algorithms improves proton radiography image clarity and spatial resolution. With advances in petawatt (PW) lasers and target preparation technology, laser-driven proton energies are approaching 100 MeV and are expected to increase further. Therefore, a new generation of compact proton radiotherapy devices based on laser accelerators, along with associated proton radiography diagnostic systems, is highly probable. The methods presented here can also be extended to higher-energy protons.

6.8. Proton Energy Dissipation Through Proton

In transfer measurements, the energy of each individual proton is recorded rather than simply counting the fraction of exiting protons. This allows for an accurate reconstruction of energy dissipation within each voxel, which is critical for density mapping. It is assumed that a full-energy detector, such as a calorimeter, has a sensitivity limited by a minimum detectable dose. The reconstructed proton path is assumed to be sufficiently accurate to identify the specific voxel traversed by each proton. The total deposited energy for N protons passing through a square voxel of side a is equal to: $\Delta K = N\int\left|\frac{dK}{d\lambda}\right|\rho(s)ds \pm N^{1/2}\sigma_{KT}$. The second term indicates the measurement error in relation to the total fluctuation regulation, specifically: $\sigma_{KT} = \left(\int\frac{d\sigma_K^2}{d\lambda}\rho(s)ds\right)^{1/2}$ .A peculiar trait of PR is that proton trajectories are stochastic and not straight because protons undergo MCS. This is commonly accounted for by estimating the most likely path for each proton and performing line integrals along the resulting curvilinear lines. In addition to energy loss PR, other contrast mechanisms have been proposed, which exploit different types of interaction of protons with a medium. In particular, these are attenuation and scattering PR. The former measures the reduction in proton flux after an object due to inelastic nuclear interactions and reconstructs a map of the nuclear attenuation coefficient. The latter estimates the angular dispersion of protons due to MCS in the object and reconstructs a parameter describing MCS, e.g., radiation length. The error in measuring the average

energy dissipation per proton (ΔK / N) decreases statistically with a reduction of 1/√ N even for a full-calorimeter. Therefore, additional protons are required to resolve smaller density fluctuations in a single radiograph image. The average energy dissipation is provided by the formula, given that the density of a single voxel in this path varies at a rate of $\delta = \Delta\rho/\rho_0$:

$$\Delta\delta K = N\left|\frac{dK}{d\lambda}\right|\delta\rho_0 a \qquad (6)$$

The condition associated with this deviation from the density is diagnosed as: $\left|\frac{dK}{d\lambda}\right|\delta\rho_0 a > N^{1/2}\sigma_{KT}$. We placed the expressions of intensity and sensitivity on the left, and set the diagnosis threshold at: $N\delta^2 a^2 = \frac{1}{\rho_0^2}\frac{\sigma_{KT}^2}{|dK/d\lambda|^2}$. The relationship becomes dose-dependent, as indicated by $D = \frac{N}{a^2}\left|\frac{dK}{d\lambda}\right|$, and we have: $D\delta^2 a^4 = \frac{1}{\rho_0^2}\frac{\sigma_{KT}^2}{|dK/d\lambda|}$. One simpler method for our analysis is to first establish the amount: $N\delta^2 a^2[cm^2] \approx \frac{0.089\lambda}{\rho_0^2}(.10k + .03)^2$ and $D\delta^2 a^4[Gycm^4] \approx \frac{1.4\times10^{-11}\lambda}{\rho_0^2}(.10k + .03)$. Figure 15 illustrates three-dimensional representations of the variations in the number of protons (N) and local dose (D) in each radiography design, based on the kinetic energy of incident protons ranging from 0 to 300 MeV. A λ thickness of 0.01, with voxels of 0.1 cm in size, was drawn for water as well as breast, brain, lung, and eye tissues.

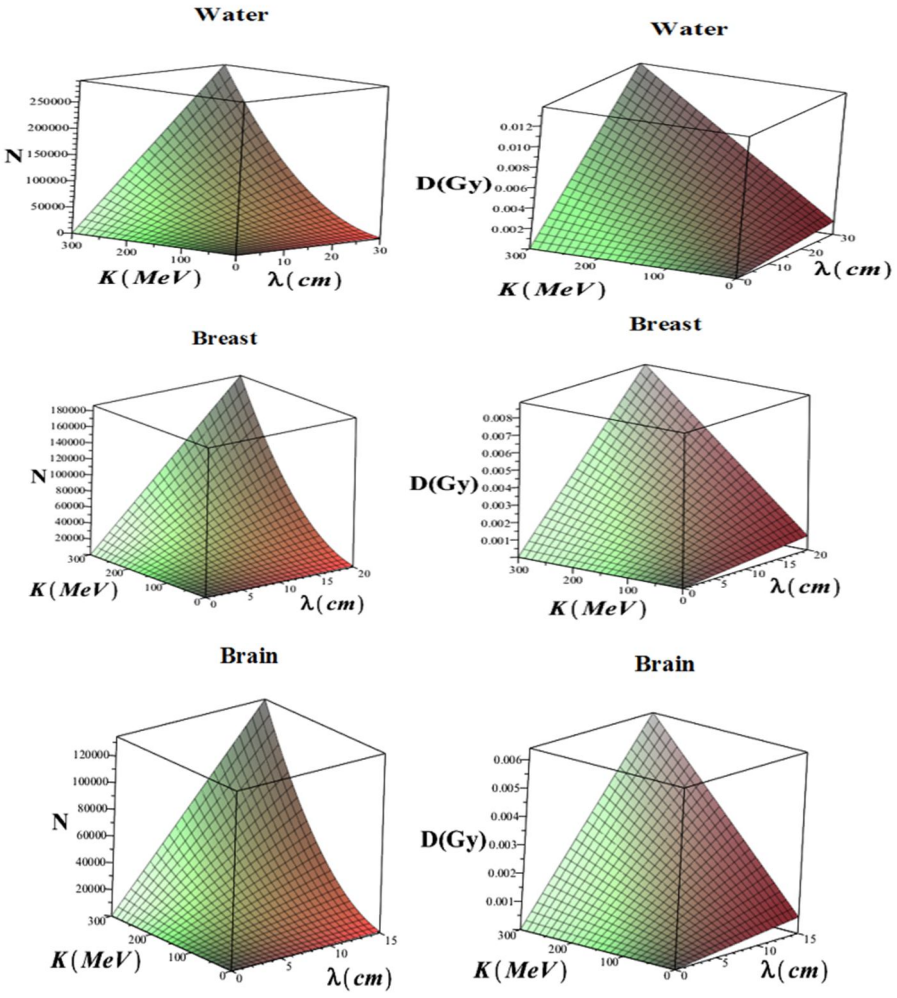

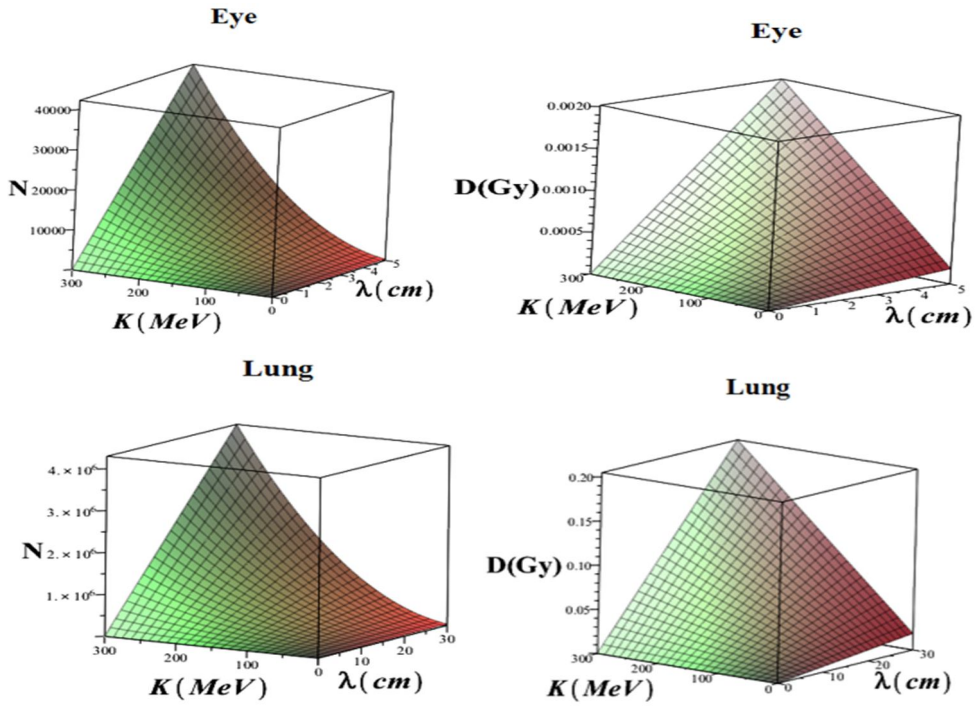

FIG. 6. 3D variations of N and D in terms of the kinetic energy of an incident proton in the range of $0 < K\,[MeV] < 300$ and thickness λ for $\delta = 0.01$ in voxels with the size of $a = 0.1\,cm$ in water and breast, brain, lung, and eye tissues.

λ is the patient's thickness. The instantaneous energy k is given by: $k \equiv {}^{K}/_{100}$,which is measured in MeV with a density of approximately $1.0\,{}^{g}/_{cm^3}$, denoted by ρ_0.The surface dose delivery is considered for a 200 MeV PB in water to detect density fluctuations of 0.01 in voxels with dimensions of 0.1 cm, for a thickness of $\lambda = 20\,g\,/\,cm^2$, since $Na\delta^2 \approx 0.094$ it is estimated that approximately 94000 protons are required to penetrate each pixel, and the local dose in each radiography project is approximately 6.6 mGy. At first glance, this dose is roughly half the size of the standard order, exceeding the amount normally received with the average transfer method.

Proton imaging is a promising technology for proton radiotherapy as it can be used for: (1) direct sampling of the tissue stopping power, (2) input information for multi-modality RSP reconstruction, (3) gold-standard calibration against concurrent techniques, (4) tracking motion, and (5) pre-treatment positioning. One of the limiting factors in imaging is noise. The imaging noise originates from two processes: the Coulomb scattering with the nucleus, producing a path deviation, and the energy loss straggling with electrons. Noise increases with the thickness of tissue traversed and decreases with higher proton energy. Scattering noise is dominant around high gradient edge whereas straggling noise is maximal in homogeneous regions. Image quality metrics are found to behave oppositely against energy, lower energy minimizes both the noise and the spatial resolution, with the optimal energy choice depending on the application and location in the imaged object.

7. Conclusions

In this work, simplified physical models of proton transport including Bethe-Bloch energy loss, energy straggling, and multiple Coulomb scattering (MCS) were employed in the 0–300 MeV energy range to analytically quantify the trade-offs and scaling relationships between dose, spatial resolution, density resolution, and voxel size. We found that the dose D is directly influenced by the voxel size alpha and the required density resolution δ, highlighting a strong dependence on voxel dimensions. Lens-focused proton radiography (PR) represents a novel imaging technique. Unlike X-ray radiography, PR employs a magnetic imaging lens system to achieve point-to-point focusing from the object to the scintillator screen, thereby minimizing blur caused by the angular divergence of scattered protons. The advantages of PR over conventional X-rays include precise

targeting of tumors, reduced radiation exposure to surrounding healthy tissues and organs, and diminished short-term and long-term side effects of radiation therapy. Clinically, PR also enables the detection of proton range variations due to anatomical changes in a patient, offering potential for improved treatment accuracy.

In general, it would be possible to use PR in combination with heavy ion gantries. The challenge in PR imaging arises from the MCS of the protons traversing different materials, causing blurring of the radiography image. Thus, to improve the image quality and identify each material in the phantom, cuts for the proton scattering angle have to be tuned carefully. The challenging matching conditions could be established already in front of the gantry and then mapped to the patient position (point-to-point focusing). Laser-driven ion accelerators can deliver high-energy, high-peak current beams and are thus attracting attention as a compact alternative to conventional accelerators. However, achieving sufficiently high energy levels suitable for applications such as PR remains a challenge for laser-driven ion accelerators.

References

[1] Engwall, E. et al., Med. Phys., 50 (9) (2023) 5723.

[2] Li, X. et al., Front. Oncol., 11 (2021) 698537.

[3] Mein, S. et al., Med. Phys., 49 (9) (2022) 6082.

[4] Klein, C. et al., Radiat. Oncol., 12 (2017).

[5] Rorvik, E., Fjera, L., Dahle, T., Dale, J., Engeseth, G., Stokkevag, C. et al., Phys. Med. Biol., 63 (2018).

[6] Gu, W., Ruan, D., Lyu, Q., Zou, W., Dong, L., Sheng, K., Med. Phys., 47 (2020) 2072.

[7] Zhang, G., Shen, H., Lin, Y., Chen, R., Long, Y., Gao, H., Med. Phys., 49 (2022) 5752.

[8] Wuyckens, S., Saint-Guillain, M., Janssens, G., Zhao, L., Li, X., Ding, X. et al., Comput. Biol. Med., 148 (2022).

[9] Engwall, E., Battinelli, C., Wase, V., Marthin, O., Glimelius, L., Bokrantz, R. et al., Phys. Med. Biol., (2022).

[10] Janson, M., Glimelius, L., Fredriksson, A., Traneus, E., Engwall, E., Med. Dosim., (2023).

[11] Tanabashi, M., Hagiwara, K., Hikasa, K., Nakamura, K., Sumino, Y., Takahashi, F., Agashe, K., Aielli, G., Amsler, C. et al., Phys. Rev. D, 98 (2018) 030001.

[12] Mein, S. et al., Radiother. Oncol., 199 (2024) 110434.

[13] Penfold, S. et al., J. Med. Radiat. Sci., 71 (2024) 27–36.

[14] Liu, G., Li, X., Zhao, L., Zheng, W., Qin, A. et al., Acta Oncol., (2020).

[15] Cao, W. et al., J. Appl. Clin. Med. Phys., 24 (2023) e13954.

[16] Paganetti, H., Botas, P., Sharp, G. et al., Phys. Med. Biol., 66 (2021) 22TR01.

[17] Giacometti, V., Hounsell, A., McGarry, C., Physica Medica, 76 (2020) 243–276.

[18] Thummerer, A., Zaffino, P., Meijers, A. et al., Phys. Med. Biol., 65 (2020) 095002.

[19] Thummerer, A., Seller Oria, C., Zaffino, P. et al., Med. Phys., 48 (2021) 7673–7684.

[20] O'Hara, C., Bird, D., Al-Qaisieh, B. et al., J. Appl. Clin. Med. Phys., 23 (2022) e13737.

[21] Seller Oria, C., Thummerer, A., Free, J. et al., Med. Phys., 48 (2021) 4498–4505.

[22] Thummerer, A., Seller Oria, C., Zaffino, P. et al., Med. Phys., 49 (2022) 6824–6839.

[23] Seller Oria, C., Thummerer, A., Free, J. et al., Med. Phys., 48 (2021) 4498–4505.

[24] Vanzi, E., Bruzzi, M., Bucciolini, M., Cirrone, G., Civinini, C., Cuttone, G. et al., Nucl. Instrum. Methods Phys. Res. A, 730 (2013) 184–190.

[25] Davies, J., Heuer, P., Bott, A., High Energy Density Phys., 49 (2023) 101067.

[26] Pearcy, J., Rosenberg, M., Johnson, T., Sutcliffe, G., Reichelt, B., Hare, J., Loureiro, N., Petrasso, R., Li, C., Phys. Rev. Lett., 132 (2024) 035101.

[27] Schaeffer, D., Fox, W., Follett, R., Fiksel, G., Li, C., Matteucci, J., Bhattacharjee, A., Germaschewski, K., Phys. Rev. Lett., 122 (2019) 245001.

[28] Li, C. et al., Phys. Rev. Lett., 123 (2019) 055002.

[29] Heuer, P., Leal, L., Davies, J. et al., Phys. Plasmas, 29 (2022) 072708.

[30] Tubman, E. et al., Nat. Commun., 12 (2021).

[31] Daido, H., Nishiuchi, M., Pirozhkov, A., Rep. Prog. Phys., 75 (2012) 056401.

[32] d'Humieres, E., Brantov, A., Bychenkov, V., Tikhonchuk, V., Phys. Plasmas., 20 (2013) 023103.

[33] Dover, N. et al., Phys. Rev. Lett., 124 (2020) 084802.

[34] Cristoforetti, G. et al., Sci. Rep., 7 (2017) 1479.

[35] Gizzi, L. et al., Appl. Sci., 7 (2017) 984.

[36] Gizzi, L. et al., Nucl. Instrum. Methods Phys. Res. A, 909 (2018) 160.

[37] Calestani, D., Villani, M., Cristoforetti, G., Brandi, F., Koester, P., Labate, L., Gizzi, L., Matter Radiat. Extremes, 6 (2021) 046903.

[38] Malko, S., Johnson, C., Schaeffer, D., Fox, W., Fiksel, G., Appl. Opt., 61 (2022) C133.

[39] Johnson, C., Malko, S., Fox, W., Schaeffer, D., Fiksel, G., Adrian, P., Sutcliffe, G., Birkel, A., Rev. Sci. Instrum., 93 (2022) 023502.

[40] Lysakovski, P., Besuglow, J., Kopp, B., Mein, S., Tessonnier, T., Ferrari, A. et al., Med. Phys., 50 (2023) 2510.

[41] Bashir, U., Siddique, M., Mclean, E., Goh, V., Cook, G., AJR, 207 (2016).

Volume 18, Number 5, 2025. pp. 725-736

Jordan Journal of Physics

ARTICLE

Electrospinning of PVA-PEG Blend with Various Cu_2O Nanoparticle Additives: Structural and Dispersion Properties

Akeel S. Alkelaby[a], **Khansaa S. Sharba**[a], **Maher H. Rasheed**[b] and **Khalid H. Abass**[c]

[a] *The General Directorate of Education in Babil, Ministry of Education in Iraq, Iraq.*

[b] *Department of Science, College of Basic Education, University of Babylon, Hilla, Iraq.*

[c] *Physics Department, College of Education for Pure Sciences, University of Babylon, Iraq.*

Doi: **https://doi.org/10.47011/18.5.12**

Received on: 21/02/2025; *Accepted on: 17/07/2025*

Abstract: This project entailed the synthesis of novel nanofibers by the electrospinning technique. The nanofibers included Poly (vinyl alcohol) (PVA) and polyethylene glycol (PEG) doped with different concentrations (0.002, 0.004, 0.006) of copper oxide (Cu_2O) at room temperature. Images from the optical microscope (OM) revealed a fine and homogenous dispersion of the nanomaterials. This was corroborated by Scanning Electron Microscopy (SEM) analysis, which showed that the delicate fibers in both the polymer blend and doped samples were randomly distributed and no signs of nanoparticle aggregation were detected. Prior to the incorporation of the Cu_2O additive, the nanofibers demonstrated an average diameter of 68.97 nm, while the inclusion of Cu_2O at varying concentrations yielded average diameters of 64.14 nm for 0.002 g, 71.35 nm for 0.004 g, and 68.46 nm for 0.006 g. Notably, these nanofibers maintained a smooth surface morphology across all samples. The transmittance progressively decreases, starting at a value of 0.996 for the unmodified PVA-PEG blend and reducing to 0.978 as the Cu_2O concentration reaches 0.006. Concurrently, the extinction coefficient demonstrates increase, rising from 0.001027 to 0.00475 with higher Cu_2O content. Similarly, the real part of the dielectric constant increases from 1.4559 to 2.1044, while its imaginary part expands from 0.00247 to 0.0137. The Wemple-DiDomenico model was utilized to compute the dispersion coefficients, comprising E_o, E_d, n_o, M_{-1}, and M_{-3}.

Keywords: PVA-PEG-Cu_2O, Nanofiber, Electrospinning, SEM, Dispersion parameters.

Introduction

Polymers have rapidly become an indispensable component of modern life, owing to their versatility, affordability, low operational expenses, ease of processing, and desirable chemical, physical, and optical properties [1]. A polymer is comprised of countless molecules, each including thousands atoms held together with covalent bonds. In addition, the molecules in a polymer are attracted to each other by various forces depending on the type of polymer [2]. Like conventional composites, a nanocomposite is made of a matrix and filler. But nanocomposites use nanoparticle fillers instead of fiber fillers used in conventional composites such as carbon or fiberglass [3]. Examples of the former include CNTs, carbon nanofibers, and other semiconductor or metal nanoparticles such as silicon, gold, silver, diamond, and copper [4]. Polymer nanofibers are an important category of nanostructured materials, with potential uses in numerous fields such as biology, electronics, medicine, protective gear, and water treatment. Recent advancements in preparation techniques such as phase separation, electrospinning, drawing, and template synthesis have enabled improvement in

Corresponding Author: Khalid Haneen Abass **Email**: pure.khalid.haneen@uobabylon.edu.iq

production processes and expanded the range of possible applications [5]. Electrospinning technique is particularly renowned for its simplicity, low expense, flexibility, and ability to manufacture one-dimensional nanostructured materials. Among all the various techniques one can use for producing such materials inexpensively and with versatility, electrospinning is particularly worth mentioning [6].

PVA or polyvinyl alcohol is increasingly being known as a highly promising polymer with some mind-boggling properties. They are characterized by good water solubility, good dielectric strength, chemical stability, and environmental friendliness. The hydroxyl groups in PVA facilitate the formation of strong interlinks in polymer composites through hydrogen bonding [7]. Poly vinyl alcohol, or PVA, is commonly used in various industries such as electronics, construction, medicine, and others. The reason is that the polymer has numerous advantages such as its water solubility and exceptional flexibility, which make it highly versatile and effortless to apply across a wide range of industrial purposes. Additionally, it is regarded as safe for both medical and food-related applications [8].

Polyethylene glycol, or PEG, is a common polymer that is widely in demand due to its availability, low cost, and safety [9]. Polyethylene glycols, or PEGs, are a family of polymers containing a variety of properties which may be liquid or solid [10]. To enhance the elasticity, additional polymers can be incorporated for the same. Utilization of plasticizers relaxes the molecular rigidity by decreasing the intermolecular forces along the polymer chain [11].

Cuprous Oxide (Cu_2O) has come into new focus for several technological applications based on its optoelectronic properties [12, 13]. The Pn3m is the space group of Cu_2O with the unit cell consisting of two copper, and four oxygen ions. These are placed with oxygen atoms in a body center cubic enclosed lattice with tetrahedrally surrounding copper ions [14]. The Cu_2O is considered an excellent photovoltaic material due to the abundance of copper on Earth, its high theoretical energy conversion efficiency of approximately 20%, its non-toxic nature, and its cost-effective production. The other reason for using Cu2O as an absorber is due to its high absorption coefficient in the visible region and its direct bandgap nature of 2.1 eV [15-17]. In recent years, Cu_2O has attracted considerable attention because of its promising applications in lithium-ion batteries [18], nanomagnetic devices [19], photocatalysis [20], transistors [21], gas sensors 22] photodetector [23] and solar cell 24,25]. In this study, we report the electrospinning fabrication of PVA-PEG-Cu2O nanofibers, and investigate their optical properties and dispersion parameters for application as a promising candidate for communication and optical devices.

Experimental

Preparation of PVA-PEG/ Cu_2O Nanofibers

In order to synthesize 2 g of PVA-PEG polymer nanofibers, the process was initiated by dissolving 1.6 g of PVA powder in 60 mL distilled water using a glass flask with a magnetic stirrer. After 45 minutes of stirring at 90 °C, the solution was completely homogenized. To this 0.4 gram of PEG was added dropwise at 90 °C.The blending was continued for a further 45 minutes until a hick homogeneous solution formed. The stirring of suspension was continued during the process to increase homogeneity. Afterwards, three portions of Cu2O (0.002; 0.004 and 0.006 g) were added into the solution while, every portion was sonicated for two minutes to disperse it throughout the mixture. After each addition of Cu2O, the mixture was left stirring for 45 min for good dispersion. As shown in Table 1, the resultant mixture was then utilized for electrospinning to produce (PVA-PEG) nanofibers with varied degrees of Cu_2O additions.

TABLE 1. Weight of PVA-PEG- Cu_2O nanocomposites.

PVA (g)	PEG (g)	Cu_2O (g)
1.6	0.4	0.0
1.6	0.4	0.002
1.6	0.4	0.004
1.6	0.4	0.006

Electrospinning Process

The solution was inserted into a 2 mL syringe that was outfitted with a stainless-steel needle after it had been thoroughly mixed. The hypodermic was subsequently positioned in front of a metal collector that was horizontally oriented. During the electrospinning process, the needle tip served as the positive electrode, while the metal collector served as the negative electrode. To make material deposition easier, the collector was covered with aluminum foil. The spinning parameters are specified in Table 2, and the electrospinning was performed at room temperature.

TABLE 2. Electrospinning Parameters for Specimen Fabrication.

Electrospinning parameters	Specification
applied voltage	24 KV
Collector distance	10 cm
Orifice size	0.7 mm
rotation speed	500 rpm
temperature	25 °C
flow rate	0.5 ml/hr

Results and Discussion

Fig.1, Table 1 shows SEM micrographs of PVA-PEG polymer blend and Cu_2O embedded in the PVA-PEG composite at concentration of 0.002, 0.004 and 0.006 magnification at x20kV and x110Kv respectively. These pictures corroborate the analysis of surface topology of the samples and distribution of Cu_2O in polymer matrix.

The average fiber diameter was 68.97 nm before use of Cu_2O. The fiber diameters were between 64.14 and 68.46 nm after the Cu2O loading determined by ImageJ software. The nanofibers had a smooth surface, while the microfibers were irregularly distributed as well as having crossing points. The stability of the liquid filament in the process of electrospinning depends mainly on molecular entanglement [26] that is an important factor for fibre structuring and homogeneity in this technique. During electrospinning, changes in fiber morphology and/or bead formation can occur as a result of interactions between solution characteristics and experimental conditions. The structure differences may be affected by the polymer-related parameters such as molecular weight, polydispersity index, glass transition temperature (Tg), isomeric structures and cross-linking.

These might also be associated with the solution (eg, composition of solvent, concentration, viscosity, electrical conductivity and dielectric strength as well as surface tension of the liquid), process (like magnitude of applied field strength, distance for deposition etc.), 42 - 44 like flow rate or electric current passed through an instrument or deposition time) or postdeposition treatment. [27]. The influence of various parameters on the morphology of electrospun polymers is illustrated in Fig. 2 [28]. Among the various electrospinning parameters, the concentration of the polymer solution plays a crucial role in fiber generation. The solution is characterized by reduced viscosity and increased surface tension when the concentration is insufficient, which leads to the formation of polymeric micro- or nanoparticles through electrospray rather than fiber development [29]. Conversely, a minor increase in concentration results in a blend of fibers and pearls. But the production of silky and homogenous nanofibers is successful if the concentration is at an optimal level [30]. Electrospun fiber morphology is also significantly influenced by viscosity. Continuous and uniform filaments are significantly opposed by low viscosity, and high viscosity can oppose the expulsion of the liquid projectile out of the solution. Proper viscosity should thus be achieved for the successful completion of electrospinning [31, 32].

Also, surface tension, which is dominated by the solvent component in large part, is one of the critical parameters for electrospinning [33]. It is well known that the shear viscosity of the mixture determines the typical diameter of nanofibers produced by electrospinning. As viscosity increases, nanofibers of greater diameters will tend to be formed, as in Eq. (1) [34]. Briefly, the diameter and morphology of nanofibers generated through electrospinning are significantly influenced by the polymer solution's viscosity and concentration and surface tension. To achieve the desired fiber properties in electrospinning, one has to achieve

an appropriate balance between these parameters.

$$d \sim \eta^{\lambda} \quad (1)$$

The given Eq. (1) establishes the connection between the average electro spun fiber diameter (d), the solution's shear viscosity (η), and the yielding exponent (λ). The exact value of the yielding exponent (λ) differs based on the particular polymer solution used, however it is usually more than 1/3 as per the scaling equation [35].

Both the voltage and viscosity of the polymer solution should be maintained within a range that is optimal for efficient electrospinning. Some factors like polymer concentration, solution flow rate, working distance, and applied voltage in the electrospinning device all together control the production of uniform morphology continuous fibers with minimal bead formation. However, extremely high solution concentration has a negative influence on the production of nanofibers as improper levels of viscosity may hinder fiber formation [36].

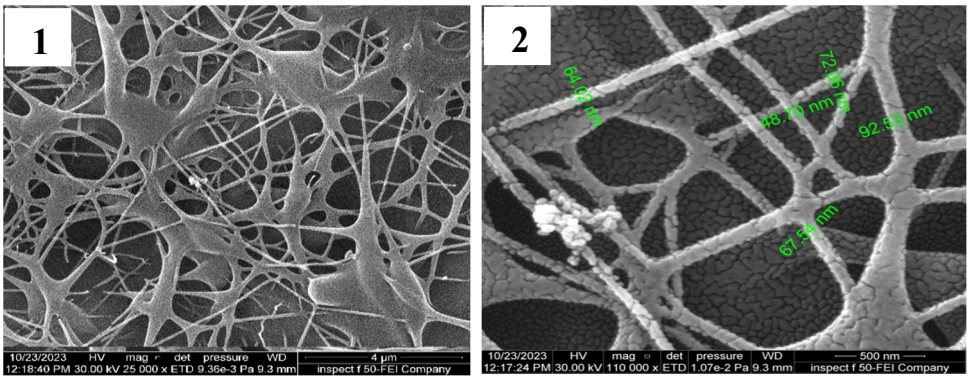

FIG. 1(A). The scanning microscopy pictures of PVA-PEG nanofibers taken at two different magnifications, 25 kx and 110 kx.

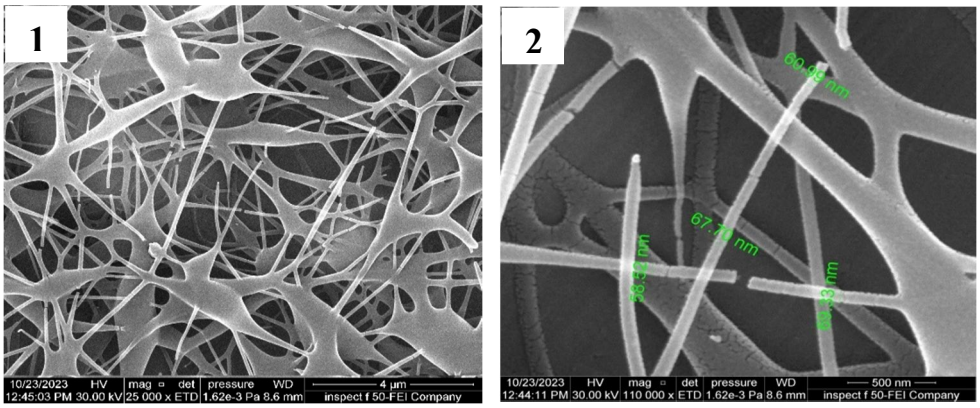

FIG. 1(B). Scanning electron micrographs taken at two different magnifications, 25 kx and 110 kx, of electrically spun PVA-PEG nanofibers containing 0.002 g Cu_2O.

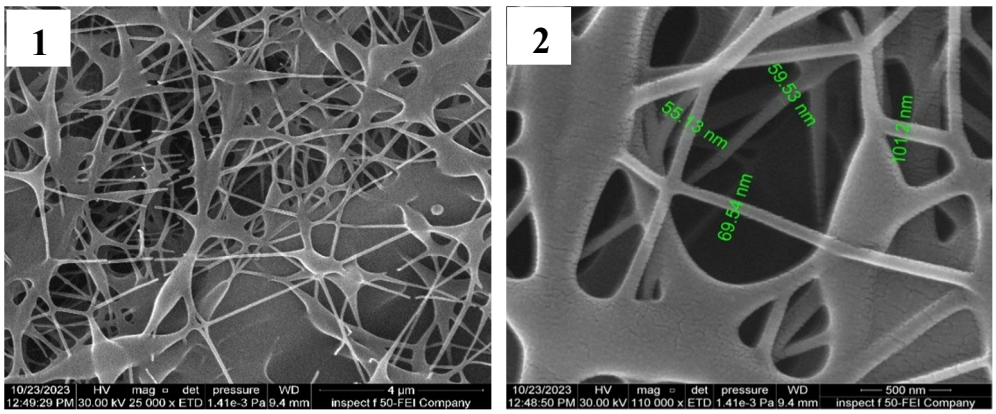

FIG. 1(C). Scanning electron micrographs taken at two different magnifications, 25kx and 110 kx, of electrospun PVA-PEG nanofibers containing 0.004 g Cu_2O.

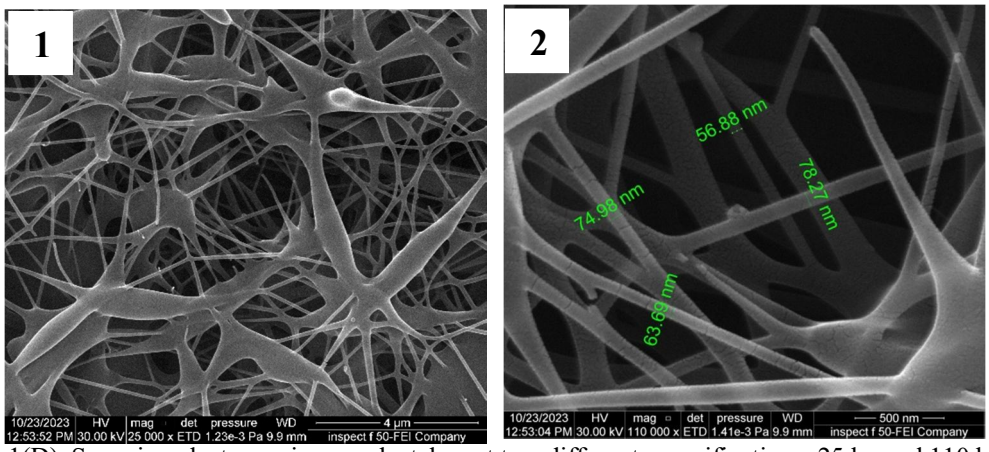

FIG. 1(D). Scanning electron micrographs taken at two different magnifications, 25 kx and 110 kx, of electrically spun PVA-PEG nanofibers containing 0.006 g Cu_2O.

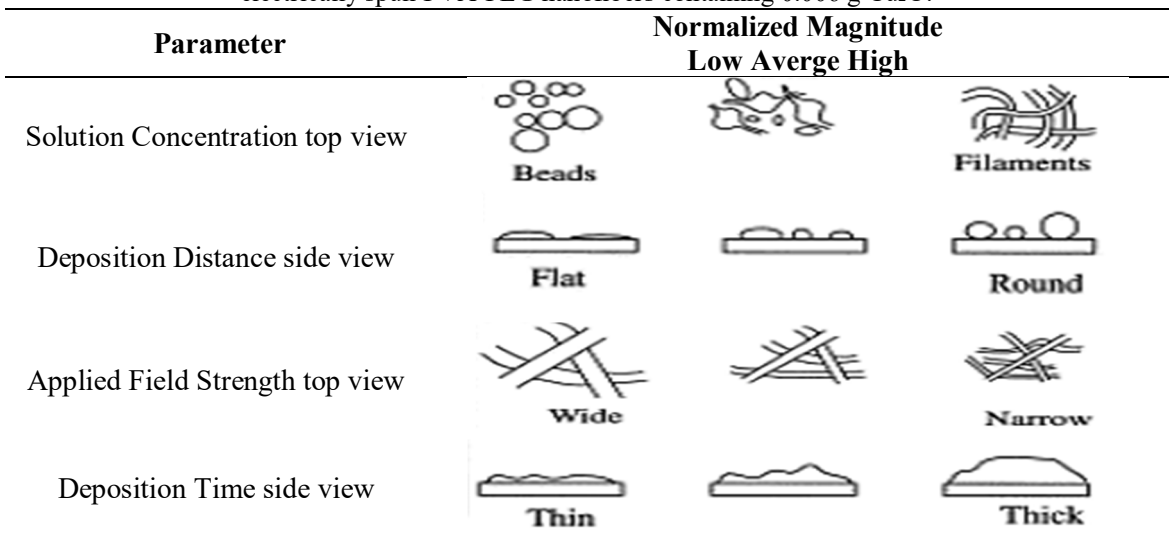

FIG. 2. a schematic representation of the impact of process parameters on the electro spun product's structure.

The optical microscope (OM) images verify the successful fabrication of PVA-PEG- Cu_2O nanofibers using the casting method. These images expose a uniform matrix with Cu_2O evenly distributed throughout the polymer blend composites. In particular, Fig. 3(a) displays the PVA-PEG blend, signifying the effective dissolution of the polymers. Parts (b, c, and d) of Fig. 3 illustrate the diffusion of Cu_2O within the PVA-PEG blend, revealing a well-dispersed distribution of nanoparticles within the blend.

Importantly, there is no nanoparticle aggregation observed to be due to the interaction between polymers and Cu2O as a result of high surface area volume ratio. At a Cu2O nanofiber weight, or loading, of 0.006 a network of pathways are established for charge carriers to transport via. This results in alteration of the material characteristics [37].

The transmittance spectra (T) were calculated by [38]:

$$T = I_T/I_o \quad (2)$$

where I_T is the intensity of transmitted rays from the film and I_o intensity of incident rays on the film.

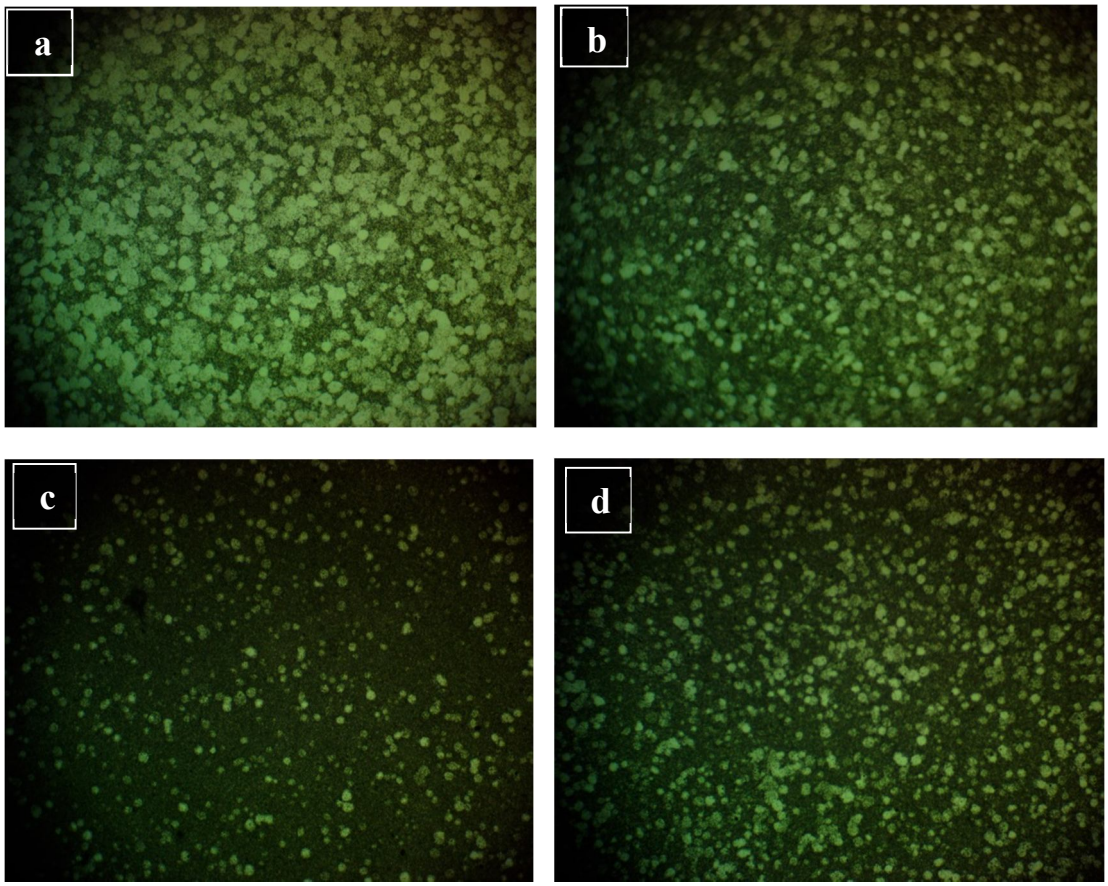

FIG. 3. Photomicrographs (100X) of (PVA- PEG) with add various content of Cu_2O: (A) 0 Cu_2O (B) 0.001 Cu_2O (C) 0.002 Cu_2O and (D) 0.003 Cu_2O.

Figure 4 presents the transmittance (T) spectra of PVA-PEG-Cu_2O nanofibers with varying concentrations of Cu_2O as a function of wavelength. Unlike the absorption spectra, the transmittance decreases progressively, starting from 0.996 for the pure PVA-PEG blend and lowering to 0.978 as the Cu_2O concentration increases up to 0.006. This observed reduction in transmittance is attributed to the incorporation of Cu_2O, which contains electrons capable of absorbing electromagnetic energy and transitioning to higher energy states. In contrast, the pure PVA-PEG sample shows significantly high transmittance due to the absence of particles. Without free electrons, such a sample requires much higher energy for electronic transitions or bond disruption [39].

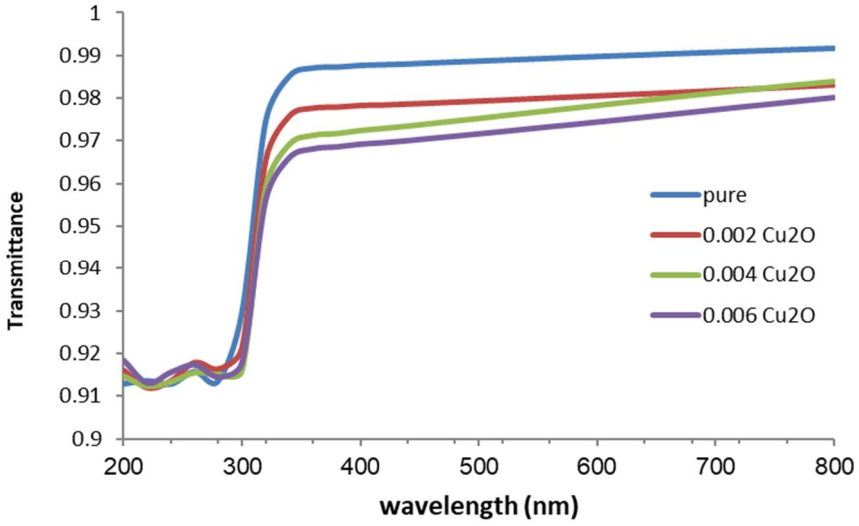

FIG. 4. The transmittance versus wavelength of PVA-PEG blend and PVA-PEG-Cu_2O Nanocomposites.

The extinction coefficient (k_o) was calculated by [40]:

$$k_o = \alpha\lambda/4\pi \quad (3)$$

Figure 5 shows the extinction coefficient (k_o) for PVA-PEG- Cu_2O nanofibers across a range of wavelengths. It shows a marked increase with higher concentrations of Cu_2O. This trend can be ascribed to the enhanced optical absorption and photon dispersion within the as the concentration of Cu_2O increases, the PVA-PEG polymer composite increases. The nanofiber samples' substantial absorbance within this range is the primary reason for the extinction coefficient's elevated values in the UV region. As a result, the nanofibers' extinction coefficient is notably pronounced at UV wavelengths. Although the absorption coefficient of the nanofibers remains relatively consistent from the visible to the near-infrared spectrum, the extinction coefficient exhibits an upward trend as the wavelength increases [41].

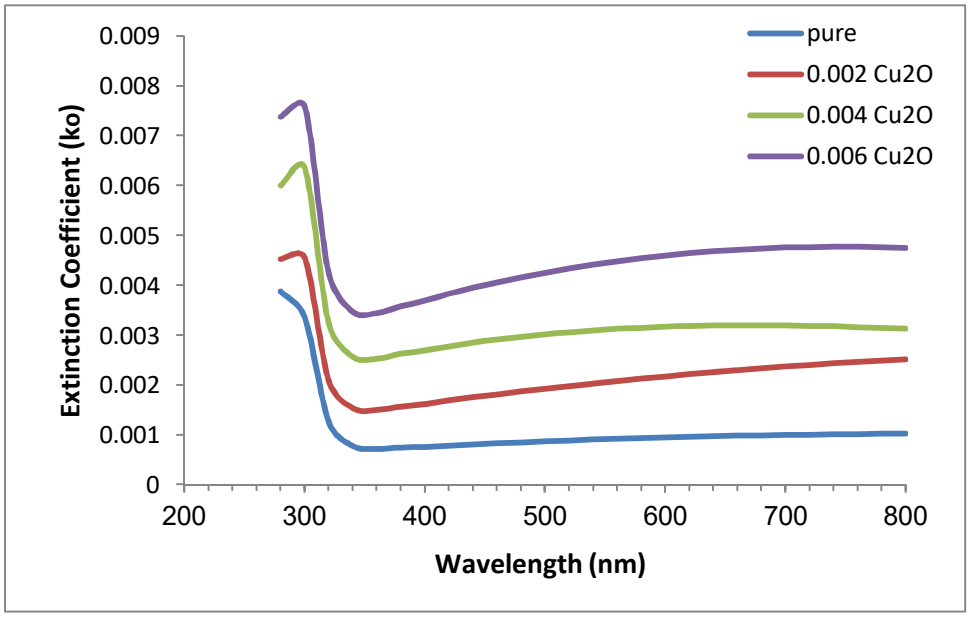

FIG. 5. The extinction coefficient versus wavelength of PVA-PEG blend and PVA-PEG -Cu_2O Nanocomposites.

Dielectric constants for two parts real (ε_1) and imaginary (ε_2) were calculated by [42]:

$$\varepsilon_1 = n^2 - k_0^2 \quad (4)$$

$$\varepsilon_2 = 2n\,k_0 \quad (5)$$

The dielectric constant is the basic source of information about the electronic band structure of materials. Slowing down light in a material is associated with the real part of the dielectric constant (ε_1), while the imaginary part (ε_2) is a key optical parameter linked to both the refractive index and the extinction coefficient.

Figures 6 and 7 show the variation of real and imaginary parts of the dielectric constant for PVA-PEG-Cu_2O nanofibers with wavelength and Cu_2O concentration.

It can be seen that both parts of the dielectric constant increase with the rise in Cu_2O concentration. This is because there is increased electrical polarization in the nanofibers, which results from the higher concentration of Cu_2O in the sample. This results in the increase in charges in the polymers that make up both the PVA-PEG blends and the PVA-PEG-Cu_2O nanofibers proportionally. The two figures also show the changes in real and imaginary part of dielectric constant versus wavelengths. This behavior is primarily due to ε1 depending more on the refractive index, and less on the extinction coefficient. In contrast, the absorbance value of the imaginary part (ε2) is significantly influenced by an increased extinction coefficient depending on wavelength and less by a refractive index that remains relatively constant, particularly in the visible and near-infrared regions. [43, 44].

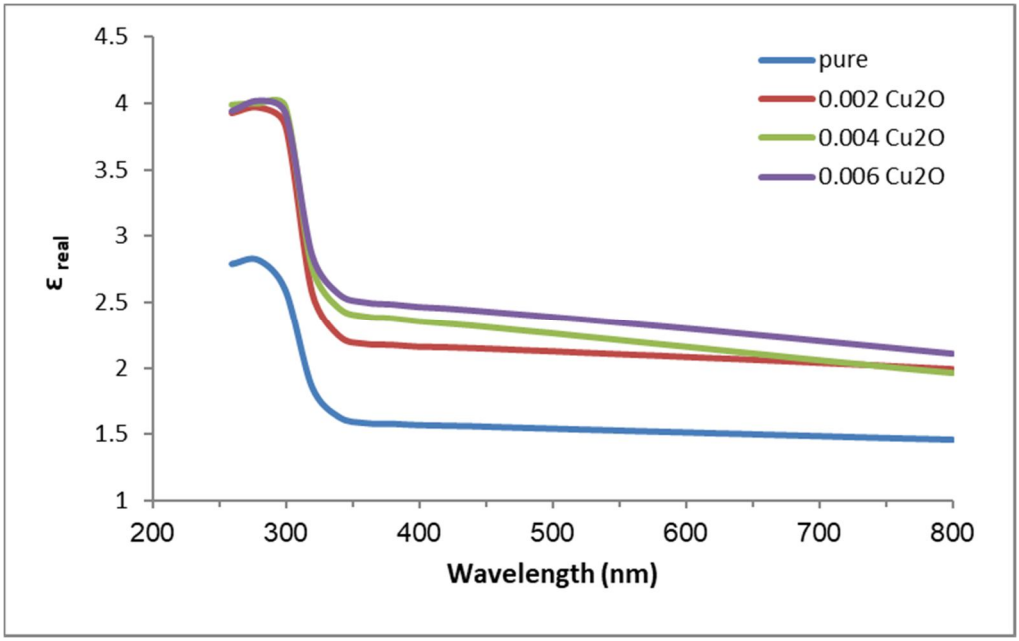

FIG. 6. The real dielectric constant with the wavelength of PVA-PEG blend and PVA- PEG-Cu_2O nanocomposites.

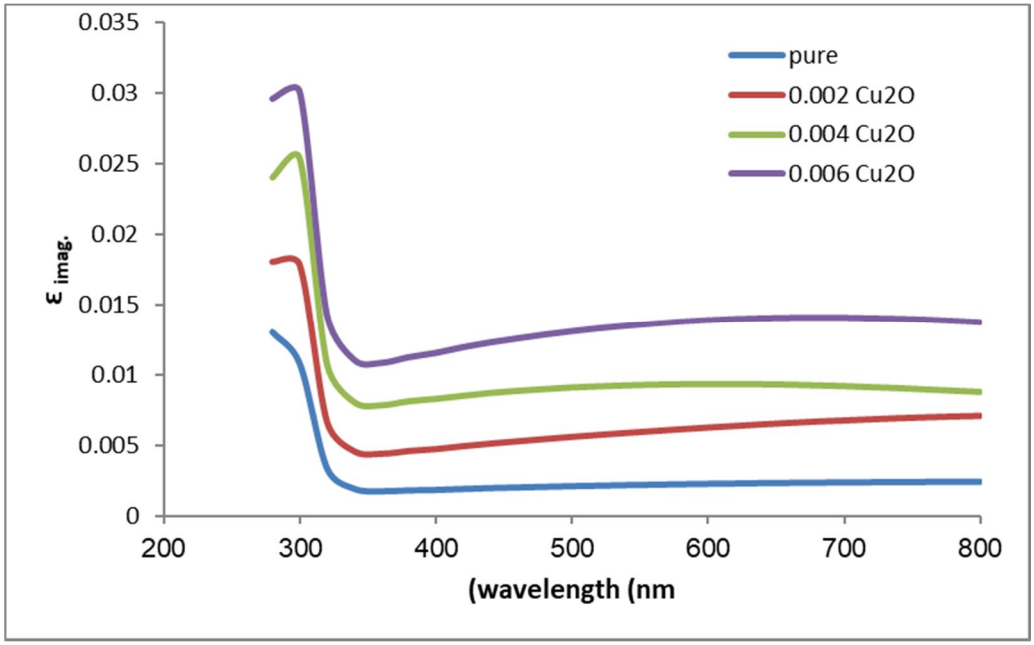

FIG. 7. The imaginary dielectric constant with the wavelength of PVA- PEG blend and PVA- PEG -Cu_2O nanocomposites.

Dispersion Parameters

The refractive index dispersion of materials has been analyzed using the single-oscillator model, which introduces the energy parameters E_d (dispersion energy) and E_o (oscillator energy). According to the Wemple and DiDomenico model, the refractive index (n) at a given photon energy *(hv)* can be expressed for both PVA-PEG blend and PVA-PEG-Cu_2O nanofibers. From the equations (6-10) the values E_o, E_d, E_g, n_0, ε_∞, M_{-1} and M_{-3} were calculated [45-49].

$$(n^2 - 1) = \frac{E_d E_o}{{E_o}^2 - (h\upsilon)^2} \quad (6)$$

$$n_0^2 = 1 + \frac{E_d}{E_o} \quad (7)$$

$$\varepsilon_\infty = n_0^2 \quad (8)$$

$$E_o^2 = \frac{M_{-1}}{M_{-3}} \quad (9)$$

$$E_d^2 = \frac{M_{-1}^3}{M_{-3}} \quad (10)$$

From the graphic representation of the relationship between $(n^2 - 1)^{-1}$ and $(h\upsilon)^2$ in

Fig. 8 used the slope $(E_0\ E_d)^{-1}$ and the intercept $(\frac{E_0}{E_d})$ to determine E_0 and E_d. Table 3 contained the calculated value, which demonstrated a decline in their values when (Cu_2O)NPs concentrations increased, the oscillator strength (E_o) and the dispersion energy linked with the energy of optical transitions (E_d) are shown to decrease as (Cu_2O)NPs increases, but the other parameters n_0, ε_∞ $M_{-1}$and M_{-3} increase. This phenomenon can be attributed to the shift of the optical transmission spectra toward longer wavelengths, which corresponds to the absorption edge shifting toward lower energy wavelengths and rise in nanomaterials' concentration results in a reduction in interparticle spacing, thereby intensifying interparticle interactions, which leads to a decrease in dispersion-related parameters. Additionally, elevated concentrations of nanomaterials significantly influence the material's optical characteristics, further contributing to variations in the dispersion parameters. The calculated optical energy gap (the approximation relation $E_o \approx 2E_g$) using the Tauc relation and the Wemple-DiDomenico estimate both had similar values. The findings concur with those of earlier researchers [50].

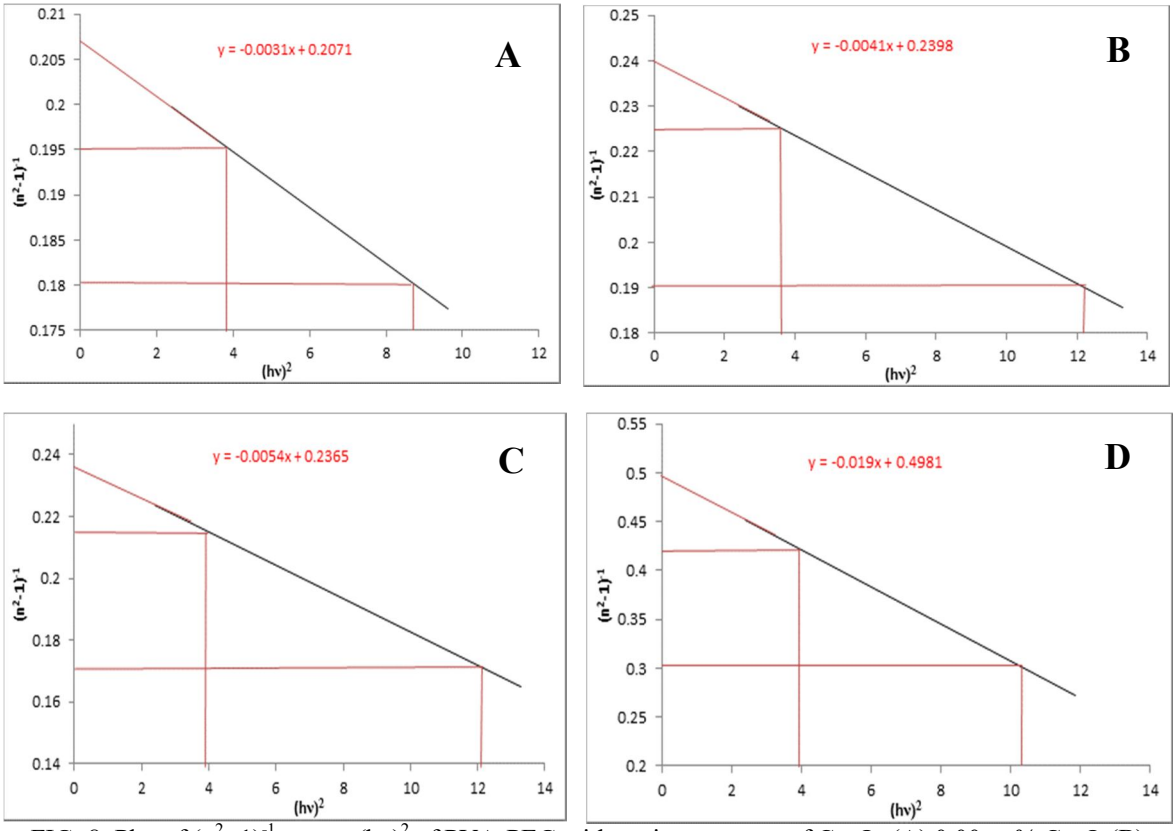

FIG. 8. Plot of $(n^2 -1)^{-1}$ versus $(h\upsilon)^2$ of PVA-PEG with various content of Cu_2O: (A) 0.00wt.% Cu_2O (B) 0.002wt.% Cu_2O (C) 0.004wt.% Cu_2O and (D) 0.006wt.% Cu_2O.

TABLE 3. Optical parameters of PVA-PEG -Cu_2O nanofibers.

parameter	0 wt.	0.002wt. Cu_2O	0.004wt. Cu_2O	0.006wt. Cu_2O
E_o	67.62	57.600	42.426	26.541
E_o	8.223	7.589	6.513	5.151
slope	0.003	0.004	0.005	0.018
E_g	4.111	3.794	3.256	2.575
E_d	39.725	31.622	27.367	10.514
n(0)	5.830	5.166	5.201	3.040
$n_o(0)$	2.414	2.273	2.280	1.743
ε	5.830	5.166	5.201	3.040
M_{-1}	4.830	4.166	4.201	2.040
M_{-3}	0.071	0.0723	0.099	0.076

Conclusion

Nanofibers of PVA-PEG-Cu_2O were synthesized with success by refining the electrospinning parameters, which included the careful adjustment of the spinning solution composition, applied voltage, spinning distance, and flow rate. Before incorporating Cu_2O, the nanofibers had an average diameter of 68.97 nm. The integration of Cu_2O resulted in average diameters ranging from 64.14 nm to 68.46 nm. Scanning electron microscopy analyses validated the presence of a smooth surface morphology in these fibers, while optical microscopy images revealed a homogenous distribution of the nanomaterial throughout the samples. The transmittance exhibited a gradual decrease, beginning at 0.996 for the pur PVA-PEG blend, and declining to 0.978 when the Cu_2O concentration increased to 0.006. Additionally, the extinction coefficient displayed a rising trend, increasing from 0.001027 to 0.00475 with higher Cu_2O content. The real part of the dielectric constant increased from 1.4559 to 2.1044, and the imaginary part grew from 0.00247 to 0.0137 as the concentration of Cu_2O augmented. Moreover, dispersion parameters, such as E_o, E_d, n_o, M_{-1}, and M_{-3}, were calculated utilizing the Wemple-DiDomenico model. These findings concerning dispersion parameters are instrumental in advancing the design and fabrication of optical devices.

Author Contribution Statement

Akeel Shakir Alkelaby, Khansaa Saleem Sharba, Maher Hassan Rasheed, and Khalid Haneen Abass contributed equally to this work. Akeel Shakir Alkelaby and Khansaa Saleem Sharba were primarily responsible for the study's conceptualization, design, methodology development, and data analysis. Maher Hassan Rasheed and Khalid Haneen Abass focused on the experimental work, data collection, and initial manuscript drafting. All authors participated in the review and editing process, provided critical revisions, and approved the final version.

Funding

This research received no specific grant from any funding agency in the public, commercial, or not-for-profit sectors.

Data Availability Statement

I have read and accept the terms of the Share Upon Reasonable Request data policy.

Statements and Declarations

This paper reports on a detailed study of the electrospinning of PVA-PEG blend matrices which contain Cu_2O nanoparticles in various additives with an emphasis on their structure and dispersion behaviour.

Competing interests

The authors have declared that no competing interests exist.

Acknowledgement

The authors are thankful to the staff at Babylon University for their cooperation and support.

References

[1] Radwan, R.M., J. Phys. D. Appl. Phys., 40 (2) (2007) 374.

[2] Al Asadi, S.M., Hamood, F.J., Abass, K.H., Mohammed, S.K., Hassan, I.M., and Latif, D.M.A., Research Journal of Pharmacy and Technology, 12 (6) (2019) 2768.

[3] Robertson, J., Materials Today, 7 (2004) 46.

[4] Devangamath, S.S. et al., J. Mater. Sci. Mater. Electron., 31 (2020) 2904.

[5] Beachley, V. and Wen, X., Prog. Polym. Sci., 35 (2010) 868.

[6] Shenoy, K.A., M.Sc. Thesis, Department of Mechanical Engineering, Wichita State University (2008).

[7] Ben Doudou, B., Vivet, A., Chen, J., Laachachi, A., Falher, T., and Poilâne, C., J. Polym. Res., 21 (4) (2014) 1.

[8] Abdali, K., Al-Bermany, E., and Abass, K.H., J. Polym. Res., 30 (4) (2023) 138.

[9] Abu-Zied, B.M. and Asiri, M.A., Int. J. Electrochem. Sci., 10 (6) (2015) 4873.

[10] Chieng, B.W., Ibrahim, N.A., Yunus, W.M.Z.W., and Hussein, M.Z., Polymers, 6 (2014) 93.

[11] Abass, K.H. and Hamed, A., J. Green Eng., 10 (7) (2020) 4166.

[12] Sawant, S.S., Bhagwat, A.D., and Mahajan, C.M., J. Nano-Electron. Phys., 8 (1) (2016) 01035(1-5).

[13] Jayathilaka, C., Kumara, L.S.R., Ohara, K., Song, C., Kohara, S., Sakata, O., Siripala, W., and Jayanetti, S., Crystals, 10 (2020) 609.

[14] Isah, K.U., Bakeko, M., Ahmadu, U., Uno, U.E., Kimpa, M.I., and Yabagi, J.A., IOSR J. Appl. Phys., 3 (2) (2013) 61.

[15] Gevorkyan, V.A., Reymers, A.E., Nersesyan, M.N., and Arzakantsyan, M.A., Int. Symp. Optics and Its Applications (OPTICS2011), 350 (2012) 012027.

[16] Umar, M., Swinkels, M.Y., De Luca, M., Fasolato, C., Moser, L., Gadea, G., Marot, L., Glatzel, T., and Zardo, I., Thin Solid Films, 732 (2021) 138763.

[17] Abbas, A. and Abass, K.H., Mater. Today: Proc., 60 (2022) 1402.

[18] Wei, H.M., Gong, H.B., Chen, L., Zi, M., and Cao, B.Q., J. Phys. Chem. C, 116 (19) (2012) 10510.

[19] Bai, Y., Yang, T., Gu, Q., Cheng, G., and Zheng, R., Powder Technol., 227 (2012) 35.

[20] Tuama, A.N., Abass, K.H., and Bin Agam, M.A., Int. J. Nanoelectron. Mater., 13 (3) (2020) 601.

[21] Salek, G., Tenailleau, C., Dufour, P., and Guillemet-Fritsch, S., Thin Solid Films, 589 (2015) 872.

[22] Lupan, O. et al., Sens. Actuators B Chem., 224 (2016) 434.

[23] Lee, W-J. and Wang, X-J., Coatings, 11 (2021) 864.

[24] Siol, S. et al., ACS Appl. Mater. Interfaces, 8 (33) (2016) 21824.

[25] Alkelaby, A.S. et al., J. Glob. Pharma Technol., 11 (4) (2019) 347.

[26] Talafha, M.F., Shaltoutb A.M.K., Abdelkawy A.G.A., and Behearyn M. Jordan Journal of Physics,18 (4) (2025) 551.

[27] Jose, J., Al-Harthi, M.A., AlMa'adeed, M.A.A., Dakua, J.B., and De, S.K., J. Appl. Polym. Sci., 132 (16) (2015).

[28] Mousa, M.S. and Hagmann, M.J. Jordan Journal of Physics, 18(4) (2025) 455.

Schubert, D.W., Macromol. Theory Simul., 28 (2019) 1900006.

[29] Wang, Q. et al., Anal. Chim., 2018 (2018) 125.

[30] Jia, Y.T., Gong, J., Gu, X.H., Kim, H.Y., Dong, J., and Shen, X.Y., Carbohydr. Polym., 67 (2007) 403.

[31] Rasheed, M.H., Hashim, F.S., and Abass, K.H., Int. J. Nanosci., 22 (3) (2023).

[32] Qader, K.Y., Ghazi, R.A., Jabbar, A.M., Abass, K.H., and Chiad, S.S., J. Green Eng., 10 (10) (2020) 7387.

[33] Zhang, M., Liu, Y.J., Xu, T.Y., and Sun, D.H., Adv Material Res, 332 (2011).

[34] Sharba, K.S., Alkelaby, A.S., and Abass, K.H., Plasmonics, 20 (2025) 6807.

[35] Mohammed, H.R.A., Al-Ogaili, A.O.M., and Abass, K.H., Mater. Today: Proc., 80 (2023) 2396.

[36] Alkelaby, A.S., Ahmadi, M.T., Esmaeili, A., Sedghi, H., and Abass, K.H., Polym. Bull., 81 (2024) 17377.

[37] Sakhil, M.D., Shaban, Z.M., Sharba, K.S., Habubi, N.F., Abass, K.H., Chiad, S.S., and Alkelaby, A.S., NeuroQuantology, 18 (5) (2020) 56.

[38] Chiad, S.S., Alkelaby, A.S., and Sharba, K.S., J. Glob. Pharma Technol., 11 (7) (2019) 662.

[39] Da Silva, M.A., Crawford, A., Mundy, J., Martins, A., Araújo, J.V., Hatton, P.V., Reis, R.L., and Neves, N.M., Tissue Eng. Part A, 15 (2) (2009) 377.

[40] Abass, K.H. and Obaid, N.H., J. Phys. Conf. Ser., 1294 (2) (2019).

[41] Tuama, A.N., Abass, K.H., and Bin Agam, M.A., Optik, 247 (2021) 167980.

[42] Sharba, K.S., Alkelaby, A.S., and Abass, K.H., Revue des Composites et des Materiaux Avances, 35 (4) (2025) 643.

[43] Dwech, M., Habeeb, M., and Mohammed, A., Ukrainian Journal of Physics, 67 (10) (2022) 757.

[44] Kadim, A.M., Abass, K.H., Abdali, K., and Musa, S.J., Nano Biomedicine and Engineering, 16 (1) (2024) 119.

[45] Al-Shawabkeh, A.F., Elimat, Z.M., and Abushgair, K.N., J. Thermoplast. Compos. Mater., 36 (2023) 899.

[46] Sharba, K.S., Alkelaby, A.S., Sakhil, M.D., Abass, K.H., Habubi, N.F., and Chiad, S.S., NeuroQuantology, 18 (3) (2020) 66.

[47] Zbala, A.A.K., Al-Ogaili, A.O.M., and Abass, K.H., NeuroQuantology, 20 (2) (2022) 62.

[48] Abass, K.H. and Latif, D.M.A., Int. J. ChemTech Res., 9 (9) (2016) 332.

[49] Wemple, S.H. and DiDomenico, M., Phys. Rev. B, 3 (4) (1971).

[50] Mohemed, B.Y., Alasdi, S., Fakfry, S., Haneen Abass, K., and Mohammed Kadim, A., HORA 2023 - 2023 5th International Congress on Human-Computer Interaction, Optimization and Robotic Applications, Proceedings (2023).

الجداول: تعطى الجداول أرقاما متسلسلة يشار إليها في النص. ويجب طباعة كل جدول على صفحة منفصلة مع عنوان فوق الجدول. أما الحواشي التفسيرية، التي يشار إليها بحرف فوقي، فتكتب أسفل الجدول.

الرسوم التوضيحية: يتم ترقيم الأشكال والرسومات والرسومات البيانية (المخططات) والصور، بصورة متسلسلة كما وردت في النص.

تقبل الرسوم التوضيحية المستخرجة من الحاسوب والصور الرقمية ذات النوعية الجيدة بالأبيض والأسود، على ان تكون أصيلة وليست نسخة عنها، وكل منها على ورقة منفصلة ومعرفة برقمها بالمقابل. ويجب تزويد المجلة بالرسومات بحجمها الأصلي بحيث لا تحتاج إلى معالجة لاحقة، وألا تقل الحروف عن الحجم 8 من نوع Times New Roman، وألا تقل سماكة الخطوط عن 0.5 وبكثافة متجانسة. ويجب إزالة جميع الألوان من الرسومات ما عدا تلك التي ستنشر ملونة. وفي حالة إرسال الرسومات بصورة رقمية، يجب أن تتوافق مع متطلبات الحد الأدنى من التمايز (1200 dpi Resolution) لرسومات الأبيض والأسود الخطية، و 600 dpi للرسومات باللون الرمادي، و300 dpi للرسومات الملونة. ويجب تخزين جميع ملفات الرسومات على شكل (jpg)، وأن ترسل الرسوم التوضيحية بالحجم الفعلي الذي سيظهر في المجلة. وسواء أرسل المخطوط بالبريد أو عن طريق الشبكة (Online)، يجب أرسال نسخة ورقية أصلية ذات نوعية جيدة للرسومات التوضيحية.

مواد إضافية: تشجع المجلة الباحثين على إرفاق جميع المواد الإضافية التي يمكن أن تسهل عملية التحكيم. وتشمل المواد الإضافية أي اشتقاقات رياضية مفصلة لا تظهر في المخطوط.

المخطوط المنقح (المعدّل) والأقراص المدمجة: بعد قبول البحث للنشر وإجراء جميع التعديلات المطلوبة، فعلى الباحثين تقديم نسخة أصلية ونسخة أخرى مطابقة للأصلية مطبوعة بأسطر مزدوجة، وكذلك تقديم نسخة إلكترونية تحتوي على المخطوط كاملا مكتوبا على Microsoft Word for Windows 2000 أو ما هو استجد منه. ويجب إرفاق الأشكال الأصلية مع المخطوط النهائي المعدل حتى لو تم تقديم الأشكال إلكترونيا. وتخزن جميع ملفات الرسومات على شكل (jpg)، وتقدم جميع الرسومات التوضيحية بالحجم الحقيقي الذي ستظهر به في المجلة. ويجب إرفاق قائمة ببرامج الحاسوب التي استعملت في كتابة النص، وأسماء الملفات على قرص مدمج، حيث يعلَم القرص بالاسم الأخير للباحث، وبالرقم المرجعي للمخطوط للمراسلة، وعنوان المقالة، والتاريخ. ويحفظ في مغلف واقٍ.

حقوق الطبع

يُشَكِّل تقديم مخطوط البحث للمجلة اعترافاً صريحاً من الباحثين بأنّ مخطوط البحث لم يُنْشَر ولم يُقَدَّم للنشر لدى أي جِهَة أخرى كانت وبأي صيغة ورقية أو إلكترونية أو غيرها. ويُشترط على الباحثين ملء أنموذج يَنُصُّ على نقْل حقوق الطبع لتُصبح ملكاً لجامعة اليرموك قبل الموافقة على نشر المخطوط. ويقوم رئيس التحرير بتزويد الباحثين بإنموذج نقل حقوق الطبع مع النسخة المُرْسَلَة للتنقيح. كما ويُمنع إعادة إنتاج أيِّ جزء من الأعمال المنشورة في المجلّة من دون إذن خَطِّيٍّ مُسْبَق من رئيس التحرير.

إخلاء المسؤولية

إن ما ورد في هذه المجلة يعبر عن آراء المؤلفين، ولا يعكس بالضرورة آراء هيئة التحرير أو الجامعة أو سياسة اللجنة العليا للبحث العلمي أو وزارة التعليم العالي والبحث العلمي. ولا يتحمل ناشر المجلة أي تبعات مادية أو معنوية أو مسؤوليات عن استعمال المعلومات المنشورة في المجلة أو سوء استعمالها.

الفهرسة: المجلة مفهرسة في:

Scopus	**Emerging Sources Citation Index (ESCI)** Journal Impact Factor 2022 0.7
ULRICHSWEB GLOBAL SERIALS DIRECTORY	

معلومات عامة

المجلة الأردنية للفيزياء هي مجلة بحوث علميّة عالمية متخصصة مُحكمة تصدر بدعم من صندوق دعم البحث العلمي والابتكار، وزارة التعليم العالي والبحث العلمي، عمان، الأردن. وتقوم بنشر المجلة عمادة البحث العلمي والدراسات العليا في جامعة اليرموك، إربد، الأردن. وتنشر البحوث العلمية الأصيلة، إضافة إلى المراسلات القصيرة Short Communications، والملاحظات الفنية Technical Notes، والمقالات الخاصّة Feature Articles، ومقالات المراجعة Review Articles، في مجالات الفيزياء النظرية والتجريبية، باللغتين العربية والإنجليزية.

تقديم مخطوط البحث

تقدم المخطوطات إلكترونيًا عن طريق موقع المجلة: https://jjp.yu.edu.jo

ويجري تحكيمُ البحوثِ الأصيلة والمراسلات القصيرة والملاحظات الفنية من جانب مُحكِّمين اثنين في الأقل من ذوي الاختصاص والخبرة. وتُشَجِّع المجلة الباحثين على اقتراح أسماء المحكمين. أما نشر المقالات الخاصّة في المجالات الفيزيائية النَشِطَة، فيتم بدعوة من هيئة التحرير، ويُشار إليها كذلك عند النشر. ويُطْلَب من كاتب المقال الخاص تقديم تقرير واضح يتّسم بالدقة والإيجاز عن مجال البحث تمهيداً للمقال. وتنشر المجلةُ أيضاً مقالات المراجعة في الحقول الفيزيائية النشطة سريعة التغيُّر، وتُشَجّع كاتبي مقالات المراجعة أو مُستَكتبيها على إرسال مقترحٍ من صفحتين إلى رئيس التحرير. ويُرْفَق مع البحث المكتوب باللغة العربية ملخص (Abstract) وكلمات دالة (Keywords) باللغة الإنجليزية.

ترتيب مخطوط البحث

يجب أن تتم طباعة مخطوط البحث ببنط 12 نوعه Times New Roman، وبسطر مزدوج، على وجه واحد من ورق A4 (21.6 × 27.9 سم) مع حواشي 3.71 سم ، باستخدام معالج كلمات ميكروسوفت وورد 2000 أو ما استُجِدَ منه. ويجري تنظيم أجزاء المخطوط وفق الترتيب التالي: صفحة العنوان، الملخص، رموز التصنيف (PACS)، المقدّمة، طرق البحث، النتائج، المناقشة، الخلاصة، الشكر والعرفان، المراجع، الجداول، قائمة بدليل الأشكال والصور والإيضاحات، ثَمَّ الأشكال والصور والإيضاحات. وتُكْتَب العناوين الرئيسة بخطٍ **غامق**، بينما تُكْتَب العناوين الفرعية بخطٍ *مائل*.

صفحة العنوان: وتشمل عنوان المقالة، أسماء الباحثين الكاملة وعناوين العمل كاملة. ويكتب الباحث المسؤول عن المراسلات اسمه مشارا إليه بنجمة، والبريد الإلكتروني الخاص به. ويجب أن يكون عنوان المقالة موجزا وواضحا ومعبرا عن فحوى (محتوى) المخطوط، وذلك لأهمية هذا العنوان لأغراض استرجاع المعلومات.

الملخص: المطلوب كتابة فقرة واحدة لا تزيد على مائتي كلمة، موضحة هدف البحث، والمنهج المتبع فيه والنتائج وأهم ما توصل إليه الباحثون.

الكلمات الدالة: يجب أن يلي الملخص قائمة من 4-6 كلمات دالة تعبر عن المحتوى الدقيق للمخطوط لأغراض الفهرسة.

PACS: يجب إرفاق الرموز التصنيفية، وهي متوافرة في الموقع http://www.aip.org/pacs/pacs06/pacs06-toc.html.

المقدمة: يجب أن توضّح الهدف من الدراسة وعلاقتها بالأعمال السابقة في المجال، لا أن تكون مراجعة مكثفة لما نشر (لا تزيد المقدمة عن صفحة ونصف الصفحة مطبوعة).

طرائق البحث (التجريبية / النظرية): يجب أن تكون هذه الطرائق موضحة بتفصيل كاف لإتاحة إعادة إجرائها بكفاءة، ولكن باختصار مناسب، حتى لا تكون تكرارا للطرائق المنشورة سابقا.

النتائج: يستحسن عرض النتائج على صورة جداول وأشكال حيثما أمكن، مع شرح قليل في النص ومن دون مناقشة تفصيلية.

المناقشة: يجب أن تكون موجزة وتركز على تفسير النتائج.

الاستنتاج: يجب أن يكون وصفا موجزا لأهم ما توصلت إليه الدراسة ولا يزيد عن صفحة مطبوعة واحدة.

الشكر والعرفان: الشكر والإشارة إلى مصدر المنح والدعم المالي يكتبان في فقرة واحدة تسبق المراجع مباشرة.

المراجع: يجب طباعة المراجع بأسطر مزدوجة ومرقمة حسب تسلسلها في النص. وتكتب المراجع في النص بين قوسين مربعين. ويتم اعتماد اختصارات الدوريات حسب نظام Wordlist of Scientific Reviewers.

Subscription Form

Jordan Journal of PHYSICS

An International Peer-Reviewed Research Journal issued by the Support of the Scientific Research and Innovation Support Fund

Published by the Deanship of Research & Graduate Studies, Yarmouk University, Irbid, Jordan

Name: ..... الأسم:

Specialty:..... التخصص:

Address: ..... العنوان:

P.O. Box:..... صندوق البريد:

City & Postal Code: ..... المدينة/الرمز البريدي:

Country: ..... الدولة:

Phone: ..... رقم الهاتف:

Fax No:..... رقم الفاكس:

E-mail:..... البريد الإلكتروني:

No. of Subscription: ..... عدد الإشتراكات:

Method of Payment:..... طريقة الدفع:

Amount Enclosed:..... المبلغ المرفق:

Signature: ..... التوقيع:

Cheques should be paid to Deanship of Research and Graduate Studies - Yarmouk University.

I would like to subscribe to the Journal
For

- One Year
- Two Years
- Three Years

One Year Subscription Rates

	Inside Jordan	Outside Jordan
Individuals	JD 8	€ 40
Students	JD 4	€ 20
Institutions	JD 12	€ 60

Correspondence

Subscriptions and Sales:

Prof. Muhammad S. Bawa'aneh
Deanship of Research and Graduate Studies
Yarmouk University
Irbid – Jordan
Telephone: 00 962 2 711111 Ext. 2074
Fax No.: 00 962 2 7211121

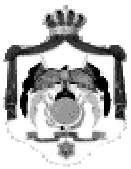

المملكة الأردنية الهاشمية

جامعة اليرموك

المجلة الأردنية
للفيزياء

مجلة بحوث علمية عالمية متخصصة محكّمة

تصدر بدعم من صندوق دعم البحث العلمي والابتكار

المجلد (18)، العدد (5)، كانون أول 2025م / رجب 1447هـ

المجلة الأردنية

للفيزياء

مجلة بحوث علمية عالمية محكّمة

المجلد (18)، العدد (5)، كانون أول 2025م / رجب 1447هـ

المجلة الأردنية للفيزياء: مجلة علمية عالمية متخصصة محكّمة تصدر بدعم من صندوق دعم البحث العلمي والإبتكار، عمان، الأردن، وتصدر عن عمادة البحث العلمي والدراسات العليا، جامعة اليرموك، إربد، الأردن.

ترسل البحوث إلى العنوان التالي:

الأستاذ الدكتور محمد سالم بواعنة

رئيس تحرير المجلة الأردنية للفيزياء

عمادة البحث العلمي والدراسات العليا، جامعة اليرموك

إربد ، الأردن

هاتف 7211111 2 962 00 **فرعي** 2074

E-mail: *jjp@yu.edu.jo* **Website**: *http:// jjp.yu.edu.jo*